Microstructure-based Constitutive Models for Residual Mechanical Behavior of Aluminum Alloys after Fire Exposure

Patrick Timothy Summers

Dissertation submitted to the faculty of the Virginia Polytechnic Institute and State University in partial fulfillment of the requirements for the degree of

Doctorate of Philosophy
In
Mechanical Engineering

Brian Y. Lattimer
Scott W. Case
Robert L. West
Norman E. Dowling
Raffaella De Vita

March 28, 2014
Blacksburg, VA

Keywords: aluminum, residual, post-fire, yield strength, strain hardening, constitutive model, kinetics, microstructure

Microstructure-based Constitutive Models for Residual Mechanical Behavior of Aluminum Alloys after Fire Exposure

Patrick Timothy Summers

ABSTRACT

Aluminum alloys are increasingly being used in a broad spectrum of applications such as lightweight structures, light rail, bridge decks, marine crafts, and off-shore platforms. The post-fire (residual) integrity of aluminum structures is of particular concern as a severe degradation in mechanical properties may occur without catastrophic failure, even for short duration, low intensity fires. The lack of research characterizing residual mechanical behavior results in an unquantified mechanical state of the structure, potentially requiring excessively conservative repair. This research aims to develop an in-depth understanding of the mechanisms governing the residual aluminum alloys so as to establish a knowledge-base to assist intelligent structural repair.

In this work, the residual mechanical behavior after fire exposure of marine-grade aluminum alloys AA5083-H116 and AA6061-T651 is characterized by extensive mechanical testing. Metallography was performed to identify the as-received and post-fire microstructural state. This extensive characterization was utilized to develop constitutive models for the residual elasto-plastic mechanical behavior of the alloys. The constitutive models were developed as a series of sub-models to predict (i) microstructural evolution, (ii) residual yield strength, and (iii) strain hardening after fire exposure.

The AA5083-H116 constitutive model was developed considering the microstructural processes of recovery and recrystallization. The residual yield strength was calculated considering solid solution, subgrain, and grain strengthening. A recovery model was used to predict subgrain growth and a recrystallization model was used to predict grain nucleation and growth, as well as subgrain annihilation. Strain hardening was predicted using the Kocks-Mecking-Estrin law modified to account for the additional dislocation storage and dynamic recovery of subgrains. The AA6061-T651 constitutive model was developed considering precipitate nucleation, growth, and dissolution. A Kampmann-Wagner numerical model was used to predict precipitate size distribution evolution during elevated temperature exposure. The residual yield strength was

calculated using solid solution and precipitate strengthening, considering both shearable and non-shearable precipitates. A modified KME law was used to predict residual strain hardening considering the additional effects of the precipitate-dislocation interactions, focusing on the efficient of dislocation (Orowan) loop storage and recovery about the precipitates. In both cases, the constitutive models were bench-marked against experimental data.

Every honest researcher I know admits he's just a professional amateur. He's doing whatever he's doing for the first time. That makes him an amateur. He has sense enough to know that he's going to have a lot of trouble, so that makes him a professional.

Charles Franklin Kettering

The scientist does not study nature because it is useful; he studies it because he delights in it, and he delights in it because it is beautiful. If it were not beautiful, it would not be worth knowing, and if nature were not worth knowing, life would not be worth living.

Jules Henri Poincaré

Dedication

For Kristy, you have brought me more happiness than I ever thought possible. Your patience as I pursued my dreams puts me forever in your debt.

For my parents and brother, you have supported me throughout my entire academic career, from kindergarten before I had any idea of what I could become to this moment which I have dreamt to achieve for so long. Thank you.

Acknowledgements

I would like to thank the following people without whom this work would not be possible:

- Prof. Brian Lattimer for your continual guidance, mentoring, and support throughout this long journey from undergrad to MSME to PhD. It has been a long uphill trek which would have never been completed had it not been for your help.
- Prof. Scott Case for your support, guidance, and patience along the way to accomplishing this goal. It is safe to say without your guidance has been invaluable in completion of this work.
- Profs. Robert West, Raffaella De Vita, and Norman Dowling for willingly sharing their insight and wisdom during this endeavor.
- The other members of the EXTREME Lab and MRG both past and present for your friendship, advice, and the many discussions, both research related and non-research related, to help pass the time and turn this experience into a fruitful one in so many ways.
- David Simmons and Darryl Link in the ESM machine shop for help and advice which greatly aided manufacture and machining of the numerous parts needed for this research.
- Mac McCord for helping countless times with mechanical, and other, testing details.
- Chris Winkler and Steve McCartney at the NCFL for help in SEM and TEM prep work including learning about machines I could not have dreamed of knowing how to use only a few short years ago.
- Jackie Woodyard for working on all of the behind the scenes pieces to make sure the research continues without a hitch.

Table of Contents

List of Figures

List of Tables

Nomenclature

SYMBOL	DESCRIPTION	UNITS
$\%RA$	tensile specimen reduction in area at fracture	%
A	current tensile specimen cross-sectional area	mm^2
A_0	initial tensile specimen cross-sectional area	mm^2
A_0	parameter related to the energy barrier for nucleation	kJ/mol
b	magnitude of the Burger's vector	m
B	heating rate	°C/min
C_{Mg}	Mg solid solution matrix concentration	wt%
C_{Mg}^0	total Mg concentration in the alloy	wt%
C_{Mg}^{eq}	equilibrium Mg concentration at the precipitate/matrix interface	wt%
$C_{Mg,0}^{eq}$	pre-exponential equilibrium concentration constant	wt%
C_{Mg}^i	Mg concentration at the precipitate/matrix interface	wt%
C_{Mg}^p	precipitate Mg concentration	wt%
d	grain size	m
d_{AR}	as-received grain size	m
d_{RX}	recrystallized grain size	m
D_0	pre-exponential constant for Mg diffusion	m^2/s
E	Young's modulus	Pa
e_{xx}	engineering strain in longitudinal direction	mm/mm
f_v	precipitate volume fraction	--
F	precipitate (obstacle) strength	Pa
$\overline{F}$	mean precipitate (obstacle) strength	Pa
F	deformation gradient	--
G	shear modulus	Pa
H	Mg solid solution strengthening constant (AA5083)	MPa/ (Mg wt%)^n
H_{Mg_2Si}	equivalent solid solution strengthening constant for Mg and Si	MPa/ (Mg wt%)$^{2/3}$
H_{Mg}	Mg solid solution strengthening constant (AA6061)	MPa/ (Mg wt%)$^{2/3}$
H_{Si}	Si solid solution strengthening constant	MPa/ (Si wt%)$^{2/3}$
H_{Cu}	Cu solid solution strengthening constant	MPa/ (Cu wt%)$^{2/3}$
H	Lagrangian displacement gradient	--
I	identity matrix	--
j	steady state precipitate nucleation rate	$\#/m^3$-s
j_0	pre-exponential term to the nucleation rate	$\#/m^3$-s
k	dislocation storage parameter for subgrains	$1/m^2$
k_1	proportionality constant for dislocation storage	1/m
k_2	proportionality constant for dynamic recovery	--

k_3	proportionality constant for dynamic recovery including subgrains	--
k_g	Hall-Petch constant for grains	MPa/m$^{1/2}$
k_{sg}	Hall-Petch constant for subgrains	MPa/m$^{1/2}$
k_Γ	precipitate line tension constant	--
k_β	constant linking yield strength to the reference state dynamic recovery rate β_0	--
$k_{\theta dp}$	constant for dynamic precipitation effects on θ	Pa
K	grain growth function	--
K_{sg}	subgrain dynamic recovery parameter proportional to volume fraction of subgrain boundaries	m
K_0	pre-exponential constant for subgrain recovery	--
l	precipitate spacing in the dislocation glide plane	m
l_p	precipitate length	m
l	current tensile specimen gage length	m
l_0	initial tensile specimen gage length	m
L	total nuclei array length per unit volume	1/mm^2
L_0	mean value of y_a for an alloy	m
M	Taylor factor	--
n	solid solution strengthening exponent	--
N	precipitate number density in a class i	#/m^3
N_0	nuclei per unit array length	1/mm
N_v	recrystallization nuclei density	1/mm^3
$p(0)$	Poisson distribution	--
P	applied load	N
P	instantaneous stored energy	kJ/mol
P_0	stored energy of deformation in as-received material	kJ/mol
P_1	subgrain dislocation storage rate	Pa^2
P_2	total dynamic recovery rate including subgrain effects	--
Q_0	recovery activation energy at long times	kJ/mol
Q_{app}	recovery apparent activation energy	kJ/mol
Q_d	activation energy for Mg diffusion in Al	kJ/mol
Q_{DSC}	DSC heat flow	mW/mg
Q_{eq}	apparent solvus boundary enthalpy	kJ/mol
Q_g	activation energy for grain boundary growth	kJ/mol
Q_{RX}	recrystallization activation energy from DSC	kJ/mol
r	precipitate radius	m
$\bar{r}$	mean precipitate radius	m
r_c	critical radius for precipitate nucleation	m
r_{cl}	precipitate radius at loss of coherency	m
r_{trans}	precipitate radius for transition from dislocation shearing to dislocation (Orowan) looping	m
R	universal gas constant, 8.314	J/mol-K
R_g	grain radius growth function	m
$\mathbf{R}$	rotation tensor	--

S_{RX}	interfacial area density separating recrystallized and untransformed material	m^2/ m^3
S_{xx}	nominal (engineering) stress in axial direction	Pa
t	time	s
t_d	traveling time between dislocations of opposite sign	s
t_p	traveling time between a precipitate and another with a dislocation (Orowan) loop	s
T	temperature	°C or K
T_p	reaction peak temperature from DSC	K
$\mathbf{U}$	right stretch tensor	--
$\mathbf{u}$	displacement vector	mm
v	precipitate growth rate	m/s
v_g	Arrhenius grain growth rate	m/s
v_0	pre-exponential growth rate constant	m/s
v_r	relative dislocation velocity	m/s
$\langle v \rangle_{CH}$	Cahn-Hagel growth rate	m/s
V_m	molar volume of the precipitate	m^3/mol
$\mathbf{X}$	position vector in Lagrangian (material) description	mm
X_{RV}	recovered volume fraction	--
X_{RX}	recrystallized volume fraction	--
y_a	annihilation distance between two dislocation of opposite sign	m
y_0	annihilation distance between two dislocations of opposite sign in a pure alloy	m
y_p	annihilation distance between two dislocations of opposite sign when at least one precipitate with a dislocation (Orowan) loop is encountered during the time required to meet another dislocation	m

Greek

α	material factor connecting dislocation density to flow stress	--
α_g	recrystallized grain shape factor	--
β	dynamic recovery rate for a commercial (real) alloy	--
β_0	dynamic recovery rate for a pure alloy (reference state)	--
β_{min}	minimum dynamic recovery rate measured from T6 state	--
β_p	increased dynamic recovery rate due to a precipitate with a dislocation (Orowan) loop	--
δ	subgrain (dislocation cell) size	m
δ_{AR}	as-received subgrain (dislocation cell) size	m
ΔH	enthalpy of reaction	mJ/mg
$\boldsymbol{\varepsilon}^{\mathbf{L}}$	logarithmic strain tensor	mm/mm
ε_f^L	logarithmic fracture strain	mm/mm

ε_{xx}^{L}	logarithmic strain in the longitudinal direction	mm/mm
κ	activation energy constant in recovery model	--
κP_0	apparent activation energy correction constant	kJ/mol
γ	precipitate/matrix interface energy	J/m^2
$\langle\lambda\rangle$	average chord length (size) of recrystallized grains	m
λ_{xx}	stretch in longitudinal direction	--
ξ	precipitate aspect ratio	--
ν	mean number of precipitates before two dislocations meet	--
ν_φ	mean number of precipitates met with an efficiently stored dislocation (Orowan) loop before two dislocations meet	--
θ_m	average subgrain misorientation angle	rad
θ	dislocation storage parameter for a commercial (real) alloy	Pa
θ_0	dislocation storage parameter for a pure alloy	Pa
θ_{dp}	dynamic precipitate dislocation storage contribution	Pa
θ_{II}	dislocation storage rate for a pure material	Pa
θ_{RX}	dislocation storage rate in recrystallized state	Pa
φ	Orowan loop storage efficiency	--
ρ	dislocation density	$\#/m^3$
σ	Cauchy (true) stress	Pa
$\sigma_{0.2\%}$	0.2% offset yield strength	Pa
σ_0	friction stress	Pa
σ_d	dislocation forest hardening	Pa
σ_g	grain strengthening	Pa
σ_p	precipitate strengthening	Pa
σ_{pure}	Al matrix strength without solutes	Pa
σ_{sat}	saturation stress	Pa
σ_{sg}	subgrain strengthening	Pa
σ_{ss}	solid solution strengthening	Pa
σ_{xx}	Cauchy (true) stress in the longitudinal direction	Pa
σ_u	Ultimate strength	Pa
σ_y	yield strength	Pa
$\sigma_{y,AR}$	as-received yield strength	Pa
$\sigma_{y,RX}$	recrystallized yield strength	Pa
σ_y^{max}	maximum yield strength (as-received T6 state)	Pa

1 Introduction

Aluminum alloys are increasingly being used in a broad spectrum of applications such as lightweight structures, light rail, bridge decks, marine crafts, and off-shore platforms. This is in large part due to aluminum's low density, moderate cost, formability/extrudability, good mechanical properties, and corrosion resistance. The increasing use of aluminum alloys has been drive by a focus on reducing weight and improving overall structure strength through use of complex sections. This has led to frequent use in critical load-bearing structures, especially where weight is a primary concern, e.g., the deckhouse in a naval vessel or helicopter landing deck on an off-shore platform (Fig. 1).

Fig. 1. Aluminum helicopter deck on offshore processing platform [1]. [Fair use determination attached in Appendix C]

An example of possible catastrophic fire damage for an offshore platform structure is shown in Fig. 2. This incident provides stark evidence of the effects of fire on such structures in rare circumstances. In the case where catastrophic failure does not occur, the structure may be excessively damaged, resulting in extremely high repair costs. Localized, shorter duration fires are a much more common occurrence, possibly resulting in significant material damage requiring localized repair. This post-fire (residual) damage occurs due to a fundamental change in material microstructural state that, for aluminum alloys, governs mechanical properties and behavior. A

structure subjected to such fire conditions requires evaluation for structural stability and assessment for damaged material replacement. Extremely limited research currently exists [2] characterizing residual aluminum alloy mechanical behavior after fire exposure to support such an effort. Some work has been performed on residual aluminum alloy mechanical behavior after a simulated weld exposure [3–5]; however, this work has limited applicability to fire exposures due exceedingly high heating rates and short exposure durations. Thus, experimental characterization of the residual mechanical behavior of aluminum alloys after fire exposure is needed to appropriate repair measures to both ensure structural stability and minimize repair costs. Likewise, a fundamental understanding of the microstructural mechanisms governing residual mechanical behavior, including their evolution due to fire, is needed.

Fig. 2. Fire damage and structural collapse of the steel structure of an offshore platform off the coast of Australia [6]. [Fair use determination attached in Appendix C]

In this work, extensive characterization of the residual mechanical behavior of the marine-grade aluminum alloys AA5083-H116 and AA6061-T651 was performed. These alloys were selected for characterization as they are commonly used in marine crafts and represent two distinct microstructural states, i.e., strain hardened (AA5083-H116) and precipitation hardened (AA6061-T651). Metallographic examination was performed to aid an understanding of the microstructural mechanisms governing residual strength, including its evolution due to fire exposure. This understanding was used to develop separate physically-based constitutive models to predict

residual mechanical behavior of the alloys after fire exposure. The models consist of (i) alloy-specific microstructural evolution laws, (ii) physically-based residual yield strength models comprising sub-models for the individual strengthening contributions of identified mechanisms, and (iii) an internal variable model to predict residual strain hardening as the competitive evolution of dislocation storage and dynamic recovery. The constitutive models are verified and bench-marked against experimental data.

This work is presented in the following chapters organized in the form of papers with relevant literature review of each topic included in individual chapters. The chapters are organized in the following manner:

- Chapter 2 – The residual mechanical behavior of the marine-grade aluminum alloys is characterized after simulated (non-isothermal) fire exposure. The mechanisms governing residual yield strength and strain hardening are introduced and discussed relative to residual property measurements.
- Chapter 3 – The AA5083-H116 constitutive model for residual mechanical behavior is developed. The governing microstructural mechanisms are discussed in further detail, relating the microstructural evolution processes, i.e., recovery and recrystallization, to residual strength. Physically-based microstructural evolution models are developed and implemented in a unified framework to predict residual elasto-plastic mechanical behavior. The model is compared against experimental data from Chapter 2.
- Chapter 4 – The AA6061-T651 constitutive model for residual mechanical behavior is developed. Model development is performed similar to that for AA5083-H116; however, a different governing microstructural process (precipitate nucleation, growth, and coarsening) is modeled. A similar, though adapted, unified framework to predict residual elasto-plastic mechanical behavior is presented. The model is compared against experimental data from Chapter 2.
- Chapter 5 – The AA5083-H116 and AA6061-T651 constitutive models are bench-marked against experiments on linearly heated and isothermally soaked specimens. The constitutive models were found to well represent the data, thus demonstrating their utility for predicting the residual mechanical behavior of arbitrarily heated materials, such as those in a real fire exposure.

2 Residual Constitutive Behavior of Aluminum Alloys

2.1 Introduction

Aluminum alloys are increasingly being used in a broad spectrum of applications such as lightweight structures, light rail, bridge decks, marine crafts, and off-shore platforms. Fire safety o is a major concern in the design of both land-based and marine aluminum structures. Limited research has been conducted on the residual mechanical behavior of aluminum following fire. This is an important issue that requires consideration to effectively evaluate the structural stability following a fire and assess replacement of structural elements exposed to fire conditions. The research presented in this chapter pertains to the residual mechanical behavior of 5xxx and 6xxx-series aluminum alloys at ambient conditions following a fire exposure.

Mechanical property degradation following an elevated temperature exposure can in part be understood through the strengthening mechanisms, which are different for each alloy type. 5xxx-series alloys are strain hardened and primarily attain their strength through grain refinement [7]. The primary reduction in strength is caused by recrystallization upon annealing (250 – 350°C), which destroys grain refinement [8]. Dislocation recovery and precipitate growth at lower temperatures (150 – 250°C) also reduce strength through subgrain coarsening [9] and dilution of the Mg solid solution content in the aluminum matrix [10]. Recrystallization is known to be a kinetic (time-temperature dependent) process [11]; therefore, strength reduction is also expected to be a kinetic process. 6xxx-series alloys are precipitation hardened (heat treated) and primarily attain their strength through precipitate growth under controlled heating (aging) to a desired state (e.g., T4 or T6) [8,12]. Elevated temperature exposure causes further precipitate growth (overaging) and strength reduction [13]. Precipitate growth, and the resulting strength reduction, has also been shown to be a kinetic process [14–16]. Due to the kinetic nature of the governing strengthening mechanisms, the residual mechanical properties must be characterized in terms of both exposure temperature and heating rate. Studies considering only exposure temperature are inadequate to fully understand residual mechanical behavior after fire.

Residual mechanical properties of 5xxx and 6xxx-series aluminum alloys have been quantified for specimens subjected to an isothermal exposure for different durations [2,17]. In these studies, AA5083-H116 and AA6082-T651 specimens were exposed to isothermal heating (100 – 500°C)

for different durations (up to 2 h) to evaluate the impact of temperature and soak time on residual mechanical properties following exposure. The primary strength reduction in both alloys occurred from 200 – 400°C, leading to decreases in yield strength of 37% and 67% for AA5083-H116 and AA6082-T651, respectively. The magnitude of the strength reduction was shown to be dependent on both isothermal exposure temperature and duration. However, experiments were performed using the same heating rate with different soak times. This makes it difficult to clearly quantify the kinetic nature of the residual mechanical properties. In addition, the coarse temperature increments produce uncertainty in the transitions in properties, limiting the ability to relate the property change with the microstructural evolution.

The effect of heating rate on aluminum residual strength following a fire can also be attained through research performed on aluminum welds. The welding process causes the parent material to experience spatially varying thermal histories with maximum temperatures and heating/cooling rates dependent on distance from the weld. Gallais, *et al.* [4] extracted micro-tensile specimens from different zones of an AA6056 friction stir weld. Lower yield stresses were measured for zones closer to the welded region; however, properties were not correlated to specific thermal histories. Maisonette, *et al.* [3] studied AA6061-T6 exposed at heating rates of 30 – 1200°C/min. A significant heating rate dependence was observed. Exposure at 30 and 1200°C/min to 400°C resulted in yield strengths of 90 MPa and 170 MPa, respectively. Additional data is needed to quantify residual mechanical properties (i.e., yield strength, ultimate strength, ductility) at intermediate exposure temperatures and heating rates; specifically at refined intervals to relate to microstructural evolution.

In this work, an experimental study was performed to investigate the detailed evolution and kinetic-dependence of aluminum alloy residual mechanical behavior. The previously discussed studies are extended, focusing on the governing influence of material microstructure. The aluminum alloys included in this work, AA5083-H116 and AA6061-T651, were selected due to their prevalence as common structural alloys and their different strengthening mechanisms. The residual mechanical behavior was characterized as a function of temperature and heating rate, specifically those expected during fire. Uniaxial tension tests were used to quantify the residual mechanical behavior at ambient conditions for specimens previously exposed to 100 – 500°C at heating rates of 5 – 250°C/min. The stress-strain relations are presented and used to quantify

changes in Young's modulus, yield strength, ultimate strength, and plastic flow (strain hardening) characteristics. The residual strength degradation mechanisms will be discussed in terms of the microstructural changes in the alloys.

2.2 Experimental

2.2.1 Materials and Test Specimens

The materials included in this study are AA5083-H116 and AA6061-T651. AA5083 is strengthened by strain hardening (cold work). It is a weldable, moderate strength alloy which exhibits good corrosion resistance in the H116 condition. AA6061 is strengthened by precipitation hardening (heat treatment). It is a weldable, high strength alloy which also exhibits good corrosion resistance. The chemical composition of the alloys received from Alcoa (Pittsburgh, PA) are shown in Table 1.

Table 1. Chemical composition (wt%) of AA5083-H116 and AA6061-T651.

Alloy	**Si**	**Fe**	**Cu**	**Mn**	**Mg**	**Cr**	**Zn**	**Ti**	**Al**
5083-H116	0.11	0.24	0.06	0.57	4.4	0.09	0.02	0.02	bal
6061-T651	0.66	0.4	0.24	0.07	0.9	0.18	0.02	0.02	bal

Rectangular dog-bone specimens were machined from the as-received plate with the longitudinal axis oriented in the rolling direction. The specimens had an overall length of 169.2 mm with a gage length and width of 50.8 and 12.7 mm, respectively. Specimen thickness was unchanged from the as-received plate thicknesses of 6.4 and 6.5 mm for AA5083 and AA6061, respectively.

2.2.2 Non-isothermal Heating

The room temperature residual mechanical properties were investigated by varying the thermal exposure on the specimens prior to mechanical testing. A constant, linear heating rate to prescribed temperatures was used followed by immediate water quenching. This process isolates the factors governing time-temperature dependent material evolution. This constant heating rate is an analog for the initial transient temperature increase during a fire.

Heating rates were developed through the results of transient thermal simulations conducted using Abaqus on an aluminum structure with varying thicknesses of insulation. The representative aluminum structure was a stiffened bulkhead that was donated to the EXTREME Lab (Fig. 3a). The Abaqus model was created to represent this structure. The model was created as a symmetric about the T-stiffener mid-line to reduce computational requirements. It comprises a 3 mm AA6061 plate with periodically attached T-sections (50 mm web, 35 mm flange, 3 mm thickness) and ceramic fiber insulation on the exposed surfaces of 0.0, 25.4, and 50.8 mm thickness (shown in Fig. 3b). The ceramic fiber insulation was applied on the T-stiffener side of the structure towards the simulated radiant heat source. The thermal boundary conditions on the insulated side of the model included the radiant heat source, convection, and re-radiation between the plate and T-stiffener. The thermal boundary conditions on the unexposed surfaces were radiation to ambient and convection. An insulated surface was applied at the T-stiffener mid-line to enforce symmetry. A UL 1709 [18] fire exposure, which is ambient to 1100°C in 300 s and remaining at this temperature for the exposure duration, was used as the fire exposure. The transient thermal results are shown in Fig. 4. The predicted temperatures shown were queried mid-length of the T-stiffener web along the mid-line. An effective heating rating rate was calculated using the material temperature rise from ambient to 50% of the steady-state temperature. Using this criterion, the effective heating rates for 0.0, 25.4, and 50.8 mm thick insulation were calculated as 250, 25, and 5°C/min, respectively. A heating rate of 20°C/min was also used to conduct a detailed material evolution study. This heating rate was chosen as it is widely used in TGA, DSC, and other techniques to characterize material evolution.

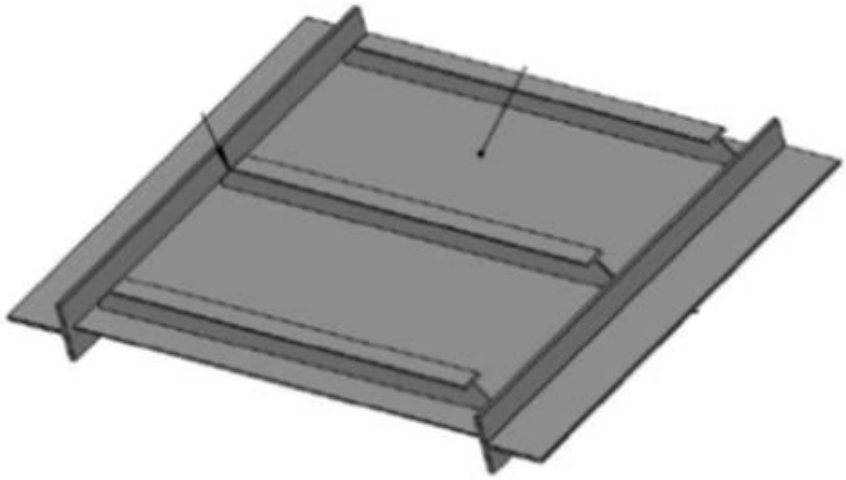

(a)

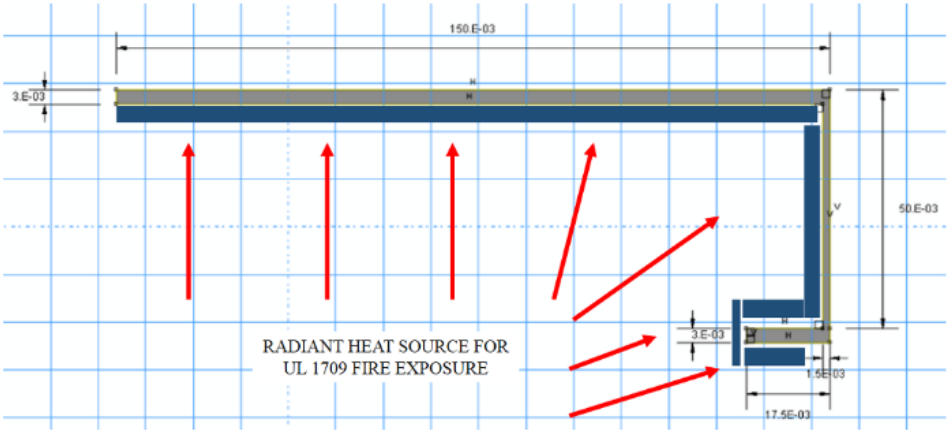

(b)

Fig. 3. Representative (a) aluminum bulkhead with T-stiffeners and (b) Abaqus transient thermal model for simulated UL 1709 fire exposure.

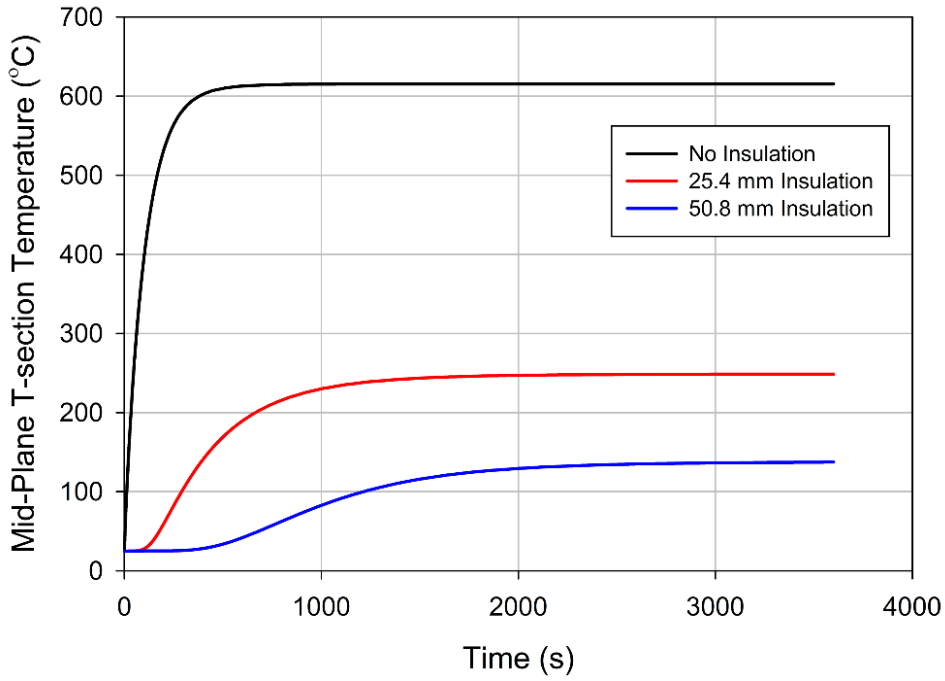

Fig. 4. Abaqus transient heat transfer model results for UL 1709 on stiffened aluminum bulk with varying thicknesses of insulation.

Sample heating was achieved using an induction heater (Ameritherm 5060LI). The specimens were heated from ambient to prescribed temperatures (up to 500°C) then immediately quenched in water, thereby arresting material microstructural evolution. The induction heater was controlled using a Micro-Epsilon optical pyrometer (8 – 14 μm spectral range) and a Watlow PID controller. An optically thick layer of Rust-Oleum® Specialty High Heat flat black enamel spray paint was applied on the sample surface to ensure accurate temperature control using the pyrometer. Thermal camera and embedded thermocouple temperature measurements were used to determine the temperature-dependent paint emissivity as 0.95 – 0.99 [19]. The induction heater coils were designed as shown in Fig. 5 to maintain temperature uniformity in the specimen gage section. Specimen heating was monitored using a FLIR SC655 (7.5 – 14 μm spectral range) thermal camera, providing full field temperature measurement. The central 25.4 mm gage length was maintained within 1% of the desired temperature for the lower heating rates (5, 20, 25°C/min) and within 3% at 250°C/min.

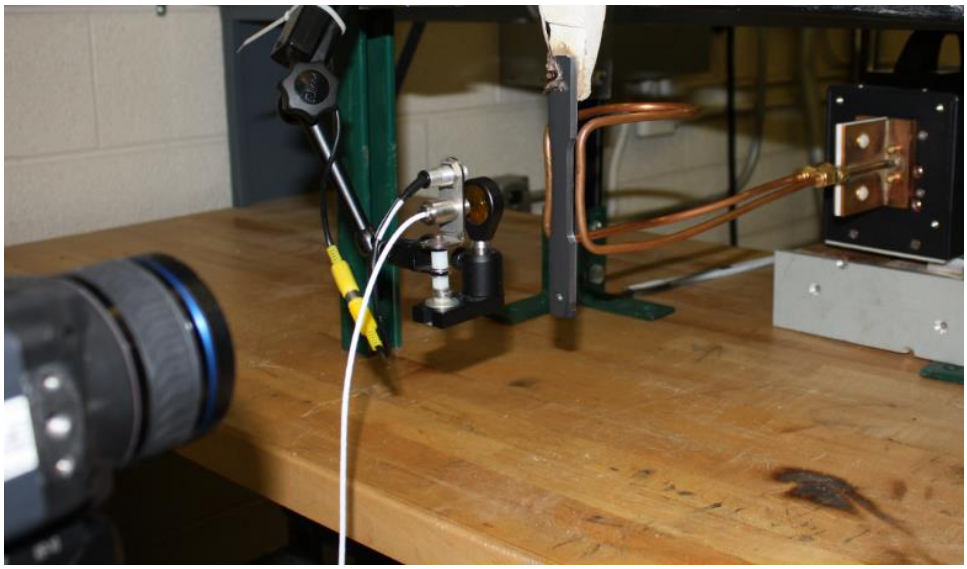

Fig. 5. Induction heater with optical pyrometer and thermal camera.

2.2.3 Mechanical Characterization

Uniaxial, quasi-static tension tests were performed at ambient conditions on previously heated samples using an Instron 5984 150 kN electro-mechanical testing machine. The tensile tests were performed at a constant displacement rate of 3 mm/min, corresponding to an initial strain rate of 10^{-3}/s. Deformation was measured using strain gages and a 3-D digital image correlation (DIC) system.

The strain gages were Vishay Micro-Measurements CEA-13-125UW-350 with a grid (gage) length of 3.175 mm. Strain gages were adhered at the center of the uniform temperature region as measured during heating using the thermal camera. The exact location differed slightly for each specimen but was approximately the specimen gage length center. The adhesive selected (Vishay Micro-Measurements M-Bond 200) cures at ambient conditions to ensure an unchanged material state.

DIC is a non-contact optical technique to measure full-field deformation of an object's surface. A stereoscopic pair of cameras are used to image a speckle-seeded object undergoing deformation. The DIC technique tracks the gray values in small neighborhoods (called subsets) during deformation. The principles of digital image correlation for material deformation were initially researched by Peters and Ranson [20] for 2-D DIC and Sutton, *et al.* [21]. An extensive overview

of DIC principles and techniques is provided by Sutton, *et al.* [22]. In addition to providing full-field deformation measurement, DIC allows for quantification of specific and multiple areas of interest.

In this work, a commercial 3-D DIC system from Correlated Solutions was used to measure full-field material deformation. The experimental 3-D DIC setup is shown in Fig. 6. High resolution (1600 x 1200 pixel), 14-bit images were captured using two Allied Vision Technologies Prosilica GX 1660 CCD cameras equipped with 100 mm Tokina f/8.0 lenses. The cameras were mounted on a tripod a distance of 0.6 m from the specimen and aligned such that the high pixel count axis was parallel to the loading axis. 3-D DIC systems require calibration for both displacement and strain calculation [23]. System calibration was performed using a calibration grid of pre-defined circular dots that was translated and rotated in the measurement area while synchronized images were acquired by both cameras. Since the spacing and size of the calibration grid was known, the parameters required for calibration of the pin-hole projection based stereo-vision model could be determined [24].

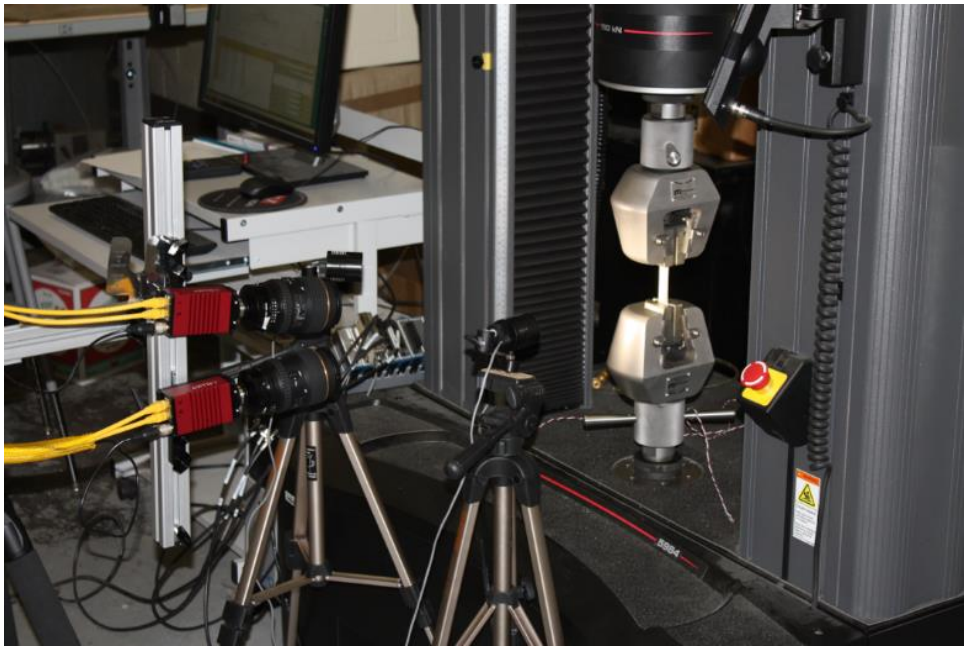

Fig. 6. 3-D digital image correlation system for displacement measurement during quasi-static tensile testing.

Accurate DIC displacement measurements require a random contrasting speckle pattern on the specimen surface with an optimal spatial variation for the given measurement. Prior to tension

testing, all specimens were painted using Rust-Oleum® Specialty High Heat flat white and black enamel spray paint. This paint was found to provide improved surface bonding and ductility compared to similar paints. An optimal speckle size between 0.05 and 0.4 mm was maintained. An example speckle pattern is shown in Fig. 7.

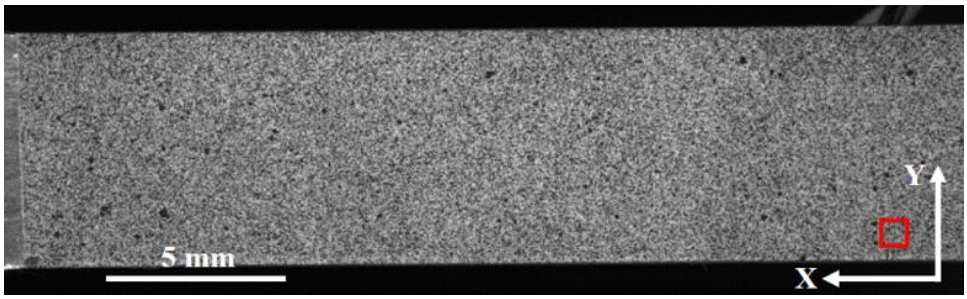

Fig. 7. Typical speckle pattern for DIC measurements. The subset size is shown (red square) by the labeled axes for comparison to the speckle size and specimen dimensions.

The DIC analysis was performed using Vic3D 2010, a commercial 3-D DIC software developed by Correlated Solutions. An "area of interest" was defined encompassing the speckle pattern over the specimen's gage length. A subset size of 41 by 41 pixels and a step size of 4 pixels were used for correlation. The subset size is shown relative to the specimen and speckle size in Fig. 7. The subset size was chosen to reduce noise and improve strain calculation accuracy. The step size enables measurement of localized strain gradients without significant averaging. If necessary, a coordinate transformation was performed to ensure the loading axis was aligned with the correlated x-direction (see Fig. 7 for definition). Subset correlation was performed using the normalized sum of squared differences criterion. The correlation optimization algorithm requires a continuous representation of the discrete gray levels in the image subsets. Therefore, an 8-tap Basis spline was used to reconstruct the discrete information as a continuous function via interpolation. Displacements and strains were averaged over a 25.4 mm gage length, which was centered on the highest temperature location measured during the prior thermal exposure.

2.2.4 Strain Calculation

Numerous strain definitions exist for analysis and modeling of material deformation. Limitations exist for specific definitions; therefore, the selected strain definition should be appropriate for its intended application. Strain gages allow for calculation of engineering strain, which is appropriate

for small strain analysis**.** The DIC displacement measurements can be used to calculate strains defined in terms of the measured displacement and deformation gradient.

The strain gage measurement of engineering strain is calculated as

$$e_{xx} = \frac{l - l_0}{l} = \lambda_{xx} - 1 \tag{1}$$

where e_{xx} is engineering strain in the axial direction, l is the current gage length (mm), l_0 is the reference (undeformed) gage length (mm), and λ_{xx} is the stretch ($\lambda = l/l_0$) in the axial direction. Engineering strain may be converted to the logarithmic (Hencky) strain definition. Logarithmic strain is calculated by integrating incremental strain, resulting in

$$\varepsilon_{xx}^{L} = \ln(1 + e_{xx}) \tag{2}$$

where ε_{xx}^{L} is logarithmic strain in the axial direction. Logarithmic strain accounts for the strain path and is appropriate for material deformation with large strains and large rotations. It is work-conjugate (defined as the pair of stress and strain rate definitions which results in calculation of work per unit volume) with Cauchy (true) stress. Logarithmic strain is the strain measure used most often in metal plasticity analysis and will be used as the primary strain definition in this work.

The full-field surface strains calculated using DIC are best understood through consideration of the displacement field measurement. The selected area of interest is divided into square subsets. A unique pattern is formed by the discrete matrix of pixel gray levels in each subset. A shape function is used to map the positions of the undeformed (reference) subsets to their positions after deformation. A correlation method is applied within the software (e.g., Vic3D) to determine the shape function coefficients based on the images. At this point, the displacements (u, v, w) that map the arbitrary reference points (X, Y, Z) to their deformed position (x, y, z) are known. The known displacements are used to define a field of vectors at the subset centers which are separated by the step size. This field of displacement vectors is subsequently used to calculate strain.

The Vic3D strain computation algorithm follows a procedure similar to that for a constant strain triangle in finite element analysis. The displacement vector field at the subset centers is divided into triangles. The triangles are associated with a reference state and the current deformed state.

The rigid body motion is easily removed using the displacement vectors. The strains are calculated from the three displacement vectors associated with each individual triangle. In general, the displacement gradient is calculated from the displacement vectors as

$$\mathbf{H} = \begin{bmatrix} \frac{\partial u}{\partial X} & \frac{\partial u}{\partial Y} \\ \frac{\partial v}{\partial X} & \frac{\partial v}{\partial Y} \end{bmatrix} \tag{3}$$

where **H** is the material displacement gradient as calculated using the partial derivative of the displacements with respect to material coordinates (Lagrangian description). This is related to the material deformation gradient as

$$\mathbf{H} = \mathbf{F} - \mathbf{I} \tag{4}$$

where **F** is the deformation gradient and **I** is the identity matrix. **F** is formally defined as **I** + Grad **u**(**X**) where **X** is the position vector in the material (Lagrangian) configuration and **u**(**X**) is the displacement of that point. Polar decomposition is used to calculate the logarithmic strain in the material (Lagrangian) configuration from **F** = **RU**. The logarithmic (Hencky) strain is calculated as

$$\varepsilon^{L} = \ln \mathbf{U} \tag{5}$$

where $\boldsymbol{\varepsilon}^{\mathbf{L}}$ is the logarithmic strain tensor, **U** is the right stretch tensor, and **R** is the rotation tensor. This process results in calculation of the local strain for each triangle. The strain is calculated at each subset center using interpolation from the four surrounding triangles. This process is repeated for all subset centers. The calculated strain tensors tend to be noisy; therefore, a Gaussian decay filter, worth 10% at the edges, was applied with a total smoothing diameter of 15 points, or 60 pixels.

2.2.5 Stress Calculation

Cauchy (true) stress is the preferred stress measure for material behavior analysis as it the true measure of stress experience by the gage section during material testing. However, the current cross-sectional area during material deformation is unknown. The engineering (nominal) stress is

therefore the only stress definition that can be directly calculated from the applied load. Experimental observations have noted a negligible change in volume for metals during plastic deformation [25]. This justifies use of an isochoric assumption to calculate Cauchy stress in terms of the undeformed area as

$$\sigma_{xx} = \frac{P}{A} = \frac{P}{A_0}\frac{l}{l_0} = S_{xx}\lambda_{xx} \tag{6}$$

where σ_{xx} is Cauchy stress (MPa), P is applied load (N), A is the current area (mm^2), A_0 is the undeformed (reference) area (mm^2), and S_{xx} is nominal stress (MPa). The isochoric assumption and above relation is valid between material yielding and until the material reaches plastic instability (necking).

The axial material stretch, λ_{xx}, in Eq. (6) may be defined in terms of the strain measures. Cauchy stress is solved for in terms of engineering strain as

$$\sigma_{xx} = S_{xx}(1 - e_{xx}) \tag{7}$$

and in terms of the logarithmic strain as

$$\sigma_{xx} = S_{xx}\exp(\bar{\varepsilon}^L_{xx}) \tag{8}$$

where $\bar{\varepsilon}^L_{xx}$ is the average logarithmic strains in the axial directions for all points in the defined DIC measurement region.

2.3 Results

Residual mechanical behavior of AA5083-H116 and AA6061-T651 following a fire exposure is provided through stress-strain relations as well as property values. Small strain analysis (i.e., Young's modulus and yield strength) was performed using the strain gage measurements. Large strain analysis (i.e., plastic behavior, ultimate strength, and fracture) was performed using DIC measurements. Analysis was performed using the logarithmic (Hencky, ε^L_{xx}) strain definition. The analysis was also performed in terms of both nominal (engineering, S_{xx}) and Cauchy (true, σ_{xx}) stress. The preferred measure in material behavior analysis is Cauchy stress. However, it is

derived from nominal stress using an isochoric assumption, which holds only at strains prior to plastic instability (necking). As a result, nominal stress was used to analyze complete material behavior, including necking and fracture. For all discussed results and analysis, the maximum exposure temperature reached during prior material elevated temperature exposure is referred to simply as temperature.

2.3.1 Stress-Strain Relations

The residual stress-strain behavior of AA5083-H116 and AA6061-T651 after heating at 20°C/min are shown in Fig. 8 to Fig. 10. The Cauchy stress-logarithmic strain relations measured using strain gages (small strains) are shown in Fig. 8. The alloys' Poisson's ratio (assumed as 0.33) was used to calculate Cauchy stress prior to yielding; the isochoric assumption was applied at larger strains. Minimal reduction in cross-sectional area occurs at small strains; therefore, nominal and Cauchy stresses are approximately equal. The nominal stress-logarithmic strain relations measured using DIC are given in Fig. 9. The Cauchy stress-logarithmic strain relations from DIC measurements are provided in Fig. 10. The nominal and Cauchy stress-logarithmic strain relations for prior exposure at different heating rates (5, 25, and 250°C/min) are shown in Fig. 11.

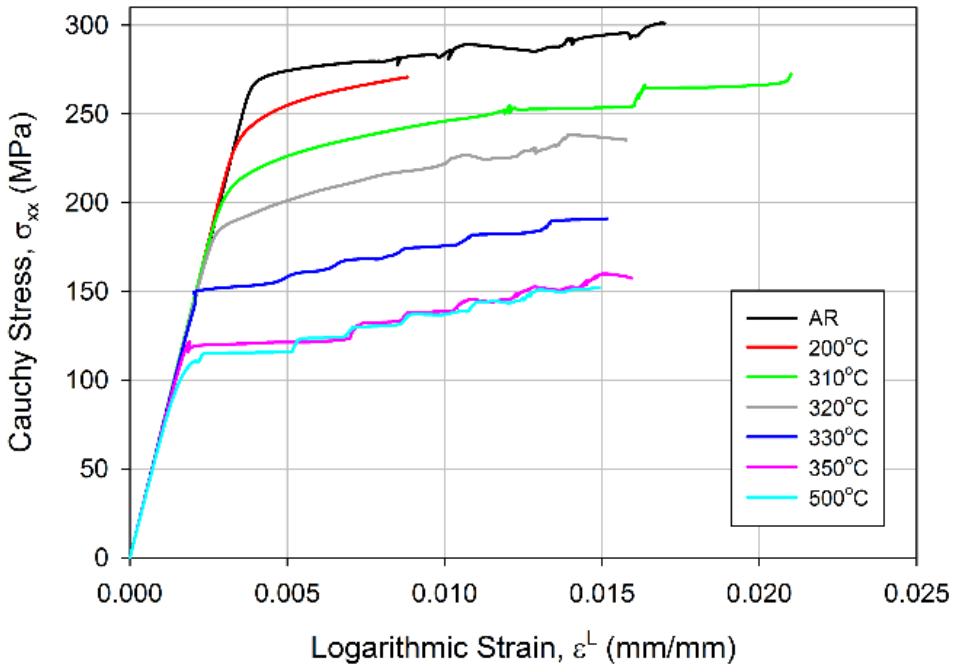

(a)

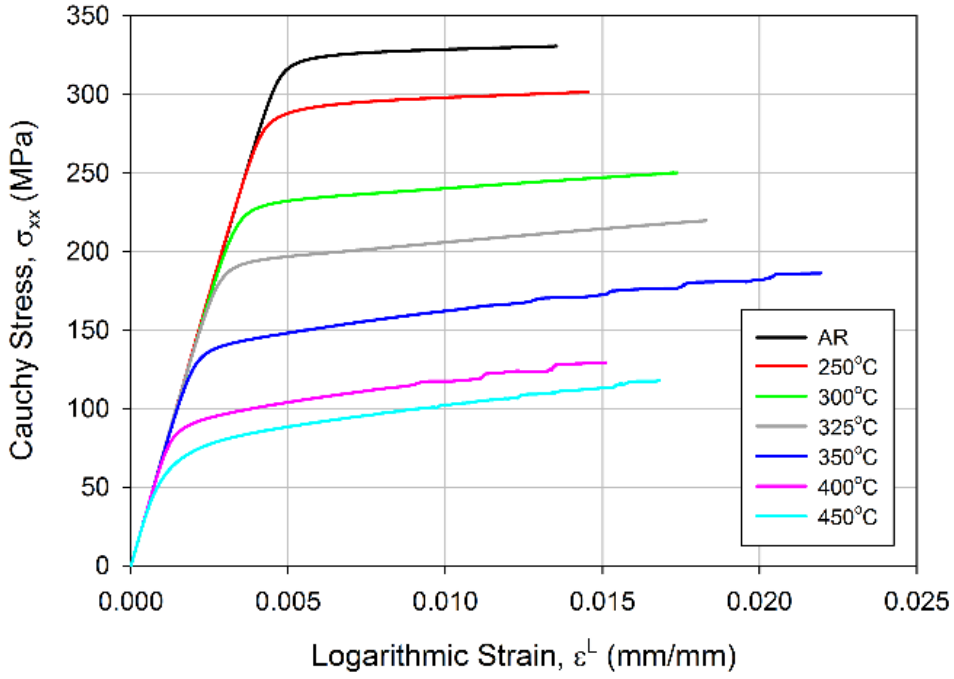

(b)

Fig. 8. Cauchy stress-logarithmic strain relations of (a) AA5083-H116 and (b) AA6061-T651 measured using strain gages after exposure at 20°C/min.

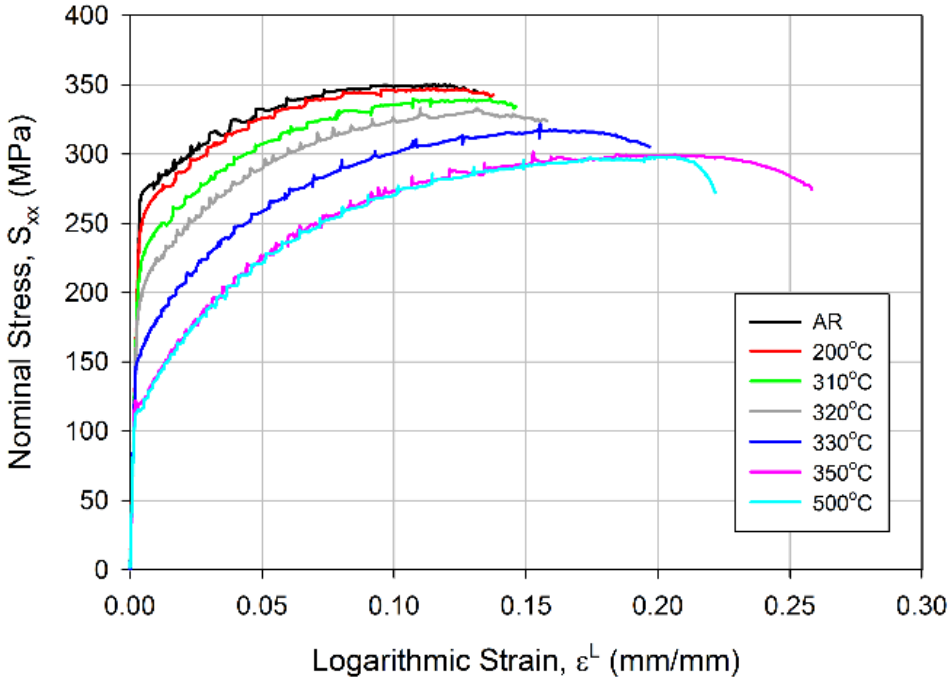

(a)

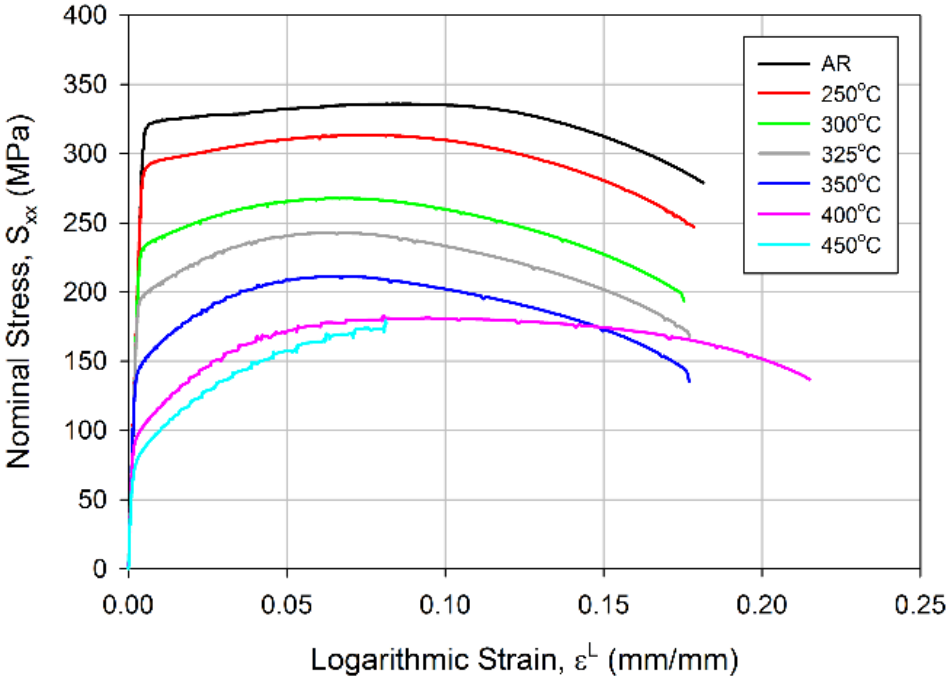

(b)

Fig. 9. Nominal stress-logarithmic strain relations of (a) AA5083-H116 and (b) AA6061-T651 measured using DIC after exposure at 20°C/min.

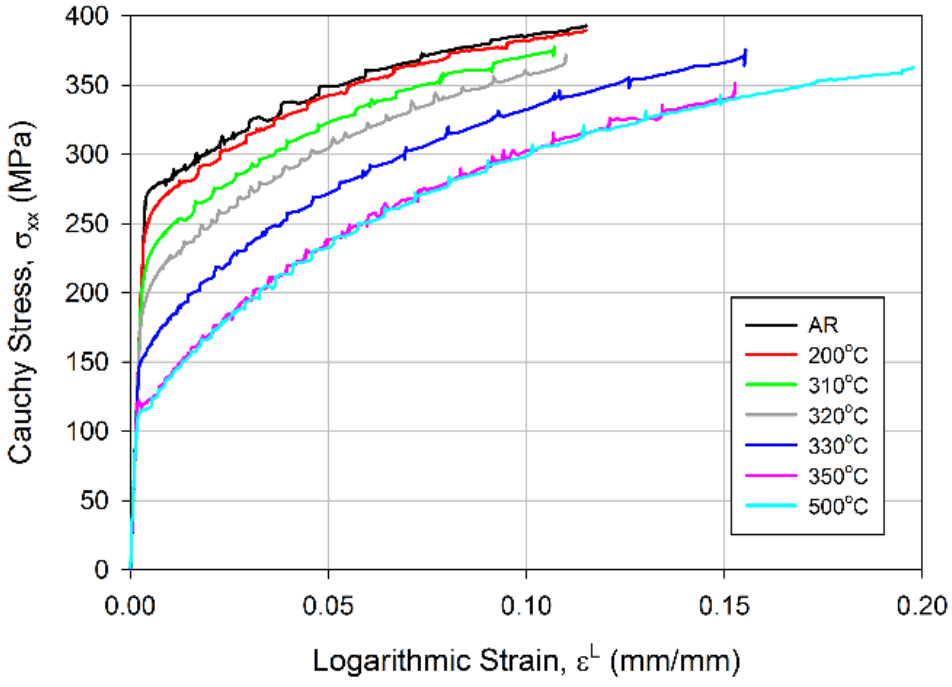

(a)

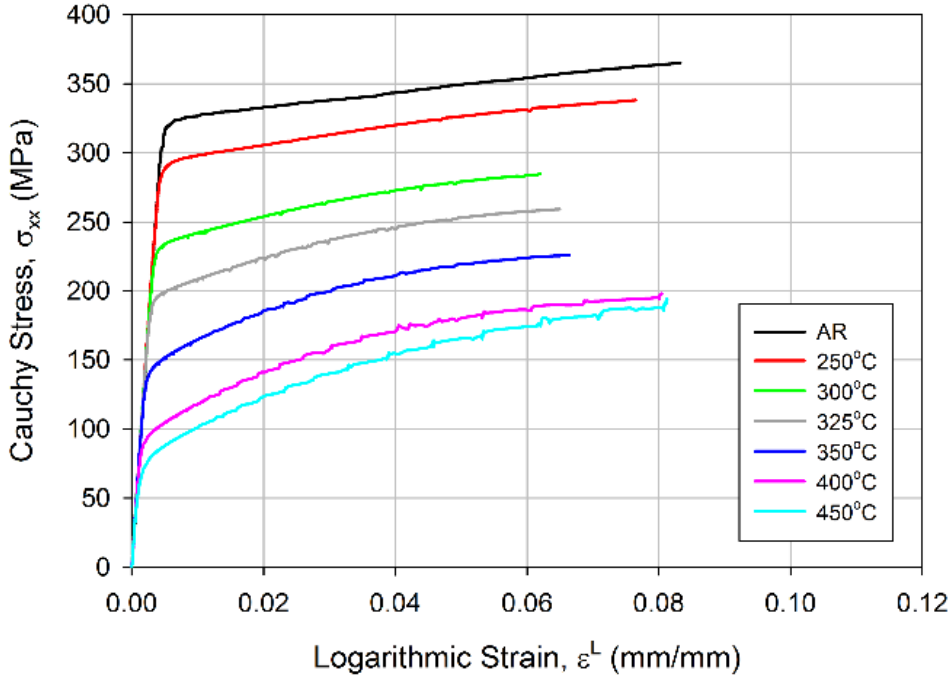

(b)

Fig. 10. Cauchy stress-logarithmic strain relations of (a) AA5083-H116 and (b) AA6061-T651 measured using DIC after exposure at 20°C/min.

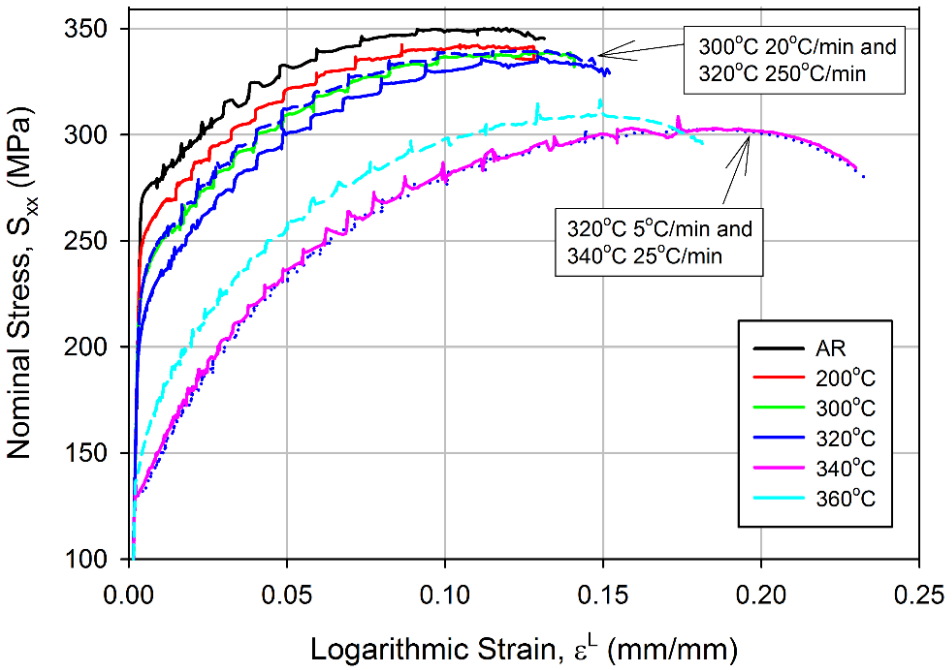

(a)

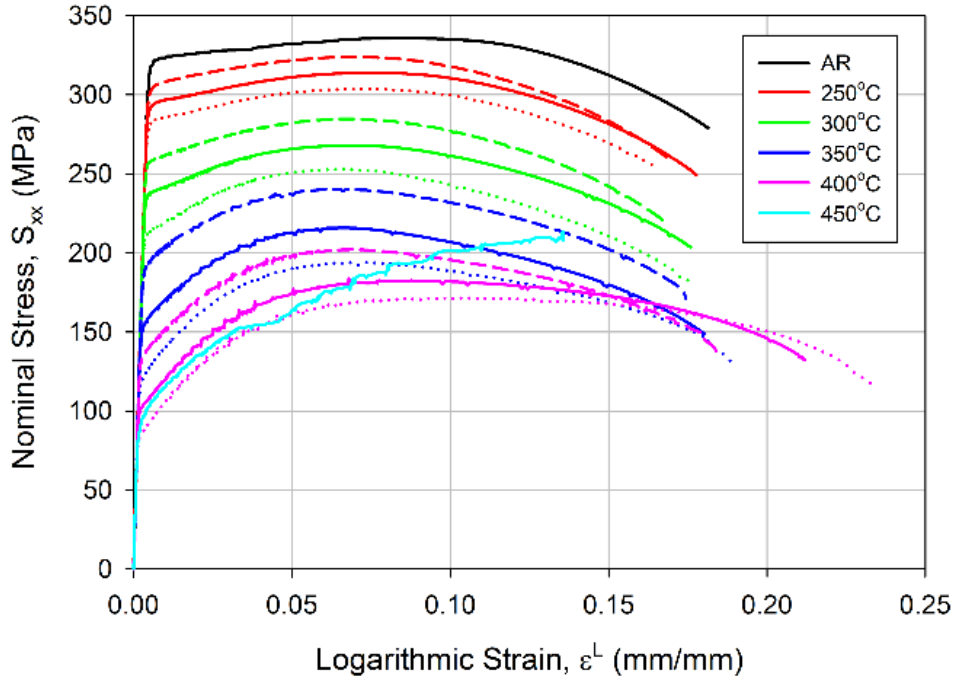

(b)

Fig. 11. Effect of heating rate on nominal stress-logarithmic strain behavior of (a) AA5083-H116 and (b) AA6061-T651. Dotted, solid, and dashed lines represent tests after exposure at heating rates of 5, 25, and 250°C/min, respectively.

The residual mechanical behavior of the alloys is considerably different. As seen in Fig. 9a and Fig. 10a, AA5083 exhibits significant strain hardening, resulting in ultimate stresses considerably

higher than the yield strength. The observed stress stepping behavior is caused by serrated yielding, also known as the Portevin-Le Chatelier (PLC) effect [26]. This behavior is common in solid solution hardened and cold worked aluminum alloys, such as AA5083. The strain at ultimate strength (which is indicative of the onset of necking) increases above ~300°C for AA5083. A nearly linear decrease in AA6061 strain at ultimate strength occurs from 200 – 300°C, as seen in Fig. 9b and Fig. 10b; the strains then increase to the as-received value at 400°C. The strain hardening rate ($d\sigma/d\varepsilon$) also changes with increasing temperature, indicating the microstructural mechanisms governing mechanical behavior undergo significant evolution from the as-received state. The hardening capacity (stress change from yield strength to ultimate strength) increases significantly with temperature for both alloys. The time-temperature dependence of the alloys was examined by varying the heating rate. As seen in Fig. 11b, AA6061 displayed a significant sensitivity to heating rate for exposures above 200°C. AA5083 is seen in Fig. 11a to have a significant heating rate sensitivity over a narrow temperature range from approximately 300 – 360°C. This is most notable for exposure to 320°C. The trends in mechanical behavior are difficult to demonstrate in graphical form other than that shown in Fig. 11a as the stress-strain relations overlap. However, the measured behavior is similar to that shown in Fig. 9a. A minor sensitivity was also observed at lower temperatures.

2.3.2 Plastic Flow Characteristics

The residual strain hardening rates ($d\sigma/d\varepsilon$), shown in Fig. 12, were used to analyze the evolution of plastic flow after elevated temperature exposure. The hardening rates were calculated using the Cauchy stress-logarithmic strain relations from DIC for specimens previously heated at 20°C/min (Fig. 10). The hardening rates were determined using a moving window polynomial fit of the experimental σ-ε relations. AA5083 required additional smoothing by considering only the maxima occurring during serrations in the σ-ε relations [27].

AA5083 experiences a steady increase in $d\sigma/d\varepsilon$ at equivalent flow stresses ($\sigma - \sigma_{0.2\%}$) with increasing temperature up to 300°C. A more rapid increase is observed with an increase in temperature from 300°C to 330°C, at which point $d\sigma/d\varepsilon$ remains unchanged with further increasing temperature.

AA6061 experiences an increase in $d\sigma/d\varepsilon$ at equivalent flow stresses and a change in slope with increasing temperature. Minor strain hardening occurs below 200°C as indicated by the low values of $d\sigma/d\varepsilon$ and relatively low strains at ultimate strength. The value of $d\sigma/d\varepsilon$ also approaches zero slope rapidly after yield. At 300°C, the material exhibited an increase in slope, indicating a higher strain hardening capacity. Further increase in temperature to 350°C results in a significant increase in $d\sigma/d\varepsilon$ and its slope. This is indicative of a substantial increase in the strain hardening capacity of the alloy. Above this temperature, the hardening rate versus equivalent flow stress is similar.

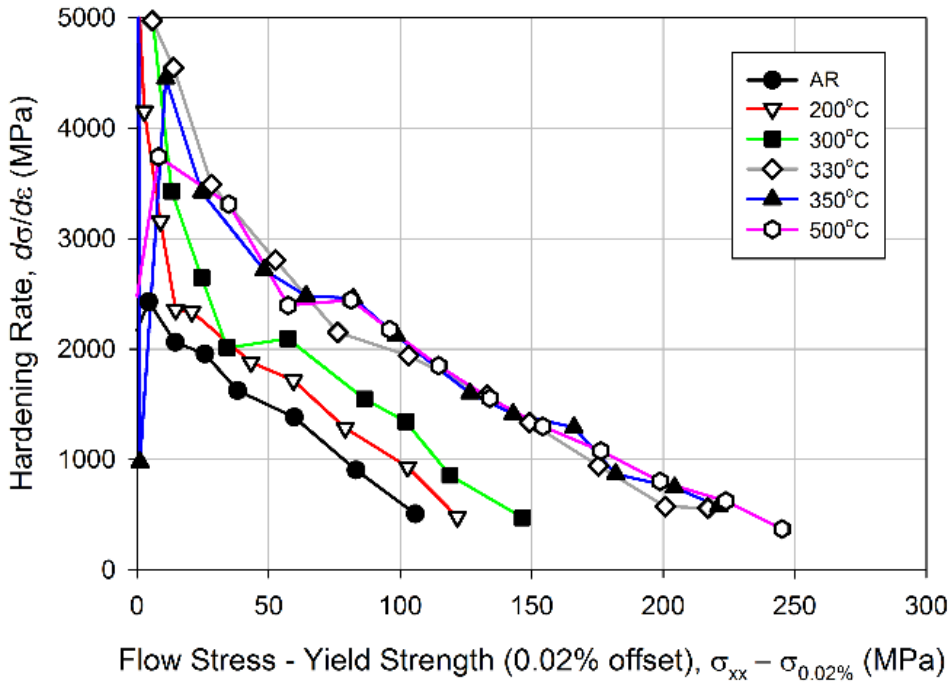

(a)

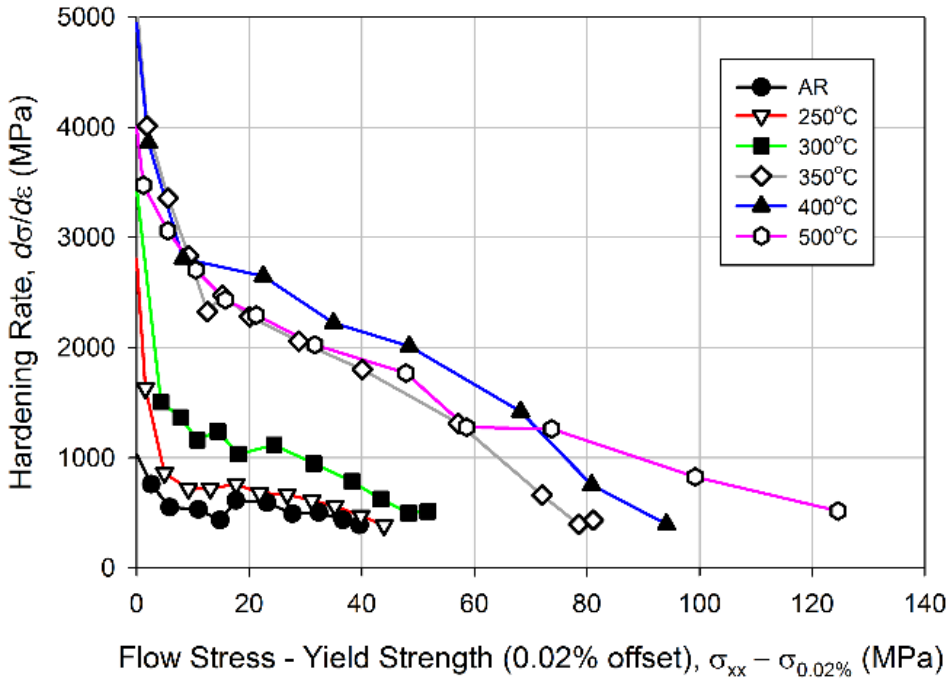

(b)

Fig. 12. Hardening rates ($d\sigma/d\varepsilon$) of (a) AA5083-H116 and (b) AA6061-T651 calculated from the Cauchy stress-logarithmic DIC strain relations for specimens previously exposed at 20°C/min.

2.3.3 *Young's Modulus*

The residual Young's modulus was calculated from the strain gage stress-strain relations shown in Fig. 8. Least-squares regression was used to calculate the slope of the initial, linear elastic portion of the uniaxial stress-strain curve. Young's moduli are shown in Fig. 13 for all specimens previously heated at 20°C/min. The error bars represent the standard deviation of three tests at the specified temperature. Similar errors bars are included in all discrete data plots. The AA6061 Young's modulus is nearly constant for all temperatures with an as-received value of 69.5 ± 0.2 GPa and an average for all tested temperatures is 69.4 GPa ±0.5 GPa. AA5083 exhibited a 2% increase in modulus from as-received to 300°C; however, it reverted to the as-received value above 350°C. The as-received AA5083 Young's modulus is 69.6 ± 0.3 GPa and the average for all tested temperatures is 70.9 GPa ±1.1 GPa.

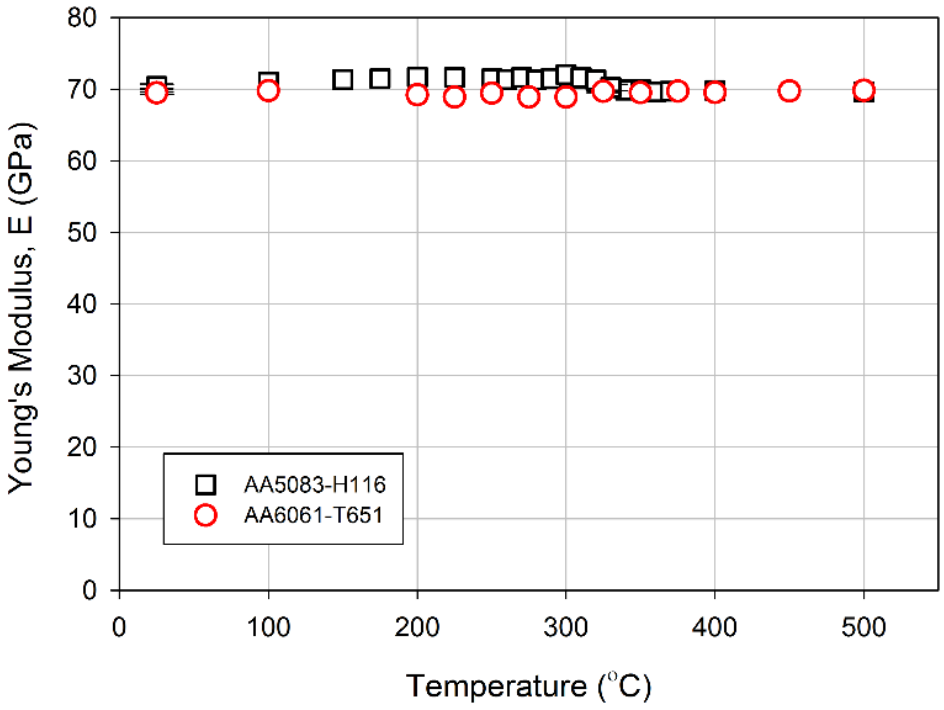

Fig. 13. Young's modulus from strain gages after exposure at 20°C/min.

2.3.4 *Yield Strength*

The yield strength of aluminum alloys is typically determined using the 0.2% strain offset method [28]. Additional yield strength definitions at smaller strain offsets are of interest when analyzing yielding behavior and constitutive model development. Yield strengths calculated using strain

offsets of 0.2% and 50 με (0.005%) are shown in Fig. 14. The time-temperature dependence of yield strength using the 0.2% offset method is shown in Fig. 15. Analysis is in reference to the 0.2% offset yield strength (Fig. 14a and Fig. 15) unless otherwise noted. A notable consequence of reducing the strain offset from 0.2% to 50 με is the decrease of AA6061 yield strength relative to AA5083. This indicates that AA5083 maintains elastic behavior to higher stress/strain levels than AA6061.

The yield strengths are reduced at relatively low temperature exposures, 150°C and 200°C for AA5083 and AA6061, respectively. AA5083 experiences an initial 40 MPa reduction in yield strength (up to 300°C). A heating rate dependence is exhibited at these temperatures (Fig. 15a). The primary AA5083 yield strength reduction (~100 MPa) occurs over a relatively narrow temperature range (~50°C). This reduction was observed to be time-temperature dependent. Specimens heated at 5, 25, and 250°C/min experienced this yield strength reduction initiating at approximately 280, 300, and 320°C, respectively. The reduction begins at approximately the same stress level, despite different initiation temperatures. The alloy reaches the same minimum yield strength (~120 MPa) regardless of heating rate.

AA6061 undergoes a relatively steady yield strength reduction from 200 – 450°C. An increase in yield strength is observed after exposure to 500°C. The time-temperature dependence of yield strength degradation is shown by the tests performed at different heating rates (Fig. 15b). The greatest dependence occurs at 350°C, with a difference of 74 MPa between 5 and 250°C/min. The minimum yield strengths are also dependent on heating rate. The yield strengths at 400°C are 87.4, 104.3, and 135.7 MPa for 5, 25, and 250°C/min, respectively.

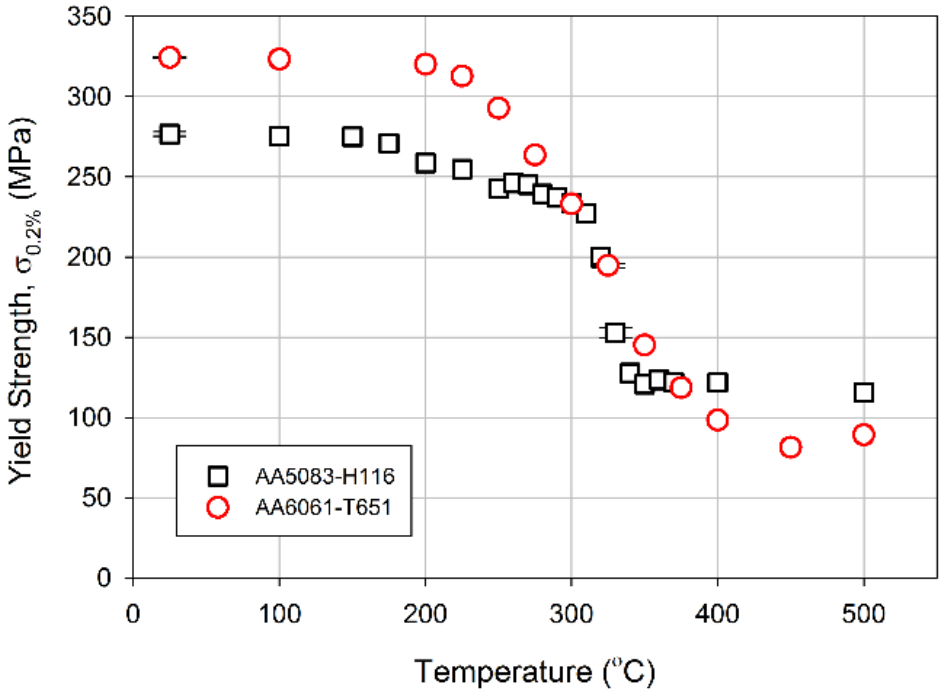

(a)

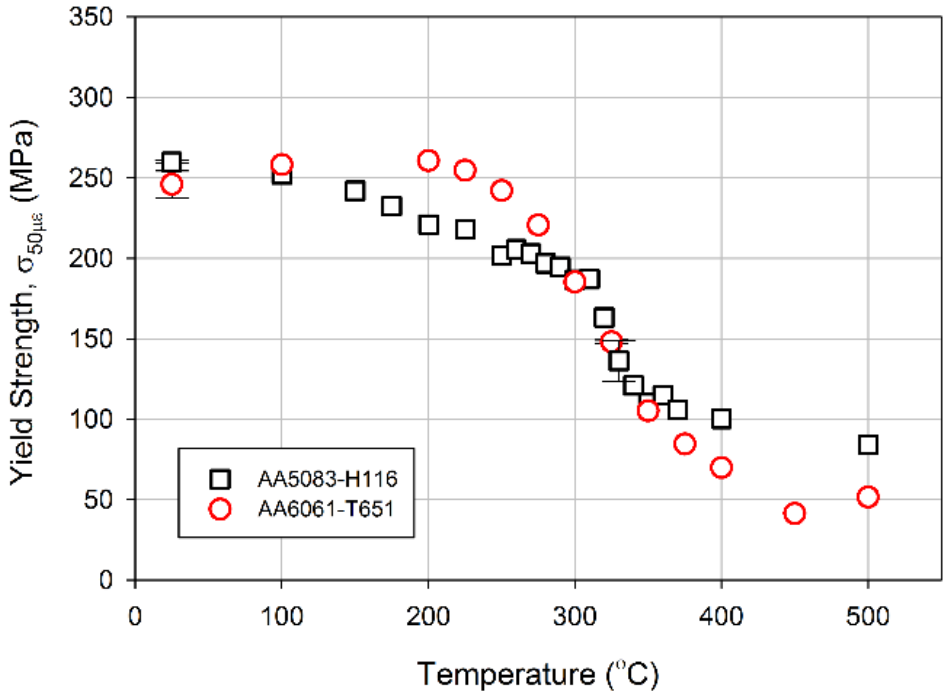

(b)

Fig. 14. Yield strengths of AA5083-H116 and AA6061-T651 calculated using strain offsets of (a) 0.2% and (b) 50με after prior exposure at 20°C/min.

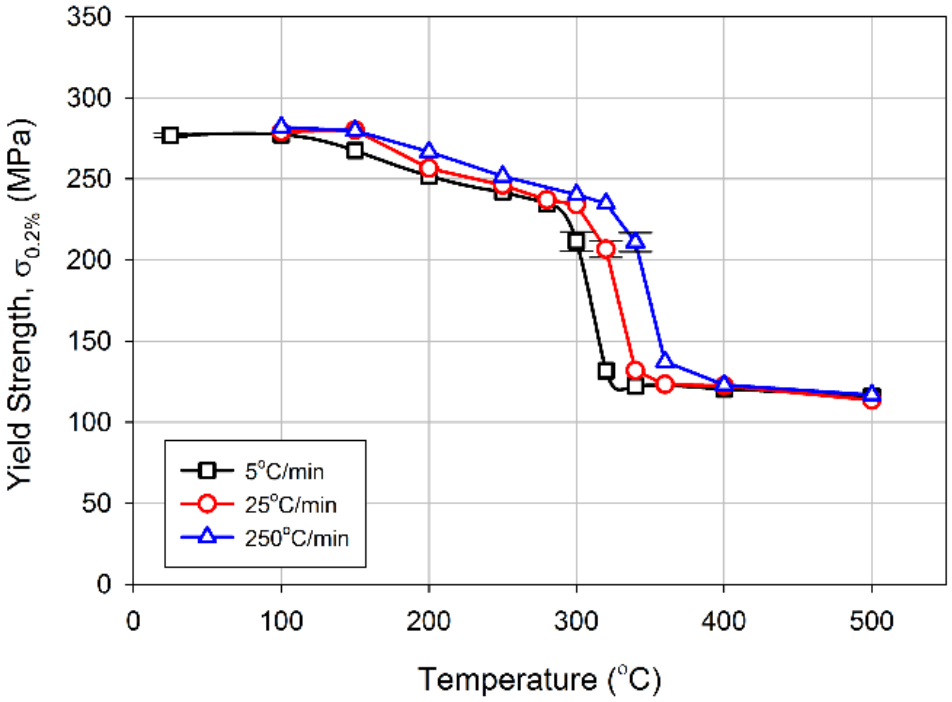

(a)

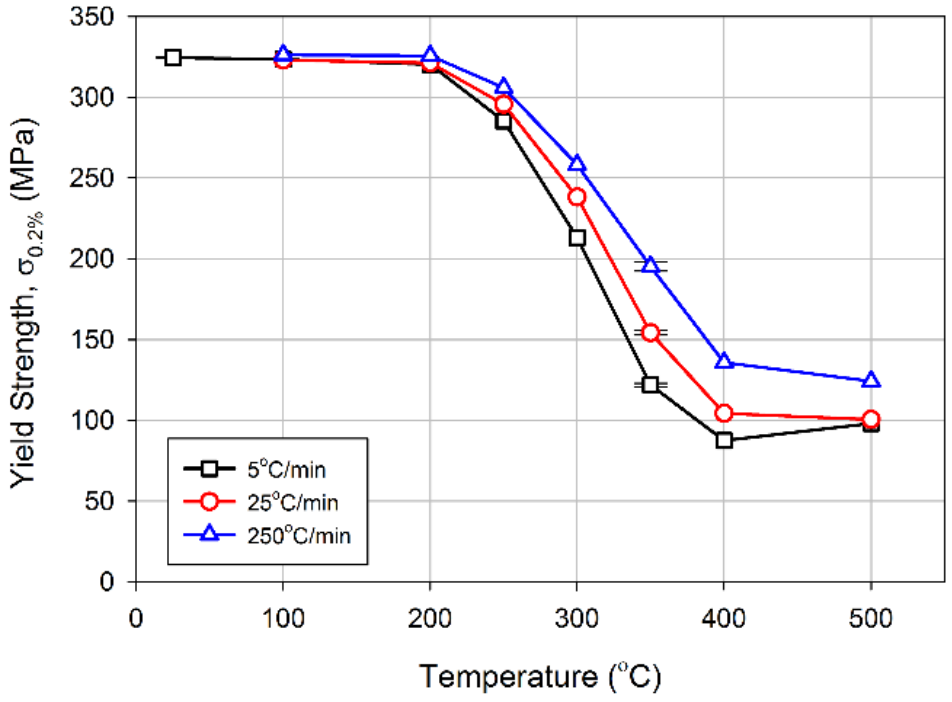

(b)

Fig. 15. Yield strength of (a) AA5083-H116 and (b) AA6061-T651 after prior exposure at different heating rates.

2.3.5 Ultimate Strength

The residual ultimate strength was determined in terms of Cauchy and nominal stress in Fig. 16. AA5083 ultimate strength remains nearly constant up to 500°C. A slight reduction (~40 MPa) occurs above 300°C, which parallels the primary yield strength reduction (Fig. 14 and Fig. 15). The reduction occurs in a nearly step-wise fashion over a narrow temperature range. The minor reduction indicates that the mechanisms governing maximum strain hardening are relatively unaffected by elevated temperature exposure. AA5083 ultimate strength is significantly dependent on heating rate over the temperature range associated with primary reduction in properties.

AA6061 experiences a more significant reduction in ultimate strength compared to AA5083. The reduction is similar to that for yield strength, indicating the governing mechanisms are likely the same. AA6061 also shows significant time-temperature dependence above 200°C.

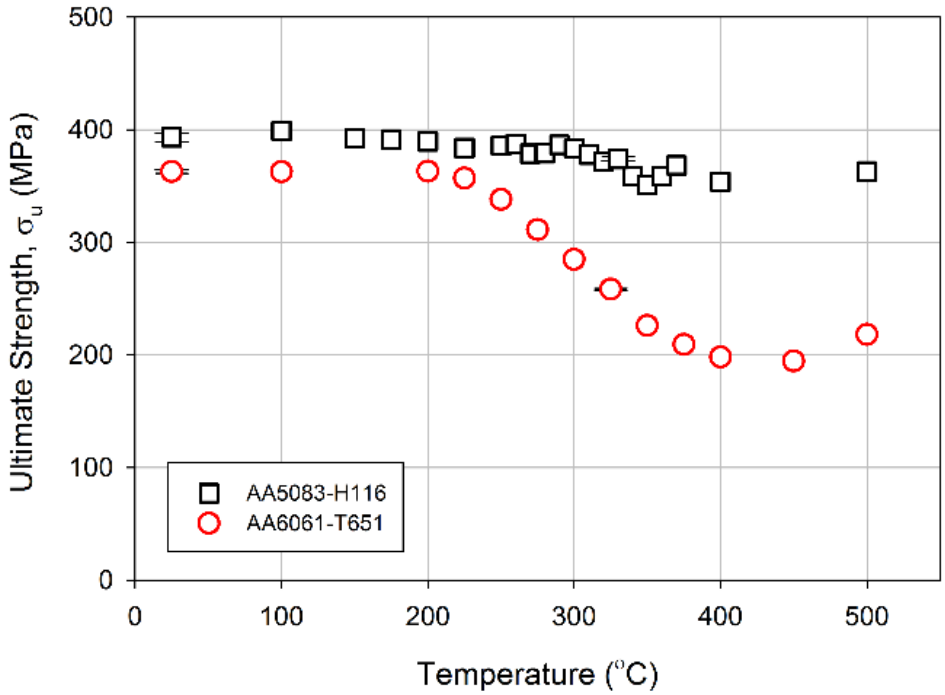

(a)

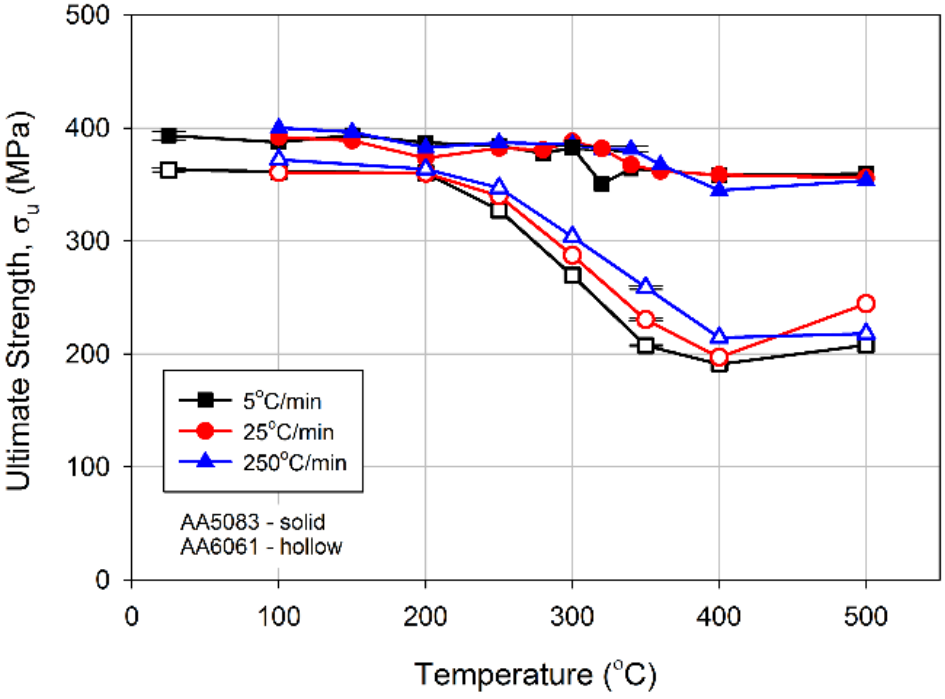

(b)

Fig. 16. Ultimate strength of AA5083-H116 and AA6061-T651 measured after exposure at (a) 20°C/min and (b) 5, 25, and 250°C/min.

2.3.6 Ductility

The ductility of AA5083-H116 and AA6061-T651 was analyzed in terms of reduction of area (%RA) and fracture strain (Fig. 17) as well as fracture morphology (Fig. 18). The two measures of ductility are complementary: fracture strain quantifies material elongation while %RA qualitatively measures diffuse necking and localization.

A distinct increase in fracture strain and %RA was measured for AA5083 exposed to temperatures above 300°C, see Fig. 17. This coincides with reductions in yield and ultimate strength. Fracture strain and %RA are nearly constant below 300°C. AA6061 fracture strain and %RA do not follow similar trends. Fracture strain remains nearly constant at ~0.18 to 400°C followed by a decrease to ~0.10. The %RA increases starting at 250°C (47% to 65%) followed by a drop to 55%. Prior heating above 400°C results in fracture strain and %RA decreases of 69% and 15%, respectively. AA6061 fracture images (Fig. 18b) show the extent of necking at fracture increases significantly from 250 to 400°C, with increasingly prominent cup-in-cone fracture. However, the fracture surface shows an increase in cleavage at 500°C. The extent of necking and, therefore, %RA, remains relatively high while fracture strain decreases.

Though not shown, the time-temperature dependence of ductility is similar to that observed for yield strength. AA5083 is primarily dependent over a narrow 50°C range starting at 280 – 320°C depending on heating rate. AA6061 exhibits significant dependence at temperatures greater than 200°C.

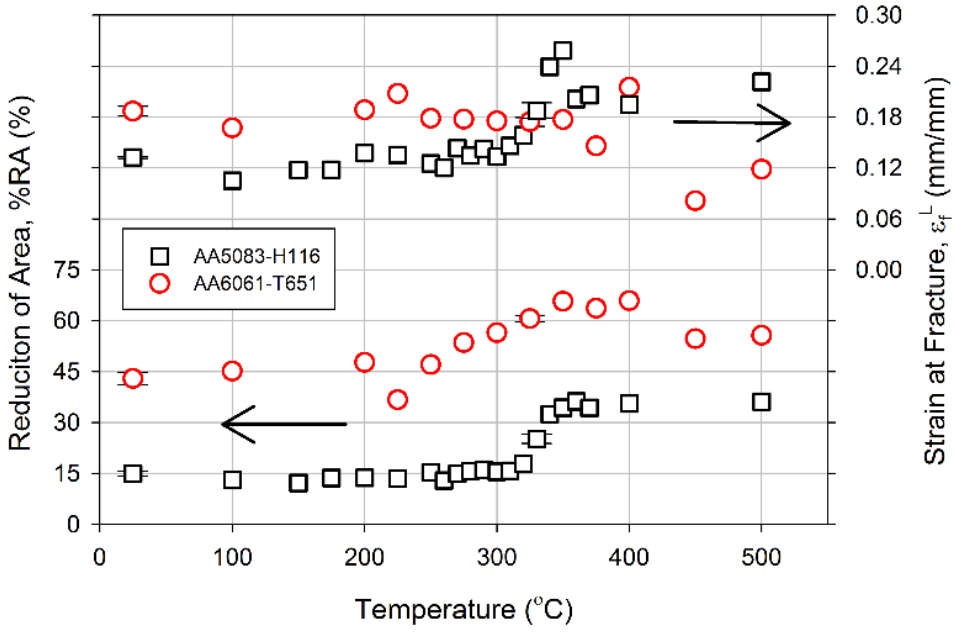

Fig. 17. AA5083 and AA6061 fracture strain and reduction of area after exposure at 20°C/min.

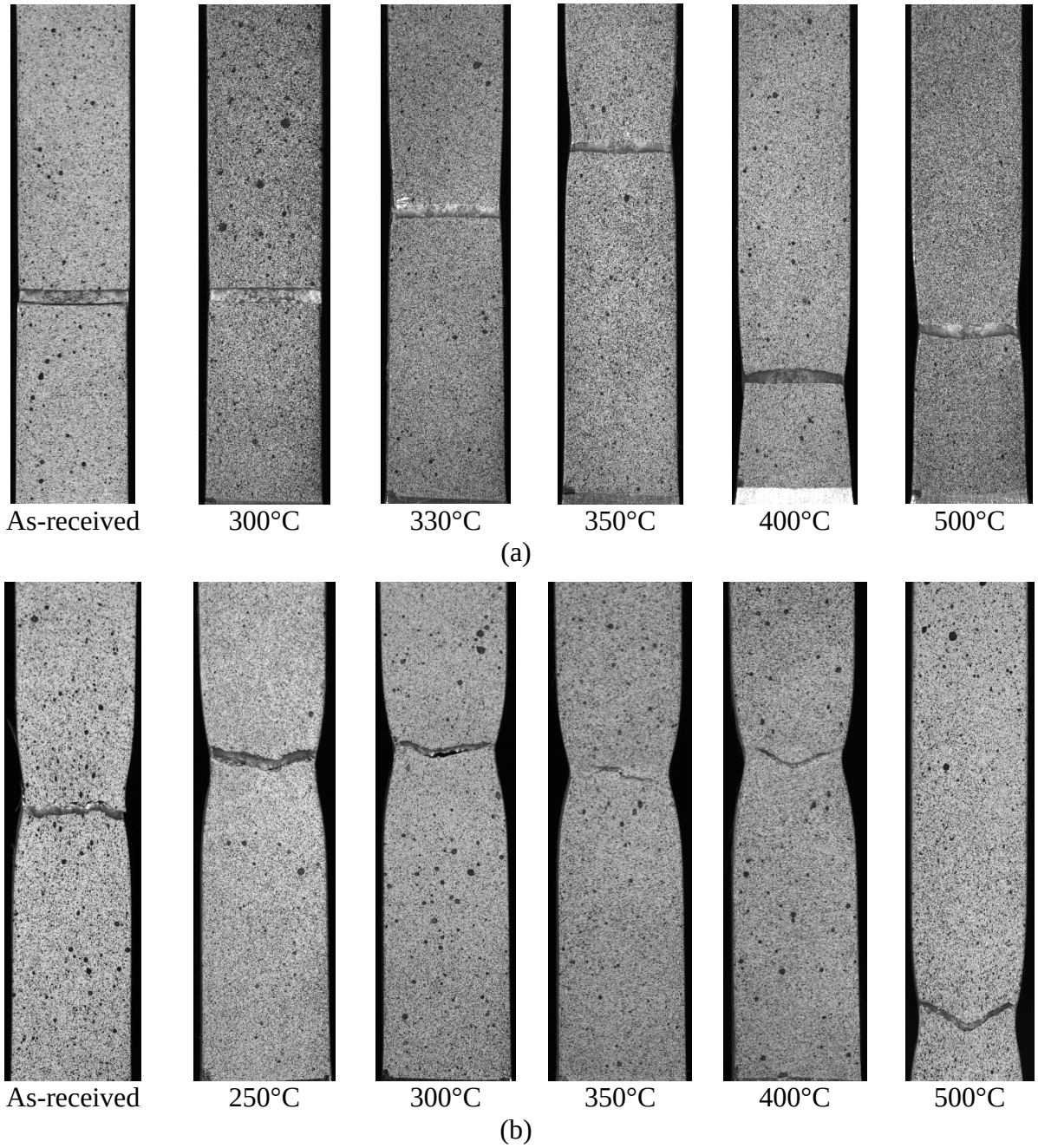

Fig. 18. Fracture morphology of (a) AA5083-H116 and (b) AA6061-T651 after prior exposure at 20°C/min.

2.4 Discussion

The experimental study in this research demonstrates that the residual mechanical behavior of AA5083-H116 and AA6061-T651 are sensitive to both prior exposure temperature magnitude and heating rate. In addition, the two alloys exhibit different evolution in their properties with

increasing exposure temperature and heating rate. This result is expected as residual mechanical behavior is governed by the relative state and evolution of the microstructural strengthening mechanisms. These mechanisms are developed during material processing, i.e., strain hardening (AA5083) and precipitation hardening (AA6061), to a state resulting in the desired mechanical properties. This state is commonly referred to as the as-received condition. Further evolution of these mechanisms at elevated temperatures governs residual mechanical behavior. In this discussion, the fundamental evolution of the various microstructural processes are described and related to the measured residual mechanical property degradation.

2.4.1 AA5083-H116 Mechanical Properties

AA5083-H116 undergoes two stages of property degradation, as shown in Fig. 14a and Fig. 15a. A slight yield strength reduction (36 MPa) initially occurs from about 150 – 280°C (Fig. 14a). This reduction exhibits a minor heating rate dependence most notable at ~200°C (Fig. 15a). Two microstructural mechanisms govern this reduction: Mg α-matrix depletion (reducing Mg solid solution hardening) and static dislocation recovery (reducing subgrain strengthening). The primary reduction in yield strength (116 MPa) occurs from 280 – 360°C (Fig. 14a); however, the specific temperature range depends on heating rate. Grain recrystallization governs this reduction. The heating rate dependence is most prominent at 320°C, with yield strengths of 132, 207, and 235 MPa for 5, 25, and 250°C/min, respectively (Fig. 15a). This is a 103 MPa (44%) difference between the tested heating rate bounds. The details of these mechanisms and their relation to property reduction are explained in the following discussion.

2.4.1.1 Initial AA5083 Property Evolution

Heating to lower temperatures, i.e., 150 – 280°C, causes a slight, but not insignificant, evolution in residual mechanical behavior. Review of the residual mechanical properties in this temperature range reveals only yield strength (Fig. 14 and Fig. 15a) and $d\sigma/d\varepsilon$ (Fig. 12) are significantly affected. Ultimate strength (Fig. 16) and ductility (Fig. 17) remain relatively unchanged from the as-received state. The microstructural processes affecting strength at these temperatures are Mg α-matrix depletion by β-phase (Al_2Mg_3) precipitation and subgrain coarsening by dislocation recovery. The described processes overlap. β-phase precipitation occurs at lower temperatures

(150 – 225°C, depending on heating rate) followed by dissolution (225 – 280°C, depending on heating rate) [10]. Recovery occurs at higher temperatures (200 – 280°C, depending on heating rate [9,29,30].

Mg solid solution strengthening can be reduced by β-phase precipitation, which depletes the α-matrix of Mg solutes. The magnitude and time-temperature dependence of Mg depletion by precipitation was examined by Popovic, *et al.* [10] for an Al-6.8wt%Mg alloy. Popovic, *et al.*, measured a 16% reduction in Mg solid solution content after a 3 h isothermal soak at 225°C, increasing to 27% for a 12 h soak at the same temperature. Thus, significant Mg α-matrix depletion requires an extended elevated temperature exposure, on the order of hours. Considering the time-scales in this research, Mg depletion is not expected to significantly affect residual yield strength even for the lowest heating rate (5°C/min). Also, the β-phase dissolves with increasing temperature (225 – 280°C, depending on heating rate [10]) thereby increasing Mg α-matrix content, which eliminates the effects of β-phase precipitation on strength. Therefore, the impact of β-phase precipitation on residual strength was negligible in this research.

Dislocation recovery is the primary microstructural process governing residual mechanical behavior during the initial yield strength reduction (up to 280 – 320°C, depending on heating rate). Recovery causes subgrain coarsening due to dislocation emission and amalgamation with neighboring subgrains [31,32]. Subgrains are intra-granular grain-like structures formed during strain hardening (cold work) [8,33]. The as-received AA5083-H116 subgrain structure is shown in Fig. 19. The average subgrain size was measured as 376 nm using the line intercept method. The hardening rate ($d\sigma/d\varepsilon$), shown in Fig. 12a, exhibits a parallel shift to higher equivalent stresses with increasing temperature below 280°C. This behavior is indicative of recovery [31]. Xing, *et al.* [34] noted discontinuous subgrain growth with increasing isothermal exposures. The size increase was minor up to 200°C (400 – 490 nm), followed by a significant increase up to 260°C (970 nm). These trends have been demonstrated independently for other alloys and heating regimens [9,30].

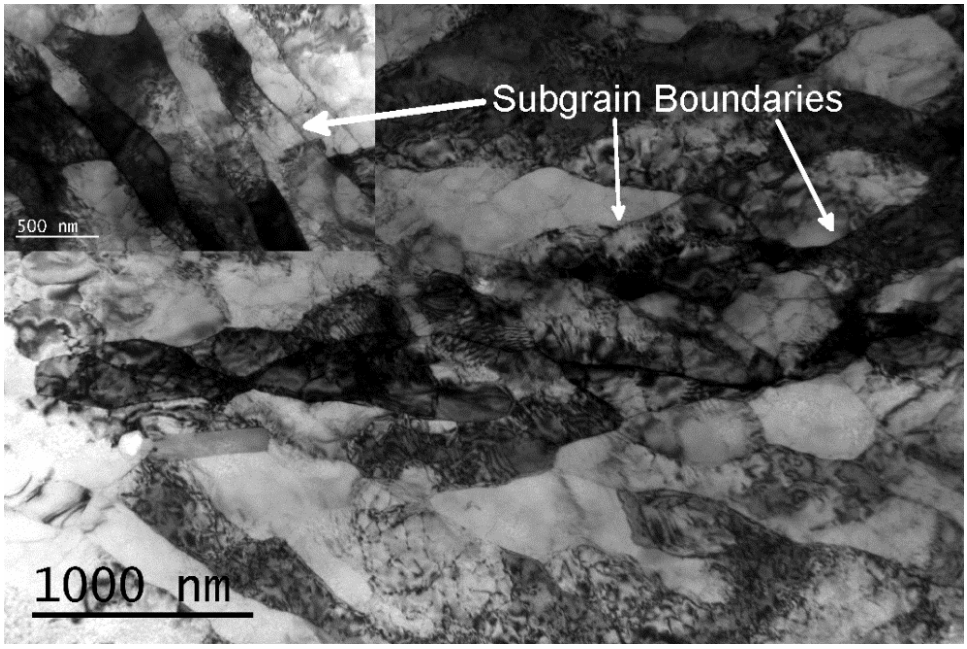

Fig. 19. TEM micrograph of as-received AA5083-H116 subgrain structure (376 nm average size).

The residual yield strength reduction due to subgrain growth was estimated to analyze how recover affects AA5083-H116 residual strength. As seen in Fig. 14a, the residual yield strength is reduced by 14% (36 MPa) from the as-received strength after exposure to 280 – 320°C, which is just prior to recrystallization. By heating to 280°C, the subgrain size was measured in Ref. [34] to increase by ~220%. Using this reduction and the subgrain size for the 5083-H116 alloy used in this study, the subgrain size was estimated to increase from 376 nm (as-received) to 830 nm (280°C). A Hall-Petch type relationship [7] was used to estimate the subgrain strengthening contribution as

$$\Delta\sigma_{sg} = k_{sg}\delta^{-1/2} \tag{9}$$

where k_{sg} is a constant determined empirically as 0.064 MPa/m$^{1/2}$ [7] and d is the average subgrain size. The yield strength reduction was calculated using Eq. (9) to be 37 MPa, which is similar to the measured reduction shown in Fig. 14a.

The kinetics of AA5083-H116 residual yield strength evolution are shown in Fig. 11a. A slight dependence on heating rate was measured. The heating rate dependence measured in this work is similar to that reported by Furu, *et al.* [30]. However, isothermal heating was employed in Ref. [30] and the residual mechanical behavior was characterized only in terms of Vickers hardness. In

Fig. 15a, the yield strength at the end of recovery (i.e., the onset of recrystallization) was measured to be approximately the same (~235 MPa) for all heating rates. This was also measured to occur for isothermal anneals at various holding times in other work [30]. This indicates a critical level of recovery is required to initiate, or aid the initiation, of recrystallization.

2.4.1.2 Primary Residual Mechanical Behavior Evolution

Heating to higher temperatures, i.e., greater than 280 – 320°C depending on heating rate, results in significant evolution of residual mechanical behavior. The residual mechanical properties, including yield strength (Fig. 14), $d\sigma/d\varepsilon$ (Fig. 15a), and ductility (Fig. 17), are affected significantly. The ultimate strength (Fig. 16a) is affected to a lesser extent. The microstructural process affecting mechanical behavior at these temperatures is recrystallization. This is the primary process governing strength degradation after elevated temperature exposure in AA5083-H116.

Recrystallization is the formation of an equiaxed grain structure in a deformed material through grain nucleation and growth by the stored energy of deformation [11]. The effect of recrystallization on AA5083-H116 is shown in Fig. 20. The elongated (textured) as-received grain structure (Fig. 20a) evolves during recrystallization to form equiaxed grains (Fig. 20b). The average grain sizes are 89 and 48 μm in the as-received and recrystallized states, respectively. The grain size strengthening contributions before and after recrystallization were calculated to be 23 and 32 MPa using the Hall-Petch relationship (for grain strengthening) in Eq. (9) with k_g = 0.22 MPa/m$^{1/2}$ [35]. The increased grain strengthening is counteracted by strength reduction due to subgrain annihilation due to grain boundary migration during growth [8]. The net result of this is a strength reduction of 112 MPa, as shown in Fig. 14a. Subgrain annihilation due to grain growth eliminates the subgrain strengthening contribution which was estimated by Huskins, *et al.* [7] to be approximately 4.5 times greater than the strengthening contribution of grains, which is similar to the contributions provided above.

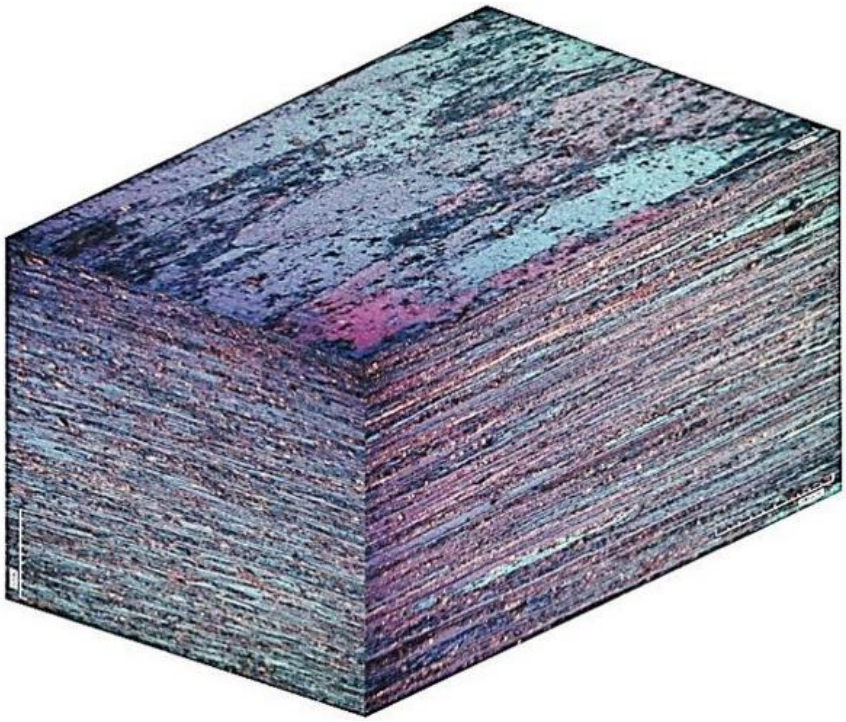

(a)

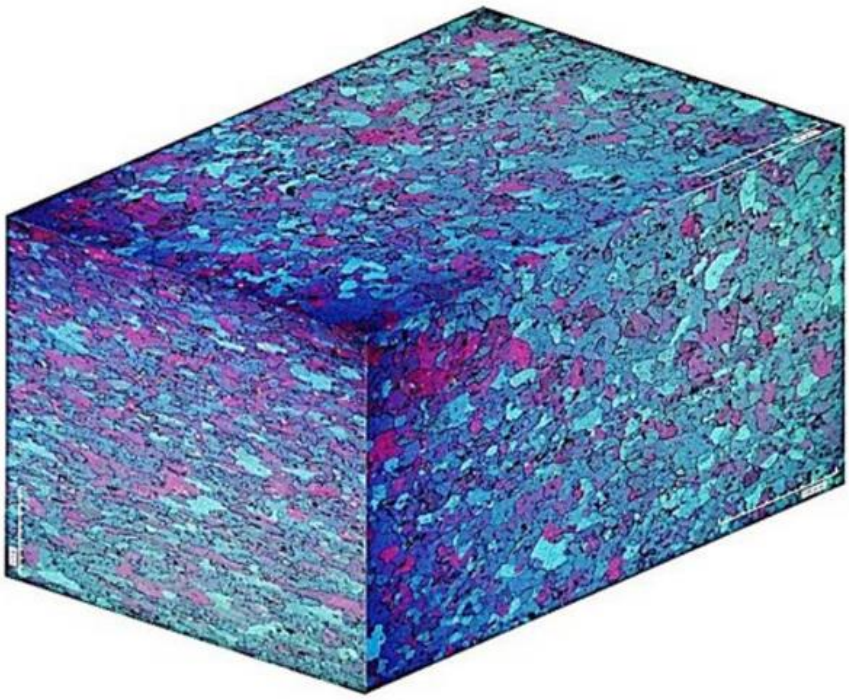

(b)

Fig. 20. AA5083-H116 grain morphology (a) as-received and (b) recrystallized after 400°C exposure.

The primary yield strength reduction was measured to be significantly dependent on heating rate from approximately 280 – 380°C, with the specific range dependent on heating rate. The heating

rate dependence is demonstrated for prior heating at 5 and 250°C/min to 320°C, which results in a 103 MPa yield strength difference. The subgrain boundaries (dislocation entanglements) which form subgrains are absorbed by grain boundaries during their nucleation and growth [8]; therefore, the kinetics of subgrain annihilation are assumed to follow that of recrystallization. The rate and magnitude of residual strength reduction during recrystallization is similar for the tested heating rates (Fig. 15a). In addition, similar residual strengths were measured at the onset of recrystallization, independent on heating rate (see in Fig. 15a). These observations were similar to those from other studies [9,30,36].

2.4.2 AA6061-T651 Mechanical Properties

AA6061-T651 undergoes a single stage of property reduction, as shown in Fig. 14a and Fig. 15b. Unlike AA5083-H116, this alloy experiences significant evolution in all characteristics of residual mechanical behavior, including yield strength (Fig. 14 and Fig. 15b), ultimate strength (Fig. 16), $d\sigma/d\varepsilon$ (Fig. 12b), and ductility (Fig. 17). Yield strength degradation initiates at 200°C, progressively decreases in magnitude (Fig. 14a), and exhibits significant heating rate dependence (Fig. 15b). This is most prevalent at 350°C where the yield strengths at 5, 25, and 250°C/min are 122, 154, and 195 MPa, respectively (Fig. 15b); a 73 MPa (37%) difference. Precipitate growth and precipitate volume fraction reduction governs the residual mechanical behavior.

It is widely accepted that the primary strengthening phase in AA6061 is the metastable β″ phase. This phase is shown in Fig. 21 for the as-received, peak-aged AA6061-T651. The alloy's strength is governed by the interaction of precipitates and dislocations. Elevated temperature growth of the strengthening phase weakens this interaction, thereby reducing yield strength. The sequence and morphology of growth has been the topic of numerous studies [12–14]. The generally accepted sequence is SSSS (supersaturated solid solution) → clusters/Guinier-Preston zones → β″ → β′ → β (Mg_2Si). The detailed evolution was measured using DSC at 20°C/min for AA6005A-T6 [5]:

- the β″ dissolution peak is identified at ~260°C;
- the β′ precipitation peak is identified at ~310°C;
- a broad β′ dissolution peak occurs from ~350 – 420°C;
- the β precipitation peak is identified at ~460°C;
- the β dissolution peak is identified at ~510°C.

β′ may also be formed directly by β″ coarsening rather than by dissolution and precipitation.

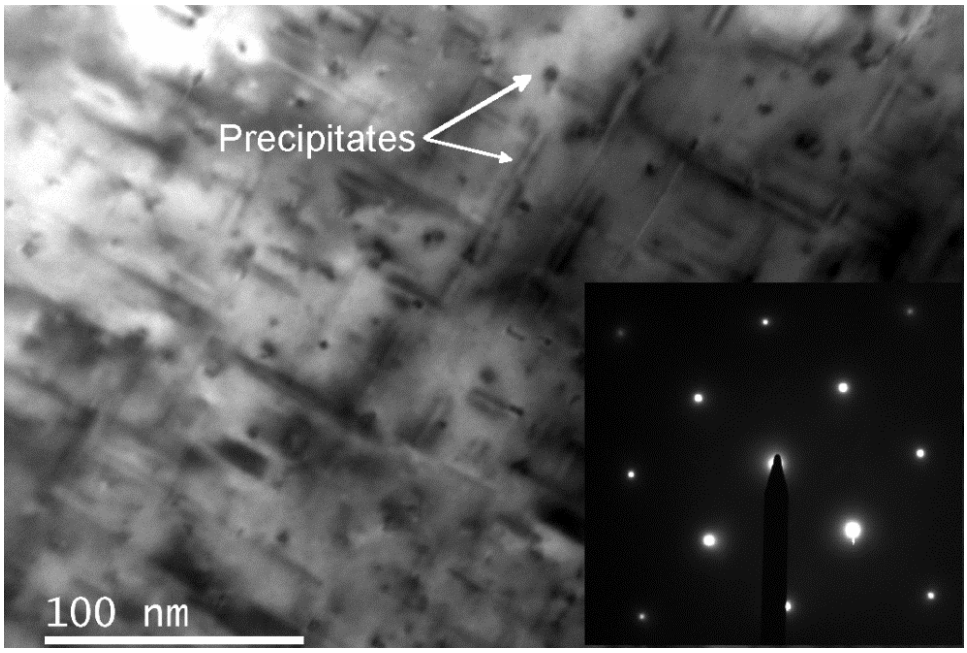

Fig. 21. AA6061-T651 precipitates (in-plane and 90° out-of-plane) imaged using bright-field TEM.

The residual yield strength reduction, as seen in Fig. 14a and Fig. 15b, occurs primarily at temperatures associated with β′ formation. The β′ phase is significantly larger and exists at a lower volume fraction than the primary β″ strengthening phase. For example, heating of peak-aged AA6005A with a mean precipitate radius (r) of 4.7 nm (volume fraction, f_v = 1.1%) to 300, 350, and 400°C results in growth to 8.8 (0.71%), 19.6 (0.50%), and 35.5 nm (0.19%), respectively [37]. The aforementioned growth from β″ to the (presumed) β′ phase is associated with a transition in the precipitate/dislocation strengthening mechanism. Smaller precipitates, typically below a critical precipitate radius of 3 – 5 nm [37–40], are sheared by dislocations and exhibit a low $d\sigma/d\varepsilon$ [8]. Strengthening for this class size of precipitates is proportional to $\sqrt{f_v r}$ [5]. Larger precipitates are bypassed by dislocations leaving a closed dislocation loop (Orowan looping). In this case, strengthening is proportional to $\sqrt{f_v}/r$ [5] and exhibit a high $d\sigma/d\varepsilon$ [8].

The strengthening mechanism transition is reflected in the residual yield strength in this research. Precipitate growth from the β″ to β′ phase occurs from approximately 250 – 300°C, which is in the same range yield strength degradation initiates (Fig. 14a). The hardening rate ($d\sigma/d\varepsilon$), shown in Fig. 12b, also evolves in accordance with a transition in strengthening mechanism. Below 250°C,

$d\sigma/d\varepsilon$ remains low (<1000 MPa), as is associated with small precipitate dislocation shearing [8]. The residual yield strength is also relatively unchanged from the as-received value. The strengthening mechanism transition is discernible after exposure to 300°C at 20°C/min, which reduces residual yield strength by 90 MPa. The hardening rate also increases to ~1600 MPa at the initiation of plastic flow. This indicates that both strengthening mechanisms are likely active in the alloy due to a precipitate size distribution [38]. Further increasing temperature results in a significant increase in initial hardening rate (>3000 MPa). This is accompanied by a significant reduction in residual yield strength (225 MPa) after exposure to 400°C. This indicates large precipitates solely exist and the governing strengthening mechanism is Orowan looping [8].

AA6061-T651 residual mechanical behavior time-temperature dependence is well-described using the kinetic-dependence of the strengthening phase. As noted previously, the strengthening precipitate/dislocation interaction is defined in terms of precipitate size and volume fraction. Therefore, the details of precipitate growth and evolution may elucidate the time-temperature dependence of the residual mechanical behavior. Doan, *et al.* [16] examined AA6061 strengthening phase precipitation using DSC at heating rates of 5 – 20°C/min. A heating rate increase from 5 to 20°C/min resulted in β″, β′, and β-phase precipitation peak temperature increases of 30, 35, and 43°C, respectively. Also, β″-phase precipitation peak temperature in an Al-1.1wt%Mg_2Si alloy increases by 43°C for an increase in heating rate from 5 to 50°C/min [14]. The measured residual yield strength of AA6061-T651, as seen in Fig. 15b, is similar to that for precipitate evolution from previous studies [14,16]. An increasing difference in strength is measured for higher exposure temperatures. For example, prior heating to 250 and 350°C at 5 and 250°C/min results in yield strength differences of 20.7 and 73.6 MPa, respectively. This is in agreement with the higher peak temperatures for the β-phase as compared to the β″-phase [16]. This result is supported by isothermally annealed AA6082, which experiences a similar reduction in properties [37]. The behavior observed in this work is also reasonably reflected by that of Maisonnette, *et al.* [3] for AA6061-T6, which was previously exposed at high heating rates, i.e., 30 – 12000°C/min.

2.5 Conclusions

The residual mechanical behavior of AA5083-H116 and AA6061-T651 was studied after elevated temperature exposure representative of fire environments. Heating was performed at several heating rates (5, 25, and 250°C/min) simulating a representative aluminum structure, with varying levels of fire protection, exposed to the UL 1709 standard fire exposure. Additional tests were performed at 20°C/min to elucidate the detailed evolution of residual mechanical properties. The main results of this investigation are provided below:

- Tensile tests showed the residual mechanical behavior is dependent on both the maximum temperature and heating rate of prior thermal exposure. It is therefore necessary to consider both of these thermal exposure details when evaluating potential property degradation after a fire.
- AA5083-H116 experiences an initial minor property reduction up to approximately 280 – 320°C (heating rate dependent) which is directly followed by a significant reduction over a 50°C span. The initial reduction is caused mostly by subgrain coarsening due to recovery. The significant property reduction above 280 – 320°C is due to recrystallization, which annihilates the subgrain structure.
- AA5083-H116 heating rate dependence is minor during the initial property reduction and significant during the primary reduction due to recrystallization.
- AA6061-T651 experiences significant property reduction from 200 to 450°C, with a slight recovery in properties at 500°C. Precipitate coarsening and the resulting evolution of the precipitate/dislocation strengthening explains the reduction in properties.
- AA6061-T651 heating rate dependence is significant, increasing from minor at the initial onset of property reduction at 200°C to significant above 300°C.

3 AA5083-H116 Residual Constitutive Model

3.1 Introduction

5xxx-series aluminum alloys are increasingly being used in a broad spectrum of applications such as lightweight structures, light rail, bridge decks, marine crafts, and off-shore platforms. This is largely due to their good combination of specific strength, weldability, and corrosion resistance. The mechanical properties of 5xxx-series alloys are obtained primarily through solid solution strengthening and grain refinement by strain hardening [7]. However, a major concern with aluminum alloy structures is fire survivability, both during and after fire exposure. A short term fire exposure may significantly alter the as-received microstructure, leading to a deterioration in residual mechanical properties after the structure has cooled to ambient conditions. A structure subjected to such conditions requires evaluation for structural stability and assessment for damaged component replacement. To support structural damage assessment, constitutive models are needed to predict the residual yield strength and strain hardening of aluminum alloys following a fire exposure.

The microstructural processes governing the residual mechanical state of 5xxx-series alloys are recovery and recrystallization [8]. Reduction in the α-matrix solute concentration also affects residual strength; however, at much longer time scales than expected in a fire scenario, as discussed in Chapter 2. Recovery has long been understood as the process by which a previously deformed (i.e., cold worked) material lowers its internal energy state at low annealing temperatures [8], resulting in dislocation structure (dislocation cells/subgrains) coarsening [30,31,34,41]. It is often understood to proceed as a thermally activated process [30], i.e., it proceeds as dependent on both time and temperature. Empirical [42–44] and mechanistic [27,45] models have been developed to analyze and predict the kinetically-dependent recovery evolution. Recrystallization is the primary process by which the stored energy of deformation is released in cold rolled aluminum alloys [11]. The process and mechanisms of nucleation, migration, and impingement of the recrystallized grain structure has been studied extensively [46–53]. Kolmogorov [54], Johnson and Mehl [55], and Avrami [56] laid the foundation for kinetic recrystallization models through introduction of the uniform impingement factor. However, several assumptions in the so-called KJMA model have been called into question [57,58]. This has led the development of more complex analytical

models which attempt to more accurately represent the geometrical evolution recrystallization [36,59–64]. More advanced computer simulations have also been developed to predict recrystallization (summary in Ref. [58]). Even with these advances, recent work [9] modeling aluminum strength during recrystallization has implemented KJMA kinetics. Thus, this work implements the analytical linear/uniform impingement model of Vandermeer and Juul Jensen [36] which more accurately represents grain nucleation and growth during recrystallization.

Recovery and recrystallization processes primarily affect the dislocation cell/subgrain and grain strengthening mechanisms [8]. As such, integration of the described kinetics models with appropriate strength models provides an integral framework to predict residual yield strength after fire exposure. Grain strengthening has classically been represented by the empirical Hall-Petch relationship. Subgrains have been the topic of significant discussion regarding their strengthening relationship, i.e., as proportional to δ^{-1} or $\delta^{-1/2}$. Furu, *et al.* [30] noted no appreciable difference when comparing these proportionalities. Hansen and colleagues [65–67] developed mechanistic strength relations proportional to $\delta^{-1/2}$, implying subgrains and grains strengthen similarly [66].

Aluminum alloy strain hardening is commonly modeled using internal state variable models, such as those based on the Kocks-Mecking-Estrin (KME) formalism [68–71]. This model was initially developed for pure FCC metals on the principles of the Taylor relation [72], which considers flow stress as proportional to the square root of dislocation density (internal state variable). The KME model describes dislocation density evolution in terms of the thermodynamic process experienced by a metal undergoing plastic deformation. The internal energy during deformation is simultaneously increased through dislocation storage and decreased by dislocation annihilation (dynamic recovery). The KME model also provides a physical basis for the empirical Palm-Voce constitutive law [73,74] and agrees well with experimental data [71].

The strain hardening of pure metals is normally modified through the addition of solutes [75,76], precipitates [38,77,78], and dislocation cells/subgrains [27,79]. Inclusion of such features in the KME model requires modification to incorporate their effects on dislocation storage and recovery. The effects of dislocation cells/subgrains are of particular interest in this research as these are the primary strengthening mechanisms in AA5083 [7]. Verdier, *et al.* [27] modified the KME model to incorporate the effects of dislocation cell/subgrain, including additional dislocation storage and

dynamic recovery. The modification results in a non-linear relationship between hardening rate and flow stress which includes the initial non-linear transient in hardening rate at the onset of Stage III hardening. The model was developed as an explicit function of dislocation cell/subgrain size. This allows for inclusion of a recovery model such that the effects of dislocation structure coarsening may be intrinsically included. The modified KME model of Verdier, *et al.* [27] was further adapted to include subgrain annihilation during recrystallization, which effectively reduces the model to the classical KME formalism. Also, non-isothermal exposures were used for model development as compared to the isothermal exposures used by Verdier, *et al.* [27]. Non-isothermal exposures are more representative of the transient heating in fire exposures (see Chapter 2); thus, the model is optimized to predict the generally arbitrary heating during fire.

The aim of this aspect of the research is development of a novel integrated modeling approach for microstructural evolution (i.e., recovery and recrystallization), residual yield strength, and strain hardening of AA5083-H116. The individual models are combined in a sequentially coupled manner forming a fully integrated, physically-based constitutive model for residual mechanical behavior of a commercial 5xxx-series aluminum alloy. The models are also developed considering non-isothermal exposures as a realistic representative of fire scenarios, whereas non-ideal (for this application) isothermal exposures are normally used for model development [9,27]. Kinetics-based models for recovery and recrystallization are developed to predict the non-isothermal microstructural evolution. Residual yield strength after a non-isothermal exposure is predicted through implementation of the microstructural evolution models in microstructural strengthening models for subgrain and grain strengthening. A strain hardening model based on the modified KME model of Verdier, *et al.* [27] is also developed. This model is adapted to include the subgrain annihilation during recrystallization in a unified manner via the developed recrystallization model. The integrated model is compared against experimental data with good agreement.

3.2 Experimental

The commercial alloy studied in this research is AA5083-H116 rolled plate (6.4 mm thickness). The H116 temper designation specifies marine-grade Al-Mg alloys with greater than 3 wt% Mg be strain hardened in its final processing step. The material also meets the ASTM B928 standard for corrosion resistance. The chemical composition is given in Table 2.

Table 2. Chemical composition of AA5083-H116 in this research.

Alloy	Mg	Mn	Si	Fe	Cu	Cr	Zn	Ti	Al
5083-H116	4.4	0.57	0.11	0.24	0.06	0.09	0.02	0.02	bal

3.2.1 Material and Non-isothermal Heating

Fire exposures were simulated using constant, linear heating rates to prescribed temperatures (up to 500°C) followed immediately by water quenching. The constant heating rate exposure is an analog for the initial transient temperature increase of aluminum during fire. A representative aluminum structure with varying thicknesses of ceramic fiber insulation was exposed to a UL 1709 [18] fire exposure in a thermal model to determine the heating rates expected during fire. Effective heating rates of 250, 25, and 5°C/min were calculated for 0.0, 25.4, and 50.8 mm thick insulation (refer to Chapter 2 for details). These heating rates are expected to encompass the range of heating rates expected in an aluminum structure during fire. Tensile test specimens were heated at these effective heating rates in addition to 20°C/min, which was used to conduct a detailed material evolution study. All test specimens were heated using an induction heater controlled by an optical pyrometer and monitored using infrared thermography. Refer to Chapter 2 for further material heating details.

3.2.2 Optical Microscopy

The described induction heater was used to heat specimens for both mechanical measurements and metallurgical observations. Optical microscopy was performed using a HIROX KH-7700 digital video microscope. Specimens were mounted in a slow hardening epoxy resin. Grinding was performed using 300 – 1200 grit SiC paper (5 steps) with a variable speed grinder/polisher. Rough polishing was performed using 5, 3, and 1 µm polycrystalline diamond paste and suspension on low-nap woven textile, medium-nap billiard, and low-nap silk polishing cloths, respectively. Final polishing was performed using 0.05 µm colloidal silica on a chemically resistant polishing cloth. Mount pressure (10 – 20 N) and grinding/polishing speed (150 – 300 rev/min) were selected to ensure minimal matrix deformation and that all constituents remained intact. Etching was performed using 50 mL of Poulton's reagent (2 mL HF, 3 mL HCl, 20 mL HNO_3, 175 mL H_2O), 50 mL HNO_3, and 40 mL of a solution of 3 g chromic acid per 10 mL H_2O. All specimens were imaged on all three material planes using crossed polarizers to show grain contrast.

3.2.3 Transmission Electron Microscopy

TEM observations were performed using a Philips EM420 microscope operating at 120 kV. The TEM foils were removed from the RD-ND plane (normal to long-transverse direction) at the center of the heated region. Thin plates with a thickness of about 250 μm were removed from full-size test specimens using a SiC wafering blade. The thin plates were slowly mechanically ground to about 90 μm thickness. TEM foils were removed from the thin plates using a 3 mm diameter Gatan TEM disc punch. The foil was thinned to electron transparency by electropolishing using a solution of 30% HNO_3 in methanol at -30°C. TEM imaging was performed by aligning to a zone axis, then tilting the sample slightly to obtain good contrast. This effectively creates a two-beam condition for dislocation imaging. Images were taken at sample tilts of less than 10°.

3.2.4 Tensile Tests

Uniaxial, quasi-static tensile tests were performed at ambient conditions on previously heated samples using an Instron 5984 150 kN electro-mechanical testing machine. Specimen heating was performed as previously described at heating rates of 5, 20, 25, and 250°C/min up to 500°C. Strains were measured using strain gages (small strain analysis) and digital image correlation (large strain analysis). Further details can be found in Chapter 2.

3.2.5 Differential Scanning Calorimetry

Differential scanning calorimetry (DSC) was performed to characterize recrystallization kinetics. DSC thermal analysis was performed in a TA Q2000 DSC (shown in Fig. 22). Nitrogen was used as a purge gas and protective gas. Small (3mm diameter) aluminum rods were machined at low-speed from the as-received plate so as to retain the as-received microstructure. Thin (1.2 mm thick) discs were machined from the rods resulting in an average sample mass of about 23 mg. Aluminum TA Tzero sample pans were used for all measurements as they are exceptionally flat and provide optimal contact with DSC cell thermocouples.

Fig. 22. TA Q2000 differential scanning calorimeter.

Prior to performing the DSC runs, a cleaning run was performed to improve repeatability. The DSC baseline needs to be carefully considered, as it is both temperature and time dependent [80]. Therefore, a specific procedure was followed. Before testing, the DSC was cycled from 20 to 400°C at 80°C/min ten times to uniformly heat the cell and reduce any initial transients. A AA5083-H116 sample was then placed in the DSC and heated at the desired heating rate to 400°C followed by cooling to room temperature. The sample was then heated a second time at the same heating rate. The second measurement provides the heat flow for the material without recovery or recrystallization, which were removed during the first heating. As a result, the second measured heat flow is the baseline. This baseline run is later subtracted from the experimental results to determine the baseline correction. This is at odds with normal practice which conducts the baseline measurement using two empty sample pans. However, extensive testing determined leaving the heated sample in the DSC resulted in the most repeatable measurements. There are several distinct advantages to this method. The variability due to using different sample pans for sample and baseline measurement is removed. Also, the bulk AA5083 heat capacity is naturally removed from the measurement. This results in only the differential heat flow due to solid state reactions in the sample. This method is comparable to the common method of using ultra-high purity (99.999%) aluminum samples for the baseline measurement. Ultra-high purity Al was not used in this research due to the relatively high trace element content (5.5 wt%) in AA5083.

3.3 Experimental Results

3.3.1 Initial Microstructural State

TEM investigation was performed to study the dislocation microstructure of AA5083-H116 in the as-received condition. The as-received dislocation structure, shown in Fig. 23, is typical of that for materials processed by strain hardening. The dislocation structure has distinctive regions with subgrains of different morphology and texture. Fig. 23b shows the transition from a region with elongated (lamellar) subgrains to one with a more cube-like texture. Deviations from the elongated structure are expected to be a few microns wide by more than about 10 μm long [34]. Close examination of the lamellar structure (Fig. 23c) reveals extended lamellar boundaries (normally parallel to the rolling direction) with interconnecting dislocation boundaries (normally parallel to the normal direction). The lamellar boundaries are well-organized and thin, demonstrating that sufficient recovery has occurred during processing to transform the initial dislocation cell structure to subgrains. A slight diffraction contrast exists between adjacent subgrains, indicating a low misorientation angle. This further supports the formation of subgrains with low angle boundaries, which are similar to grain boundaries except with a much lower misorientation angle and, therefore, lower boundary energy. This concept is essential when considering the subgrain strengthening contribution. The majority of subgrain interiors are nearly free of dislocations; however, some locations have a relatively high level of interior dislocations. Few intermetallic particles, primarily of type Al-Mn, were identified in the structure.

The as-received subgrain size was determined from a series of TEM images in the RD-ND material plane. The lineal intercept method was used to determine the average subgrain size. Measurement lines were drawn perpendicular to that of the elongated-subgrain regions. 10 images were used to calculate an average subgrain size of 376 nm. The as-received subgrain size is similar to that obtained in other studies [7].

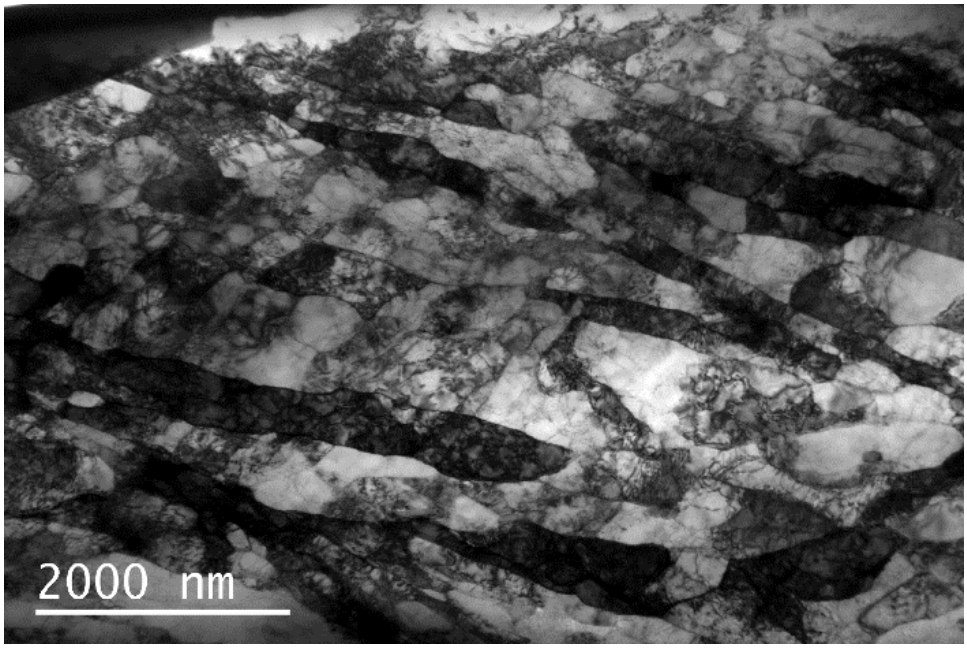

(a)

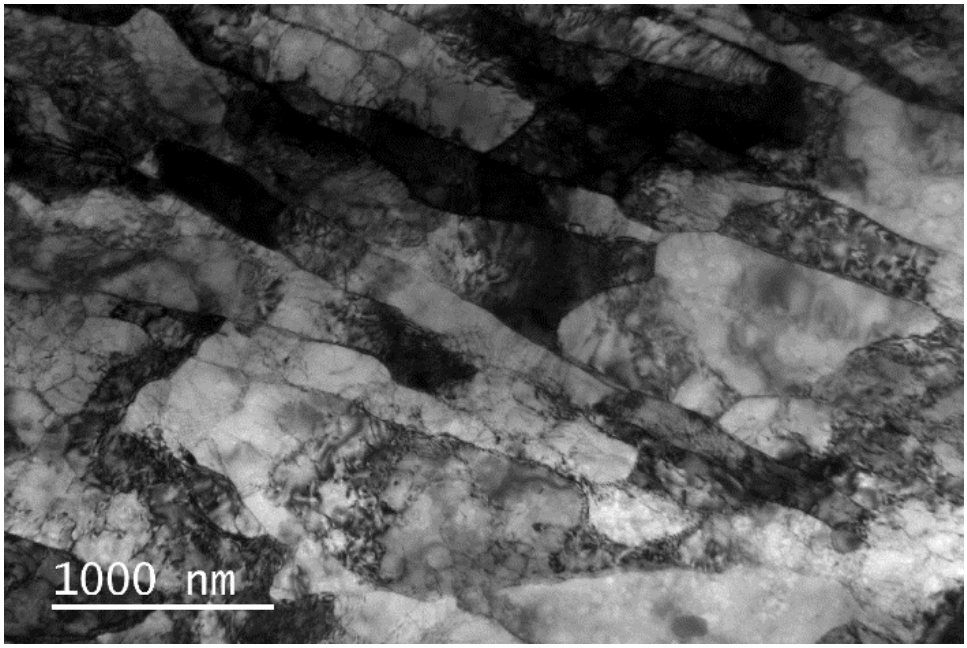

(b)

(Fig. 23 continued on next page)

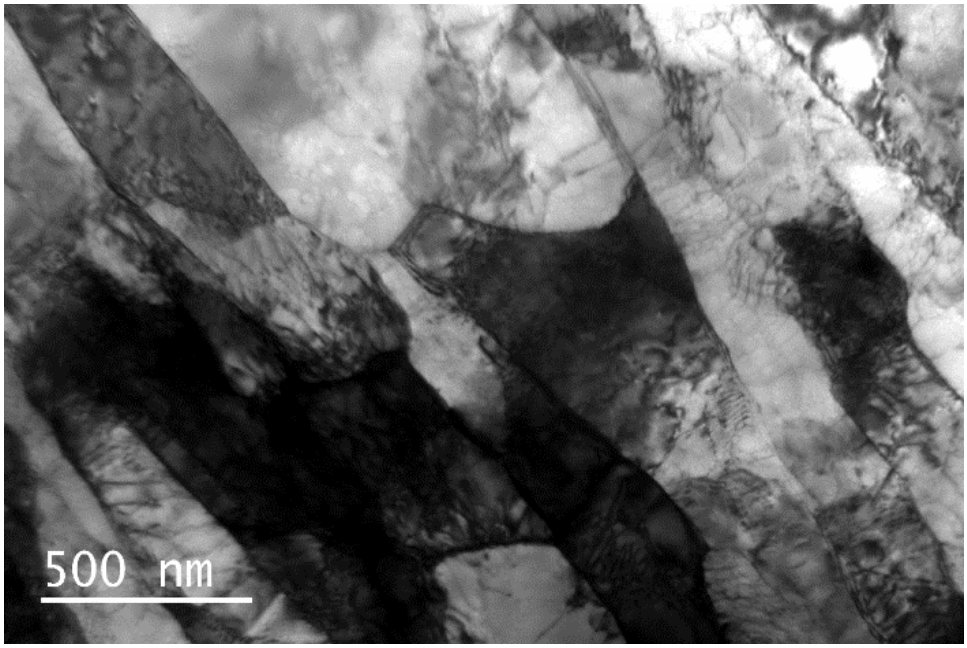

(c)

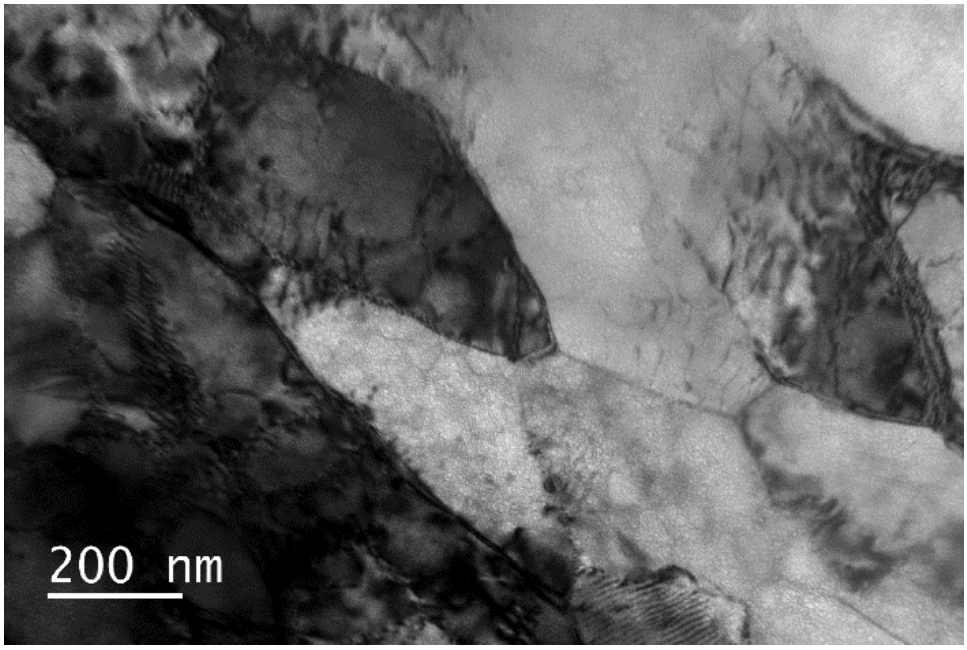

(d)

Fig. 23. AA5083 as-received dislocation structure showing a structure typical of strain-hardened aluminum alloys a different magnifications. Regions in (a) exhibit distinct rolling texture and cube texture.

The as-received grain size was determined from a series of optical micrographs. All three material planes were imaged under cross-polarized light after polishing and etching. A 3-D reconstruction of the as-received grain structure is shown in Fig. 24. The as-received grain structure is elongated

in the rolling direction, with grains about 10 μm thick and 50 μm wide (normal to rolling direction), on average. The average grain size was determined using the lineal intercept method. 10 images were used to calculate the average intercept length on each material plane. These average intercept lengths were used to calculate an average grain size of 89 μm. This grain size is similar to that measured in other studies [7].

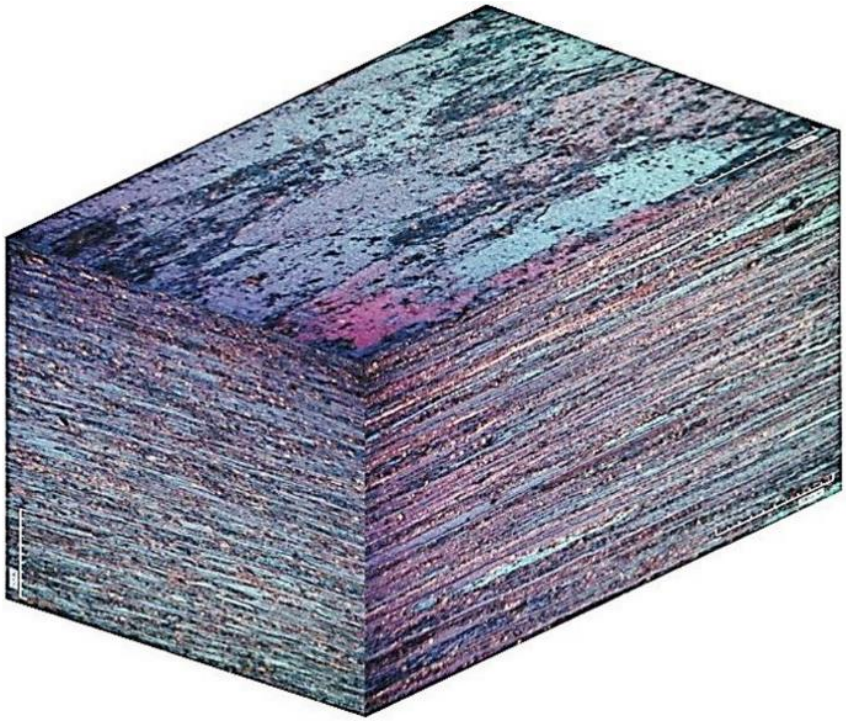

Fig. 24. AA5083-H116 as-received grain structure.

3.3.2 States Resulting from Non-Isothermal Heating

TEM and optical microscopy was performed on samples heated at 20°C/min to select temperatures to characterize microstructural evolution due to recovery and recrystallization. The fully recrystallized grain structure is shown in Fig. 25. The recrystallized grain structure is highly equiaxed with an average grain size of 48 μm. The recrystallization process initiates at areas of high strain such as at grain boundaries or intermetallic particles. The new grain nucleates and grows through the existing grain structure, impinging other nucleated grains until the process is complete [33]. This state is shown for AA5083 heated at 20°C/min to 400°C in Fig. 25. The recrystallization process itself is a kinetically-driven process. Further details on recrystallization kinetics are provided in the following section.

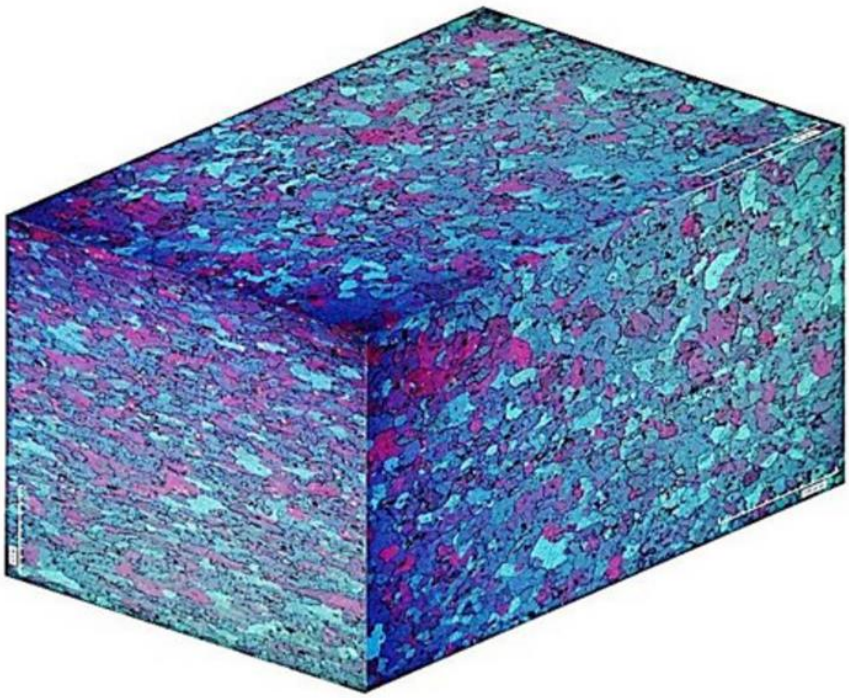

Fig. 25. AA5083-H116 recrystallized grain structure after heating to 400°C at 20°C/min.

The dislocation microstructure evolution during non-isothermal evolution is significantly more complex than that for the grain structure. The dislocation microstructure evolves in two distinct stages: recovery and recrystallization. AA5083-H116 recrystallization initiates at about 300°C at 20°C/min; recovery is the dominant process at lower temperatures. The microstructural evolution during recovery is consistent with Type II recovery [31,32], which is subgrain coarsening. The results in this work are supplemented by the extensive studies of Xing, *et al.* [81] on dislocation structures during recovery.

Heating to temperatures below 200°C (at 20°C/min) resulted in little increase in average subgrain size. The aspect ratio of the lamellar structures remained approximately that in the as-received material. At temperatures above 200°C, the dislocation structure exhibited significant coarsening until the onset of recrystallization. Coarsening was notably more significant for the non-lamellar structured subgrains. The lamellar structure aspect ratio also sharply decreased, resulting in a nearly equiaxed structure just prior to recrystallization. Refer to Fig. 26 for detailed evolution data. The rapid change in aspect ratio signifies that the lamellar boundaries coarsen at a much higher rate than the interconnecting dislocation boundaries. Xing, *et al.* [34] attributed the

different coarsening rates to the relative misorientation angles of the respective boundaries. Schematics of dislocation structure coarsening for the rolling texture component (lamellar structure) and other texture component (cube-like structure) have been provided in Fig. 27.

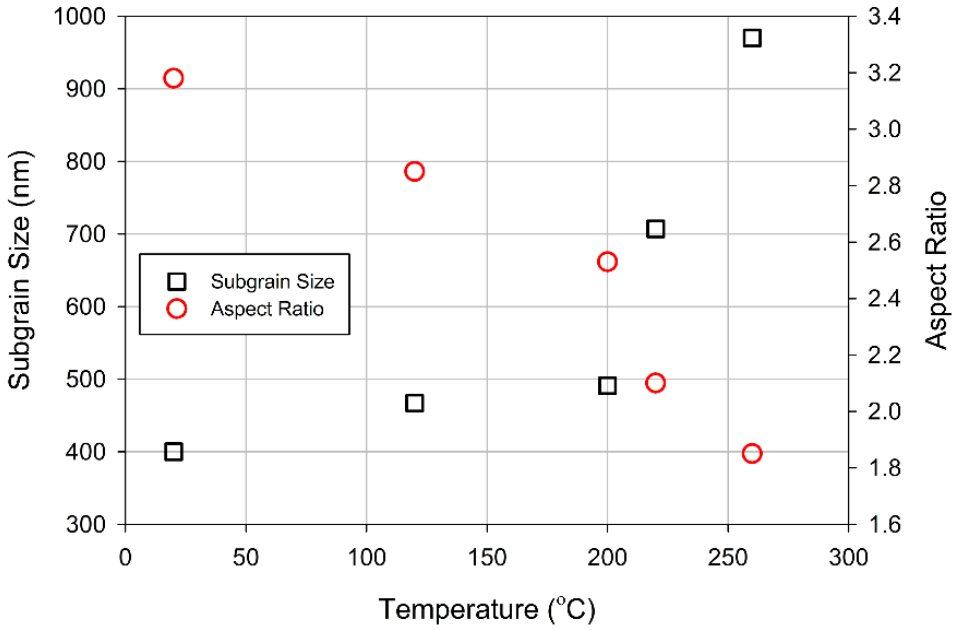

Fig. 26. Subgrain coarsening and lamellar structure aspect ratio evolution during low temperature annealing (2h isothermal anneals at listed temperature) [34].

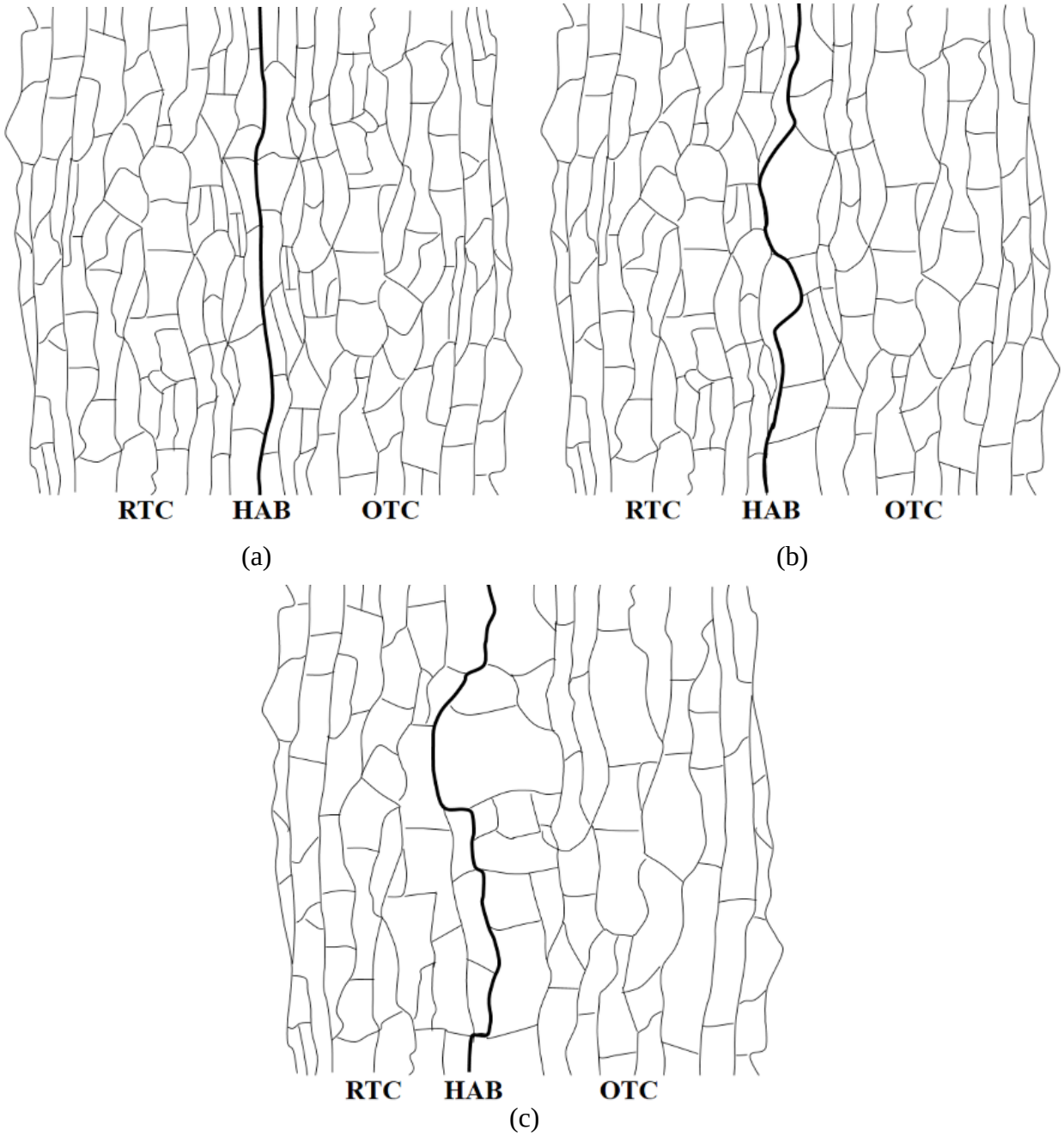

Fig. 27. Schematics of dislocation structure coarsening during recovery: (a) as-received structure, (b) early stages of recovery (~200°C), and (c) later stages of recovery (~250°C). Note the slight coarsening in rolling texture component (RTC) compared to the significant coarsening in the other texture component (OTC).

3.3.3 DSC Measurements of Recrystallization Kinetics

The DSC thermograms of AA5083-H116 obtained at heating rates from 5 – 80°C/min are shown in Fig. 28a. Each thermogram has an exothermic peak, which corresponds to the stored energy of

cold rolling released during recrystallization. Higher heating rates clearly correspond to higher recrystallization peak temperatures. This association was verified by optical microscopy. The exothermic peaks were isolated from the DSC thermogram to perform further analysis. A reference line was drawn from the initiation to end of the recrystallization peak. The DSC heat flow was then subtracted from this line. The resulting isolated peaks are shown in Fig. 28b for all heating rates. These were used to determine the recrystallization peak temperatures. The enthalpy of reaction was calculated by integrating the DSC peaks using

$$\Delta H = \int_0^\infty Q_{DSC} dT \tag{10}$$

where ΔH is the enthalpy of reaction and Q_{DSC} is the DSC heat flow. Peak temperatures and enthalpies of reaction are given in Table 3.

Table 3. AA5083-H116 DSC recrystallization peak temperatures and enthalpies of reaction.

***Heating Rate* (°*C/min*)**	**Peak Temp (°C)**	**Enthalpy of Reaction (mJ/mg)**
5	319.4	-0.2362
10	329.6	-0.3538
20	343.8	-0.3080
40	354.8	-0.2664
80	364.7	-0.2080

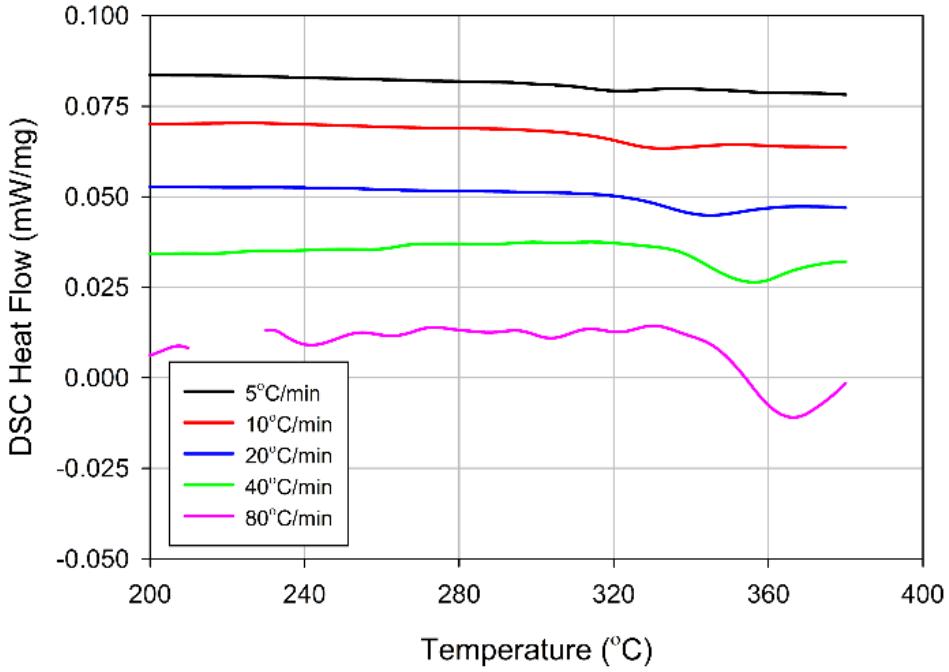

(a)

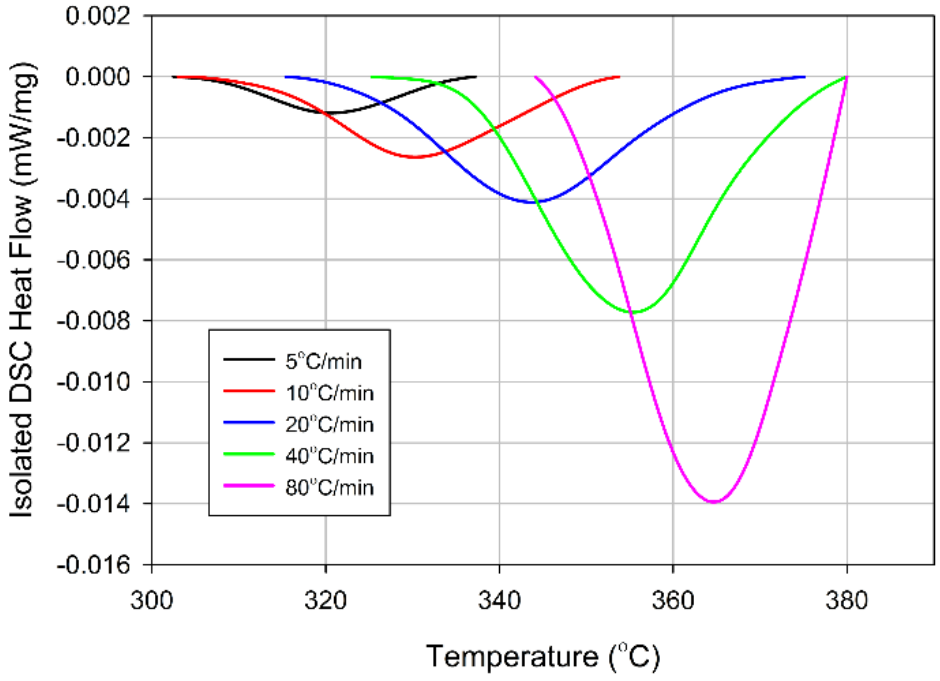

(b)

Fig. 28. AA5083-H116 differential heat flow obtained at different heating rates.

The activation energy for recrystallization, Q_{RX}, was determined using the Type B-1.95 isoconversion method, which has been shown to be highly accurate [81]. This method evaluates the variation in reaction peak temperature using the following expression:

$$\ln\left(\frac{B}{T_p^{1.95}}\right) = -\frac{Q_{RX}}{RT_p} + \text{constant} \tag{11}$$

where B is the heating rate, R is the universal gas constant, and T_p is the reaction peak temperature. The peak temperature is used as it is easily separated from other reactions and approximately corresponds to the same degree of transformation for all heating rates. The relationship in Eq. (11) was linearized and plotted (Fig. 29). Q_{RX} was calculated using the slope of a line fitted by least-squares regression to the data. Using this method, Q_{RX} was found to be 182 kJ/mol. This value is almost exactly that found for nanocrystalline AA1050 (178 kJ/mol) [9]. Additionally, this activation energy compares well with that determined using stereology for grain boundary migration in 90% cold-rolled AA1050 (172 – 183 kJ/mol) [36]. The activation energy suggests that grain boundary migration is solute-limited [36], which would be expected as AA5083 heavily relies on a dense solute atmosphere for strengthening.

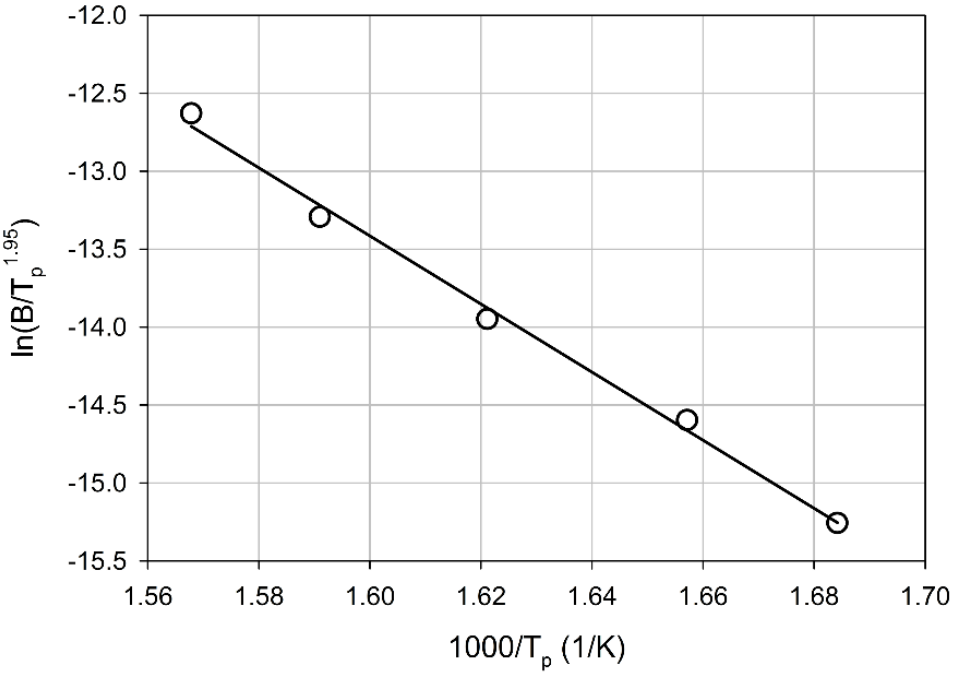

Fig. 29. Activation energy plot of $\ln(B/T_p^{1.95})$ versus the reciprocal of the absolute reaction peak temperature from AA5083-H116 DSC data.

3.4 Recovery Model

3.4.1 Non-isothermal Recovery Model

It is well known that recovery of the dislocation structures proceeds as a kinetic process. Early efforts to develop a kinetic recovery model were empirical in nature. One such early model was that developed by Kuhlmann, *et al.* [42]. However, this model predicts a finite (non-zero) recovery rate as the recovery process completes. This issue was corrected by Borelius, *et al.* [43]. Both models [42,43] are mechanistically based on the relaxation of the stored energy of deformation. A summary of these and other early kinetics models is given by Bever and Maddin [44]. Recently, more advanced models have been developed. A mechanistic model was developed by Nes [45]; however, the developed rate equations are integrated approximations of the Kuhlmann model [42]. Verdier, *et al.* [27] developed an internal stress relaxation recovery model, which improves on the Friedel model [82]. A disadvantage of this model is the introduction of additional model parameters which must be calibrated.

The Borelius model [43] provides a balance between representative capability and limited model parameters. Vandermeer and Hansen [9] successfully adapted the Borelius empirical recovery model [43] for a commercial aluminum alloy cold deformed to strains of 2 and 4. This work utilizes this adaptation as a basis to develop a non-isothermal recovery model. This section provides a summary of model development, including underlying assumptions as well as a description of basic model features.

The model used in this work was based on the recovery rate equation proposed by Borelius,

$$\frac{dP}{dt} = -PK_0 \exp\left[-\frac{Q_0 - \kappa P}{RT}\right] \tag{12}$$

where P is the instantaneous stored energy, t is time, K_0 is a pre-exponential factor, Q_0 is the activation energy, and κ is a constant. The constants, K_0, Q_0, and κ, are dependent on the governing recovery mechanism.

A disadvantage in the use of stored energy (P) as the model state variable is that it is not an easily quantified experimentally. This makes model calibration and implementation difficult. To avoid this issue, a series of proportionality relations were assumed

$$P \propto \rho \text{ and } \sqrt{\rho} \propto \sigma_y \tag{13}$$

where ρ is the dislocation density and σ_y is the yield strength. Thus, yield strength is relatable to stored energy and has the advantage of being a readily measurable quantity. The proportionality constants inherent to Eq. (13) were eliminated by assessing recovery as a fractional relationship with yield strength, that is

$$X_{RV} = \frac{\sigma_y - \sigma_{y,RX}}{\sigma_{y,AR} - \sigma_{y,RX}} \tag{14}$$

where X_{RV} is unity minus the fraction recovered, $\sigma_{y,RX}$ is the yield strength in the fully recrystallized state, and $\sigma_{y,AR}$ is the yield strength of the as-received material. $\sigma_{y,RX}$ is used due to the difficulty in separating recovery from recrystallization (refer to Ref. [9] for a detailed discussion).

From Eq. (13), P is clearly proportional to σ_y^2; therefore, X_{RV}^2 will be used as the kinetic state variable in the model. Applying this to Eq. (12) results in

$$\frac{dX_{RV}^2}{dt} = -X_{RV}^2 K_0 \exp\left[-\frac{Q_0 - \kappa P_0 X_{RV}^2}{RT}\right] \tag{15}$$

where P_0 is the stored energy of deformation in the as-received state. Eq. (15) is a thermally-activated rate equation with an apparent activation energy

$$Q_{app} = Q_0 - \kappa P_0 X_{RV}^2 \tag{16}$$

which is a function of the fraction recovered. An apparent activation energy of this form is in agreement with the observations of Michalak and Paxton [83] who observed an increase in activation energy with increasing fraction recovered.

The recovery rate equation was adjusted for use in non-isothermal heating in the following form

$$\frac{dX_{RV}^2}{dT} = -\frac{X_{RV}^2 K_0}{B}\exp\left[-\frac{Q_0 - \beta P_0 X_{RV}^2}{RT}\right] \quad (17)$$

where B is the heating rate. This form of the recovery rate equation is able to accommodate arbitrary heating rates and temperature profiles via the heating rate. The model parameters, K_0, κP_0, and Q_0, are assumed to be solely determined by the governing recovery mechanisms and independent of the exposure temperature. Thus, the recovery model may be implemented for non-isothermal heat treatments which include large temperature variations.

3.4.2 Recovery Model Calibration

The recovery model in Eq. (17) was calibrated using tensile mechanical tests for AA5083-H116 specimens exposed from 5 – 250°C/min (refer to Chapter 2 for details). The model implemented by Vandermeer and Hansen [9] was used as a basis for model parameters. It is worth noting that the model parameters in Ref. [9] were developed on the time-scale of many hours (up to 1000 h). Recrystallization initiates in an under an hour for all thermal exposures in this research; therefore, parameters likely require adjustment for prediction on these short time-scales.

The apparent activation energy relation in Eq. (16) was determined by separately considering the activation energy (Q_0) and apparent correction activation energy (κP_0). For a commercially pure Al alloy, Vandermeer [9] found that Q_0 was almost exactly that for self-diffusion in aluminum, 124 kJ/mol [84]. κP_0 was found to not follow any systematic variation with temperature, the average value was determined as 36 kJ/mol [9]. The observed effect of varying this parameter (κP_0) is to alter the onset of recovery. Parameter identification using data for AA5083-H116 in this study resulted in κP_0 = 50 kJ/mol.

The pre-exponential factor **(**K_0) was identified by comparison with the tested thermal exposures. The effect of this parameter is to change the slope of recovered fraction decrease as a function of temperature. Parameter identification resulted in an optimal value of $K_0 = 2 \times 10^6$ 1/s. This compares well to the average value (4.05×10^5 1/s) in Ref. [9]. A single value for K_0 is used in this research as compared to annealing temperature dependent values used in Ref. [9].

3.4.3 Recovery Model Results

The thermal exposures applied in mechanical testing were applied to as-received AA5083-H116. The predicted and experimental kinetic parameter as a function of maximum temperature reached and heating rate is shown in Fig. 30a.

It can be seen in Fig. 30a that recovery does not initiate for the non-isothermal exposures until 100°C for 5°C/min and about 140°C for 250°C/min. The increasing initiation temperature for recovery measured experimentally is well represented by model predictions. As can be seen, the slope of recovered fraction is relatively unchanged for the different heating rates. This is true of the experimental data and model predictions. At about 300°C, the reduction in experimental fraction recovered begins to drastically reduce due to the onset of recrystallization. The predictions are in good agreement with the fraction recovered determined experimentally.

The predicted fraction recovered may also be used to calculate the recovered subgrain size. A well-known empirical flow stress relation for subgrain strengthening is

$$\sigma_y = \sigma_0 + k_{sg}\left(\frac{1}{\delta}\right)^n \tag{18}$$

where σ_0 is frictional stress, k_{sg} is a constant, δ is the subgrain size, and the exponent n has different values (e.g., 1 or ½) assigned to it based on an assumed strengthening relationship. In this work, it was assumed that subgrain strengthening follows an n = ½ relationship, which is the same as that used in numerous studies [45,65,67,85] and the Hall-Petch relationship. Rewriting Eq. (18) in normalized form

$$X_{RV} = \frac{\sigma_y - \sigma_0}{\sigma_{y,AR} - \sigma_0} = \left(\frac{\delta_{AR}}{\delta}\right)^n \tag{19}$$

where δ_{AR} is the as-received subgrain size (376 nm) [86]. Solving for the instantaneous subgrain size

$$\delta = \frac{\delta_{AR}}{X_{RV}^2} \tag{20}$$

Subgrain sizes calculated using the predicted recovered fraction (see Fig. 30a) are shown in Fig. 30b. Model predictions are compared against subgrain sizes from Ref. [34], which were measured for specimens annealed at the shown temperatures for 2 h. The general trend of the experimental data is well predicted. Model predictions for 5°C/min are slightly delayed compared to experimental data, as would be expected due to the large difference in annealing time.

All parameters of the non-isothermal recovery model are provided in Table 4.

Table 4. AA5083-H116 non-isothermal recovery model parameters.

Parameter	**Significance**	**Value**	**Source**
K_0	Pre-exponential term to recovery model	2 x 10^6 1/s	σ_y from tests at 20°C/min (Fig. 30a)
Q_0	Activation energy for recovery (self-diffusion)	124 kJ/mol	[9,84]
κP_0	Apparent activation energy constant	50 kJ/mol	σ_y from tests at 20°C/min (Fig. 30a)
δ_{AR}	As-received subgrain size	376 nm	Lineal intercept of Fig. 23

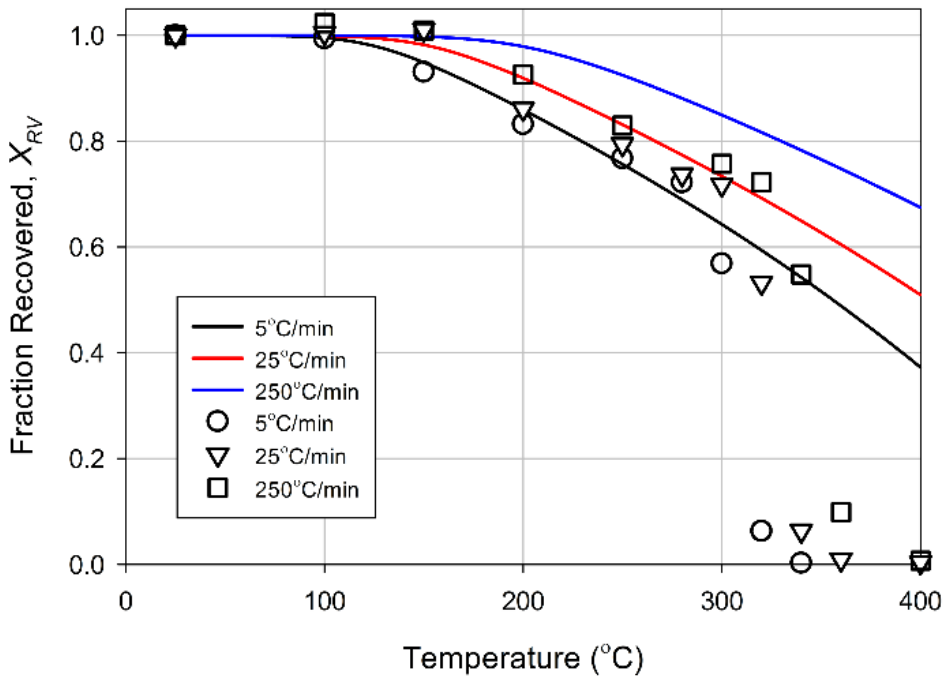

(a)

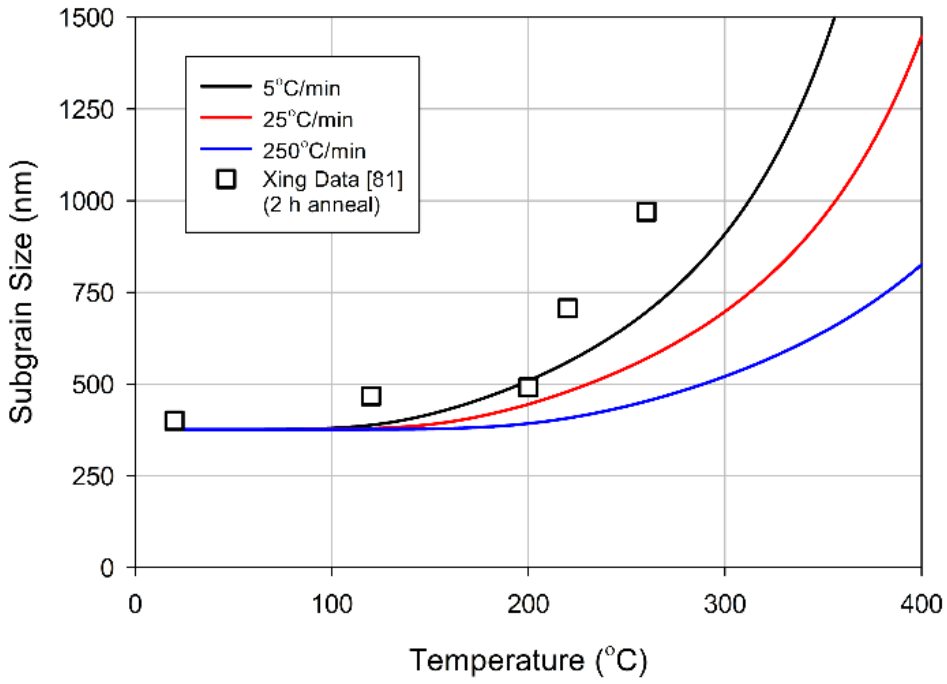

(b)

Fig. 30. Non-isothermal recovery kinetics: (a) fraction recovered and (b) subgrain size versus maximum temperature reached. Model predictions are lines and experimental data are symbols.

3.5 Recrystallization Model

3.5.1 Non-isothermal Recrystallization Model

Numerous models exist for the nucleation and growth process during recrystallization, ranging from empirical to computer-based simulations. These models can generally be classified as purely empirical or microstructurally-based. Austin and Rickett [87] initially suggested an empirical model which well characterizes kinetic data; however, it has no physical basis. Kolmogorov [54], Johnson and Mehl [55], and Avrami [56] developed the first kinetic models that took impingement into account. The KJMA model utilizes the abstract extended volume concept which allows for grains to nucleate and grow in already transformed regions. If the new phase is distributed randomly throughout the volume, the extended volume may be related to the true volume. Avrami suggested the following general expression

$$X_{RX} = 1 - \exp\left[-B \cdot t^{k}\right] \tag{21}$$

where t is the reaction time and, for the case of recrystallization, B is equated to a thermally-activated Arrhenius relationship and k describes the recrystallized grain shape. However, several issues arise in the use of this model, which are discussed in Ref. [58]. A primary issue is the assumption of randomness. Deviations from KJMA kinetics may result from early site-saturated nucleation (particle stimulated nucleation) and initially heterogeneous stored energy due to cold deformation, such as due to AA5083-H116 strain hardening.

New modeling methodologies were extensively pursued due to the described issues with the KJMA model, primary involving some level of computer simulation. A brief summary of these models is given by Vandermeer and Juul Jensen [62]. The microstructural path methodology (MPM) class of models are of particular interest in this research. MPM models improve and extend the KJMA approach, analytically describing the recrystallization process through the inclusion of additional microstructural descriptors. Initial MPM models were developed by Vandermeer and colleagues [59–61] in a general fashion to incorporate numerous nucleation and growth laws. Vandermeer and Juul Jensen [62] relaxed the randomness assumption of the KJMA approach in development of a linear/uniform nucleation and growth MPM model. This model was simplified to two parameters by fitting to experimental data and considering the recrystallization as a bulk

averaged process [63,64]. The linear/uniform impingement MPM was successfully implemented in Ref. [36] for cold-deformed AA1050. Additional studies have implemented this model successfully [88–90].

The primary advantage of the linear/uniform impingement MPM model is its representative ability of the complex recrystallization process in cold-rolled materials. This is noted in Ref. [36], including the following observations of cold-deformed AA1050:

- Avrami plots (-ln(1-X_{RX}) vs. time) at various annealing temperatures display two-stage linear behavior, with a transition in slope at $X_{RX} \approx 0.15$.
- The partial path function of S_{RX} plotted against X_{RX} was not centered about $X_{RX} = 0.5$, as would be the case with Avrami-like behavior.
- A transient, initial ($X_{RX} \leq 0.15$) decreasing growth rate was measured followed by a constant growth through recrystallization completion.

The above is evidence of evolving impingement behavior requiring a geometrically representative two-stage MPM model rather than the classical KJMA model. The linear/uniform impingement MPM model of Vandermeer and Juul Jensen [62] is suited to model the described behavior [36]. In the model, impingement is predicted in two stages as visualized in Fig. 31. Early impingement (Fig. 31a) resembles the uniform pattern of the KJMA model. The randomness assumption is somewhat violated in practice as nucleation preferentially occurs at areas of high stored energy (strain), i.e., particles or grain boundaries. At later stages, nuclei are clustered in colonies at the grain boundaries. This is mathematically idealized in the model as linear arrays, which are randomly placed in the modeled representative volume (Fig. 31b). Impingement (Fig. 31c) becomes pinched off in one dimension (linear impingement). Grains appear in three dimensions as random linear arrays (“string of pearls”). Random nucleation with uniform impingement continues to occur in the other two dimensions. This results in a notably faster conversion rate than predicted by the KJMA model due to the existence of additional nuclei in the representative volume.

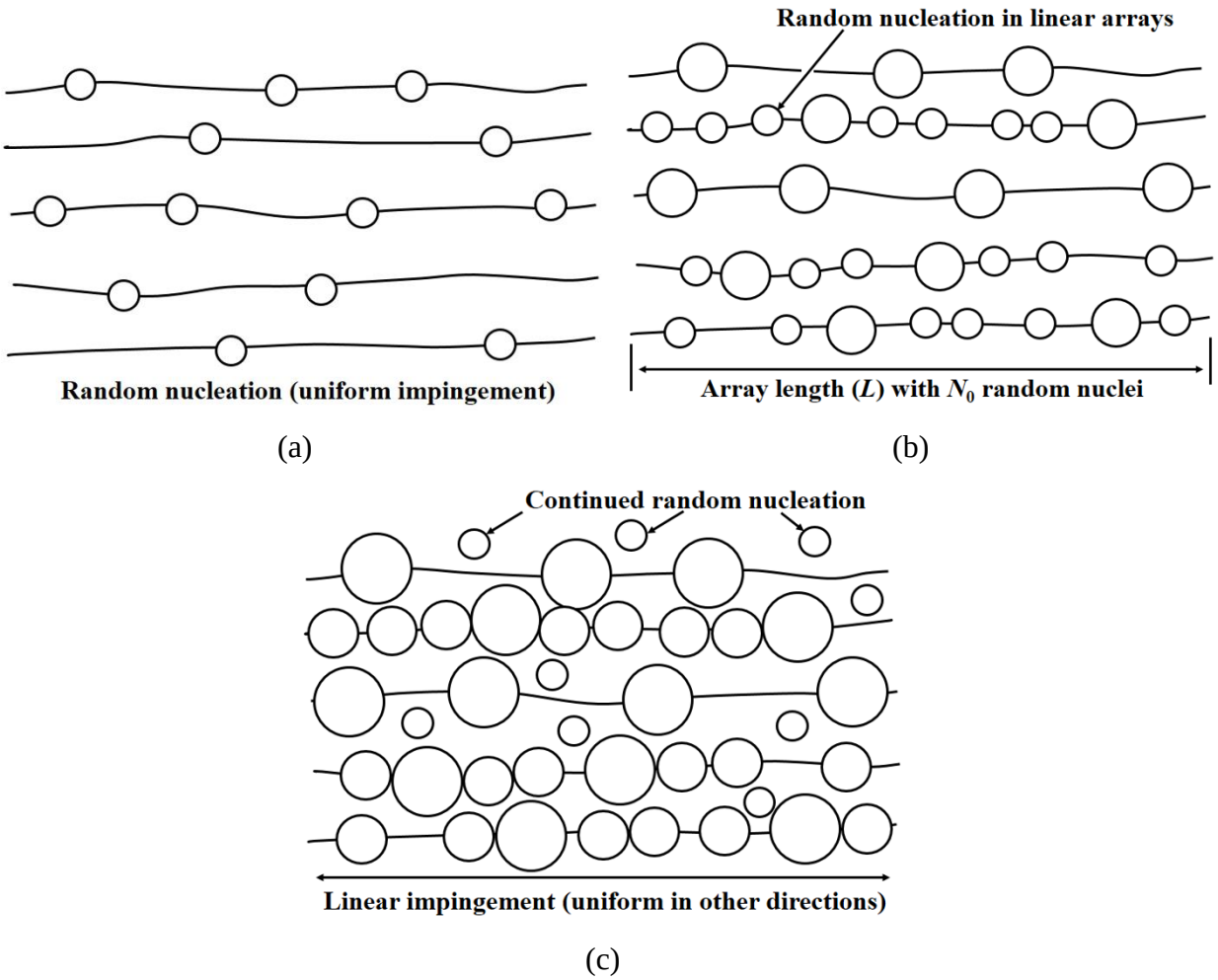

Fig. 31. Schematic of the linear/uniform MPM model idealization of recrystallization evolution. (a) Initial uniform nucleation and impingement (similar to KJMA model). (b) Random placement of linear arrays of nuclei (defined array length, L, with N_0 random nuclei). (c) Linear impingement occurs along linear arrays, uniform nucleation and impingement continues in other two directions.

In this research, the linear/uniform impingement MPM model is utilized in the development of a non-isothermal recrystallization model. This model is described in detail in Refs. [36,62,63]. A summary of the basic model features and its implementation is provided in this section. Details of the model assumptions are provided in Ref. [91].

The linear/uniform impingement MPM model utilizes a radius function (R) to define the average grain growth for all texture components. The radius function may be experimentally evaluated or implemented in a model by integrating the Cahn-Hagel growth rate. The Cahn-Hagel growth rate [92,93] is classically defined as

$$\langle v \rangle_{CH} = \frac{1}{S_{RX}} \cdot \frac{dX_{RX}}{dt} \tag{22}$$

where $\langle v \rangle_{CH}$ is the Cahn-Hagel growth rate. Grain boundary migration may be assumed to be a thermally-activated process, such that the temperature-dependent growth rate follows an Arrhenius relationship as

$$v_g = v_0 \exp\left(-\frac{Q_g}{RT}\right) \tag{23}$$

where v_g is the Arrhenius grain growth rate, v_0 is a pre-exponential constant (mathematically defined as velocity at infinite temperature), and Q_g is the activation energy of grain boundary growth. Note, Q_g is dependent on the rate controlling process for grain growth in the alloy of interest.

The basic features of the linear/uniform impingement model are as follows [36,91]:

- Nuclei are clustered in colonies which are idealized as linear arrays
- Nuclei occur randomly along the total array length per unit volume (L)
- N_0 total nuclei exist per unit array length, growth begins at short times compared to that measured experimentally
- Nucleation is site-saturated and is therefore not time-dependent
- Grain shape is spherical while unimpinged

The linear/uniform impingement MPM model is given by

$$-\ln(1 - X_{RX}) = \frac{\pi L}{4N_0^2}\left[K^2 + 2(K+1)\exp(-K) - 2\right] \tag{24}$$

$$\frac{S_{RX}}{1 - X_{RX}} = \frac{\pi L}{N_0}\left[K - K\exp(-K)\right] \tag{25}$$

where $K = 2R_gN_0$ and R_g is the grain radius function given by integrating the average grain growth rate, given in Eq. (23). Integrating the average growth rate and adjusting for non-isothermal exposures results in

$$\frac{dR_g}{dT} = \frac{v_0}{B}\exp\left(-\frac{Q_g}{RT}\right) \tag{26}$$

A Runge-Kutta algorithm is used to solve the above equation as a function of temperature (with linear heating rate, B). The recrystallization evolution (X_{RX} and S_{RX}) is determined by inserting the calculated average grain radii from Eq. (26) into Eq. (24) and Eq, (25).

In the above model, the parameters L and N_0 effectively describe the predicted recrystallization process. In addition, the product of these parameters gives the recrystallization nuclei density (N_v), that is, $N_v = LN_0$. This combined with Eq. (26) defines the nucleation and growth kinetics of the MPM model. Vandermeer and Juul Jensen [36] determined the model parameters for cold-deformed AA1050 (true strain of 2.3) as L = 2400 1/mm^2 and N_0 = 116 1/mm, resulting in N_v = 27.9 x 10^4 1/mm^3. The above MPM model was also applied to cold-rolled AA1200 (true strain of 2) by Vandermeer, *et al.* [90] resulting in model parameters of L = 58500 1/mm^2, N_0 = 58.5 1/mm, and N_v = 51 x 10^4 1/mm^3. Note, despite drastically different values for L, the N_0 and N_v parameters remain within a factor of two for the alloys.

It is also possible to estimate the final recrystallized grain size using N_v. From Underwood [94], this is calculated as

$$d_{RX} \approx 0.75 N_v^{-1/3} \tag{27}$$

where d_{RX} is the recrystallized grain size. The estimated recrystallized grain size for AA1050 and AA1200 were 11.4 and 9.4 μm, compared to 14.8 and 10.5 μm determined experimentally.

The final component of the non-isothermal model is prediction of the recrystallized grain size. Vandermeer [89] derived a partial path function for grain size from the linear/uniform impingement MPM model. However, this function represents limiting behavior at higher volume fractions recrystallized where uniform impingement occurs. An empirical relation was determined by Vandermeer and Juul Jensen [36] based on experimental data for a cold-deformed alloy. This relationship is

$$\langle \lambda \rangle = d_{RX} X_{RX}^{1/2} \tag{28}$$

where $\langle\lambda\rangle$ is the average chord length (size) of the recrystallized grains. This representation was successfully implemented in several other studies [88,95]. Thus, this simplistic relation is used to predict recrystallized grain size in this work.

3.5.2 Recrystallization Model Calibration

The non-isothermal recrystallization model requires parameter identification for the linear/uniform impingement MPM model (L and N_0) and the average grain growth rate model (v_0).

The MPM model parameters, L and N_0, govern the microstructural path character. A tabulated fitting method was suggested in Ref. [36]; however, in this case, a simpler method was employed. As noted, the d_{RX} may be estimated using Eq. (27) and $N_v = LN_0$. Estimation of d_{RX} using Eq. (27) in this manner has been well documented for cold-deformed/rolled alloys [36,88,90]. Therefore, the first identification metric was performed using Eq. (27). A second metric is required because two parameters must be simultaneously identified. This is accomplished using the recrystallized grain path function from Ref. [89], given as

$$\langle\lambda\rangle = \frac{1}{\alpha_g}\left(\frac{16}{9\pi L}\right)^{1/2}[-\ln(1-X_{RX})]^{1/6}X_{RX}^{1/3} \tag{29}$$

where α_g is a grain shape factor assumed to be unity. Predictions are compared against the experimentally verified empirical relation in Eq. (28). The MPM model parameters are identified using both metrics simultaneously. The values (L = 2400 1/mm^2 and N_0 = 116 1/mm) from Ref. [36] were used as initial conditions for this procedure and iteratively optimized to the described metrics. Thus, model parameters were identified as L = 280 1/mm^2 and N_0 = 15 1/mm.

The grain growth rate pre-exponential constant, v_0, must also be determined. A KJMA representation of grain growth data was used as an initial approximation. A procedure similar to that for the MPM model parameters was followed. Normalized yield strengths from mechanical tests at 20°C/min (see Chapter 2) were used to determine v_0 = 5 x 10^{15} 1/s. A KJMA model was implemented by Vandermeer and Juul Jensen [36] for the later stages of AA1050 recrystallization, determining v_0 = 1 x 10^{15} 1/s. The slight difference in values may be due to the different alloys under investigation.

The remaining parameters, Q and d_{RX}, were identified from experiment. The recrystallized grain size, d_{RX}, was measured stereologically in Fig. 25. The activation energy for grain boundary migration, which is used in the Arrhenius relation for grain growth rate in Eq. (26), may be equated to the activation energy determined in the DSC analysis. As discussed, the activation energy determined by DSC analysis of the exothermic peaks (Fig. 28) was 182 kJ/mol, which is similar to that in other studies: 178 kJ/mol [9], 172 – 183 kJ/mol [36], and 183 kJ/mol [96]. The exothermic peaks were also experimentally verified to coincide with recrystallization. Thus, it is assumed that the activation energy determined via DSC analysis is that of the rate controlling process for grain boundary migration; therefore, Q = 182 kJ/mol.

3.5.3 Recrystallization Model Results

Thermal exposures applied for the tensile mechanical tests (5, 20, 25, 250°C/min) were applied to as-received AA5083-H116. The measured yield strengths were normalized between the initial strength at the onset of recrystallization (~235 MPa) and the fully annealed strength (~120 MPa). This method is supported by measurements in Chapter 2 and other work [30] which measured about the same yield strengths at the onset of recrystallization. Model results are shown against normalized experimental data in Fig. 32.

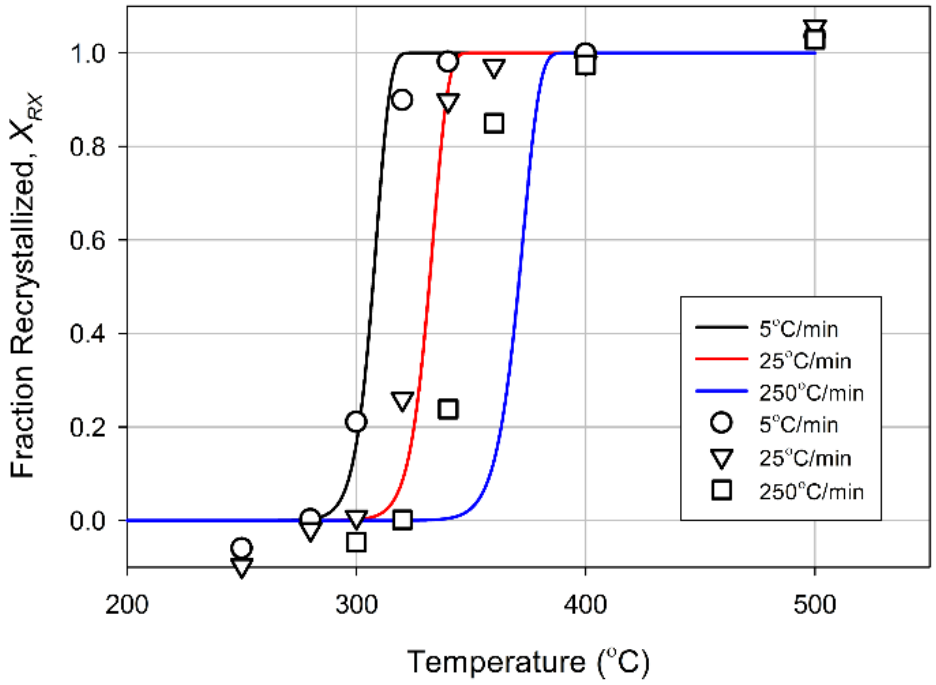

(a)

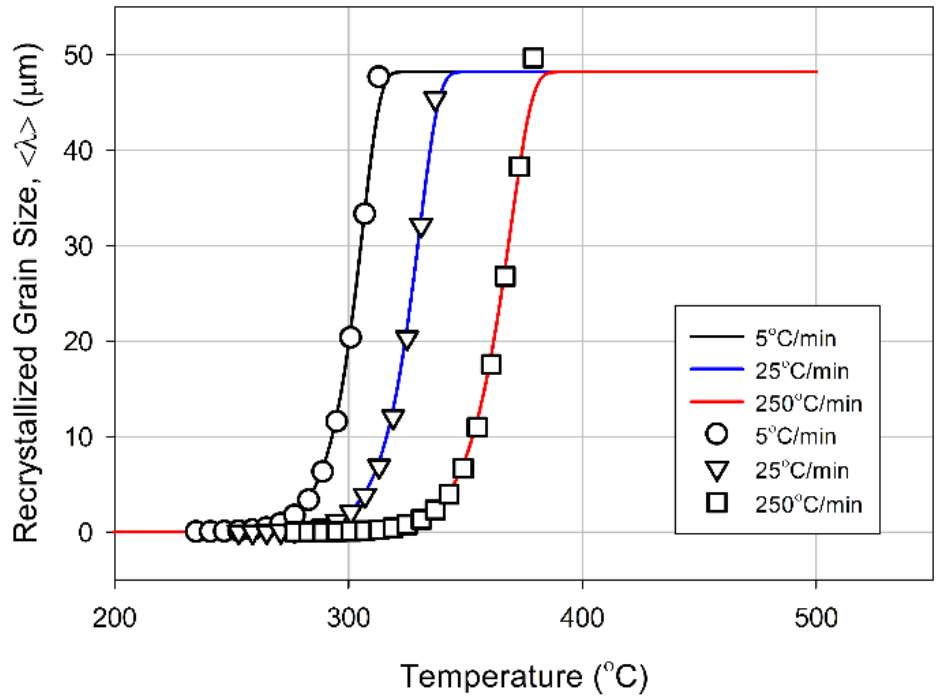

(b)

Fig. 32. Non-isothermal recrystallization model predictions of (a) X_{RX} (lines – model, symbols – normalized σ_y from Ch. 2) and (b) $\langle\lambda\rangle$ (lines – Eq. (28), symbols – Eq. (29)) as a function of maximum exposure temperature.

It can be seen in Fig. 32a that the trend in yield strength reduction due to non-isothermal heating is in good agreement with linear/uniform impingement MPM model predictions. The evolution characteristics of the MPM model is compared against the KJMA model (exponent = 2) [9] and the empirical Austin-Rickett model [58,87] in Fig. 33 (20°C/min). All models initially ($X_{RX} < 0.1$) predict nearly identical evolutions. Note, the initial Avrami-like behavior (uniform impingement) of the MPM model is expected as the linear arrays are randomly populated with recrystallization nuclei. A transition region is noted from about $X_{RX} \approx 0.1 - 0.2$, as is expected from experimental observations [36,89]. The MPM model predicts a faster conversion rate with increasing X_{RX} due to the predicted transition from uniform to linear impingement. This is evidenced by higher X_{RX} at a given temperature compared to the KJMA model ($X_{RX} > 0.1$). For example, at 340°C the difference in predicted X_{RX} is 0.10, while at 350°C the difference is 0.22. Also, the MPM model predicts the recrystallization process to complete ~10°C before the KJMA model. These aspects exemplify the necessity for an accurate recrystallization model in order to accurately capture the rapid yield strength reduction during recrystallization.

All parameters of the non-isothermal recrystallization model are provided in Table 5.

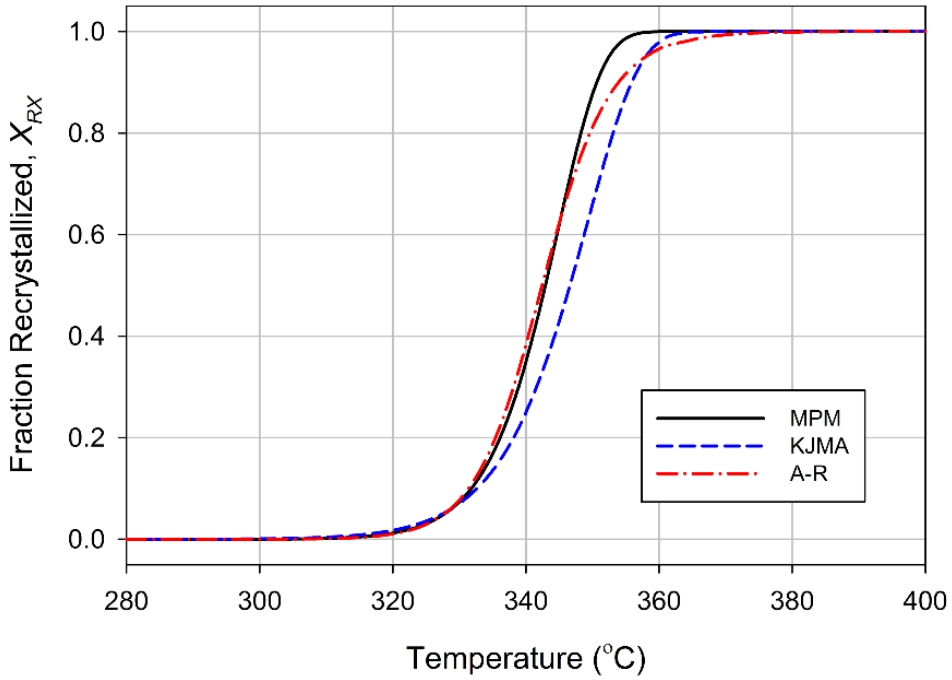

Fig. 33. Recrystallization model schematization for non-isothermal heating at 20°C/min.

Table 5. AA5083-H116 non-isothermal recrystallization model parameters.

Parameter	Significance	Value	Source
Q_g	Activation energy for grain boundary growth	182 kJ/mol	Q_{RX} from DSC
v_0	Pre-exponential term for grain growth rate	5 x 10^{15} 1/s	Normalized σ_y over RX (Fig. 32a)
L	Total array length per unit volume	280 1/mm^2	
N_0	Total recrystallization nuclei per unit array length	15 1/mm	
d_{RX}	Recrystallization grain size	48.2 μm	Lineal intercept of Fig. 24

3.6 Yield Strength Estimation

In this section, a yield strength model based on the microstructural features of AA5083-H116 is developed. The non-isothermal recovery and recrystallization models from Section 3.4 and 3.5 are implemented to capture the evolution in yield strength after non-isothermal thermal exposure.

The yield strength comprises the strengthening contributions of the microstructural features of the alloy, specifically (i) the friction stress (σ_0), (ii) the solid solution content (σ_{ss}), (iii) precipitate contributions (σ_p), (iv) grain contributions ($\Delta\sigma_g$), and (v) subgrain contributions ($\Delta\sigma_{sg}$). These are linearly superposed to calculate the total yield strength (σ_y) as:

$$\sigma_y = \sigma_0 + \sigma_{ss} + \sigma_p + \Delta\sigma_{sg} + \Delta\sigma_g \tag{30}$$

Linear superposition is assumed valid as the individual microstructural features strengthen at different length scales, thus there is negligible interaction. It is assumed that the thermal exposures in this research are too short to result in a significant reduction in solid solution content due to β-phase precipitation [86]. Thus, the solid solution strengthening contribution, σ_{ss}, will be assumed constant. As noted in previous discussion, TEM analysis did not reveal a high concentration of intermetallic precipitates; therefore, precipitate strengthening, σ_p, is considered negligible. The subgrain strengthening contribution, $\Delta\sigma_g$, is reduced by recovery and is annihilated by recrystallization; therefore, recovery and recrystallization models were implemented. The grain strengthening contribution, $\Delta\sigma_g$, is solely dependent on recrystallization.

3.6.1 Solid Solution

Two primary solutes exists within the AA5083 aluminum matrix: Mg and Mn. Here, the Mg is assumed to remain in solid solution in the as-received state. The high solubility of Mg in Al and the lack of Mg containing precipitates [97] makes this a reasonable assumption. The extensive STEM work of Huskins, *et al.* [7] also supports this assertion. The Mn solutes are not expected to remain in solid solution, rather, Mn-rich precipitates are expected to be formed [97,98]. Thus, Mn solid solution strengthening is considered negligible.

The solid solution strengthening contribution is commonly defined as

$$\sigma_{ss} = \sigma_{pure} + H\left(C_{Mg}\right)^{n} \tag{31}$$

where σ_{pure} is the strength without the solutes which are solution hardening the alloy, C_{Mg} is the Mg matrix solute concentration, and H and n are constants. Ryen, *et al.* [98] investigated several commercial purity Al-Mg alloys, examining the effects of Mg solid solution content on yield strength. Form this work, the constants for Eq. (31) are obtained: H = 13.8 MPa/(Mg wt%)^n and n = 1.14. This results in a solid solution strengthening contribution for AA5083-H116 (C_{Mg} = 4.4 wt% Mg) of σ_{ss} = 75 MPa.

Ryen, *et al.* also investigated several alloys to determine σ_{pure}. The alloy with trace elements closest to that in AA5083-H116 is AA1050 (0.09 wt% Fe and 0.27 wt% Si). Thus, σ_{pure} in Eq. (31) is taken as $\sigma_{pure} = \sigma_{\mathrm{AA1050}}$ = 19.3 MPa. In this work, σ_{pure} is assumed to include both the friction stress (normally assumed ~10 MPa) and the hardening contribution of trace elements, i.e., Fe and Si. Therefore, the friction stress (σ_0) in Eq. (30) is defined as $\sigma_0 = \sigma_{pure}$ = 19.3 MPa.

3.6.2 Grains

Typically, the yield strength contribution of grain boundaries is assumed proportional to the inverse square of the average grain size. This is described by the Hall-Petch relation

$$\Delta\sigma_g = k_g d^{-1/2} \tag{32}$$

where k_g is the Hall-Petch constant and d is grain size. Last, *et al.* [35] estimated the Hall-Petch constant for an Al-4wt%Mg as k_g = 0.22 MPa-m$^{1/2}$. Implementing the as-received grain size (d_{AR} = 89 μm) and fully recrystallized grain size (d_{RX} = 48 μm) in Eq. (32) results in $\Delta\sigma_{g,AR}$ = 23 MPa and $\Delta\sigma_{g,RX}$ = 32 MPa, respectively. In order to preserve nomenclature continuity with the non-isothermal recrystallization model, the above relation is rewritten as

$$\Delta\sigma_g = k_g\langle\lambda\rangle^{-1/2} \tag{33}$$

In this case, $\langle\lambda\rangle$ is the recrystallized grain size which follows the empirical relation with X_{RX} given in Eq. (28).

A few assumptions are made in order to implement the non-isothermal recrystallization model with the defined strengthening models. The friction stress is assumed constant throughout all thermal exposures such that it can be removed from any evolution law. The recrystallization process is also assumed to occur in a complementary fashion, i.e., the unrecrystallized volume fraction is 1 – X_{RX}. The grain boundary evolution is also assumed to follow the transformation path of the predicted recrystallized fraction, X_{RX}. From these assumptions, the grain strengthening contribution may be described as

$$\Delta\sigma_g = X_{RX}k_g\langle\lambda\rangle^{-1/2} + (1 - X_{RX})k_g d_{AR}^{-1/2} \tag{34}$$

where d_{AR} is the as-received grain size (89 μm). Substituting Eq. (28) for $\langle\lambda\rangle$, results in

$$\Delta\sigma_g = X_{RX}^{3/4}k_g d_{AR}^{-1/2} + (1 - X_{RX})k_g d_{AR}^{-1/2} \tag{35}$$

Utilizing this relation, the yield strength contribution of the partially recrystallized structure may be obtained.

3.6.3 Subgrains

Subgrains are the primary strengthening mechanism in cold-rolled 5xxx-series alloys [7]. The subgrains also factor heavily in the residual yield strength evolution after prior thermal exposure. Subgrains coarsen due to recovery at relatively low temperatures and are annihilated by grain boundary migration during recrystallization [8].

Subgrain strengthening is considered to be mechanistically similar to grains [66]; however, with lower effectiveness due to lower misorientation angles. Hansen and colleagues [65–67] studied dislocation structure strengthening mechanisms, developing mechanistic relations to calculate the strengthening contributions. The first relation is developed from the assumption that dislocation pileup at the boundaries is the operative mechanism. This relation is given as

$$\Delta\sigma_{sg} = G\sqrt{b\theta_m}\delta^{-1/2} \tag{36}$$

where G is the shear modulus, b is the Burgers vector, and θ_m is the misorientation angle. The other relation is developed by relating the total dislocation density to that internal to the cellular dislocation network, which is negligible for heavily cold-rolled metals, and the dislocation density of the boundaries. Assuming a mixed tilt/twist boundary, a relation for dislocation forest hardening due to grain boundary ledge dislocation is arrived at

$$\Delta\sigma_{sg} = M\alpha G\sqrt{3b\theta_m}\delta^{-1/2} \tag{37}$$

which simplifies to

$$\Delta\sigma_{sg} = 1.25G\sqrt{b\theta_m}\delta^{-1/2} \tag{38}$$

assuming $M = 3$ and $\alpha = 0.24$ [67]. Experimental evidence for the dominance of either mechanism has not been reported [66]. However, the relations demonstrate dislocation structures strengthen proportional with the structural parameters as $\sqrt{\theta_m}$. Thus, subgrain boundaries (low angle boundaries, $\theta_m \leq 15°$) theoretically strengthen less effectively than grain boundaries (high angle boundaries, $\theta_m \geq 15°$).

Subgrain strengthening may also be assumed to follow the empirical Hall-Petch relation in Eq. (32). Note, the mechanistic relations in Eqs. (36) and (38) also follow the Hall-Petch formalism as they are proportional to $\delta^{-1/2}$ with the constant, k_{sg}, defined mechanistically. The Hall-Petch relation for subgrains is given as

$$\Delta\sigma_{sg} = k_{sg}\delta^{-1/2} \tag{39}$$

The empirical constant, k_{sg}, is typically estimated as $0.2 \cdot k_g - 0.5 \cdot k_g$ [7]. Huskins, *et al.* [7] empirically determined $k_{sg} = 0.064$ MPa-m$^{1/2}$ for AA5083-H131.

The empirical relation in Eq. (39) was examined for use in this research. The constant, k_{sg}, was determined such that the total predicted yield strength was that measured experimentally in the as-received condition. From this, $k_{sg} = 0.10$ MPa-m$^{1/2}$. Comparatively, the mechanistic constant from Eq. (36) is $k_{sg} = 0.097$ MPa-m$^{1/2}$ and from Eq. (38) is $k_{sg} = 0.124$ MPa-m$^{1/2}$ for $G = 26400$ MPa and $\theta_m = 2.7°$ [34]. The mechanistic relation in Eq. (36) agrees well with the empirically determined constant; therefore, this will be used to determine subgrain strengthening in this work.

Implementation of the subgrain strengthening model requires consideration of recovery and recrystallization processes. Similar assumptions to those made for the grain strengthening model during recrystallization have been made in development of this model. The subgrain size model in Eq. (20) is substituted for δ in Eq. (36) to implement recovery-induced subgrain coarsening, resulting in

$$\Delta\sigma_{sg} = G\sqrt{b\theta_m}\left(\frac{\delta_{AR}}{X_{RV}^2}\right)^{-1/2} \tag{40}$$

where X_{RV} is the fraction recovered from Eq. (17). The effects of recrystallization are added in a similar manner. Grain boundary migration results in annihilation of the subgrain boundaries, thus

$$\Delta\sigma_{sg} = (1 - X_{RX})G\sqrt{b\theta_m}\left(\frac{\delta_{AR}}{X_{RV}^2}\right)^{-1/2} \tag{41}$$

where X_{RX} is the fraction recrystallized from Eq. (24). Utilizing this relation, the yield strength contribution of the partially recovered and recrystallized structure may be predicted.

3.6.4 Results and Discussion

The complete non-isothermal yield strength model is given by

$$\sigma_y = \sigma_0 + H\left(C_{Mg}\right)^n + \left[X_{RX}^{3/4} k_g d_{AR}^{-1/2} + (1 - X_{RX}) k_g d_{AR}^{-1/2}\right] + (1 - X_{RX}) G\sqrt{b\theta_m}\left(\frac{\delta_{AR}}{X_{RV}^2}\right)^{-1/2} \quad (42)$$

The first parameter on the right hand side is the friction stress. The second parameter is from the solid solution strengthening model. The bracketed parameter group implements grain strengthening with the first and second terms representing grain nucleation and growth, and grain annihilation, respectively. Both processes are a function of recrystallized fraction, X_{RX}. The fifth term on the right hand side implements subgrain strengthening, including subgrain coarsening as a function of X_{RV} and subgrain annihilation, due to recrystallization, as a function of X_{RX}.

The yield strength is predicted using Eq. (42) with the predicted fraction recovered, X_{RV}, from Eq. (17) and fraction recrystallized, X_{RX}, from Eqs. (24) and (26). Comparison with experimental data is shown in in Fig. 34. All model parameters are given in Table 6.

Table 6. AA5083-H116 yield strength model parameters.

Parameter	**Significance**	**Value**	**Source**
σ_0	Friction stress including Fe, Si solutes	19.3 MPa	AA1050 [98]
H	Constant for effect of Mg solutes on σ_{ss}	13.8 MPa/(Mg wt%)^n	[98]
n	Hardening exponent for Mg solutes	1.14	[98]
k_g	Hall-Petch constant for grain strengthening	0.22 MPa-m$^{1/2}$	[35]
d_{AR}	As-received grain size	89 μm	Lineal intercept of Fig. 24
d_{RX}	Recrystallized grain size	48 μm	Lineal intercept of Fig. 25
G	Shear modulus	26400 MPa	
b	Magnitude of Burger's vector	0.286 nm	
θ_m	Mean misorientation angle of subgrains	2.7°	[34]
δ_{AR}	As-received subgrain size	376 nm	Lineal intercept of Fig. 23

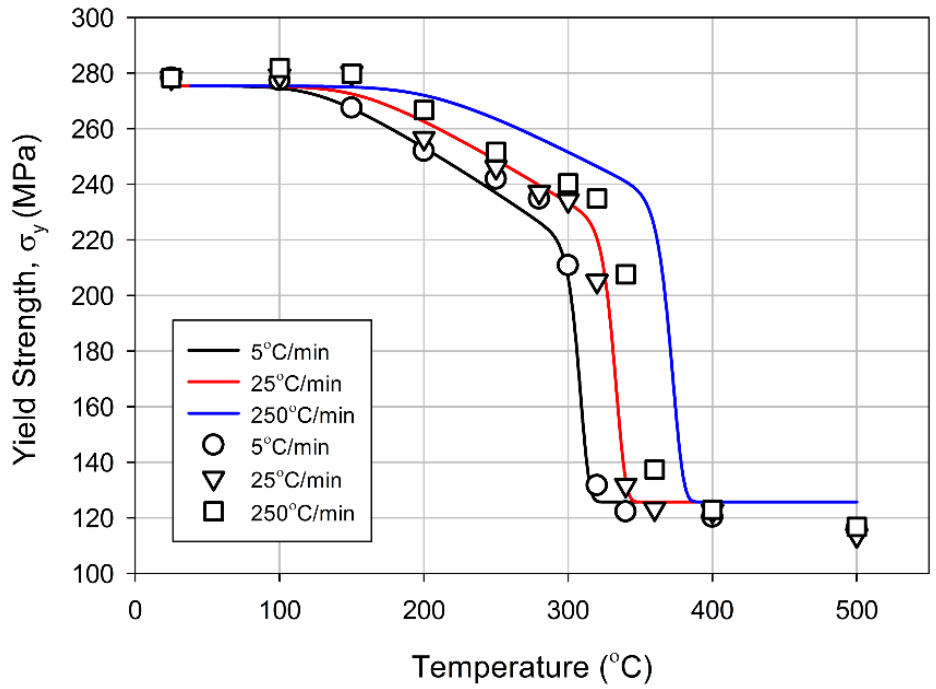

Fig. 34. Yield strength model predictions (lines) compared against experimental data (symbols).

The experimentally measured residual yield strength after thermal exposure is well represented in Fig. 34 by the yield strength model predictions. The discrepancy at 250°C/min is explained by the small amount of time from reaching the desired temperature to water quenching. Model simulations have shown that a 5 s hold at the maximum temperature accounts for this disagreement. The recovery process which causes the initial yield strength reduction at lower temperatures (below 280 – 320°C, depending on heating rate) is predicted by the model, specifically by the recovery and subgrain strengthening. The primary reduction, which occurs from about 280 – 380°C, depending on heating rate, is caused by recrystallization. The onset of recrystallization is also captured by the model. The yield strength evolution during recrystallization is predicted by the grain and subgrain strengthening models; the kinetics are predicted by the recrystallization model. The predicted yield strength after recrystallization has completed (125.7 MPa) is also in agreement with experimental data, with predicted contributions of σ_0 = 19.3 MPa, σ_{ss} = 74.7 MPa, $\Delta\sigma_{sg}$ = 0 MPa, and $\Delta\sigma_g$ = 31.7 MPa.

The yield strength also depends on heating rate: the lower the heating rate, the lower the yield strength for a given maximum temperature. This effect is clearly associated with further subgrain coarsening and an earlier onset of recrystallization, which results in a comparative yield strength

reduction. The predicted behavior is as expected based on the individual recovery and recrystallization kinetics models. Note, slight deviations in the recrystallization model kinetics from that in AA5083-H116 may result in differences of up to 100 MPa between predicted and experimental yield strengths. This may occur even when equivalent fractions recrystallized differ by only 10°C. This demonstrates the sensitivity of this model, or any recrystallization-strength model, to inaccurate kinetics.

The agreement observed in Fig. 34 validates the coupled approach used in this research. Knowledge of the recovery and recrystallization path is required to account for the yield strength reduction due to non-isothermal exposure. Moreover, the grain and subgrain strengthening constants, k_g and k_{sg}, are exceedingly important as they scale the model predictions based on the perceived strengthening of grains and subgrains.

3.7 Strain Hardening Model

In this section, a strain hardening model based on the microstructural features of AA5083-H116 is developed. This model is developed in conjunction with the residual yield strength model (Section 3.6) to provide a complete description of residual elasto-plastic behavior after fire exposure.

Aluminum alloy strain hardening has been supposed to be the competitive evolution of the dislocation structure in terms of dislocation storage and dynamic recovery (dislocation annihilation or rearrangement) [68–70]. In this supposition, the dislocation structure is assumed to maintain similitude, an assumption supported by TEM analysis [71]. Verdier and colleagues [27,41] considered the effects of a cellular dislocation structure (i.e., subgrains in AA5083-H116) on strain hardening, including dislocation structure evolution during recovery. The subgrains in AA5083-H116 undergo sequential evolution due to recovery (subgrain growth) and recrystallization (subgrain annihilation). The non-isothermal recovery and recrystallization models from Section 3.4 and 3.5 are therefore implemented to capture subgrain evolution and its effect on strain hardening.

3.7.1 AA5083-H116 Strain Hardening Behavior

The strain-hardening rate at ambient after prior thermal exposure has been detailed in Chapter 2. It has been reproduced in Fig. 35 for clarity of discussion. Several features of note are observed. Recovery ($T \leq 300$°C in Fig. 35) affects hardening rate negligibly except at stresses near yielding (transition from Stage II to Stage III hardening). Recrystallization causes a significant reduction in hardening rate at constant stress. It is surmised, after the elastic regime, the hardening behavior follows an empirical Palm-Voce constitutive law [73,74]

$$\frac{d\sigma}{d\varepsilon} = \theta\left(1 - \frac{\sigma}{\sigma_{sat}}\right) \tag{43}$$

where θ is the hardening rate at σ = 0 and σ_{sat} is the saturation stress which the exponential relationship approaches at infinite strain. The above relation is characteristic of pure FCC metals deformed at a constant strain rate in the Stage III hardening regime. The above initiates after Stage II hardening completes.

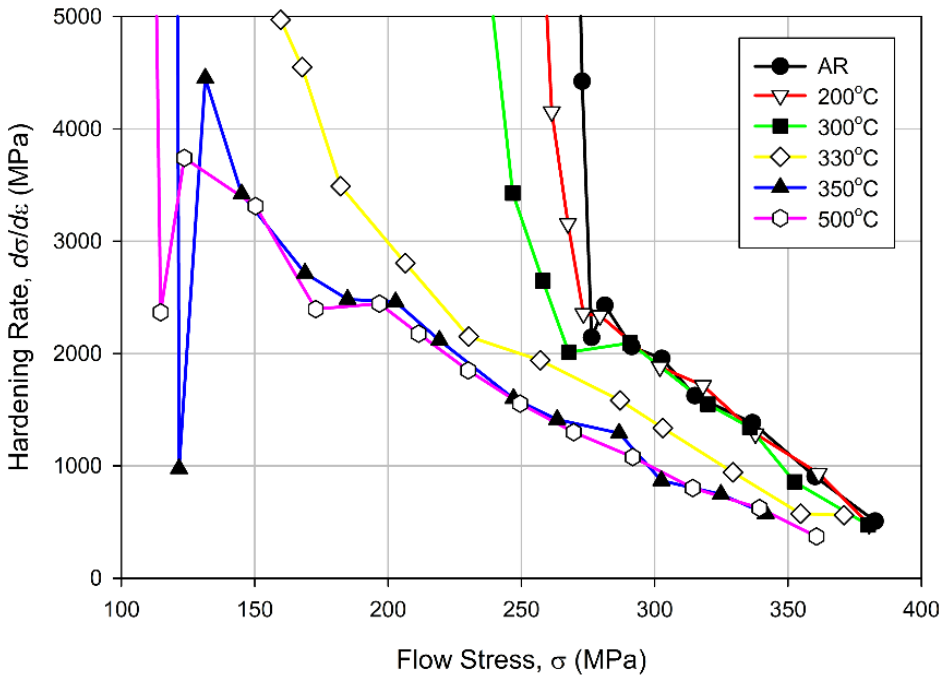

Fig. 35. Strain hardening rate versus flow stress after prior thermal exposure at 20°C/min.

The values of θ and σ_{sat} evolve as a function of the microstructure, which changes due to recovery and recrystallization during a thermal exposure. The Palm-Voce law in Eq. (43) was fit to the

stress-strain relations from tensile mechanical tests on specimens previously exposed at 20°C/min. The parameters, θ and σ_{sat}, are reported in Fig. 36a. As can be seen, both parameters follow a trend with the evolved microstructure, as the evolution due to recrystallization is clearly discerned. These parameters can also be characterized by a "master" curve using parameter normalization, as shown in Fig. 36b. As is shown, a single master curve, fitted by least-squares regression (slope = -488.1), was fit to experimental data. This demonstrates the strain-hardening mechanisms evolves by a similar mechanism for all tested thermal exposures.

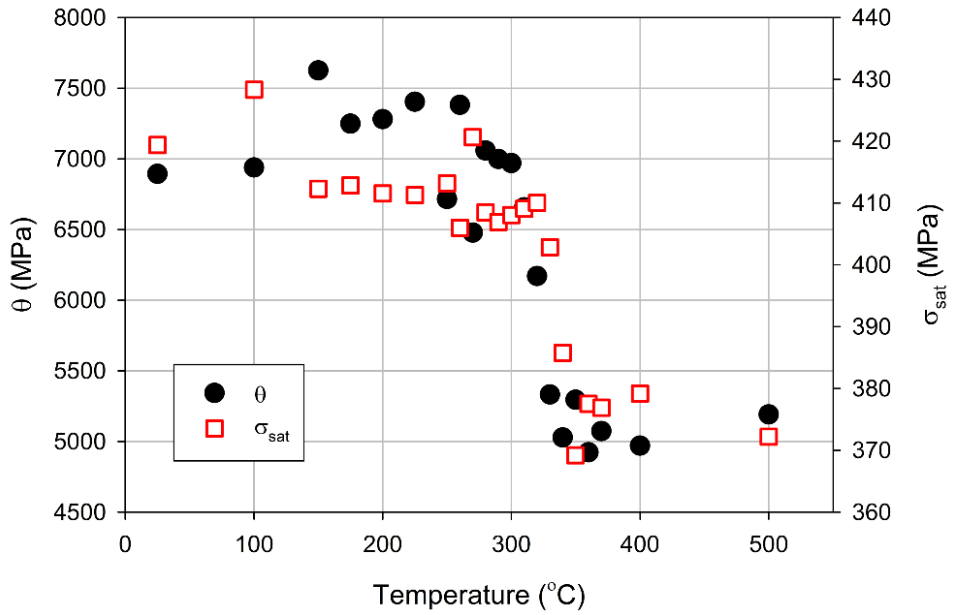

(a)

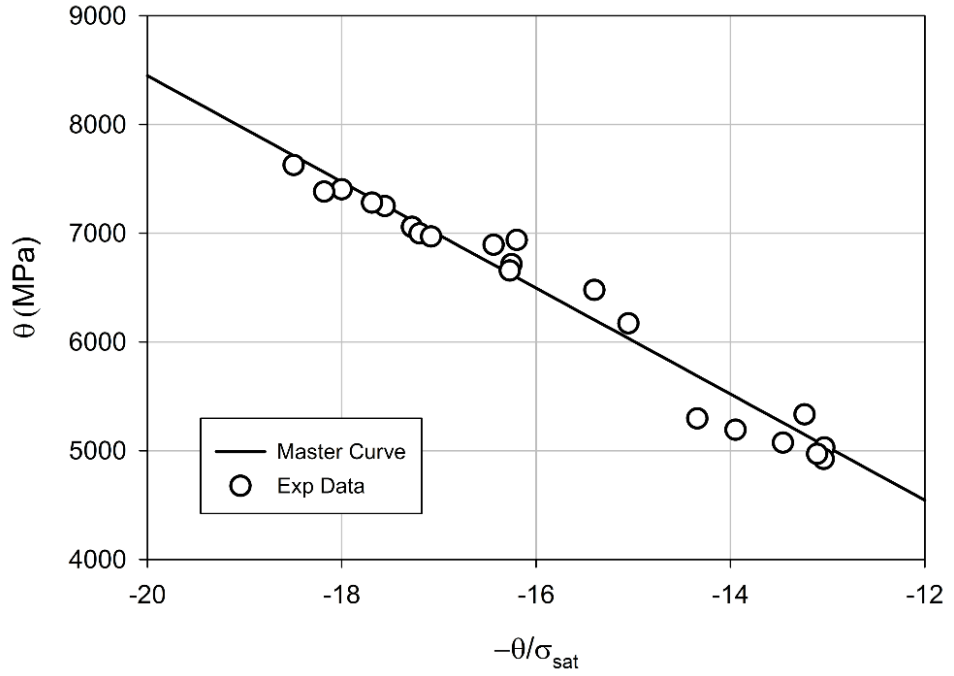

(b)

Fig. 36. Evolution of Palm-Voce law strain-hardening parameters as (a) a function of temperature and (b) normalized with a fitted "master" curve.

3.7.2 KME Model

For pure metals, the Kocks-Mecking-Estrin (KME) model [68–70] links the evolution in dislocation density, ρ, to the local plastic shear strain, γ,

$$\frac{d\rho}{d\gamma} = k_1\sqrt{\rho} - k_2\rho \tag{44}$$

where k_1 and k_2 are proportionality constants. The first term ($k_1 = 1/b$) on the right hand side signifies a storage of dislocations, and increasing dislocation density, due to dislocation pinning by immobile obstacles, such as solutes. The second term ($k_2 = L_0/b$, where L_0 is the annihlation distance in a dislocation pair of opposite sign) represents dynamic recovery of dislocations by mutual annihilation [71]. Dislocation interactions are related to ρ via the flow stress contribution of forest hardening

$$\sigma = M\alpha Gb\sqrt{\rho} \tag{45}$$

where M is the Taylor factor and α is a material dependent constant normally between 0.15 and 0.5 [99]. Combining Eq. (44) and (45) and the definition of the Taylor factor (i.e., $M = \sigma/\tau = \gamma/\varepsilon$) results in a strain-hardening law of the Palm-Voce formalism

$$\frac{d\sigma}{d\varepsilon} = \theta_0\left(1 - \frac{\sigma}{\sigma_{sat,0}}\right) \tag{46}$$

where $\theta_0 = M^2\alpha Gbk_1/2$ and $\sigma_{sat,0} = M\alpha Gbk_1/k_2$. For commercial alloys, apparent values for θ_0 and $\sigma_{sat,0}$ must be determined, i.e., θ and σ_{sat}, as these describe the behavior of pure metals. Several experimental studies [100–102] have shown that a linear relationship between hardening rate, θ, and flow stress, as dictated by Eq. (46), holds for aluminum alloys in solid solution. However, it can be seen in Fig. 35 that the hardening rate is a slightly non-linear function of stress throughout Stage III hardening. This is in agreement with the work of Verdier, *et al.* [27] and Chu and Morris [100], which examined the effect of dislocation structures, such as subgrains, on strain hardening behavior.

3.7.3 KME Model including Subgrain Effects

As discussed, AA5083-H116 has an extensive subgrain network developed by cold rolling. Verdier, *et al.* [27] developed a modified KME model which incorporates the additional storage and dynamic recovery of the cellular dislocation structure. An integral assumption in this model is that the initial dislocation structure is preserved at least for the first few percent strain during tensile deformation. This assumption is supported by the work of Chu and Morris [100].

A new form of KME relation in Eq. (44) is introduced to account for the dislocation structure

$$\frac{d\rho}{d\gamma} = k_1\sqrt{\rho} + k - k_3\rho \tag{47}$$

where $k = 1/b\delta$. This term, k, accounts for the additional dislocation storage by the subgrain boundaries. k is similar to that introduced in a modified KME relation for Orowan loop storage in precipitation hardening alloys [38,102,103]. The total dynamic recovery is represented by k_3 as

$$k_3 = k_2 + \frac{K_{sg}}{\delta} \tag{48}$$

The contribution of the subgrain boundaries has been added to the intrinsic dynamic recovery coefficient, k_2. Verdier, *et al.* [27] describes K_{sg} as roughly proportional to the volume fraction of subgrain boundaries. It should vary as the ratio of the subgrain boundary width to subgrain size, thereby effectively describing the dynamic recovery efficiency of the dislocation structure.

Eqs. (45), (47), and (48) are combined to develop the modified KME constitutive law as

$$\frac{d\sigma}{d\varepsilon} = \theta_0 + \frac{P_1}{\sigma} - P_2\sigma \tag{49}$$

where P_1 represents subgrain dislocation storage and P_2 is total dynamic recovery. P_1 and P_2 are defined as

$$P_1 = M^3(\alpha G)^2\frac{b}{2\delta} \quad \text{and} \quad P_2 = \frac{\theta_0}{\sigma_{sat,0}} + \frac{KM}{2\delta} \tag{50}$$

These parameters are modified to include the effects of recrystallization by assuming that the portions associated with subgrains, i.e., those which are a function of δ, follow subgrain evolution

during recrystallization. Thus, these terms are reduced to zero due to subgrain annihilation. This is integrated in Eq. (50) as

$$P_1 = (1 - X_{RX})M^3(\alpha G)^2 \frac{b}{2\delta} \quad \text{and} \quad P_2 = \frac{\theta_0}{\sigma_{sat,0}} + (1 - X_{RX}) \frac{K_{sg} M}{2\delta} \tag{51}$$

After recrystallization completes, the modified KME constitutive law effectively reduces to the classical KME law in Eq. (46), which does not account for the effects of dislocation structures.

3.7.4 Modified KME Model Calibration

The modified KME constitutive law in Eqs. (49) and (51) was calibrated by adjusting K through comparison with tensile mechanical tests of specimens previously exposed at 20°C/min (see Chapter 2). Following the method in Ref. [27], θ_0 was assumed constant as θ of the recrystallized state (refer to the Palm-Voce law in Eq. (43) and Fig. 36a). Thus, it is approximated as θ_0 = 5000 MPa. Implementing this assumption in Eq. (49), P_1 and P_2 are determined from experimental data using non-linear least-squares regression.

P_1 and P_2 are linearly related through substitution for δ in Eq. (50) as

$$P_1 = (M\alpha G)^2 \frac{b}{K_{sg}} \left(P_2 - \frac{\theta_0}{\sigma_{sat,0}} \right) \tag{52}$$

K_{sg} is therefore determined from the slope of the least-squares regression fitted line in Fig. 37. This results in K_{sg} = 1030 nm. The magnitude of this value is notably larger than theoretically determined in Ref. [27]. However, the alloy in this research is a commercial alloy and therefore includes other effects such as a uniform distribution of subgrain sizes and varying organization of the dislocation structures forming the subgrain boundaries. These effects are not included in the theoretical model basis, which is related to pure metals. This may explain the difference of calibrated K versus theory.

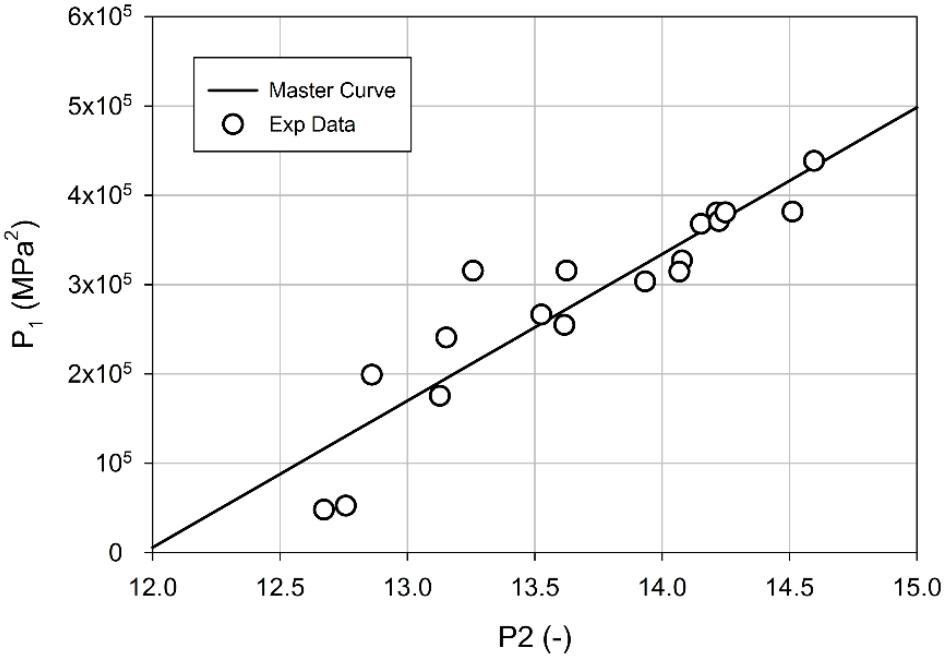

Fig. 37. Evolution of model parameters P1 and P2 during recovery and recrystallization, which cause parameters to progress along the fitted line towards the origin.

The final parameter to be determined is the trapping distance for mutual dislocation annihilation, L_0. Eq. (52) is used with experimental values for P_1 and P_2 from all tensile tests performed at 20°C/min and K from the previous analysis to calculate the mean value as L_0 = 16.6 nm.

All parameters of the modified KME model are provided in Table 7.

Table 7. Modified AA5083-H116 KME model parameters.

Parameter	**Significance**	**Value**	**Source**
M	Taylor factor	3.07	[98]
α	Constant linking dislocation density to flow stress	0.3	[27]
b	Magnitude of Burger's vector	0.286 nm	
G	Shear modulus	26400 MPa	AA5083-H116
L_0	Annihilation distance between two dislocations of opposite signh	16.6 nm	Mean value from Eq. (52) for 20°C/min tests
K_{sg}	Efficiency of dislocation walls for dislocation annihilation	1030 nm	Least squares fit to data in Fig. 37 and Eq. (52)
θ_0	Stage II hardening rate	5000 MPa	θ of 20°C/min tests in RX state

3.7.5 Results and Discussion

The coupled non-isothermal constitutive model is given by the modified KME constitutive law in Eqs. (49) and (51) which uses the non-isothermal yield strength model in Eq. (42) as the initial condition to calculate flow stress. Model parameters for the constitutive law are given in Table 7 and yield strength model are given in Table 6. Microstructural evolution due to prior non-isothermal heating implemented using the recovery model (X_{RV} from Eq. (17), δ from Eq. (20), parameters from Table 4) and the recrystallization model (X_{RX} from Eqs. (24) and (26), parameters from Table 5).

The modified KME model predictions are compared with experimental data (20°C/min heating rate) in Fig. 38. Several possible material states are shown: (a) as-received, (b) partially recovered (T = 225°C), (c) partially recrystallized (T = 320°C), and (d) fully recrystallized (T = 400°C). It is evident the model is capable of predicting the measured strain hardening behavior after prior thermal exposure. The overall agreement between predictions and experiment is good at the shown conditions, which encompass those possible in AA5083-H116. The slightly increased initial hardening rate (plastic strain < 0.05) after recrystallization is particularly well represented. The ultimate strength behavior, which has been shown to reduce by ~40 MPa due to recrystallization (Chapter 2), is also reflected by model predictions. The strain hardening behavior approaches approximately the same saturation stress for all conditions in Fig. 38, as is expected from experiment.

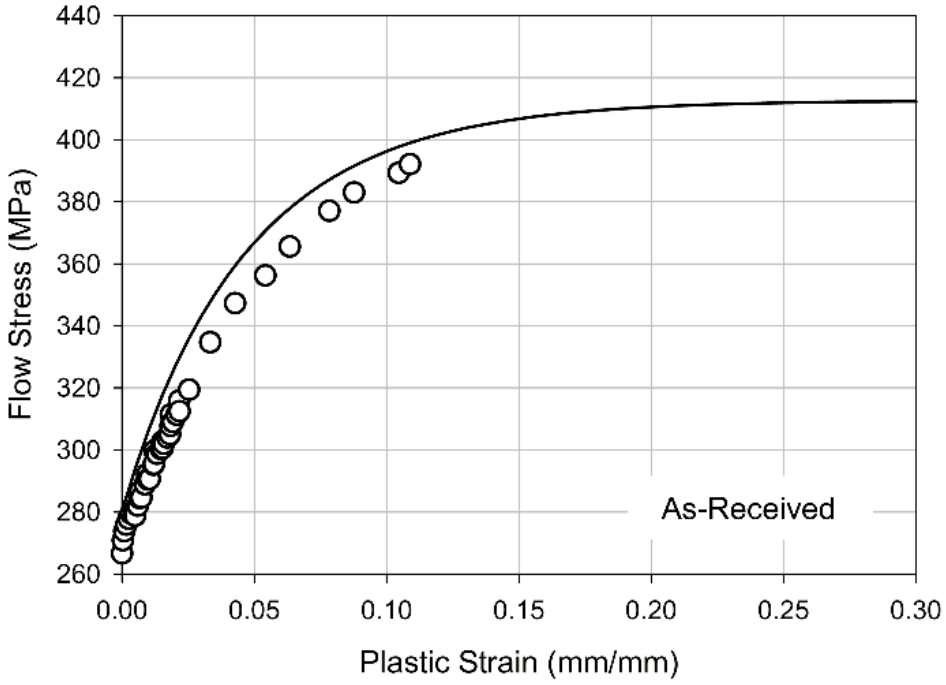

(a)

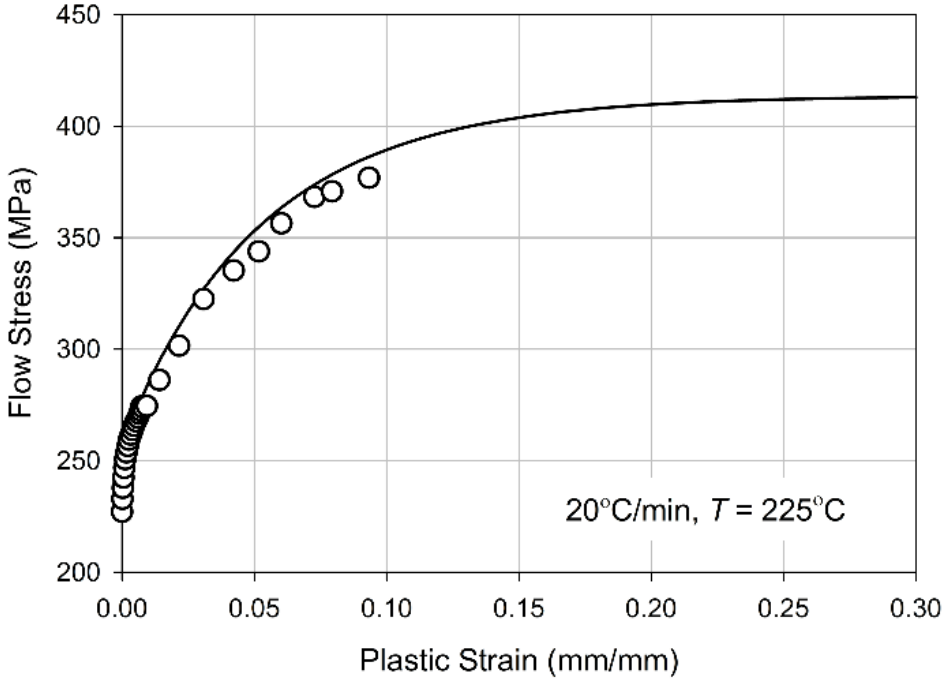

(b)

(Fig. 38 continued on next page)

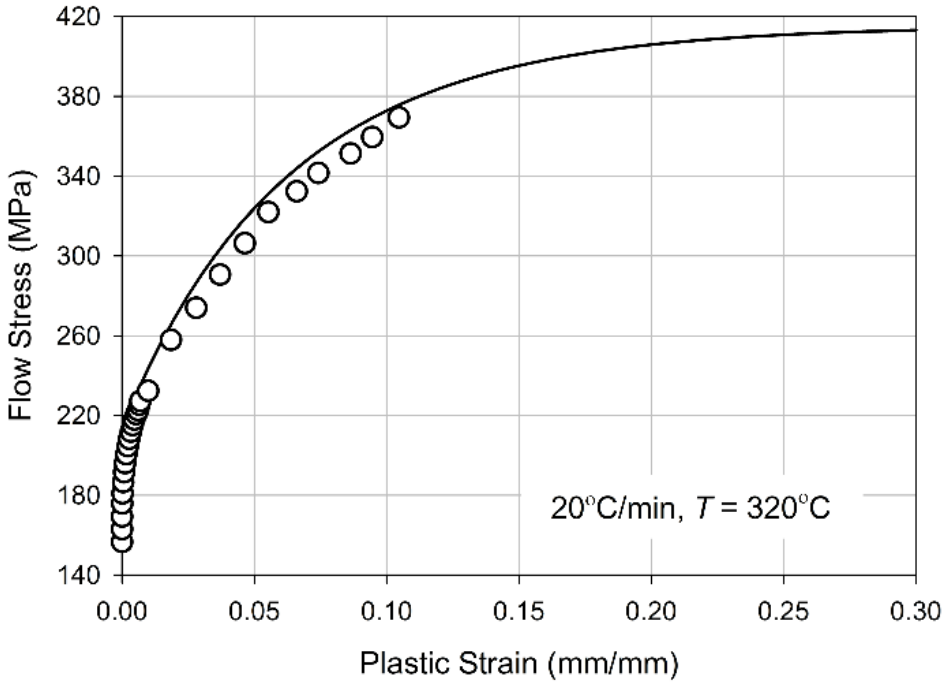

(c)

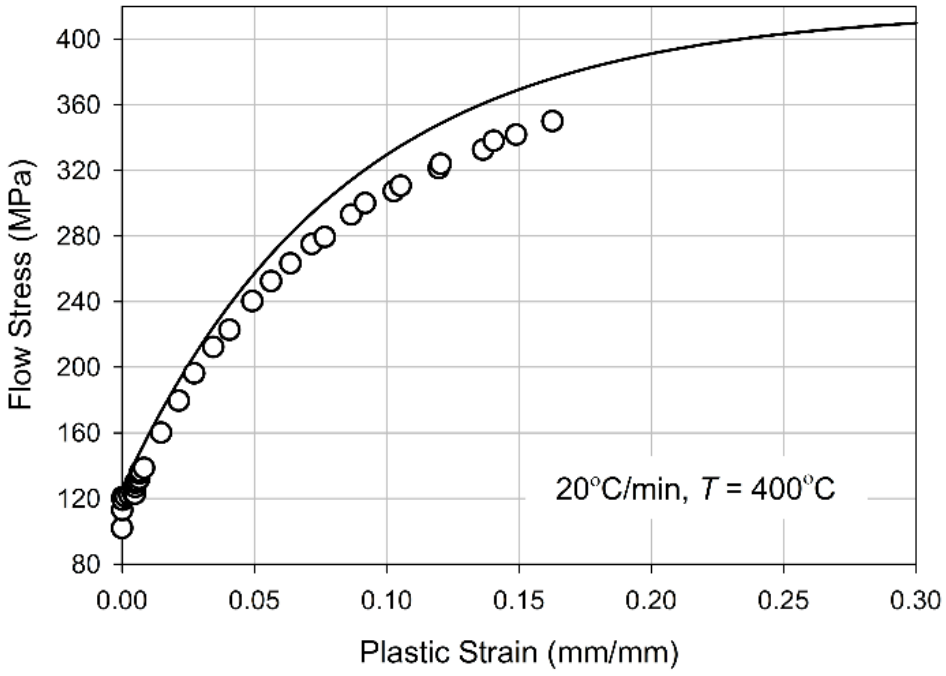

(d)

Fig. 38. Modified KME constitutive law predictions compared to experiment for (a) as-received, (b) partially recovered, (c) partially recrystallized, and (d) fully recrystallized AA5083-H116.

The model predictions were also compared to experimental data to study the effect of heating rate for prior material heating to a constant temperature (320°C). This is shown in Fig. 39. The figure shows experimental data for specimens previously heated at the three tested heating rates: 5, 25, and 250°C/min. The temperature (320°C) was chosen as it spans the range of possible material states: fully recrystallized (5°C/min), partially recovered (25°C/min), and partially recovered (250°C/min). As is shown, the model shows good agreement with the experimental data in Fig. 39. The evolution in strain hardening behavior at the different heating rates is well represented.

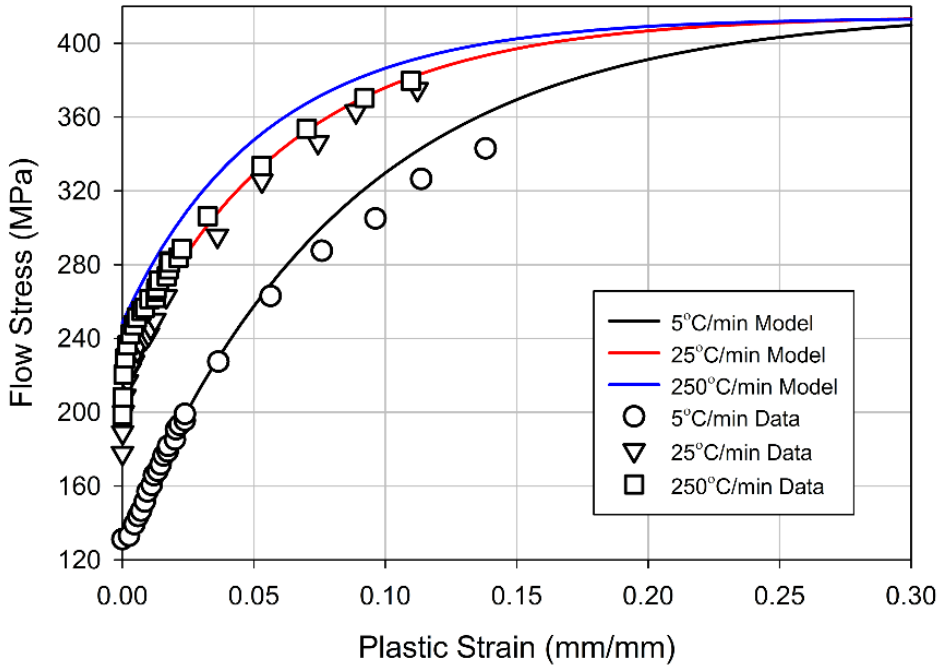

Fig. 39. Modified KME constitutive law predictions for heating to 320°C for different heating rates.

The agreement observed in Fig. 38 and Fig. 39 validates the coupled approach for predicting the strain hardening behavior developed in this research. The model has been demonstrated to incorporate the effects of non-isothermal heating on residual constitutive behavior, including strain hardening and yield strength.

3.8 Conclusions

A coupled non-isothermal model was developed for AA5083-H116 constitutive behavior after exposure to non-isothermal heating. The model describes the microstructural, strength, and strain hardening behavior evolution after thermal exposure. The coupled model is described as follows

- Kinetics-based sub-models are required to prediction microstructural evolution due to recovery and recrystallization.
- Recovery has been represented using an empirical kinetics model with a linearly varying activation energy. Model parameters were determined using hardness testing on specimens heated over a range of heating rates (5 – 80°C/min).
- Recrystallization is mechanistically represented using a linear/uniform impingement MPM model, which accounts for deviation in recrystallization from the uniform impingement of KJMA kinetics. The kinetics parameters were determined in part through DSC analysis to measure the activation energy of the rate controlling process for grain boundary migration.
- The residual yield strength is estimated using a superposition of individual strengthening contributions of friction stress, solutes, subgrains, and grains. The subgrain strengthening contribution is calculated according a mechanistic Hall-Petch-type relation, where the constant is calculated based on microstructural features, namely average misorientation angle. Grain strengthening is calculated using the empirical Hall-Petch relationship.
- Implementation of the recovery and recrystallization kinetics model in the described yield strength model resulted in predictions in good agreement with experimental data after non-isothermal exposure. Analysis showed the yield strength model is especially sensitive to the constants, k_{sg} and k_g, for subgrain and grain strengthening, respectively.
- The KME constitutive law was modified to incorporate the effects of the subgrain structures using the implementation of Verdier, *et al.* [27]. The model was further modified to include the effects of recrystallization, specifically that of subgrain annihilation. After recrystallization, this reduces the developed model to that of the basic KME formalism.
- The modified KME constitutive law was implemented as a coupled model with the previously described yield strength, recovery kinetics, and recrystallization kinetics models. The model predicts the experimentally measured initial transient in hardening rate and minimal evolution

in ultimate strength (saturation stress) due to microstructural evolution. The model shows good agreement with the strain hardening behavior measured for numerous possible material states.

In summary, a coupled constitutive model has been developed to predict the residual constitutive behavior of AA5083-H116 after non-isothermal exposure. The model has been successfully verified against experimental tensile mechanical tests. The coupled approach can be applied in a straightforward manner to predict the residual AA5083-H116 constitutive behavior after fire exposure.

4 AA6061-T651 Residual Constitutive Model

4.1 Introduction

6xxx-series aluminum alloys are increasingly being used in a broad spectrum of applications such as lightweight structures, light rail, bridge decks, marine crafts, and off-shore platforms. This is largely due to their good combination of specific strength, weldability, extrudability, and corrosion resistance. The mechanical properties of 6xxx-series alloys are obtained primarily through precipitation hardening, specifically precipitation of the meta-stable β″ phase [38]. However, a major concern with aluminum alloy structures is fire survivability, both during and after fire exposure. A short term fire exposure may significantly alter the as-received microstructure, leading to a deterioration in residual mechanical properties after the structure has cooled to ambient conditions. A structure subjected to such conditions requires evaluation for structural stability and assessment for damaged component replacement. A constitutive model capable of predicting the residual yield strength and strain hardening would is needed to support such an analysis.

The microstructural process governing the residual mechanical state of 6xxx-series alloys is precipitate growth and dissolution [8]. The solid solution content and, thereby, the strengthening contribution of Mg and Si in the α-matrix also varies with precipitate size and number density (volume fraction). The primary strengthening phase nucleated and grown during artificial aging (i.e., T6 temper) is the β″ phase, which is a coherent, needle-like precipitate [12,13]. Elevated temperature exposure (i.e., overaging) results in the appearance of the semi-coherent, rod-like β′ phase [13]. The β′ phase has a significantly lower strengthening capacity compared to the β″ phase [13]. Numerous models are available in the literature for precipitate evolution, including analytical, internal variable models [104–107], numerical class size models [37–40,108–116], and atomistic Monte Carlo simulations. The analytical approach fails when complicated diffusion processes are involved due to the interaction of different size precipitates [104]. This is the case for commercial alloys, e.g., AA6061, in an aged (hardened) state, e.g., T4 or T6. A numerical class size model, which implements the complete precipitate size distribution (PSD), is therefore required. The Kampmann-Wagner numerical (KWN) model [117] is commonly implemented [37–40,108–116] in a finite difference formulation [39] to model PSD evolution at elevated temperatures. This model describes the nucleation, growth, and dissolution processes using a

diffusion-based methodology assuming spherical precipitates. Recent studies [115,116] have relaxed this assumption in an effort to model growth of needle-like precipitates common in aluminum alloys. The KWN model has the distinct advantage of providing a complete description of PSD evolution, thus providing an accurate depiction of the microstructural state for implementation in strength or strain hardening models. This is critical considering the precipitate-dislocation strengthening interaction is dependent on precipitate size.

The precipitate growth and dissolution processes primarily affect the precipitate-dislocation interactions thereby affecting material strength [8]. As such, integration of a precipitate evolution model, which predicts the solid solution content and PSD evolution, with appropriate strength models provides a framework to predict residual yield strength after fire exposure. Precipitates are the primary microstructural contributors to yield strength in precipitation hardened Al alloys. Initial work in development of a precipitate-dislocation interaction based strength model was reported by Shercliff and Ashby [118,119] with critical advances made by Deschamps and Brechet [120,121]. In this model, a transition radius (r_{trans}) is defined such that precipitates with a smaller radius are sheared by dislocations and those with a larger radius are bypassed (Orowan loop). The model implements functions such that strength increases with $r^{1/2}$ for $r < r_{trans}$ and with $1/r$ for $r > r_{trans}$. Deschamps and Brechet [121] demonstrated that a model using only mean radius and volume fraction may be sufficient to estimate yield strength assuming a Gaussian distribution of precipitate radii. Myhr, *et al.* [37] advanced this concept by calculating precipitate strength using a weighted mean value from predicted PSD radii. This model has been widely implemented for Al alloys [37,38,40,108,109,111,115,116,122].

The strain hardening on Al alloys is commonly modeled using internal state variable models, such as those of the Kocks-Mecking-Estrin (KME) formalism [68–71]. This model was initially developed for pure FCC metals on the principles of the Taylor relation [72], which considers flow stress as proportional to the square root of dislocation density (internal state variable). The KME model describes dislocation density evolution in terms of the thermodynamic process experienced by a metal undergoing plastic deformation. The internal energy is increased by deformation through dislocation storage; however, it is simultaneously reduced by dislocation annihilation (dynamic recovery). The KME model also provides a physical basis for the Palm-Voce [73,74] constitutive law and agrees well with experimental data [71].

Though the KME formalism is valid only for pure metals, it is common to assume a generalized form such that the plastic slope varies linearly with flow stress [38,75,77,78,101,102]. Thus, the effects of microstructural features, such as solutes and precipitates, may be included in the model. Marthinsen, Nes, and colleagues [123–128] developed a two state variable strain hardening model which has been used to describe the effect of grain size on strain hardening for Al alloys containing non-shearable precipitates [126–128]. Estrin [103] generalized the KME model to include effects present in solute and precipitate hardened Al alloys. A new term was introduced to the KME formalism to account for Orowan loop storage around non-shearable precipitates. A similar modification was proposed by Barlat, *et al.* [129]. This model has been applied to several precipitate containing Al alloy systems [38,102,130,131]. Simar, *et al*. [38] adapted such an approach to model strain hardening of AA6005A-T6 after thermal exposures such as those experienced during welding. A generalized form of the KME law was implemented, focusing on the effects of Orowan loop storage stability on dislocation storage and dynamic recovery rates.

The aim of this aspect of the research is development of an integrated modeling approach for PSD evolution, yield strength, and strain hardening of AA6061-T651. The models were developed considering non-isothermal exposures rather than isothermal exposures as this is considered more representative of fire scenarios (see Chapter 2). This expands on similar integrated models which were developed and verified against isothermally heated 6xxx-series alloys, including AA6005A, AA6056, AA6063, and AA6082 [38,40,77,108]. The model in this research was developed for AA6061, necessitating significant adaptation of alloy-specific parameters. The KWN model was implemented to predict PSD evolution including precipitate nucleation, growth, and dissolution. The residual yield strength model is based on solid solution and precipitate strengthening contributions, with precipitate strengthening predicted using a precipitate-size weighted mean strength. The dislocation structure modified KME model of Simar, *et al.* [38] was implemented to predict the strain hardening behavior after fire exposure. The integrated model is compared against experimental data.

4.2 Experimental

The commercial alloy studied in this research is AA6061-T651 rolled plate (6.5 mm nominal thickness). The T651 temper designation dictates the Al-Mg-Si alloys is solutionized, stress-

relieved by stretching, then artificially aged to peak/optimal mechanical properties. The chemical composition is given in Table 8.

Table 8. Chemical composition of AA6061-T651 in this research.

Alloy	**Mg**	**Si**	**Fe**	**Cu**	**Mn**	**Cr**	**Zn**	**Ti**	**Al**
6061-T651	0.90	0.66	0.40	0.24	0.07	0.18	0.02	0.02	bal

4.2.1 Material and Non-isothermal Heating

Fire exposures were simulated using constant, linear heating rates to prescribed temperatures (up to 500°C) followed immediately by water quenching. The constant heating rate exposure is an analog for the initial transient temperature increase of aluminum during fire. A representative aluminum structure with varying thicknesses of ceramic fiber insulation was exposed to a UL 1709 [18] fire exposure in a thermal model to determine the heating rates expected during fire. Effective heating rates of 250, 25, and 5°C/min were calculated for 0.0, 25.4, and 50.8 mm thick insulation (refer to Chapter 2 for details). These heating rates are expected to encompass the range of heating rates experienced in an aluminum structure during fire. Tensile test specimens were heated at these effective heating rates in addition to 20°C/min, which was used to conduct a detailed material evolution study. All test specimens were heated using an induction heater controlled by an optical pyrometer and monitored using infrared thermography. Refer to Chapter 2 for further material heating details.

4.2.2 Optical Microscopy

The described induction heater was used to heat specimens for both mechanical measurements and metallography. Optical microscopy was performed using a HIROX KH-7700 digital video microscope. Specimens were mounted in a slow hardening epoxy resin. Grinding was performed using 300 – 1200 grit SiC paper (5 steps) with a variable speed grinder/polisher. Rough polishing was performed using 5, 3, and 1 µm polycrystalline diamond paste and suspension on low-nap woven textile, medium-nap billiard, and low-nap silk polishing cloths, respectively. Final polishing was performed using 0.05 µm colloidal silica on a chemically resistant polishing cloth. Mount pressure (10 – 20 N) and grinding/polishing speed (150 – 300 rev/min) were selected to ensure minimal surface deformation and that all constituents remained intact. Etching was

performed using 50 mL of Poulton's reagent (2 mL HF, 3 mL HCl, 20 mL HNO_3, 175 mL H_2O), 50 mL HNO_3, and 40 mL of a solution of 3 g chromic acid per 10 mL H_2O. Specimens were imaged on all three material planes using crossed polarizers to show grain contrast.

4.2.3 Transmission Electron Microscopy

TEM observations were performed using a Philips EM420 microscope operating at 120 kV. The TEM foils were removed from the RD-ND plane (normal to long-transverse direction) at the center of the heated region. Thin plates with a thickness of about 250 μm were removed from full-size test specimens using a SiC wafering blade. The thin plates were slowly mechanically ground to about 90 μm thickness. TEM foils were removed from the ground plates using a 3 mm diameter Gatan TEM disc punch. The foil was thinned to electron transparency by single jet electropolishing using a solution of 30% HNO_3 in methanol at -30°C. TEM imaging was performed by aligning to the $<100>_{Al}$ zone axis closest to the polished plane. Images were taken at sample tilts of less than 10°.

4.2.4 Tensile Tests

Uniaxial, quasi-static tensile tests were performed at ambient conditions on previously heated samples using an Instron 5984 150 kN electro-mechanical testing machine. Strains were measured using strain gages (small strain analysis) and digital image correlation (large strain analysis). Further details can be found in Chapter 2.

4.3 Experimental Results

4.3.1 Initial Microstructural State

TEM investigation was performed to study as-received AA6061-T651 precipitate size distribution and morphology. The as-received precipitate state, shown in Fig. 40, is typical of peak aged (i.e., T6 or T6xx) Al-Mg-Si alloys. The micrograph shows a high density of needle-like β″ precipitates in the imaging plane and perpendicular to the imaging plane. The mean precipitate length was determined from a series of TEM images, totaling measurement of 100 precipitates. The mean

value was determined as 23.5 ± 3.9 nm. This agrees well with other studies of Al-Mg-Si alloys [3,115].

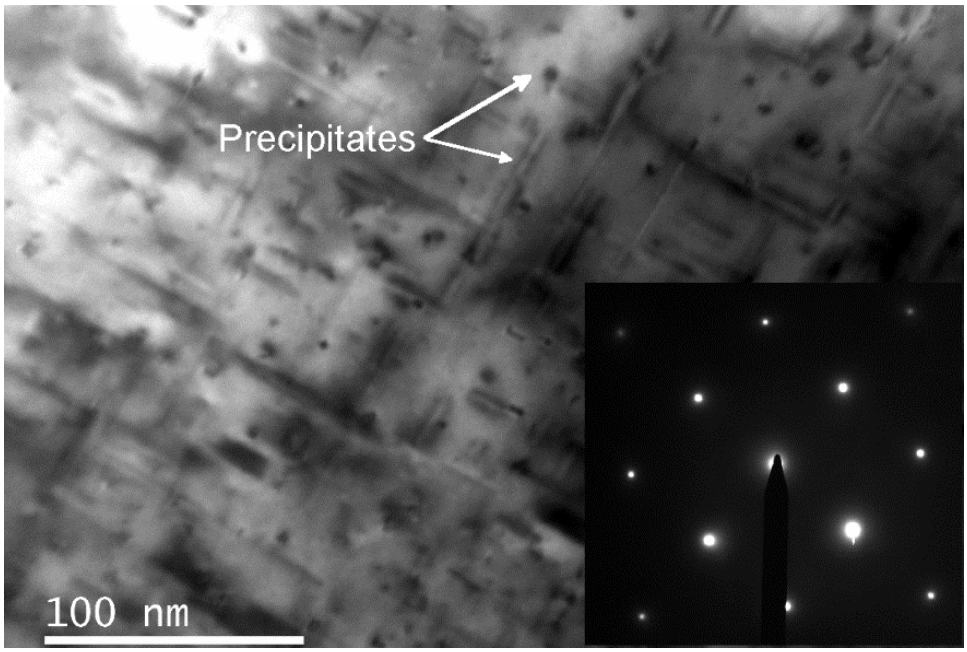

Fig. 40. AA6061-T651 as-received precipitate state imaged using TEM in the $<100>_{Al}$ zone axis.

Accurate precipitate radius measurement requires HRTEM due to the diffraction contrast present in classical TEM at high magnifications. HRTEM micrographs from Maisonnette, *et al.* [3] are also shown in Fig. 41. The precipitate aligned in the $[100]_{Al}$ direction has about a 1.3 nm radius. Weak aligned diffraction spots reveal a partially disordered state associated with pre-β″ phases [3]. The T6 material state was found in Ref. [3] to have rods of length 20 ± 9 nm and radius 2.0 ± 0.3 nm, resulting in an estimated volume fraction of f_v = 1.6 ± 0.1%. This agrees well the small-angle neutron scattering (SANS) work of Bardel, *et al.* [115], which found a radius of 1.7 ± 0.3 nm and an aspect ratio of ξ = 7 ± 3. The volume fraction was calculated as 1.6 ± 0.1%, which agrees well with Ref. [3]. An aspect ratio of ξ = 10 ± 2 is calculated for AA6061-T651 in this work assuming the mean precipitate radius is the same as that in Ref. [3] (2.0 ± 0.3 nm). This agrees well with Refs. [3] and [115].

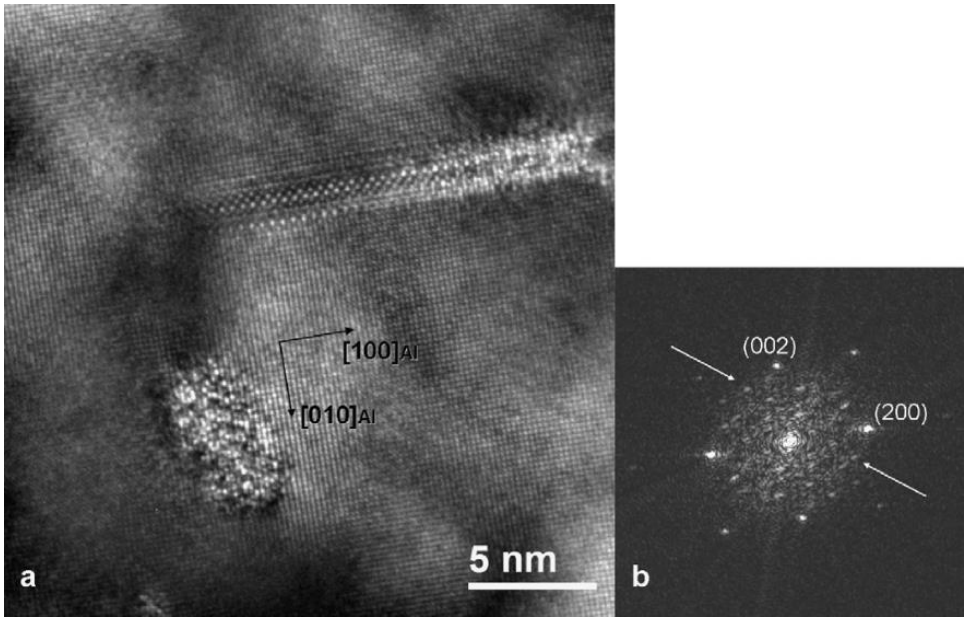

Fig. 41. HRTEM micrographs of AA6061-T6 precipitates: (a) high magnification lattice image; (b) diffractogram (numerical Fourier transform) of micrograph showing diffraction spots (arrows) from precipitates in addition to square lattice from FCC Al along [001] [3]. [Reproduced with permission]

The precipitate size distribution (PSD), including size characteristics and number density, governs the as-received strength and precipitate growth and dissolution at elevated temperatures. Simar, *et al.* [38] measured the PSD for an AA6005A-T6 alloy using TEM analysis. The PSD shown in Fig. 42 has been adjusted to calculate an equivalent precipitate radius assuming all precipitates are of equal length. The total number density of precipitates (5.7×10^{22} #/m^3) is lower than that measured in the detailed AA6061 analysis of Donnadieu, *et al.* [132] (10^{23} #/m^3). The lower precipitate density is supported by the relative Mg/Si content of the alloys; AA6005A (0.48 wt% Mg, 0.81 wt% Si) contains less Mg than AA6061 (0.90 wt% Mg, 0.66 wt% Si). This logically results in a lower T6 precipitate density due to a lack of Mg solutes. The PSD in Fig. 42 was therefore adapted for AA6061 by applying a scaling factor (1.88) to achieve a total precipitate density of 10^{23} #/m^3. The scaled PSD is implemented in this work as the initial precipitate state for analysis and model development.

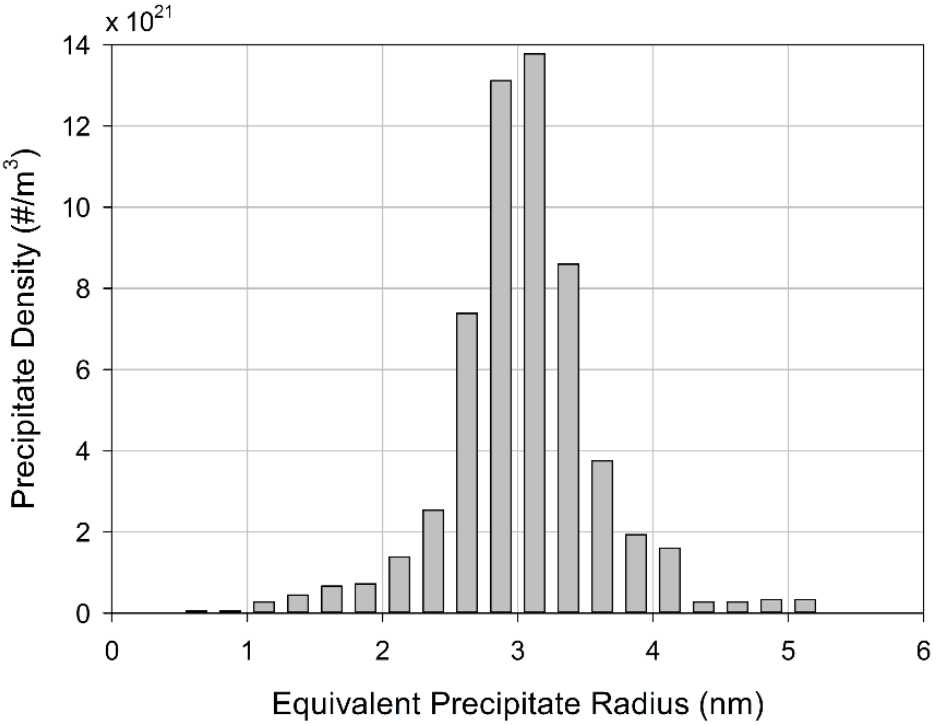

Fig. 42. β″ precipitate size distribution (PSD) in as-received AA6005A-T6, considering all precipitate lengths are equal to the mean length [38].

The as-received grain size was determined from a series of optical micrographs. All three material planes were imaged using cross-polarized light after polishing and etching. A 3-D reconstruction of the as-received grain structure is shown in Fig. 43. The as-received grain structure is primarily equiaxed with a slight elongation in the rolling direction. The average grain size was determined using the lineal intercept method. At least 10 images were used to calculate the average intercept length on each material plane. These average intercept lengths were used to calculate an average grain size of 150 μm in the as-received condition.

Fig. 43. AA6061-T651 as-received grain structure.

4.3.2 States Resulting from Non-Isothermal Heating

Elevated temperature evolution of the as-received PSD occurs by growth and dissolution of the metastable β″ phase. The evolving precipitate sequence and morphology has been the topic of numerous studies [12–14,132,133]. The generally accepted sequence is SSSS (supersaturated solid solution) → clusters/Guinier-Preston (GP) zones → β″ → β′ → β (Mg_2Si). The detailed evolution was measured using DSC at 20°C/min for AA6005A-T6 [5]:

- the β″ dissolution peak is identified at ~260°C;
- the β′ precipitation peak is identified at ~310°C;
- a broad β′ dissolution peak occurs from ~350 – 420°C;
- the β precipitation peak is identified at ~460°C;
- the β dissolution peak is identified at ~510°C.

β′ may be formed directly by β″ coarsening or by β″ dissolution and β′ precipitation. The described sequence, with β″ → β′ coarsening, will be considered in this work. Further details, including

phase composition and morphology, are given in Donnadieu, *et al.* [132], Edwards, *et al.* [12], and Ravi and Wolverton [133]. The generally accepted phase compositions are given in Table 9 [3].

Table 9. Composition of Al-Mg-Si precipitates.

Phase	**Composition**
GP zone	Mg_1Si_1
β″	Mg_5Si_6
β′	Mg_9Si_5
β	Mg_2Si

Several studies [3,37,38,40,115] have analyzed the evolution of the as-received microstructure in the T6 state (Fig. 40) after elevated temperature exposure. Maisonnette, *et al.* [3] measured significant precipitate growth after heating at 900°C/min to 300°C and 400°C. After heating to 300°C, β″ rods were observed with length 25 ± 15 nm and radius 1.5 ± 0.5 nm. After heating to 400°C, precipitate f_v was significantly reduced and the β′ phase was measured to be length 120 ± 50 nm and radius 4 ± 2 nm. These observations were confirmed by Bardel, *et al.* [115] for an identical material using SANS. Precipitate details from Ref. [115] are provided in Table 10. High heating rates were used in Ref. [115]; however, the specimen heated at 30°C/min to 400°C is representative of that in this work. Significant precipitate growth and dissolution is measured, specifically mean radius growth from 1.7 to 21 nm and a 0.5% f_v reduction. Thus, given the similarities in heating, similar morphological evolution is expected in this work.

Table 10. Precipitate morphology measured using SANS [115]. MT represents specimens heated at 900°C/min to a maximum temperature. HR represents heating at various heating rates (in °C/min) to 400°C.

State	**Mean radius (nm)**	**Aspect ratio, $\xi = l_p/r$**	**Vol. fraction (%)**
T6	1.7 ± 0.3	7 ± 3	1.6 ± 0.1
MT200	1.4 ± 0.1	12 ± 6	1.4 ± 0.1
MT300	1.3 ± 0.1	20 ± 10	1.5 ± 0.1
MT400	8.5 ± 0.5	15 ± 4	1.3 ± 0.2
MT500	3.5 ± 3.5	5 ± 5	0.1 ± 0.1
HR30	21 ± 3	9 ± 1	1.1 ± 0.1
HR300	8.1 ± 0.1	9 ± 1	1.2 ± 0.1
HR900	8.5 ± 0.5	15 ± 4	1.3 ± 0.2
HR12000	9.4 ± 1.2	20 ± 5	1.3 ± 0.1

TEM micrographs of AA6005 precipitate morphology in the as-received state and after further heating are shown in Fig. 44 (Myhr, *et al.* [40]). Note, a heating regimen representative of welding was used in Ref. [40], with 3000°C/min heating to the desired temperature, a 10 s hold, and 1800°C/min cooling to ambient. The as-received β″ precipitates (Fig. 44a) are similar to that in this work for AA6061-T651 (Fig. 40). Significant growth of larger precipitates is observed after heating to 315°C (Fig. 44b-c); smaller precipitates begin dissolving as Mg/Si solutes are emitted to the Al matrix. This is indicative of the dual pathway for growth/dissolution based on relative precipitate/matrix concentrations and annealing temperature [37,38]. Further heating to 390°C causes severe coarsening and dissolution (Fig. 44d). Precipitate morphology in this case is similar to that in Ref. [115] after heating to 400°C at 30°C/min.

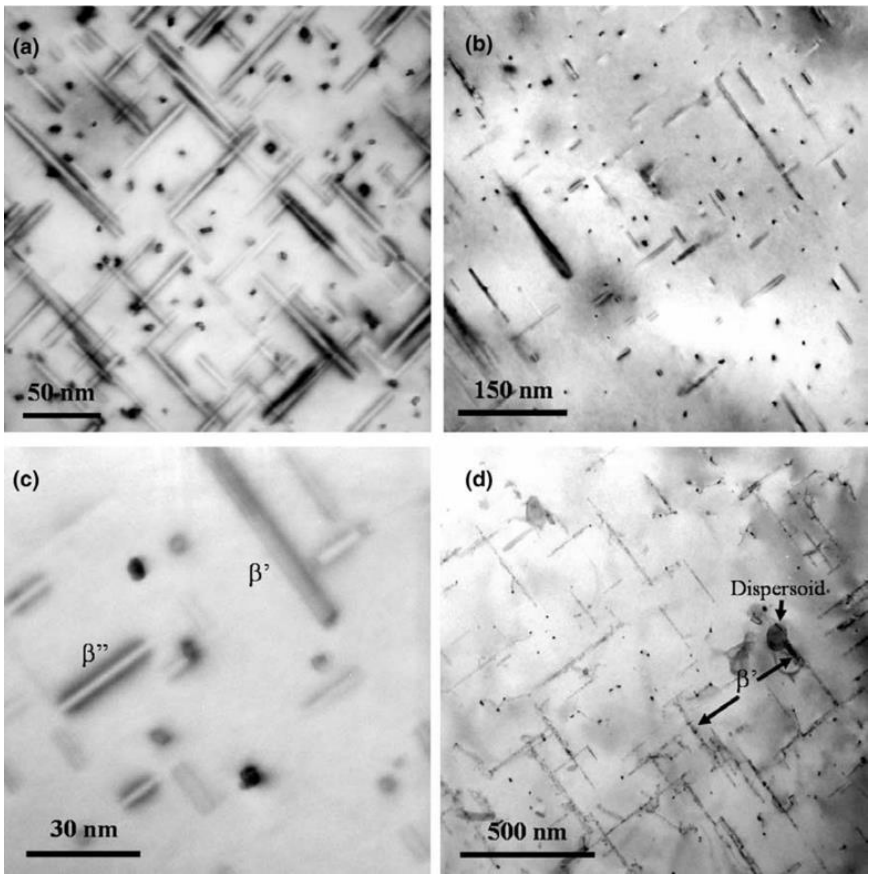

Fig. 44. TEM micrographs of AA6005 precipitates imaged in the $<100>_{Al}$ zone axis after prior heating. (a) Artificially aged with needle-shaped β″ precipitates, (b) mixture of coarse and fine rod-shaped precipitates after heating to 315°C, (c) high magnification view of (b), and (d) coarse rod-shaped precipitates after heating to 390°C [40]. [Reproduced with permission]

The grain size after elevated temperature exposure at 20°C/min was analyzed identically to that described previously for the as-received state. The analysis revealed insignificant evolution in the grain structure, with grain size approximately that in the as-received condition.

4.4 Kampmann-Wagner Numerical (KWN) Model

Classical nucleation and growth theories (CNGTs) have been widely used for modeling PSD evolution during elevated temperature exposure. Such theories were originally posed by Kampmann and Wagner [117]. Myhr, *et al.* [37] and Deschamps, *et al.* [121] initially adapted the KWN model to Al alloys by implementing a unique β″/β′ phase, thereby simplifying the complex precipitation sequence. This approach was extended to non-isothermal heat treatments in further work by Myhr [40]. These initial models have been extensively implemented for Al alloys [38,40,108,111,114–116] including adaptations for heterogeneous precipitation [108,111], various metastable precipitates [111], ternary/quaternary phases [108], and non-spherical precipitates [115,116]. Perez, *et al.* [114] discussed the necessity of modeling the entire PSD evolution using a class size approach rather than a mean radius approximation. The class size concept captures the precipitate size dependent interactions occurring during nucleation, growth, and dissolution.

Simar, *et al.* [38] implemented the KWN model in a manner that provides a balance between representative capability and limited complexity. In this model, nucleation, growth, and dissolution processes are assumed to occur as spherical precipitates with an equivalent radius defined based on equivalent precipitate length. The model was verified through extensive characterization and analysis, reinforcing the concepts originally implemented by Myhr, *et al.* [40]. The PSD interaction and evolution during growth/dissolution were modeled using an Eulerian multi-class approach described by Perez, *et al.* [114]. This section provides a summary of model development, including underlying assumptions as well as a description of basic model features. A detailed model description is given by Simar, *et al.* [134].

4.4.1 Nucleation Law

Neglecting the incubation time for nucleation, the steady state nucleation rate is expressed as

$$j = \frac{dN}{dt} = j_0 \exp\left[-\frac{A_0^3}{(RT)^3\left[\ln\left(C_{Mg}/C_{Mg}^{eq}\right)\right]^2}\right]\exp\left(-\frac{Q_d}{RT}\right) \tag{53}$$

where j_0 is the pre-exponential nucleation constant, R is the universal gas constant, T is the temperature, A_0 is a parameter related to the energy barrier for nucleation, C_{Mg} is the mean Mg solute content in the matrix, C_{Mg}^{eq} is the equilibrium Mg concentration at the precipitate/matrix interface, and Q_d is the activation energy for Mg diffusion. The dependence of C_{Mg}^{eq} on temperature is given by an Arrhenius relationship

$$C_{Mg}^{eq} = C_{Mg,0}^{eq}\exp\left(-\frac{Q_{eq}}{RT}\right) \tag{54}$$

where $C_{Mg,0}^{eq}$ is a pre-exponential equilibrium constant and Q_{eq} is the apparent solvus boundary enthalpy.

4.4.2 Precipitate Growth/Dissolution Law

The growth/dissolution rate is given by the Whelan formalism, assuming diffusion control, as

$$v = \frac{dr}{dt} = \frac{1}{r}\frac{\left(C_{Mg} - C_{Mg}^{i}\right)}{\left(C_{Mg}^{p} - C_{Mg}^{i}\right)}D_0\exp\left(-\frac{Q_d}{RT}\right) \tag{55}$$

where r is the precipitate radius, C_{Mg}^{p} is the precipitate Mg concentration, C_{Mg}^{i} is Mg concentration at the precipitate/matrix interface, and D_0 is the pre-exponential diffusion constant. In terms of Eq. (55), dissolution occurs if $C_{Mg} < C_{Mg}^{i}$ (r decreases) and growth if $C_{Mg} > C_{Mg}^{i}$ (r increases). The interface concentration is given by the Gibbs-Thomson equation, which in the case of binary precipitates is given by

$$C_{Mg}^{i} = C_{Mg}^{eq}\exp\left(\frac{2\gamma V_m}{rRT}\right) \tag{56}$$

where γ is the precipitate/matrix interface energy and V_m is the molar volume of the precipitate. The radius of nucleated precipitates may be deduced from the above set of equations. Assuming precipitation occurs at $C_{Mg} = C_{Mg}^{i}$ (i.e., $dr/dt = 0$) and solving for r in Eq. (56) results in

$$r_c = \frac{2\gamma V_m}{\ln\left(C_{Mg}/C_{Mg}^{eq}\right) RT} \tag{57}$$

where r_c is the critical radius for precipitate nucleation.

4.4.3 Continuity Equation and Numerical Discretization

The continuity equation for the precipitate number density in a single class size (further described below) is given as

$$\frac{\partial N_i}{\partial t} = -\frac{\partial (N_i v_i)}{\partial t} + j \tag{58}$$

where the *i* subscript represents the given parameter for a single class. The above equation may be linearized with time assuming a timestep of Δt.

The control volume approach of Perez, *et al.* [114] (after Myhr, *et al.* [39]) is implemented in this work in a Eulerian reference frame. A visualization of this approach is provided in Fig. 45 [114]. Applying the continuity equation in Eq. (58), the number density (N) of a given class size (index i) is calculated using the number densities and growth rates (v) of neighboring class sizes (indexed i-1 and i+1). Thus, a mass balance for class size i results in [114]

$$\begin{aligned} N_{i,t+\Delta t} = N_{i,t} &+ \frac{\Delta t}{\Delta r} v_{i-1,t}\left[\mathrm{SIGN}\left(v_{i-1,t}\right)N_{i-1,t} + \mathrm{SIGN}\left(-v_{i-1,t}\right)N_{i,t}\right] \\ &- \frac{\Delta t}{\Delta r} v_{i,t}\left[\mathrm{SIGN}\left(v_{i,t}\right)N_{i,t} + \mathrm{SIGN}\left(-v_{i,t}\right)N_{i+1,t}\right] \end{aligned} \tag{59}$$

where Δr is the class size and SIGN(x) is 1 if $x > 0$ and 0 otherwise.

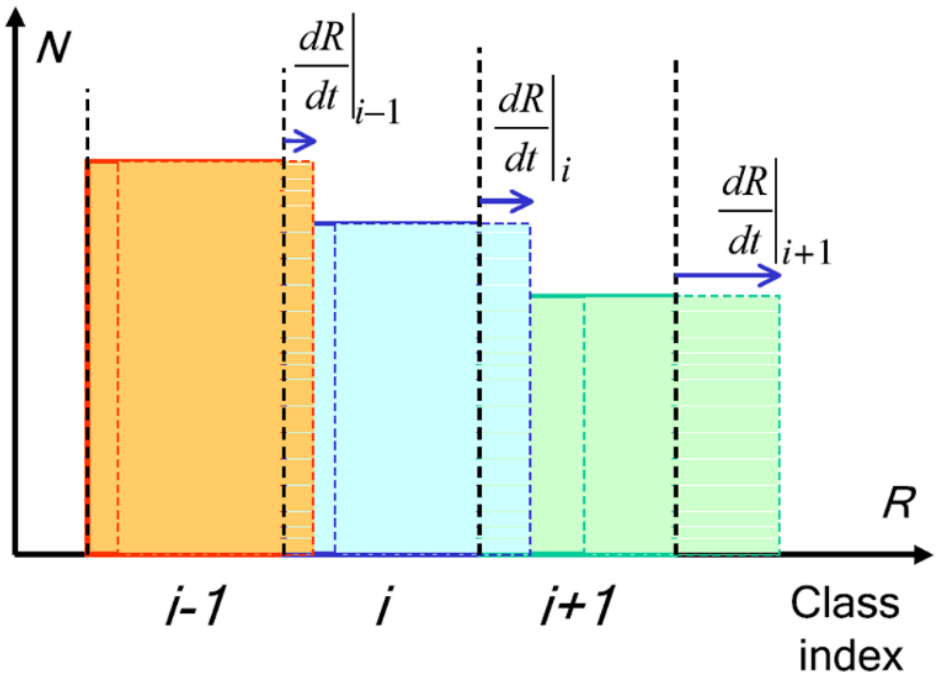

Fig. 45. Precipitate growth/dissolution using a control volume approach in an Eulerian reference frame. Fluxes between neighboring classes are calculated at each timestep [114]. [Reproduced with permission]

In such an approach, an initial PSD (i.e., Fig. 42) is prescribed at $t = 0$. The total number of class sizes (given by i_{max}) are allowed to grow or decrease as dictated by the KWN model, specifically by Eq. (55) applied to i_{max}. However, the model may predict unrealistic growth rates (approaching infinity) for very small class sizes due to the $(1/r)$ term in Eq. (55). This behavior is eliminated by defining a cut-off radius such that the inequality $C_{Mg}^{p} > C_{Mg}^{i}$ holds. Additionally, a new size class (i_{max+1}) is predicted if the largest size class (i_{max}) has a positive growth rate, resulting in an unrestrained increase in the number of size classes. This is avoided by defining a threshold for class creation, typically 1 precipitate/m^3.

An adaptive timestep is calculated as part of the KWN model implementation. This is done to ensure precipitate growth occurs within a single class size. This concept is realized as

$$\Delta t = \frac{\Delta r}{2} \frac{1}{\max|v_i|} \tag{60}$$

It should be noted that v_i occurs for the smallest class size in the KWN model implementation.

The final continuity relations implemented are calculations of the PSD mean descriptive values. The volume fraction of precipitates, f_v, is defined as

$$f_v = \sum_i \frac{4}{3}\pi r_i^3 N_i \tag{61}$$

The Mg concentration in the matrix, C_{Mg}, is calculated in terms of precipitate volume fraction as

$$C_{Mg} = \frac{C_{Mg}^0 - C_{Mg}^p f_v}{1 - f_v} \tag{62}$$

where C_{Mg}^0 is the total Mg concentration in the alloy, assuming all Mg will precipitate into Mg_2Si precipitates. The mean precipitate radius, $\bar{r}$, is calculated as

$$\bar{r} = \frac{\sum_i r_i N_i}{\sum_i N_i} \tag{63}$$

4.4.4 KWN Model Calibration

KWN model parameters were calibrated using the mechanical tests described in Chapter 2 for AA6061-T651 specimens exposed from 5 – 250°C/min and data available in the literature. The KWN model implementation of Simar, *et al.* [38] was used as a basis for model parameters. The work of Gallais, *et al.* [108], Myhr and colleagues [37,40,111], and Bardel, *et al.* [115] was also used to a lesser extent. Note, except for Ref. [115], all other models were developed for other 6xxx-series alloys (e.g., AA6005A).

The as-received mean precipitate radius was obtained from Fig. 42 as 3.04 ± 0.3 nm. The as-received Mg concentration, C_{Mg}^0, is given in Table 8. The precipitate/matrix interface energy, γ, is taken as 0.108 J/m^2 from Bardel, *et al.* [115]. This interface energy resulted in a prediction of the correct precipitate number density (10^{23} #/m^3 [132]) after a simulated T6 heat treatment [115]. This is compared to γ = 0.26 J/m^2 used in Refs. [38] and [40] which has been optimized for AA6005. The remaining parameters are governed by the binary Mg-Si precipitate system and are not alloy-specific; therefore, the remaining parameters are taken from other studies of 6xxx-series alloys. The parameters for Mg solute diffusion are taken as the generally accepted values used by Gallais, *et al.* [108]. The remaining parameters are identical to those implemented in Ref. [38].

4.4.5 KWN Model Results

The thermal exposures applied in mechanical testing were applied to as-received AA6061-T651 PSD using the KWN model. Fig. 46 shows the predicted PSD evolution after heating at 20°C/min. It can be seen the PSD experiences negligible change up to 250°C. This is expected as the residual yield strength (Fig. 14) is relatively unaffected at 250°C. Further heating to 300°C results in a notable increase in precipitate density at $r > 4$ nm. Further heating to 350°C results in significant precipitate growth with $\bar{r} \approx 6.5$ nm. The PSD is also broadened with a large proportion of precipitates having large radii. The maximum precipitate density of a single class is also reduced significantly. The predicted PSD evolution is in good agreement with the overall trend expected from residual yield strength measurement (Fig. 14).

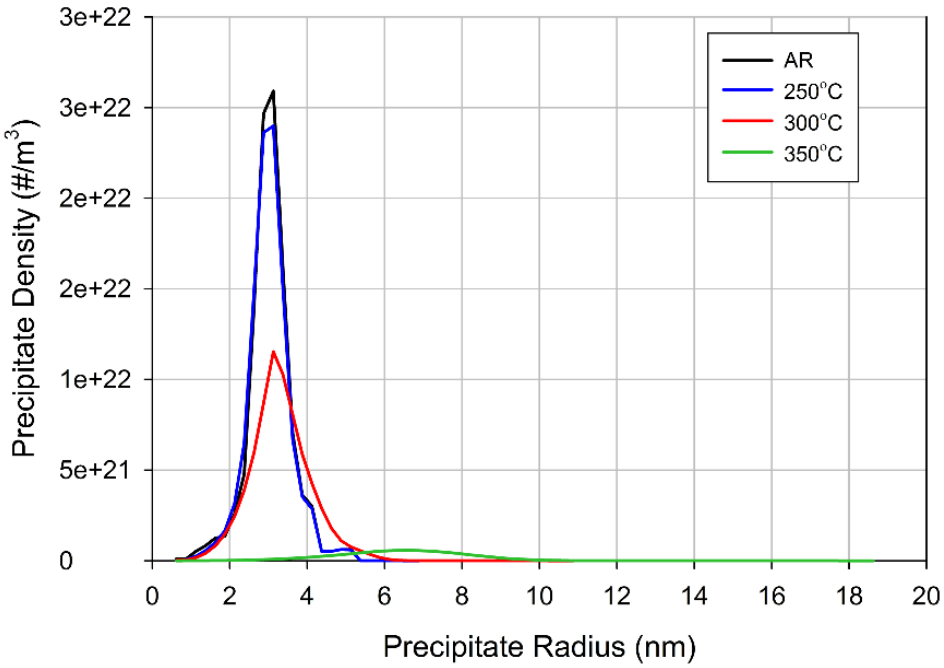

Fig. 46. Predicted precipitate size distributions after to heating at 20°C/min to 250, 300, and 350°C.

The predicted PSD evolution as a function of heating rate is shown in Fig. 47. The PSD variation after heating at 5 – 250°C/min to 350°C (Fig. 47a) is significant. The PSD at 250°C/min is largely unchanged from the as-received state; however, at 5°C/min, precipitates have grown significantly. The PSD is also considerably broadened. The PSDs after heating to 400°C (Fig. 47b) are similar to that for 350°C; however, the PSD is further broadened and peak values are reduced. The mean radii are about twice that predicted at 350°C. This is representative of the measured yield strength

reduction with increased heating from 350 to 400°C. The predicted mean precipitate radii and precipitate volume fractions are shown in Fig. 48. The predicted PSD evolution (Fig. 47) is well described by the calculated mean descriptive values, i.e., r – Eq. (63) and f_v – Eq. (61).

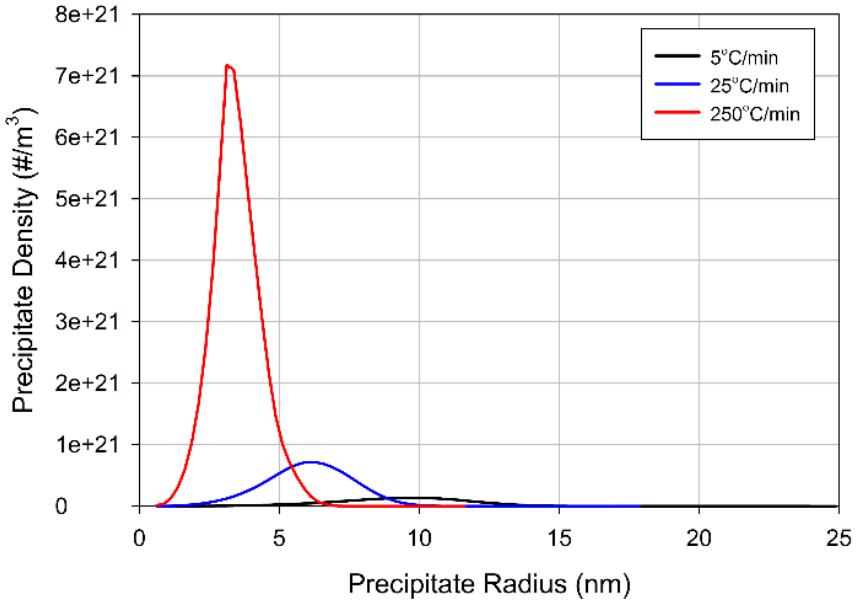

(a)

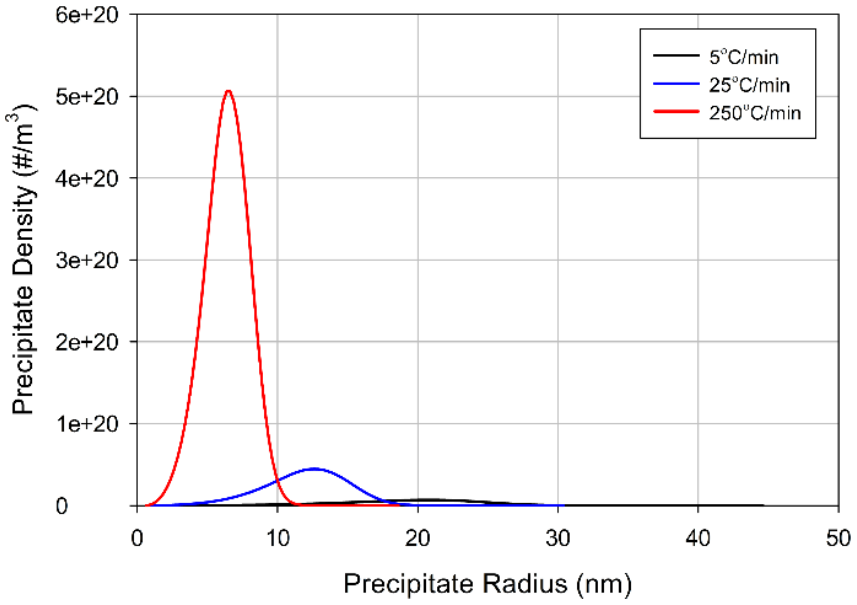

(b)

Fig. 47. Predicted precipitate size distribution as a function of heating rate after heating to (a) 350°C and (b) 400°C.

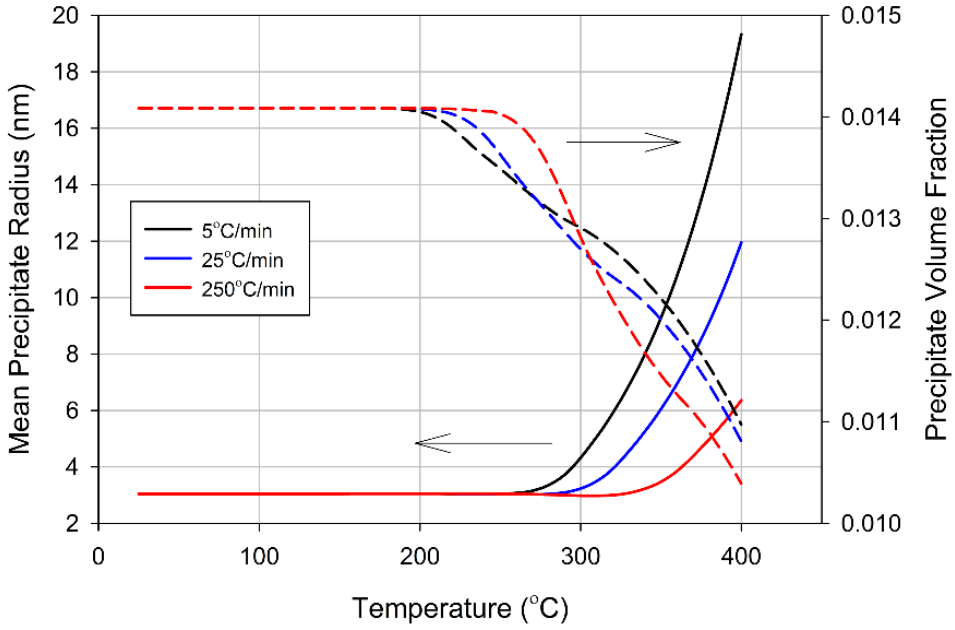

Fig. 48. Predicted mean precipitate radius and volume fraction as a function of heating rate and exposure temperature.

All parameters used in the KWN model to predict PSD evolution are provided in Table 11.

Table 11. KWN model parameters.

Parameter	**Significance**	**Value**	**Source**
$\bar{r}_{AR}$	As-received equivalent radius	3.044 nm	Fig. 42 [38]
C_{Mg}^{0}	Mg content of AA6061-T651	0.90 wt%	Table 8
C_{Mg}^{p}	Mg content of Mg_2Si	63.4 wt%	[39]
j_0	Pre-exponential constant for nucleation	3 x 10^{37} #/m^3-s	[38]
A_0	Energy barrier for nucleation	18.6 kJ/mol	[38]
V_m	Molar volume of Mg_2Si	3.95 x 10^{-5} m^3/mol	[39]
$C_{Mg,0}^{eq}$	Pre-exponential constant to C_{Mg}^{eq}	290 wt%	[40]
Q_{eq}	Apparent boundary solvus enthalpy	41 kJ/mol	[40]
D_0	Pre-exponential constant for Mg diffusion	1.24 x 10^{-4} m^2/s	[108]
Q_d	Activation energy for Mg diffusion	130.6 kJ/mol	[108]
γ	Precipitate/matrix interface energy	0.108 J/m^2	[115]

4.5 Yield Strength Estimation

In this section, the residual yield strength model based on the precipitate-dislocation interaction of AA6061-T651 is developed. The KWN model from Section 4.4 is implemented to capture the evolution in yield strength after non-isothermal thermal exposure.

AA6061 yield strength includes several microstructural strengthening contributions, specifically (i) the friction stress (σ_0), (ii) the solid solution content ($\Delta\sigma_{ss}$), (iii) precipitate contributions ($\Delta\sigma_p$), (iv) grain contributions (σ_g), and (v) dislocation forest hardening contributions (σ_g). These are linearly superposed to calculate the total yield strength (σ_y) as:

$$\sigma_y = \sigma_0 + \Delta\sigma_{ss} + \Delta\sigma_p + \sigma_g + \sigma_d \tag{64}$$

Linear superposition is assumed valid as the individual microstructural features strengthen the alloy at different length scales, thus negligible interaction is assumed. The friction stress of pure aluminum is taken as the commonly accepted 10 MPa. The grain strengthening contribution (σ_g) is assumed negligible compared to that for solutes and precipitates. As discussed, the grain size was measured as about 150 μm in all states. Assuming the Hall-Petch relationship is valid, $\sigma_g = k_g d^{-1/2}$, with a Hall-Petch constant of k_g = 0.04 MPa/m$^{1/2}$ [135], resulting in $\sigma_g \approx 3$ MPa. This is compared with solute and precipitate contributions on the order of 100 – 250 MPa [38]. The dislocation forest hardening contribution is given by the Taylor relation ($\sigma_d = M\alpha Gb\rho^{-1/2}$); however, σ_d is assumed to be much smaller than $\Delta\sigma_p$ and is thus ignored. Solid solution, $\Delta\sigma_{ss}$, and precipitate, $\Delta\sigma_p$, strengthening evolve due to precipitate nucleation, growth, and dissolution; the KWN model was implemented to account for these processes. Based on the above, microstructurally based strengthening models are needed for solutes ($\Delta\sigma_{ss}$) and precipitates ($\Delta\sigma_p$) to include in Eq. (64) to predict residual yield strength.

The solid solution strengthening contribution, $\Delta\sigma_{ss}$, is expressed as [136]

$$\Delta\sigma_{ss} = H_{Mg_2Si} C_{Mg}^{2/3} + H_{Cu} C_{Cu}^{2/3} \tag{65}$$

where H_{Mg_2Si} is a constant associated with equivalent Mg and Si solid solution strengthening, H_{Cu} is a constant associated with Cu solid solution strengthening, and C_{Cu} is the Cu concentration in the matrix. H_{Mg_2Si} is determined by a precipitate (Mg_2Si) concentration balance of H_{Mg} and H_{Si}

$$H_{Mg_2Si} = H_{Mg} + H_{Si}\left(\frac{100 - C_{Mg}^p}{C_{Mg}^p}\right) \tag{66}$$

where H_{Mg} and H_{Mg} are constants associated with Mg and Si solid solution strengthening, respectively.

The precipitate strengthening contribution, $\Delta\sigma_p$, is defined assuming a dislocation has to overcome all obstacles during glide on a slip plane to induce a macroscopic strain. A detailed overview of underlying assumptions is given in Refs. [121,137]. $\Delta\sigma_p$ may be expressed as

$$\Delta\sigma_p = \frac{M\bar{F}}{bl} \tag{67}$$

where M is the Taylor factor, $\bar{F}$ is the mean obstacle strength, b is the magnitude of the Burger's vector, and l is the precipitate spacing on the glide plane. Precipitate spacing, l, is given in terms of Friedel's statistical model [137]

$$l = \sqrt{\frac{2\pi}{3}}\frac{\bar{r}}{\sqrt{f_v}} \tag{68}$$

An alloy contains a distribution (i.e., PSD in Fig. 42) of weak, shearable and strong, non-shearable precipitates. The mean obstacle strength may be calculated using a summation rule as

$$\bar{F} = \frac{\sum_i F_i N_i}{\sum_i N_i} \tag{69}$$

where F_i is the obstacle strength corresponding to class size with a precipitate radius of r_i. F_i is a function of precipitate radius. For weak precipitates, it is assumed F_i is proportional to r_i as long as it is smaller than a defined transition radius (r_{trans}) [121,137]

$$F_i = 2k_\Gamma G b^2 \left(\frac{r_i}{r_{trans}}\right) \tag{70}$$

where k_Γ is a line tension constant ~0.5 [138], G is the shear modulus, and r_{trans} is a radius where the precipitate-dislocation interaction transitions from shearing to Orowan looping. The variable r_{trans} generally corresponds to the precipitate radius at maximum strength (i.e., as-received in the T6 state) [38]. Note, this expression, originally suggested by Gerold [137], does not explicitly account for the many complex mechanisms involved in the precipitate-dislocation interaction. The relation in Eq. (70) is extended to precipitates where $r_i > r_{trans}$ as

$$F_i = 2k_\Gamma G b^2 \tag{71}$$

This relation represents a constant strengthening interaction independent of precipitate radius, such as that due to Orowan looping.

The precipitate-dislocation strengthening interaction relations in Eqs. (70) and (71) are implemented in Eq. (67) such that the strengthening proportionalities with precipitate radius, i.e., $r^{1/2}$ for $r < r_{trans}$ and with $1/r$ for $r > r_{trans}$ [118–121], are maintained.

4.5.1 Results and Discussion

The complete non-isothermal yield strength model is obtained by substitution of Eqs. (68) – (71) into Eq. (67), resulting in

$$\sigma_y = \sigma_0 + H_{Mg_2Si} C_{Mg}^{2/3} + H_{Cu} C_{Cu}^{2/3} + \frac{M}{b}(2k_\Gamma G b^2)^{-1/2} \sqrt{\frac{3f_v}{2\pi}} \frac{\bar{F}^{3/2}}{\bar{r}} \tag{72}$$

where the mean obstacle strength, $\bar{F}$, is calculated using Eq. (69). The governing parameters describing PSD evolution are the Mg concentration in the matrix, C_{Mg}, mean precipitate radius, $\bar{r}$, precipitate volume fraction, f_v, and mean precipitate strength, $\bar{F}$. These parameters are a function of the PSD predicted by the KWN model. All model parameters are shown in Table 12.

Table 12. AA6061-T651 residual yield strength model parameters.

Parameter	**Significance**	**Value**	**Source**
M	Taylor factor	2	Textured alloy [38]
G	Shear modulus	27 GPa	[37,39,40]
b	Magnitude of Burger's vector	0.286 nm	
σ_0	Friction stress of pure Al	10 MPa	[37,39,40]
H_{Cu}	Cu solid solution strengthening constant	46.4 MPa wt%$^{2/3}$	[37,39,40]
H_{Mg}	Mg solid solution strengthening constant	29.0 MPa wt%$^{2/3}$	[37,39,40]
H_{Si}	Si solid solution strengthening constant	66.3 MPa wt%$^{2/3}$	[37,39,40]
r_{trans}	Precipitate strength transition radius	3.044 nm	Mean radius of PSD in Fig. 42
k_Γ	Line tension constant	0.40	σ_y in T6 state

The predicted residual yield strength using Eq. (72) is shown in Fig. 49. The initial PSD is that of the as-received material (Fig. 42). The KWN model predicts PSD evolution during heating at a prescribed heating rate (i.e., 5, 20, 25, or 250°C/min) to temperatures up 500°C.

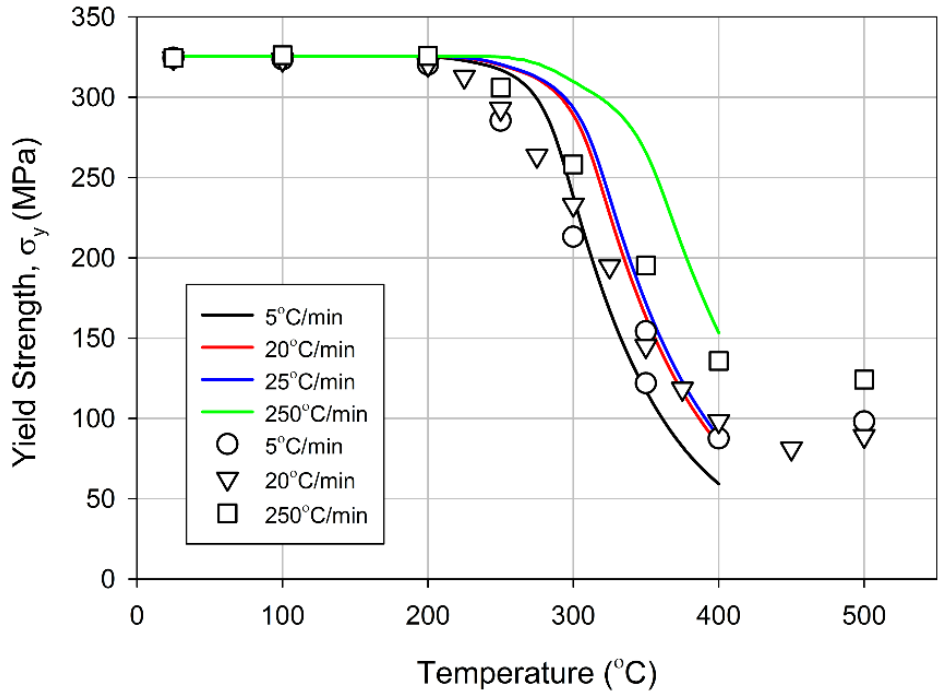

Fig. 49. AA6061-T651 residual yield strength model predictions (lines) compared against experimental data (symbols).

The experimental evolution of yield strength after thermal exposure is well represented by model predictions in Fig. 49. As expected, thermal exposures below 250°C do not cause a significant reduction in yield strength. Above 300°C, the yield strength decreases until it reaches a state corresponding to complete dissolution of precipitates. The significant reduction in yield strength (~240 MPa reduction) is governed by the PSD evolution predicted by the KWN model. This is exemplified by the similar trends followed by the predicted yield strength (Fig. 49) and the PSD predicted by the KWN model (Fig. 47 and Fig. 48).

The residual yield strength also depends on heating rate: the lower the heating rate, the lower the residual yield strength at a given maximum temperature. The effect of heating rate on yield strength is well captured by the model (Fig. 49). This effect is clearly associated with an earlier onset of precipitate growth and dissolution, which results in a relative reduction in yield strength.

Note, the larger discrepancy at 250°C/min is partially explained by the small amount of time from reaching the desired temperature to water quenching.

The predictions in Fig. 49 show good agreement with measured AA6061-T651 residual yield strengths, thus validating the coupled approach. This also demonstrates the necessity to model the complete PSD when predicting precipitate growth and dissolution, as is verified in other work (see Refs. [38,114,115]). The use of mean descriptive parameters (i.e., $\bar{r}$, f_v, and $\overline{F}$) has also been demonstrated as an adequate methodology to model precipitate strengthening. The critical parameter in calculating residual yield strength is k_Γ, which describes the relative strengthening due to the precipitate-dislocation interaction. The value reported by Simar, *et al.* [38] ($k_\Gamma = 0.45$) required adjustment to accurately predict AA6061-T651 residual yield strength evolution., thus demonstrating its alloy-specific nature. The remaining parameters in Table 12 are relatively constant for the given Mg-Si precipitate system.

4.6 Strain Hardening Model

In this section, the strain hardening model based on the microstructural features of AA6061-T651 is developed. This model is developed with the residual yield strength model (Section 4.5) to provide a complete description of residual elasto-plastic behavior after fire exposure.

Aluminum alloy strain hardening has been attributed to the competitive evolution of the dislocation structure in terms of dislocation storage and dynamic recovery (dislocation annihilation or rearrangement) [68–70]. In the case of precipitation hardened alloys (e.g., AA6061-T651), few models have been proposed to predict strain hardening behavior as a function of microstructure. As discussed in Section 4.5, thermal exposure above ~250°C results in a transition from precipitate shearing by dislocations to Orowan looping (precipitate storage of dislocations due to pinning, bowing, and unpinning of a bypassing dislocation) due to precipitate growth. Several authors [102,103,131] considered the additional dislocation storage of Orowan loops through introduction of a term inversely proportional to obstacle spacing in the dislocation glide plane. The obstacle density in the glide plane is effectively a function of precipitate volume fraction, as described in Eq. (68). The KWN model, described in Section 4.4, is implemented to capture the PSD evolution and how the evolving precipitate size and distribution affects strain hardening.

The modified KME law for precipitate strengthened aluminum alloys is defined in the following section. An overview of AA6061-T651 strain hardening behavior after prior thermal exposure is provided using the Palm-Voce formalism. The classical KME law is introduced and then modified to a generalized form of the Palm-Voce formalism to account for precipitate-induced effects on strain hardening behavior. Several physically-based parameters are introduced to accurately depict the effects of precipitate growth and dissolution as predicted by the KWN model.

4.6.1 AA6061-T651 Strain Hardening Behavior

The strain hardening rate at ambient after prior thermal exposure was discussed in Chapter 2. It has been reproduced in Fig. 50 for clarity of discussion. Several features of note are observed. The initial hardening rate ($d\sigma/d\varepsilon$) is very low (655 MPa) in the as-received state. Initial precipitate growth and yield strength reduction ($T \leq 300$°C in Fig. 49) causes only a minor increase in hardening rate. Further precipitate coarsening, associated with more prevalent Orowan looping (refer to PSD evolution in Fig. 46), results in a significant increase in hardening rate at constant stress. The plastic slope also follows a linear relationship with flow stress for all shown conditions, which agrees with literature for Al alloys in solid solution [100–102]. Therefore, it is surmised after the elastic regime, the hardening behavior follows a Palm-Voce law [73,74]

$$\frac{d\sigma}{d\varepsilon} = \theta\left(1 - \frac{\sigma}{\sigma_{sat}}\right) \tag{73}$$

where θ is the hardening rate at $\sigma = 0$, σ_{sat} is the saturation stress which the exponential relationship approaches at infinite strain. Note, the relation may also be defined using the dynamic recovery rate $\beta = \theta/\sigma_{sat}$. The above relation is characteristic of commercial (real) FCC metals deformed at a constant strain rate in the Stage III hardening regime. The θ_0 and β_0 parameters for the dislocation storage rate and dynamic recovery rate, respectively, are reserved for a pure alloy. The apparent parameters θ and β will be defined in terms of commercial alloys, e.g., AA6061-T651.

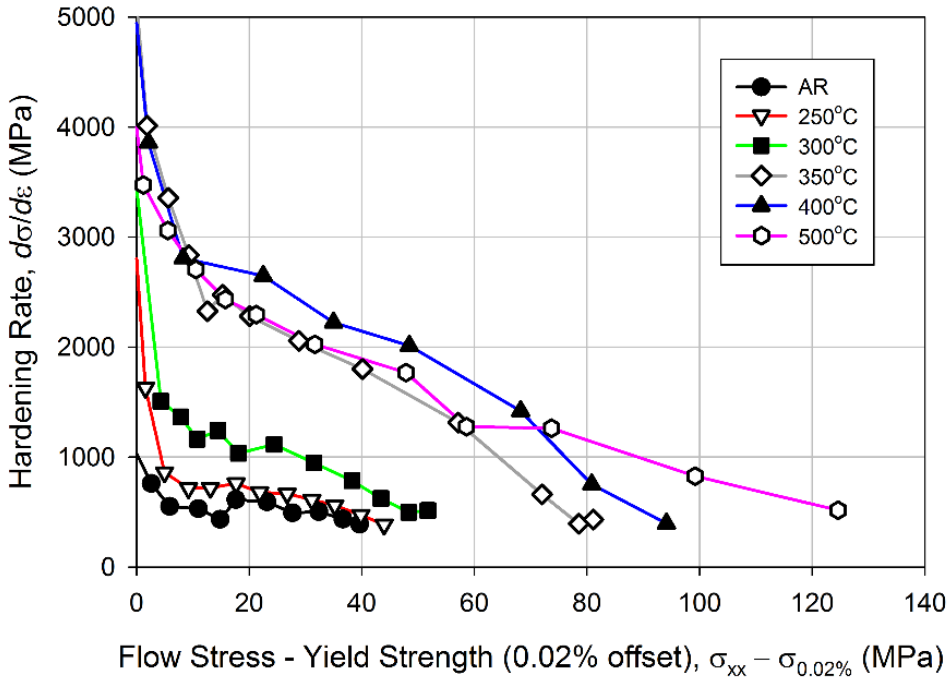

Fig. 50. Strain hardening rate versus flow stress after prior thermal exposure at 20°C/min.

The values of θ and β evolve as a function of the PSD evolution during a thermal exposure. The Palm-Voce law in Eq. (73) was fit to the stress-strain relations from tensile mechanical tests on specimens previously exposed at 20°C/min. The parameters, θ and β, are reported in Fig. 51a. The parameters evolve as a function of the evolving microstructure; evolution due to precipitate growth and dissolution is clearly discerned. These parameters can also be characterized by a "master" curve (Fig. 51b). A linear relationship was observed for exposures below 350°C. This roughly corresponds to temperatures associated with formation of the semi-coherent β′ phase [5], which is associated with a drastic shift in strain hardening behavior [38]. The master curve was fit to this data using linear regression (slope = -73.2). At higher temperatures, the relationship deviates from linear demonstrating a fundamental evolution in the governing microstructural mechanisms. A correlation can be drawn to PSD evolution (Fig. 46) as the precipitates undergo significant growth and dissolution from 300 – 350°C.

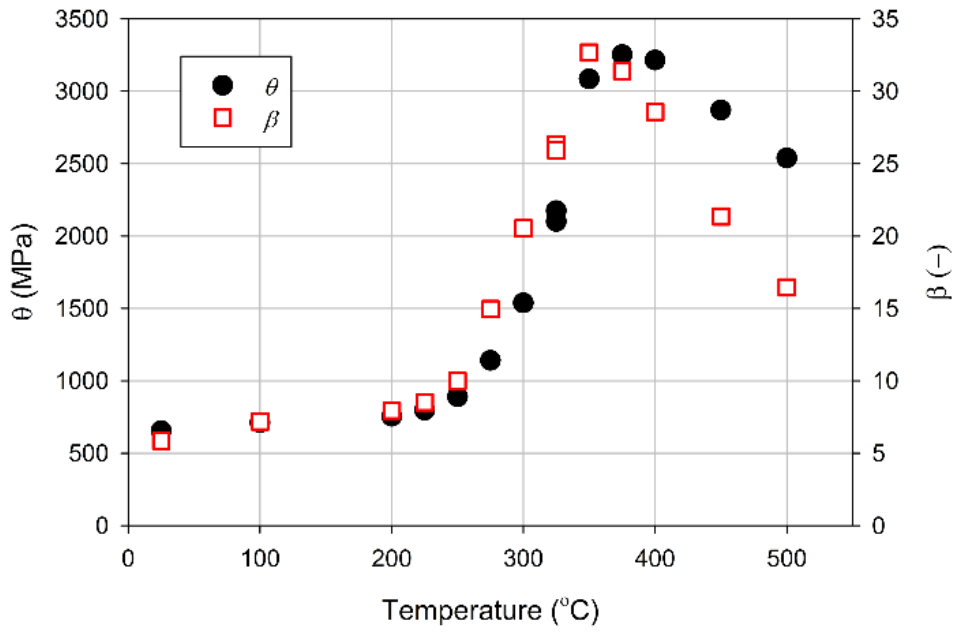

(a)

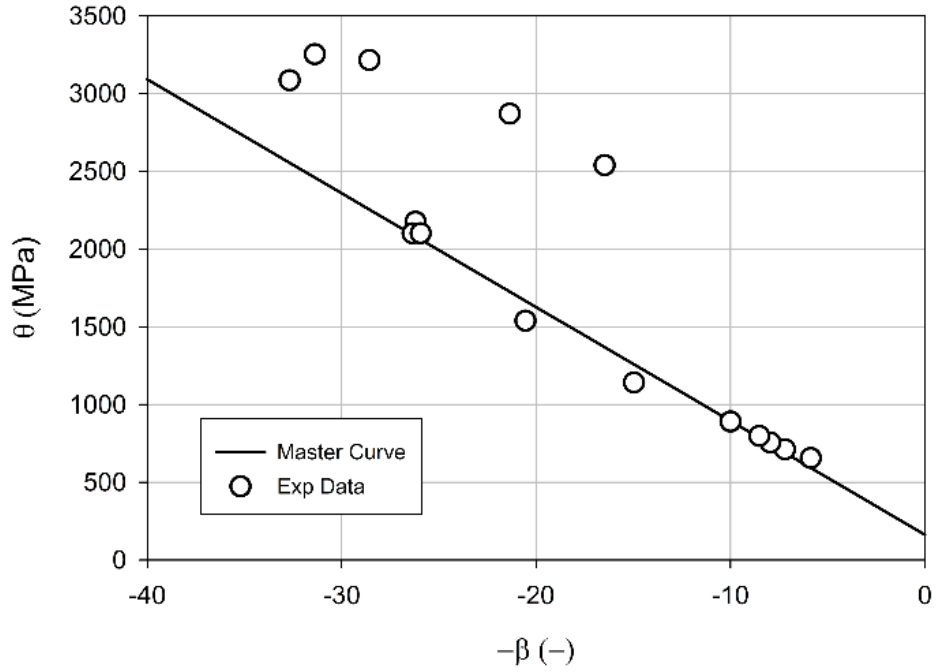

(b)

Fig. 51. Evolution of Palm-Voce law strain-hardening parameters as (a) a function of temperature and (b) normalized with a linear "master" curve below 350°C.

4.6.2 KME Model

For pure metals, the Kocks-Mecking-Estrin (KME) model [68–70] links the evolution in dislocation density, ρ, to the local plastic shear strain

$$\frac{d\rho}{d\gamma} = k_1\sqrt{\rho} - k_2\rho \tag{74}$$

where k_1 and k_2 are proportionality constants. The first term ($k_1 = 1/b$) on the right hand side signifies a storage of dislocations (increasing ρ) due to dislocation pinning by immobile obstacles, such as solutes or precipitates. The second term ($k_2 = L_0/b$, where L_0 is the mean annihilation distance in dislocation pairs of opposite sign) represents dynamic recovery of dislocations by mutual annihilation [71]. Dislocation interactions are related to ρ via the flow stress contribution of forest hardening using the Taylor relation

$$\sigma = M\alpha Gb\sqrt{\rho} \tag{75}$$

where M is the Taylor factor and α is a material dependent constant normally between 0.15 – 0.5 [99]. Combining Eq. (74) and (75) and the definition of the Taylor factor (i.e., $M = \sigma/\tau = \gamma/\varepsilon$) results in a strain-hardening law of the Palm-Voce formalism

$$\frac{d\sigma}{d\varepsilon} = \theta_0 - \beta_0\left(\sigma - \sigma_y\right) \tag{76}$$

where $\theta_0 = M^2\alpha Gbk_1/2$ and $\beta_0 = k_2M/2$. As discussed, apparent values θ and β are used in this work for AA6061-T651 and θ_0 and β_0 refer to pure metals. Thus, the above relation is rewritten for commercial aluminum alloys, e.g., AA6061-T651, as

$$\frac{d\sigma}{d\varepsilon} = \theta - \beta\left(\sigma - \sigma_y\right) \tag{77}$$

Fig. 50 shows the hardening rate is approximately a linear function of flow stress, as is described by Eq. (77), thus verifying this constitutive model as appropriate for AA6061-T651.

4.6.3 KME Model with Orowan Loop Storage

As discussed in Section 4.5, the as-received PSD evolves during elevated temperature exposure thereby degrading the residual mechanical properties. Several authors [102,103,131] have introduced Orowan loop storage effects to the KME model through addition of a term inversely proportional to l (see Eq. (68)) in Eq. (74). Simar, *et al.* [38] modified the KME model to include Orowan loop storage and dynamic recovery associated with precipitate growth. In this work, this approach is adapted to AA6061-T651 to predict strain hardening behavior after fire exposure. This section describes the KME law modification including definition of several effects which modify the dislocation storage rate, θ, and dynamic recovery rate, β.

The effects of Orowan loop storage by non-shearable precipitates are included in the KME relation in Eq. (74) as [102,103,131]

$$\frac{d\rho}{d\gamma} = k_1 + \frac{1}{bl} - k_2\rho \tag{78}$$

Substitution of the Taylor factor, M, and the Taylor relation in Eq. (75) results in

$$\frac{d\sigma}{d\varepsilon} = \theta_0 + \frac{\alpha^2 G^2 b M^3}{2l\left(\sigma - \sigma_y\right)} - \beta_0\left(\sigma - \sigma_y\right) \tag{79}$$

Thus, the apparent dislocation storage parameter, θ, in Eq. (77) may be expressed as

$$\theta = \theta_0 + \frac{\alpha^2 G^2 b M^3}{2l\left(\sigma - \sigma_y\right)} \tag{80}$$

The above relation is simplified by assuming the increase in $(\sigma - \sigma_y)$ during plastic deformation is small, i.e., $(\sigma_{sat} - \sigma_y)$ is not large. Thus, a mean value of $(\sigma - \sigma_y)$ may be substituted in the third term of Eq. (80). The mean is derived from Eq. (76) using apparent values θ and β as $\overline{\left(\sigma - \sigma_y\right)} \approx (\sigma_{sat} - \sigma_y)/2 = \theta/(2\beta)$. As can be seen in Fig. 50, the hardening rate is an approximately linear function of $(\sigma - \sigma_y)$. Thus, θ may be assumed independent of flow stress within a reasonable approximation, i.e., the Stage II to Stage III hardening transition is ignored. Inserting the expression for l from Eq. (68) in Eq. (80), a linearized expression for θ is obtained

$$\frac{\theta}{G} = \frac{\theta_0}{G} + \alpha^2 G M^3 \frac{\beta}{\theta} \sqrt{\frac{3f_v}{2\pi}} \left(\frac{b}{\bar{r}}\right) \tag{81}$$

which may also be written as

$$\frac{\theta}{G} = \frac{\theta_0}{2G} + \sqrt{\left(\frac{\theta_0}{2G}\right)^2 + \alpha^2 M^3 \beta \left(\frac{b}{\bar{r}}\right) \sqrt{\frac{3f_v}{2\pi}}} \tag{82}$$

4.6.3.1 Orowan Loop Storage Efficiency

The distinct transition in precipitate-dislocation interaction from shearing to Orowan looping implemented in the yield strength model (Section 4.5) is an idealization. In reality, Orowan loops are not efficiently stored until loss of precipitate coherency, i.e., Orowan loop storage is precipitate radius dependent [139]. Precipitates slightly larger than r_{trans} will be bypassed (i.e., dislocation loop storage). Further plastic deformation causes an increasing pileup intensity from dislocation accumulation [134]. If the precipitate is coherent with the matrix, the local stress will increase until the precipitate is sheared and the dislocation self-annihilates [139]. This process occurs easily when r is close to r_{trans}; however, the critical stress for precipitate shearing increases with precipitate radius [139]. An efficiency factor, φ, is thus introduced to account for the stability of Orowan loop storage. The evolution of this factor is elucidated by considering the extreme cases:

- $r = r_{trans}$: no Orowan loops are stored as the precipitate is sheared and the dislocation will immediately self-annihilate. Thus, $\varphi = 0$ when $r \leq r_{trans}$.
- $r = r_{cl}$ (r_{cl} is the radius corresponding to loss of coherency): all Orowan loops are stored. Thus, $\varphi = 1$ when $r \geq r_{cl}$.

φ is defined as the proportion of potential Orowan loops that will not self-annihilate with increases in stress [134]. Thus, the Orowan storage may be imagined as becoming more efficient with increasing precipitate radius. The relation between the two extremes is written as [38]

$$\varphi = \frac{\bar{r} - r_{trans}}{r_{cl} - r_{trans}} \tag{83}$$

4.6.3.2 Dynamic Precipitation Effects

The dynamic nature of an unstable solid solution during plastic deformation results in a hardening effect on the material [38]. Precipitation from a supersaturated solid solution (i.e., $C_{Mg} > C_{Mg}^{eq}$), requires diffusion whether by static or dynamic processes. Dislocation motion during plastic deformation assists diffusion through vacancy formation [140], diffusion short circuits, or through ballistic transport of solutes [38]. This may result in increased strength by dynamic segregation at dislocation junctions or dynamic precipitation [110]. Plastic deformation may therefore induce precipitation; the kinetics are governed by plastic strain (dynamic) rather than time (static). Dynamically nucleated precipitates increase precipitate strengthening ($\Delta\sigma_p$), thereby increasing flow stress during plastic straining. The $\Delta\sigma_p$ relation for $r < r_{trans}$ (Eq. (70)) also dictates that further increases in r and f_v cause additional flow stress increases. Note, dynamic precipitation is expected to increase as plastic strain increases [134]. Therefore, the summary effect of dynamic precipitation will be an increase in θ by a new quantity θ_{dp}. Deschamps, *et al.* [110] asserted that the hardening contributions of dislocation storage (θ_0) and dynamic precipitation (θ_{dp}) can be added linearly. Utilizing this, Simar, *et al.* [38] proposed a linear relationship between excess solute and θ_{dp}

$$\theta_{dp} = k_{\theta dp}\left(\frac{C_{Mg} - C_{Mg}^{eq}}{C_{Mg}^{0} - C_{Mg}^{eq}}\right) \tag{84}$$

where the parenthetical fraction is the relative remaining excess solute and $k_{\theta dp}$ is an adjustable parameter calculated from the difference between θ after a solution heat treatment and a minimum value with (ideally) no dynamic precipitation.

4.6.3.3 Yield Strength Effects on Dynamic Recovery

As detailed in the KME model derivation in Eq. (76), the dynamic recovery rate, β_0, is proportional to the annihilation distance between two dislocations of opposite sign, defined here as y_a [75]. Dislocations annihilate when the interaction stress (Gb/y_a) exceeds the yield strength. Thus, β_0 decreases with increasing yield strength. Additional processes affect the dynamic recovery rate. Dynamic precipitation increases yield strength thereby decreasing β_0. Dynamic precipitation also depletes the solid solution Mg content thus increasing dislocation mobility out of the glide plane.

The yield strength increases with decreasing Mg matrix concentration as an indirect effect related to dynamic precipitation. This potentially results in a further β_0 decrease. For the sake of simplicity, Simar *et al.* [38] assumed β_0 as inversely proportional to yield strength. Defining a reference minimum, β_{min}, at which maximum yield strength occurs, σ_y^{max}, β_0 is expressed as [38]

$$\frac{1}{\beta_{min}} - \frac{1}{\beta_0} = k_\beta \left(\frac{\sigma_y^{max} - \sigma_y}{G} \right) \tag{85}$$

where k_β is a constant evaluated using the initial β_0 and σ_y for a solution heat treated specimen.

4.6.3.4 Effect of Orowan Loop Storage on Dynamic Recovery

A modification of the KME constitutive law to account for the effects of Orowan loop storage on strain hardening is implemented [38]. As discussed, Orowan loop formation affects θ by the loop storage efficiency (φ); however, β is also affected. The mobile dislocation interactions with and without precipitates effects are schematized in Fig. 52. There are two potential interactions [38]:

- Case 1: The dislocation spacing (y_a) and travel time (t_d) are such that dislocations annihilate prior to encountering a precipitate with an Orowan loop. In this case, $y_a = y_0$ (the annihilation distance when no dislocation is stored), thus, $\beta = \beta_0$.
- Case 2: At least one precipitate with a stored dislocation is encountered during the time interval t_d. The dislocation annihilates with the Orowan loop causing a shift in glide plane. The dislocation glide is "de-localized" and the effective y_a will be larger thereby increasing β to β_p. β can be interpreted using the critical annihilation distance at the precipitate/matrix interface, y_p, thereby allowing definition of $\beta_p \approx 2y_p/b$, which is independent of precipitate radius [75].

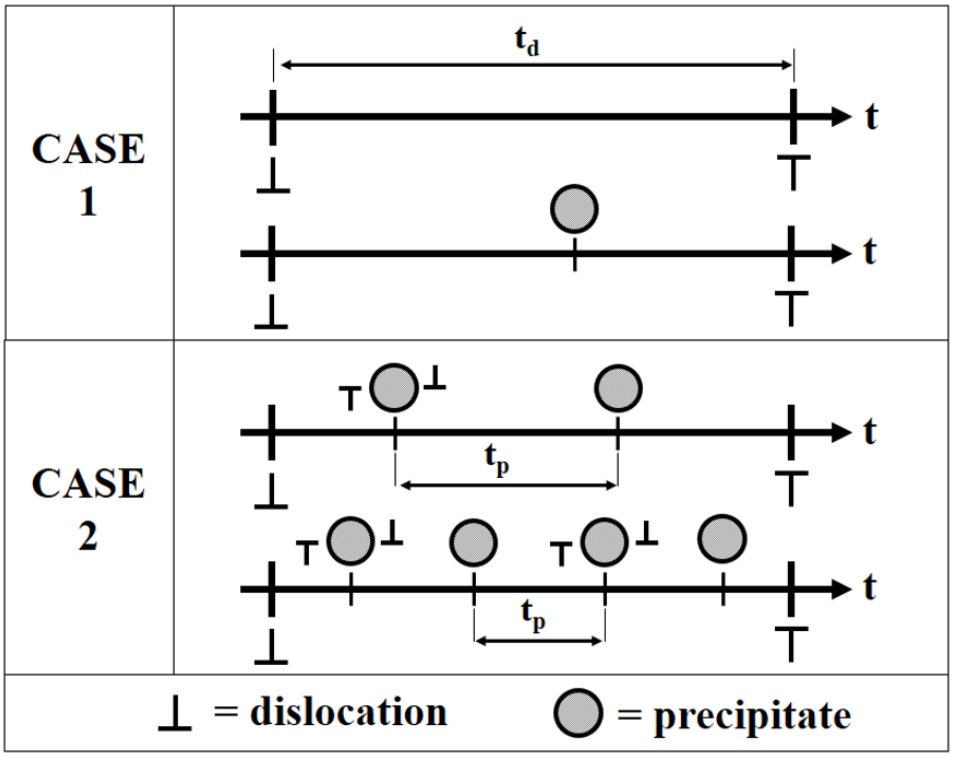

Fig. 52. The effect of Orowan loop storage on mobile dislocation annihilation distance (y_a); traveling time between dislocations of opposite sign shown as t_d; $1/t_p$ is precipitate distribution frequency.

The described cases may occur simultaneously during plastic deformation of an alloy containing precipitates with Orowan loop storage. Assuming the probability of Case 1 may be termed $p(0)$, then y_a may be written as

$$y_a = y_0 p(0) + y_p\big(1 - p(0)\big) \tag{86}$$

In the same manner, assuming β_p may be inferred using y_p, β may be written as

$$\beta = \beta_0 p(0) + \beta_p\big(1 - p(0)\big) \tag{87}$$

where $p(0)$ follows a Poisson distribution [38]. In developing this distribution, definition of the traveling times in Fig. 52 is required. The traveling time between dislocations of opposite sign is defined as $t_d = L_0/v_r$, where L_0 is the mean value of y_a and v_r is the relative dislocation velocity. The traveling time between a precipitate and another with a dislocation loop is defined as $t_p = l/v_r$, where l is given by Eq. (68). The mean number of precipitates encountered before two moving

dislocations meet is therefore given by $v = t_d/t_p$. Applying the Orowan storage efficiency factor, φ, results in $v_\varphi = v\varphi$. The described effects are combined to express v_φ as [134]

$$v_\varphi = \varphi \frac{t_d}{t_p} = \varphi \frac{L_0}{l} = \sqrt{\frac{3}{2\pi}} \frac{\sqrt{f_v} L_0 \varphi}{\bar{r}} \tag{88}$$

Applying a Poisson distribution to above and solving for $p(0)$ results in [38]

$$p(0) = \exp\left(-v_\varphi\right) = \exp\left(-\sqrt{\frac{3}{2\pi}} \frac{\sqrt{f_v} L_0 \varphi}{\bar{r}} \right) \tag{89}$$

This relation is applied to Eq. (87) to include the effects of Orowan loop storage on β.

4.6.3.5 Generalized KME Model Parameters

The apparent dynamic storage rate, θ, defined in Eq. (82) and the apparent dynamic recovery rate, β, are modified to include the various microstructural effects as follows

- Orowan loop storage efficiency: the $(1/r)$ term in Eq. (82) is multiplied by φ to include the effects of precipitate radius on the dislocation storage rate, θ
- Dynamic precipitation: θ is modified by linearly superposing θ_0 and θ_{dp}, defined in Eq. (84)
- Orowan loop storage: β is defined using Eqs. (87) and (89) to account for Orowan loop effects
- Yield strength effect on β: β_0 in Eq. (87) is defined as a function of σ_y using Eq. (85)

The final expressions for θ and β for use in the KME formalism in Eq. (77) are thus defined as

$$\frac{\theta}{G} = \frac{\theta_0 + \theta_{dp}}{2G} + \sqrt{\left(\frac{\theta_0}{2G}\right)^2 + \alpha^2 M^3 \beta \varphi \left(\frac{b}{\bar{r}}\right) \sqrt{\frac{3 f_v}{2\pi}}} \tag{90}$$

$$\beta = \beta_0 \exp\left(-\sqrt{\frac{3}{2\pi}} \frac{\sqrt{f_v} L_0 \varphi}{\bar{r}} \right) + \frac{2 y_p}{b} \left(1 - \exp\left(-\sqrt{\frac{3}{2\pi}} \frac{\sqrt{f_v} L_0 \varphi}{\bar{r}} \right) \right) \tag{91}$$

The mean precipitate radius, $\bar{r}$, and volume fraction, f_v, are calculated using the PSD predicted by the KWN model described in Section 4.4.

The classic KME model was extended by implementing several microstructure-based parameters to account for the effects of dynamic precipitation (θ_{dp}), Orowan loop stability (φ), yield strength (β_{min}), and Orowan loop storage (Eq. (87)). Fig. 53 schematically demonstrates the effect of these parameters on θ and β for a representative thermal exposure of 20°C/min. The dislocation storage parameter, θ, is largely unaffected by including the effects of dynamic precipitation. θ_{dp} primarily affects θ during the aging process, i.e., thermal exposure from a solutionized or naturally aged state. Inclusion of the storage efficiency factor, φ, reduces θ for radii slightly greater than r_{trans}, i.e., the T6 state. This results in a proportional increase from θ_0 to that at the loss of coherency. The dynamic recovery rate, β, increases slightly due to inclusion of effects associated with yield strength (i.e., annihilation distance). Orowan loop storage efficiency is included which significantly modifies β including transitional effects at loss of coherency.

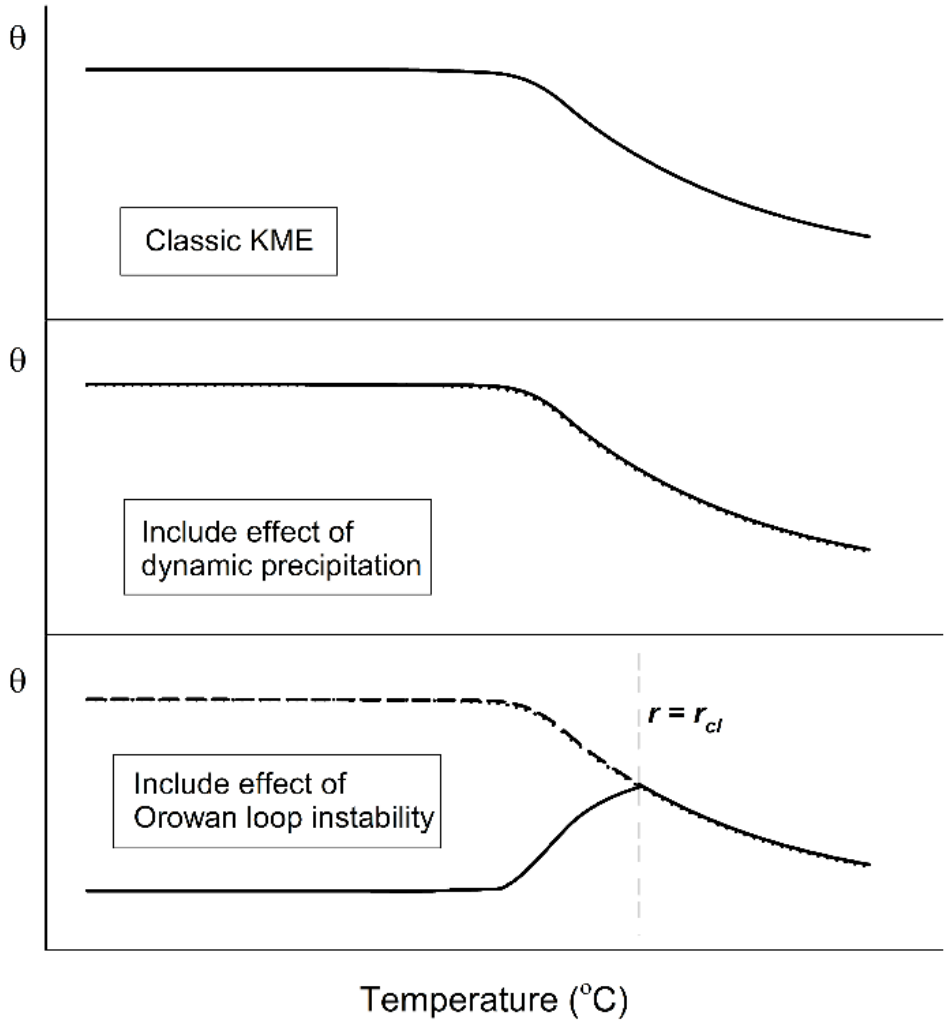

(a)

(Fig. 53 continued on next page)

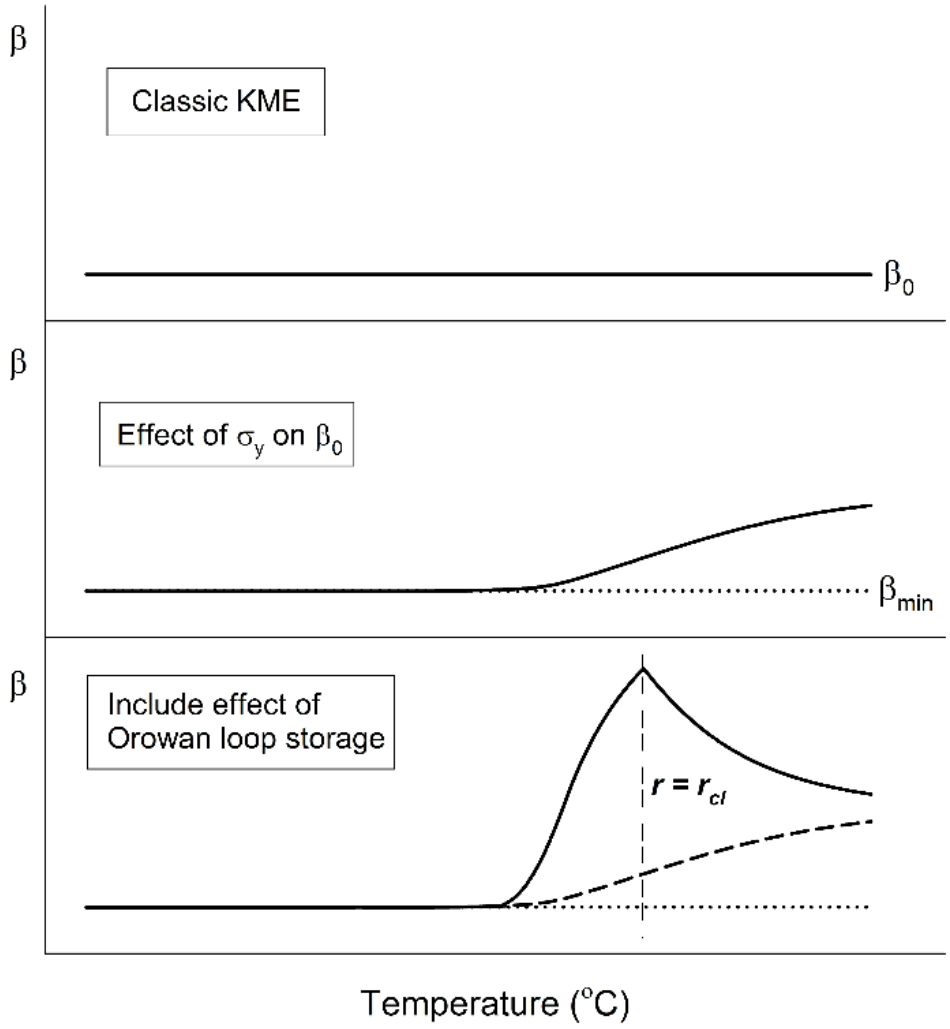

(b)

Fig. 53. Schematic of the effect of including various microstructural effects in the extended KME model as compared to the classic KME model. The variations have been shown for thermal exposures relevant to that in a fire exposure.

4.6.4 KME Model Calibration

The generalized KME model dislocation storage rate, θ, and dynamic recovery rate, β, are detailed in Eqs. (90) and (91), respectively. Model parameters were identified through analysis using tensile mechanical tests of specimens previously heated at 20°C/min. The identification procedure involved several steps as described below.

The dislocation storage parameter, θ_0, is defined as that in the absence of dynamic precipitation and Orowan loops. This parameter was evaluated using Fig. 51a. θ in the as-received state (θ =

655 MPa) is only slightly different than that for pure Al ($\theta_0 \approx G/30$ = 900 MPa) when all solutes have been precipitated as coherent, shearable precipitates [101]. Thus, θ_0 is reasonably defined as that in that measured in the as-received state, $\theta_0 = \theta_{AR}$ = 655 MPa.

The minimum dynamic recovery rate in Eq. (85) is simply taken as the minimum in Fig. 51a, which is that in the as-received T6 state, β_{min} = 5.9. This is appropriate as this relation scales the dynamic recovery rate to yield strength evolution.

The radius of loss of coherency, r_{cl}, used to calculate φ was identified from the peak transition measured for θ and β in Fig. 51a. The hardening parameters (θ and β) are plotted against predicted $\bar{r}$ from the KWN model in Fig. 54. Both θ and β reach a maximum at $\bar{r} \approx 8$ nm. The sharp decrease in θ is particularly indicative of a loss of precipitate coherency. Thus, r_{cl} = 8 nm. This value is notably less than that in Ref. [38] (r_{cl} = 25 nm). Loss of precipitate coherency occurs as the β″ coarsens to the semi-coherent β′ phase. The β′ phase is characterized as ribbon-like with a diameter of ~10 nm [141,142] which corresponds approximately to the predicted value when corrected to an equivalent precipitate radius. Thus, r_{cl} = 8 nm is considered a reasonable approximation for the loss of coherency.

The mean value of dislocation spacing, L_0, is calculated using the Taylor relation in Eq. (75) by assuming that $L_0 = \rho^{-1/2} = M\alpha Gb/(\sigma - \sigma_y)$. The KME model was modified under the premise that the increase in flow stress is small such that $(\sigma - \sigma_y) \approx (\sigma_{sat} - \sigma_y)/2$. From Eq. (77), θ and β are defined as those with no Orowan loop storage or dynamic precipitation, i.e., θ_0 and β_{min}. Thus, substituting these parameters in the Taylor relation results in

$$L_0 = M\alpha Gb\frac{2\beta_{min}}{\theta_0} \tag{92}$$

This results in L_0 = 42 – 139 nm for the classical range of the α parameter, i.e., 0.15 – 0.5 [99].

The final parameters, α and y_p, were identified through analysis of θ and β as a function of predicted $\bar{r}$ (Fig. 54). y_p was determined from the experimental β values for samples heated at 20°C/min. Optimal agreement was achieved for y_p = 13 nm. This is significantly higher than would be expected in the absence of Orowan loops ($y_a \approx 1$ nm) [75]. Similarly, α was determined from the experimental θ values for samples heated at 20°C/min. Optimal agreement was achieved for α =

0.15. This value is within the classically defined range (0.15 – 0.5 [99]). Applying α to Eq. (92) results in L_0 = 42 nm.

All parameters of the KME model defined by the generalized relations for θ (Eq. (90)) and β (Eq. (91)) are provided in Table 13.

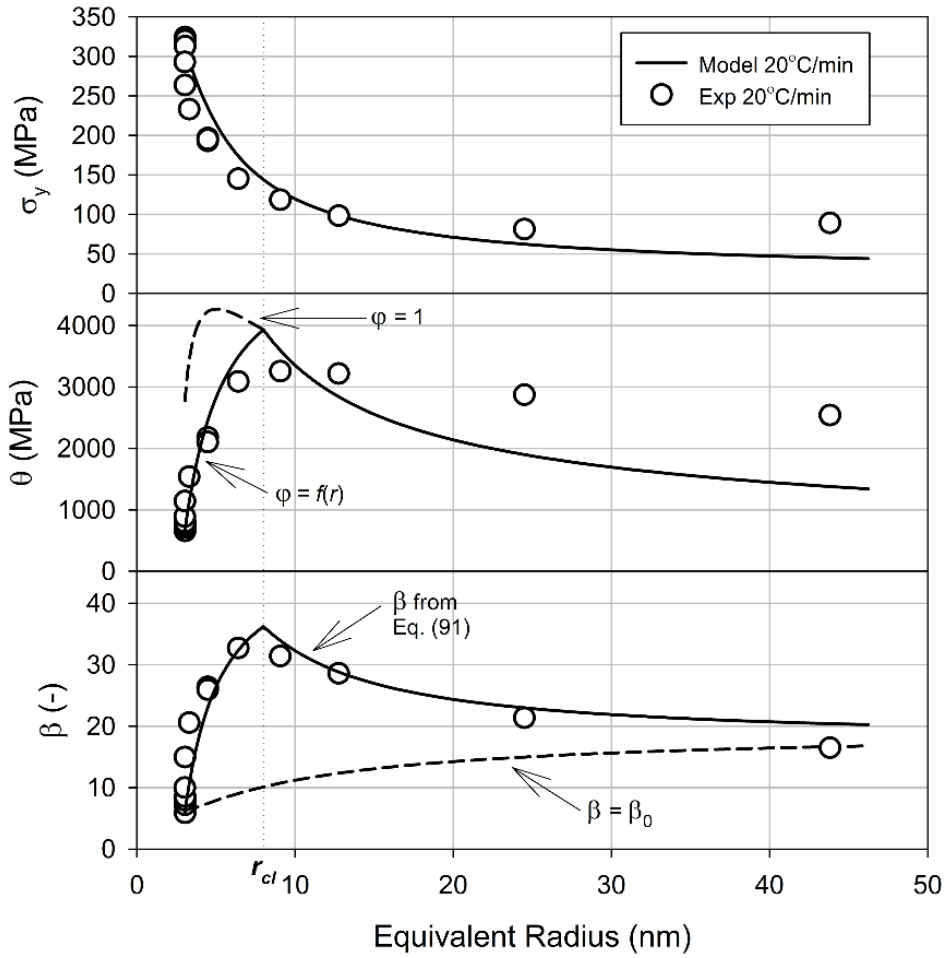

Fig. 54. KME model parameter evolution as a function of predicted mean radius for AA6061-T651 heated at 20°C/min: (a) yield strength, σ_y, (b) dislocation storage rate, θ, and (c) dynamic recovery rate, β.

Table 13. Modified KME model parameters.

Parameter	Significance	Value	Source
θ_0	θ if no dynamic precipitation or Orowan loops	655 MPa	θ minimum in Fig. 51a
β_{min}	β at maximum σ_y	5.9	β minimum in Fig. 51a
$k_{\theta dp}$	Constant for θ_{dp} in Eq. (84) for dynamic precipitation effects	1210 MPa	θ for a solution heat treated sample and the AR material
σ_y^{max}	maximum yield strength (T6 state)	324 MPa	σ_y of as-received material
k_β	Constant linking σ_y to β	10.6	β for a solution heat treated sample and the AR material
r_{cl}	Equivalent radius of loss of coherency	8 nm	$\bar{r}$ of θ and β transition in Fig. 54
L_0	Mean value of distance between two dislocations of opposite sign	42 nm	Eq. (92)
α	Constant linking shear stress to dislocation density	0.15	Optimized from θ of 20°C/min samples
y_p	Annihilation distance when at least one precipitate exists between dislocations of opposite sign	13 nm	Optimized from β of 20°C/min samples

4.6.5 Results and Discussion

The coupled non-isothermal constitutive model is given by the modified KME constitutive law defined by the Palm-Voce formalism in Eq. (77) and the generalized relations for θ and β in Eqs. (90) and (91), respectively (see Table 13 for parameters). The model uses the non-isothermal residual yield strength model in Eq. (72) as the initial condition to calculate flow stress (see Table 12 for parameters). The models incorporate prior non-isothermal heating using predictions from the KWN model, specifically the PSD (r_i and N_i), $\bar{r}$, and f_v. The KWN precipitate evolution model is defined in Eqs. (53) – (63) with parameters listed in Table 11. Using the models calibrated for AA6061-T651, the initial PSD (Fig. 42) is the only input required other than the thermal exposure to predict the residual yield strength and strain hardening behavior after fire exposure.

The modified KME model predictions are compared with experimental data (20°C/min heating rate) in Fig. 55. Several examples of possible material states are shown: (a) as-received, (b) slightly overaged (T = 300°C), (c) overaged (T = 350°C), and (d) massively overaged (T = 400°C). It is obvious the model is capable of predicting the measured strain hardening behavior after

previous thermal exposure. The overall agreement between predictions and experiment is good at the shown conditions, which encompass those expected after fire exposure for AA6061-T651.

Thermal exposure above ~250°C results in precipitate growth such that $\bar{r} > r_{trans}$. In the classical KME approach, this would result in an instantaneous transition from precipitate shearing to Orowan looping (see $\varphi = 1$ in Fig. 54). Inclusion of the storage efficiency, φ, allows the model to reflect θ evolution due to increasing Orowan loop storage. Also, Fig. 54 demonstrates inclusion of Orowan loop storage is critical for model accuracy, as a constant value for dynamic recovery (β_{min}) or a value solely governed by yield strength (β_0 in Eq. (85)) is inadequate to represent β evolution. Thus, the model includes these microstructural effects in the generalized θ and β relations which allows for it to capture the strain hardening evolution from as-received (Fig. 55a) to overaged (Fig. 55b,c).

Massive overaging ($T \geq 350$°C) results in a continued decrease in yield strength (Fig. 49); however, a distinct transition in θ and β is measured at the loss of precipitate coherency at r_{cl} (Fig. 54). The transition from increasing to decreasing θ and β with increased thermal exposure is well captured by the model. This is due to the inclusion of the Orowan storage efficiency, φ, in predicting β. This agreement is reflected for the KME model prediction in Fig. 55d ($T = 400$°C), which occurs above the loss of precipitate coherency (~375°C at 20°C/min).

Model predictions were also compared to experimental data to study the effect of heating rate for prior material heating to a constant temperature (350°C). This is shown in Fig. 56. The figure contains experimental data for specimens previously heated at 5, 25, and 250°C/min. The temperature (350°C) was chosen as it coincides with significant PSD evolution. The tested heating rates span a large range of possible PSDs at this temperature. As is shown, the model shows good agreement with the experimental data. Note, somewhat competing effects of θ and β occur for 5°C/min ($\theta \approx 3600$ MPa, $\beta \approx 34$) and 25°C/min ($\theta \approx 3350$ MPa, $\beta \approx 31$). This results in a nearly identical prediction of strain hardening; however, the predicted strain hardening at both heating rates remains reasonable. Overall, the evolution in strain hardening behavior at different heating rates is well represented by the model.

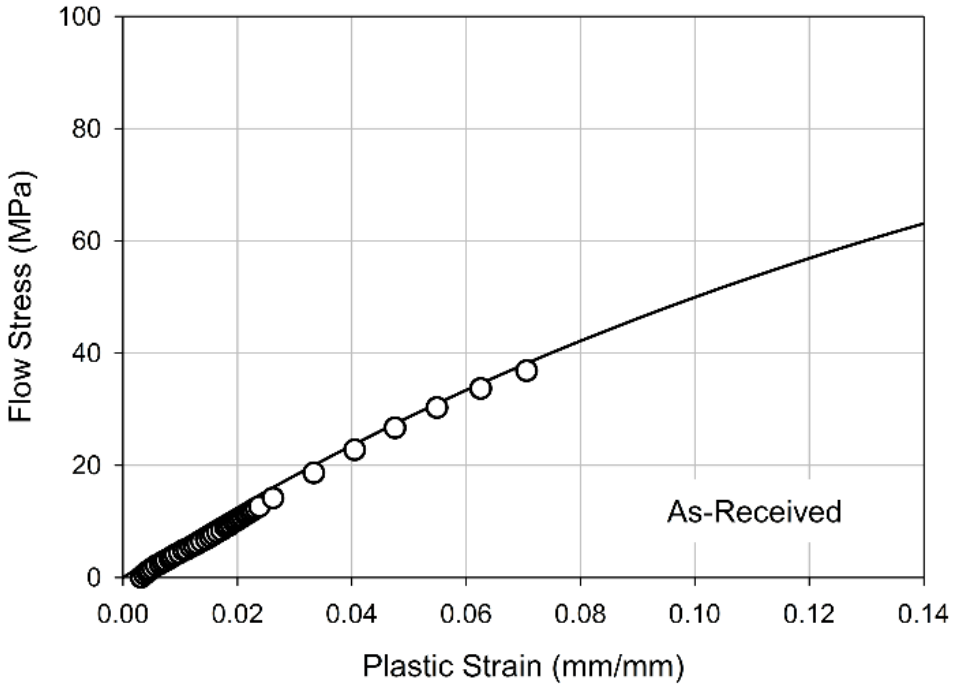

(a)

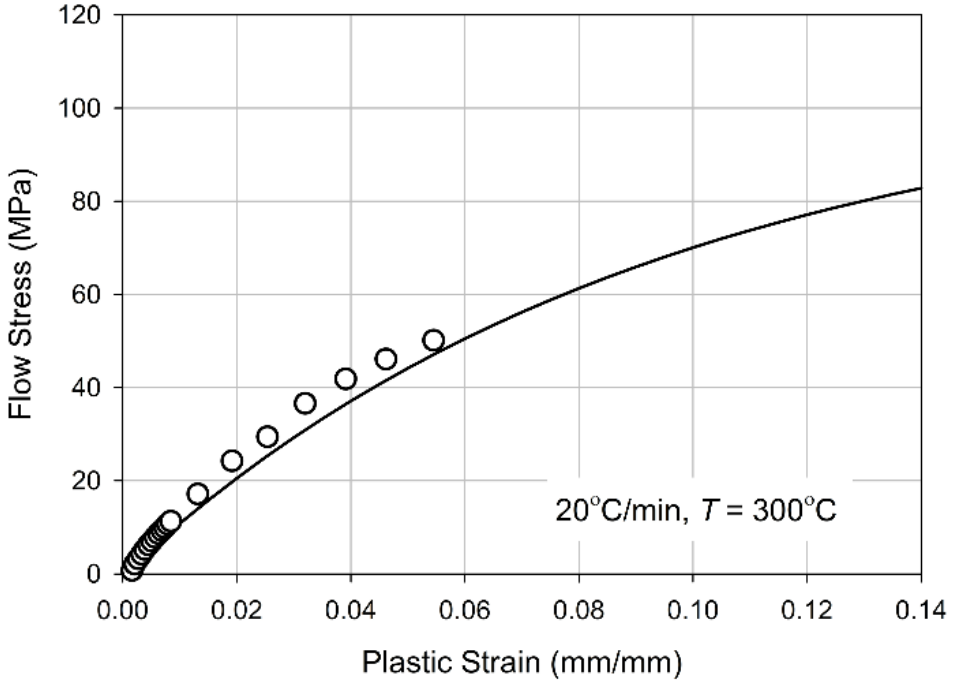

(b)

(Fig. 55 continued on next page)

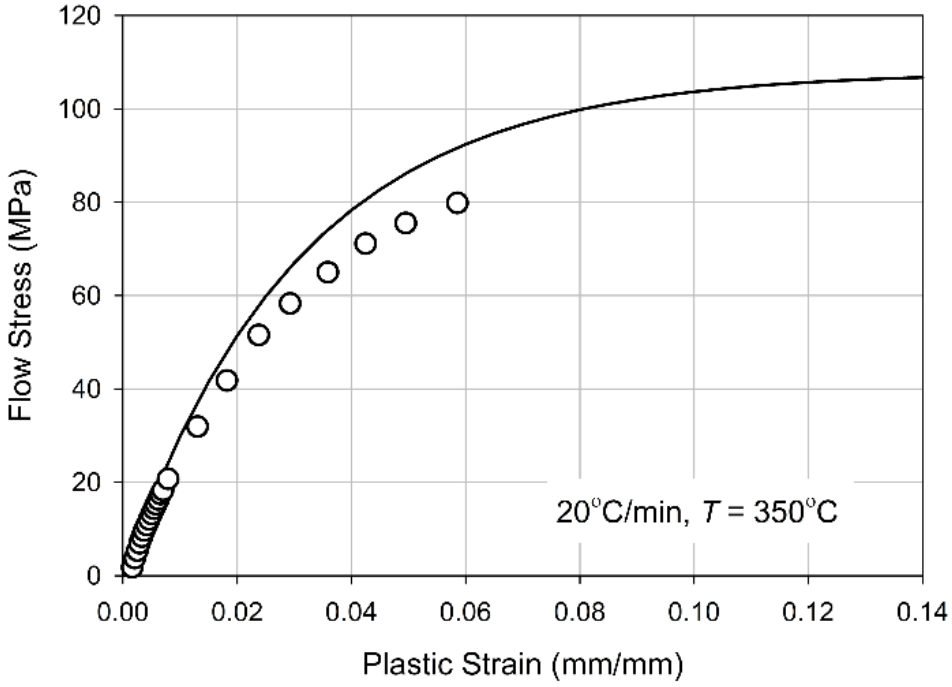

(c)

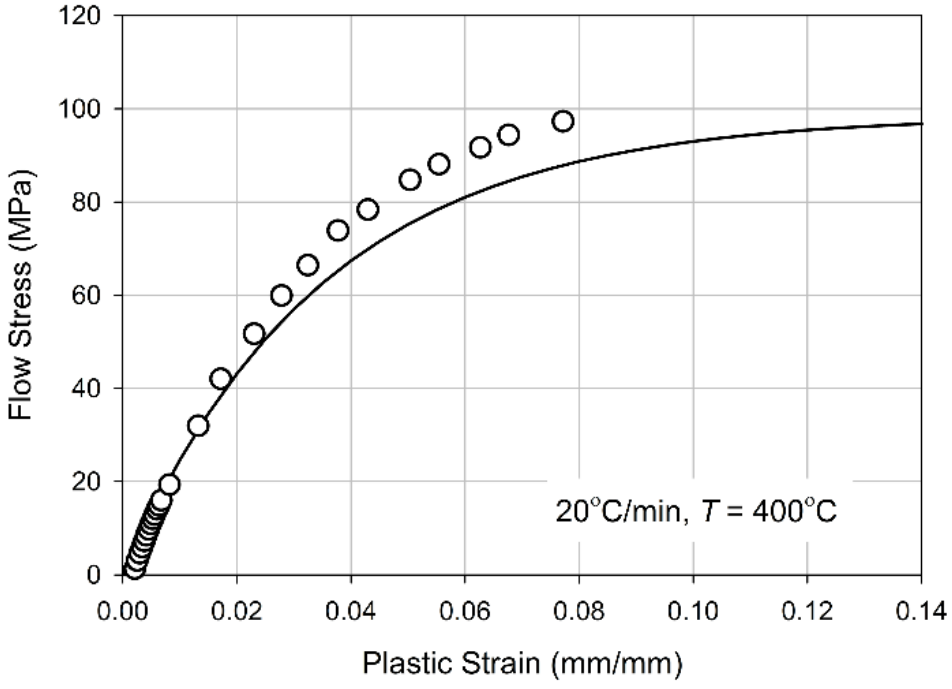

(d)

Fig. 55. Modified KME constitutive law predictions compared to experiment for AA6061-T651 (a) as-received, (b) slightly overaged to 300°C, (c) overaged to 350°C, and (d) massively overaged to 400°C.

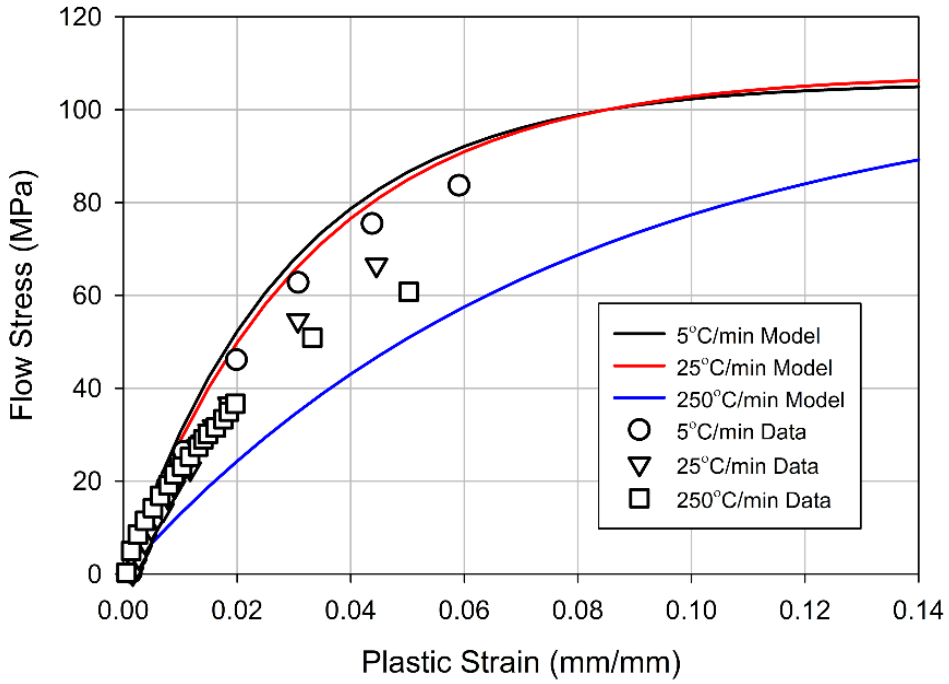

Fig. 56. Modified KME constitutive law predictions for heating to 350°C for different heating rates.

The agreement observed in Fig. 55 and Fig. 56 validates the coupled approach for predicting the strain hardening behavior implemented in this research. The model has been demonstrated to incorporate the effects of non-isothermal heating on residual constitutive behavior, including strain hardening and yield strength.

4.7 Conclusions

A coupled non-isothermal model was developed for AA6061-T651 constitutive behavior after exposure to non-isothermal heating such as due to fire exposure. Distinct sub-models were used to predict (i) precipitate size distribution (PSD) evolution, (ii) residual yield strength, and (iii) strain hardening after thermal exposure. The coupled model is described as follows

- Diffusion-based precipitate evolution models are required to predict precipitate size distribution (PSD) evolution due to precipitate nucleation, growth, and dissolution.
- PSD evolution during a non-isothermal thermal exposure has been represented using a classical Kampmann-Wagner numerical (KWN) model. Model parameters were identified using Refs. [38–40,108,115] as a basis. The initial, as-received PSD was taken as that from Simar, *et al.*

[38], which was modified to have a total precipitate density equivalent to that in Ref. [132] for AA6061 (10^{23} #/m^3). Alloy-specific PSD identification, including precipitate size and number density, is necessary as precipitate strengthening is highly dependent on PSD details and total volume fraction. For example, the PSDs for AA6005 [38] and AA6056 [108] are not directly applicable to AA6061. PSD evolution is modeled using an Eulerian class size approach as described by Perez, *et al.* [114].

- The residual yield strength is estimated using linear superposition of individual strength contributions of friction stress, solutes, and precipitates. Precipitate strengthening is calculated as a macroscopic, bulk average effect of the precipitate-dislocation interaction. Precipitate spacing in the glide plane is calculated using the Friedel statistical model. Precipitate strengthening is calculated on a class size basis as precipitate shearing by dislocations (for small precipitates) or Orowan looping (for large precipitates).
- Implementation of the KWN model in the described yield strength model resulted in predictions which reasonably represented non-isothermal experimental data. Non-isothermal exposure was chosen as the basis for model development due to its representative nature of the transient heating in fire exposure (see Chapter 2). This is compared to isothermal exposures used in other works [38,40,77,108]. In this sense, the model is developed in a manner more representative of exposures encountered in its intended end use. Also, parameter analysis shows the residual yield strength model is especially sensitive to the line tension constant, k_Γ, which must be determined on an alloy specific basis.
- Strain hardening was modeled using a modified KME constitutive law after Simar, *et al.* [38]. Orowan loop storage by precipitates is incorporated, including its effectiveness as a function of precipitate size during elevated temperature growth. The model generalizes the dislocation storage rate, θ, and dynamic recovery rate, β, through inclusion of precipitate related microstructural effects, including Orowan loop storage efficiency and dynamic precipitation. The modified θ and β parameters are implemented in the Palm-Voce form of the classical KME relation. The model was developed in Ref. [38] for AA6005A-T6 and therefore required extensive parameter adjustment to accurately represent AA6061-T651 strain hardening. Model parameters were calibrated using experimental data after non-isothermal exposure, thus optimizing the model for residual material states after fire exposure.

- The modified KME constitutive law was implemented as a coupled model with the previously described KWN and residual yield strength models. The model predicts the experimentally measured evolution in θ and β including the transition in behavior at the loss of precipitate coherency. The model shows good agreement with the strain hardening behavior measured for several possible material states after non-isothermal exposure. As with the residual yield strength model, the use of non-isothermal exposures more accurately represents those expected during fire exposures.

In summary, a coupled constitutive model has been developed to predict the residual constitutive behavior of AA6061-T651 after non-isothermal exposure. The model has been successfully validated against experimental tensile mechanical tests.

5 Prediction of Residual (Post-Fire) Mechanical Behavior of AA5083-H116 and AA6061-T651 using Constitutive Models

5.1 Introduction

Aluminum alloys are increasingly being used in a broad spectrum of applications such as lightweight structures, light rail, bridge decks, marine crafts, and off-shore platforms. The residual structural state after a severe fire has significant implications affecting structural integrity and safety. Constitutive models validated against data for samples exposed to different types of heating that reflect fire exposures are needed to assist in determining the residual material state of an aluminum structure following a fire exposure.

AA5083-H116 and AA6061-T651 residual mechanical behavior after simulated fire exposures was extensively characterized in Chapter 2. The residual (post-fire) mechanical properties were elucidated in terms of the kinetically (time-temperature) dependent evolution of the governing microstructural mechanisms. This data was used as a basis to develop mechanistic constitutive models to predict the residual mechanical behavior of AA5083-H116 (see Chapter 3) and AA6061-T651 (see Chapter 4). In these models, microstructural evolution was predicted as a function of thermal exposure using independent physically-based microstructural evolution models for each governing mechanism. The residual yield strength and strain hardening behavior were predicted mechanistically using the evolved microstructural state, which governs mechanical behavior. Residual yield strength was predicted using a composite model that combined the contributions of the different microstructural strengthening mechanisms in the respective alloys. For AA5083, recovery [9,43] and recrystallization [36] models were used to predict the evolution in the subgrain and grain structure. For AA6061, a modified Kampmann-Wagner numerical (KWN) model [38,117] was used predict precipitate evolution including nucleation, growth, and dissolution. Strain hardening was predicted using separate physically-based internal state variable models based on the Kocks-Mecking-Estrin (KME) model [68–70]. The KME model was modified to reflect the microstructural features of each alloy, i.e., subgrains in AA5083 [27] and dislocation (Orowan) looping of precipitates in AA6061 [38]. Thus, separate mechanistic constitutive models have been developed for AA5083-H116 and AA6061-T651 requiring only the prior thermal exposure as input to predict residual mechanical behavior.

The aim of the present paper is to bench-mark the AA5083-H116 and AA6061-T651 constitutive models developed in Chapter 3 and Chapter 4, respectively, with materials exposed to conditions more closely reflecting a fire exposure. A brief overview of the constitutive models is given including the microstructural evolution, yield strength, and strain hardening sub-models. Validation mechanical tests and heating were performed similar to that in Chapter 2; however, specimens were heated at a constant heating rate then held isothermally at a prescribed temperature for varying times. This exposure contrasts the data used for development of the models (constant heating to a prescribed temperature followed by immediate water quenching). Also, these thermal exposures more accurately reflect that possibly experienced during a fire. The predicted residual yield strength and strain hardening models are bench-marked against experimental data.

5.2 Constitutive Models

This section provides a brief overview of the physically-based models developed to predict the residual constitutive behavior of AA5083-H116 and AA6061-T651 after fire exposure. Refer to Chapter 3 (AA5083-H116) and Chapter 4 (AA6061-T651) for model details. The chemical compositions of the alloys are shown in Table 14.

Table 14. Chemical composition (wt%) of AA5083-H116 and AA6061-T651.

Alloy	**Si**	**Fe**	**Cu**	**Mn**	**Mg**	**Cr**	**Zn**	**Ti**	**Al**
5083-H116	0.11	0.24	0.06	0.57	4.4	0.09	0.02	0.02	bal
6061-T651	0.66	0.4	0.24	0.07	0.9	0.18	0.02	0.02	bal

Fundamentally, the constitutive behavior of Al alloys, or for any alloyed metal, is governed by the microstructural state [8]. Thus, the logical conclusion may be drawn that residual constitutive behavior, i.e., yield strength and strain hardening behavior, after fire exposure is governed by microstructural evolution. Microstructural evolution is also known to be a kinetically-driven process, i.e., it is time-temperature dependent [8]. This is an important distinction as it invalidates empirical maximum temperature approaches to predict residual mechanical behavior, such as that of Qiang, *et al.* [143] for high strength steels. The microstructural features that strengthen aluminum are alloy specific, hence the separate models for AA5083-H116 and AA6061-T651.

The constitutive models are defined by three sub-models for microstructural evolution, residual yield strength, and residual strain hardening behavior. The residual microstructural state is

predicted by kinetics-based microstructural evolution models, which are alloy specific based on the physics of microstructural evolution. The residual yield strength is additively calculated from individual microstructural strengthening models. The residual microstructural state after fire exposure is intrinsically incorporated in the strength models using the kinetics-based microstructural evolution models. The alloy specific sub-models are further discussed in the following sections.

5.2.1 AA5083-H116 Constitutive Model

5.2.1.1 Recovery and Recrystallization Models

AA5083-H116 derives its primarily derives its strength from Mg in solid solution and grain structure refinement from cold-work during material processing [7]. During a fire exposure, the microstructure evolves in two distinct processes: recovery and recrystallization.

Recovery reduces the stored energy of the dislocation structure by several processes [31]. Fig. 57 shows the as-received dislocation structure internal to the grains. Note, the cellular structure is referred to as subgrains as they are similar to grains, however, at a sub-micron size. Recovery results in subgrain growth in AA5083-H116. This process is dominant prior to the onset of recrystallization (below 280 – 320°C, depending on heating rate, see Chapter 2 and 3). As recovery proceeds, the activation energy has been noted to increase due to the evolving active recovery mechanisms [83]. Therefore, a non-isothermal kinetics model with an apparent activation energy dependent on recovery progress is adapted from the Borelius recovery model [43]. The recovery model is given as

$$\frac{dX_{RV}^2}{dT} = -\frac{X_{RV}^2 K_0}{B} \exp\left[-\frac{Q_0 - \beta P_0 X_{RV}^2}{RT}\right] \tag{93}$$

where X_{RV} is the recovered fraction where zero corresponds to fully recovered, K_0 is a pre-exponential factor, B is the heating rate, Q_0 is the activation energy as recovery completes, R is the universal gas constant, T is the temperature, and κP_0 is a parameter group which corrects for the apparent activation energy as recovery initiates. The model parameters, K_0, κP_0, and Q_0, are

assumed to be solely determined by the governing recovery mechanisms and independent of the exposure temperature.

The recovered fraction predicted by Eq. (93) may also be used to calculate subgrain growth. Applying the well-known Hall-Petch relation, i.e., $\sigma_y = \sigma_0 + k\delta^{-1/2}$ where k is a proportionality constant and δ is the subgrain size, and placing in a normalized form results in

$$X_{RV} = \frac{\sigma_y - \sigma_0}{\sigma_{y,AR} - \sigma_0} = \left(\frac{\delta_{AR}}{\delta}\right)^n \tag{94}$$

Rearranging to solve for δ

$$\delta = \frac{\delta_{AR}}{X_{RV}^2} \tag{95}$$

where δ_{AR} is the as-received subgrain size. Thus, subgrain growth is predicted solely as a function of the as-received microstructure and the recovery model in Eq. (93).

Recrystallization releases the stored energy of deformation induced in the material during cold-work during material processing. Fig. 58 shows the as-received and recrystallized grain structures. The as-received grains are elongated (~200 µm long) and pancake-like (~10 µm thick, ~50 µm wide). This transforms to an equiaxed structure (48 µm diameter) after recrystallization. In cold-worked Al alloys, e.g., AA5083-H116, recrystallization nuclei cluster in areas of high stored energy (strain) [33]. This clearly violates the randomness assumption [58] of the commonly used KJMA recrystallization kinetics model [54–56]. Also, cold-worked Al alloys have shown evolving impingement behavior (uniform → linear) during recrystallization [36]. Thus, a linear/uniform impingement microstructural path model (MPM) developed by Vandermeer and colleagues [36,62–64] was implemented for AA5083-H116 recrystallization. Refer to Chapter 3 and Refs. [36,91] for assumptions and detailed model development.

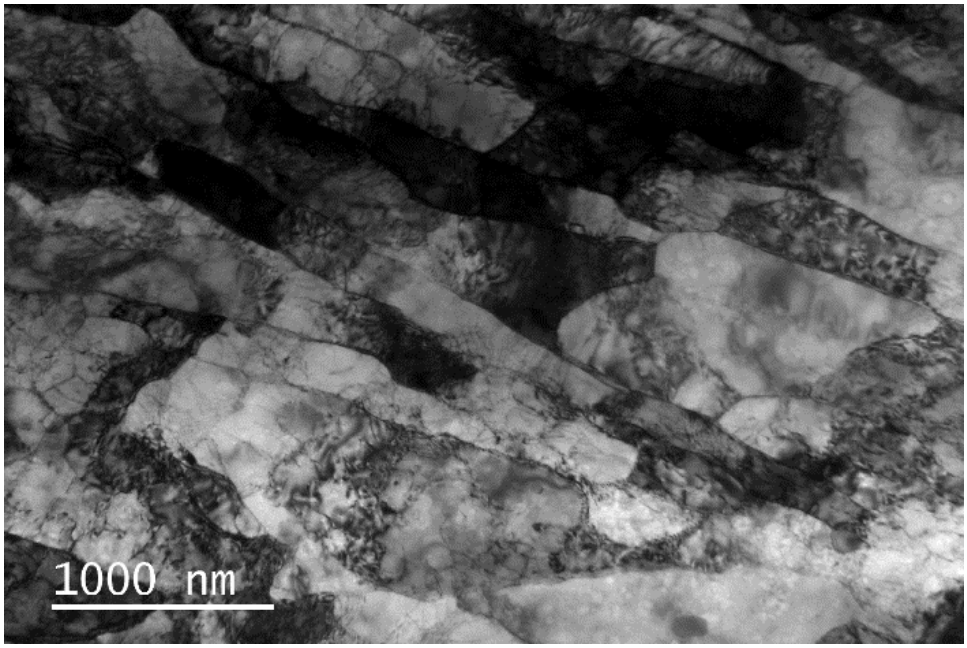

(a)

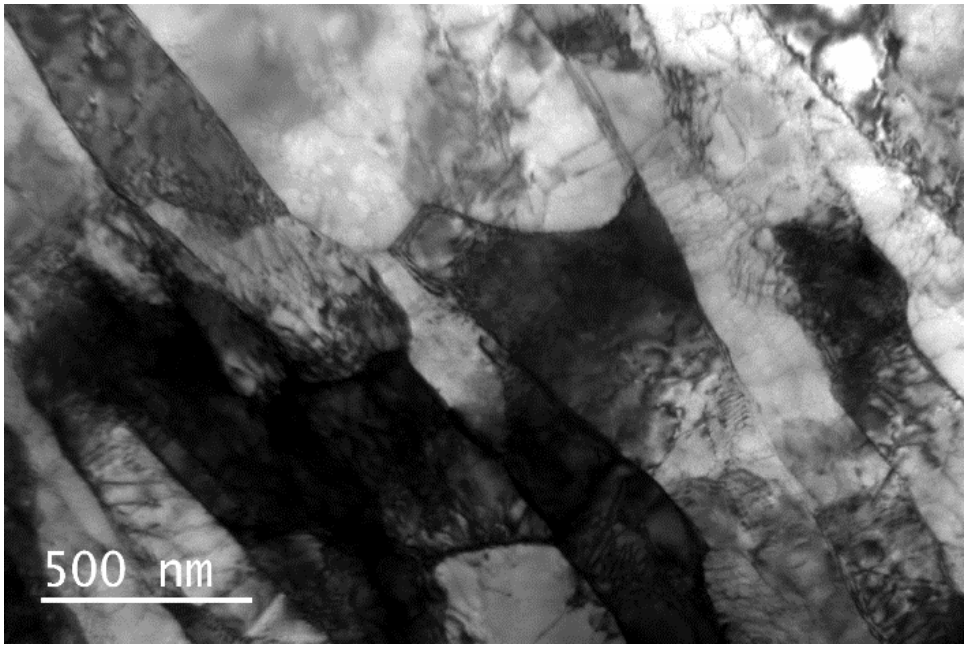

(b)

Fig. 57. AA5083-H116 as-received dislocation structure (subgrains). Average subgrain size from 10 micrographs is 376 nm.

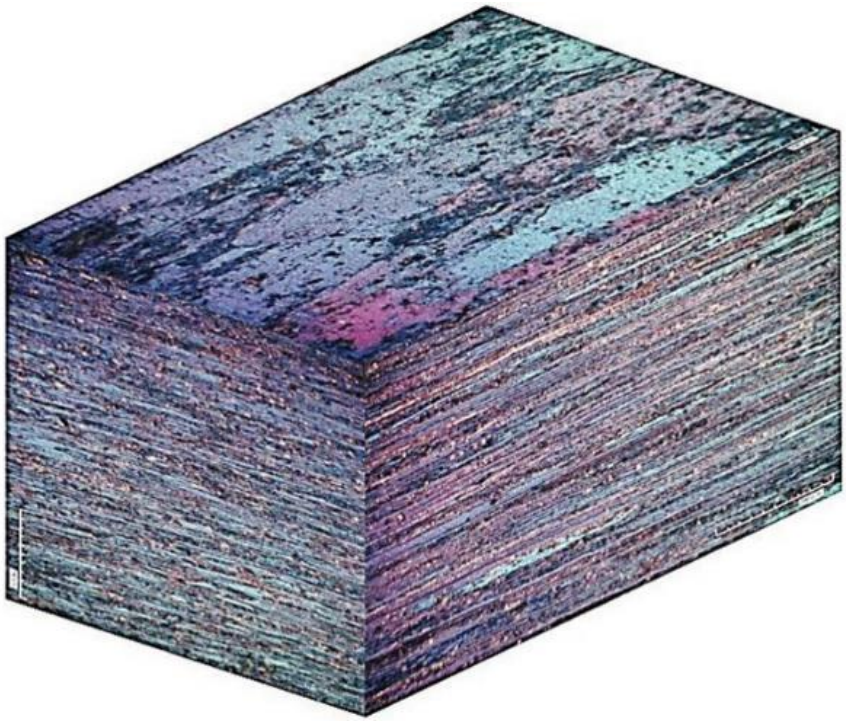

(a)

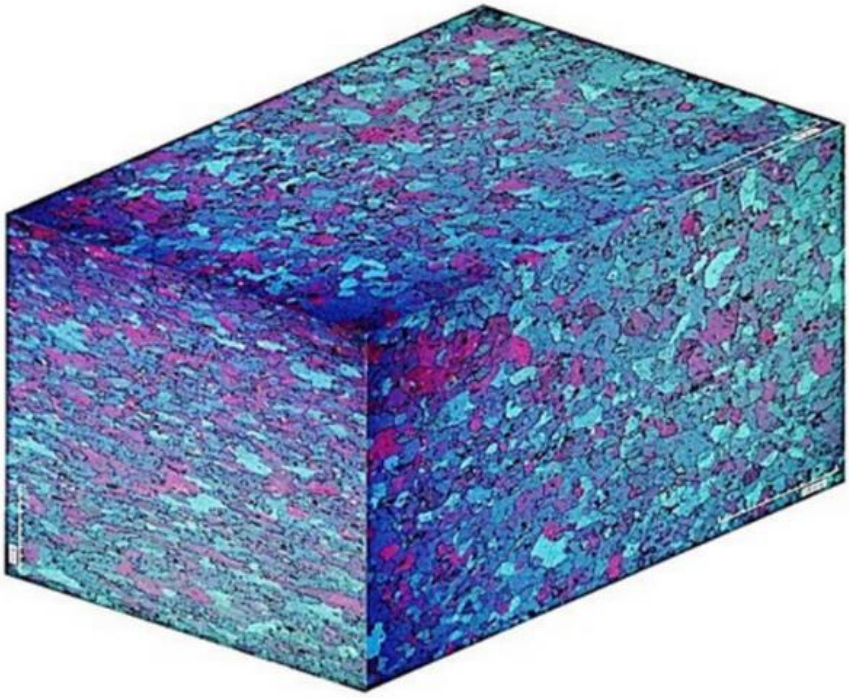

(b)

Fig. 58. AA5083-H116 (a) as-received grain structure (d = 89 μm) and (b) recrystallized grain structure (d = 48 μm).

The linear/uniform impingement MPM model is given by

$$X_{RX} = 1 - \exp\left(-\frac{\pi L}{4N_0^2}[K^2 + 2(K+1)\exp(-K) - 2]\right) \tag{96}$$

where X_{RX} is the recrystallized fraction (one corresponds to completely recrystallized), L is the total recrystallization nuclei array length per unit volume, N_0 is the total nuclei per unit array length, and $K = 2R_gN_0$. R_g is the grain growth radius function given by

$$\frac{dR_g}{dT} = \frac{v_0}{B}\exp\left(-\frac{Q_g}{RT}\right) \tag{97}$$

where v_0 is a pre-exponential constant (mathematically defined as velocity at infinite temperature) and Q_g is the activation energy of the rate controlling process for grain boundary growth.

An empirical recrystallized grain growth relation based on experimental data for cold-deformed Al alloys [83] was implemented

$$\langle\lambda\rangle = d_{RX}X_{RX}^{1/2} \tag{98}$$

where d_{RX} is the grain size in the recrystallized state.

5.2.1.2 Residual Yield Strength Model

AA5083-H116 derives its strength from Mg in solid solution and grain structure refinement from cold-work during material processing. During a fire exposure, the evolving microstructure due to recovery affects the subgrain strengthening contributions and recrystallization affects the subgrain and grain strengthening contributions. Solution hardening is assumed constant due to negligible precipitation (see Chapter 2 and 3 for details). Refer to Chapter 3 for a more detailed derivation of the residual yield strength model.

The yield strength includes the strengthening contributions of (i) the friction stress (σ_0), (ii) the solid solution content (σ_{ss}), (iii) grains ($\Delta\sigma_g$), and (iv) subgrains ($\Delta\sigma_{sg}$). These are linearly superposed to calculate the total yield strength (σ_y) as:

$$\sigma_y = \sigma_0 + \sigma_{ss} + \Delta\sigma_{sg} + \Delta\sigma_g \tag{99}$$

Linear superposition is assumed valid as the individual microstructural features strengthen at different length scales, thus there is negligible interaction. Subgrain strengthening, $\Delta\sigma_g$, is reduced by recovery and is annihilated by recrystallization; therefore, recovery (X_{RV} in Eq. (93)) and recrystallization (X_{RX} in Eq. (96)) models were implemented. Grain strengthening, $\Delta\sigma_g$, is solely dependent on recrystallization (X_{RX} in Eq. (96)).

The complete non-isothermal residual yield strength model is given by

$$\sigma_y = \sigma_0 + H\left(C_{Mg}\right)^n + \left[X_{RX}^{3/4} k_g d_{AR}^{-1/2} + (1 - X_{RX}) k_g d_{AR}^{-1/2}\right] + (1 - X_{RX}) G\sqrt{b\theta_m}\left(\frac{\delta_{AR}}{X_{RV}^2}\right)^{-1/2} \tag{100}$$

The first parameter on the right hand side is the friction stress assumed as that for AA1050 which includes the additional effects of Fe and Si solutes [98]. The second parameter is from the solid solution strengthening model. The bracketed parameter group incorporates grain strengthening with the first and second terms representing grain nucleation and growth, and grain annihilation, respectively. Both processes are a function of recrystallized fraction, X_{RX}. The fifth term on the right hand side implements subgrain strengthening, including subgrain coarsening as a function of X_{RV} and subgrain annihilation due to recrystallization as a function of X_{RX}.

The non-isothermal residual yield strength model was developed in Chapter 3. In the as-received state, the strength contributions are calculated as σ_0 = 19.3 MPa, σ_{ss} = 74.7 MPa, $\Delta\sigma_{sg}$ = 158 MPa, and $\Delta\sigma_g$ = 23 MPa, resulting in $\sigma_{y,AR}$ = 275 MPa. In the recrystallized condition, σ_0 = 19.3 MPa, σ_{ss} = 74.7 MPa, $\Delta\sigma_{sg}$ = 0 MPa, and $\Delta\sigma_g$ = 31.7 MPa, resulting in $\sigma_{y,RX}$ = 125.7 MPa. These values agree well with the experimentally measured values $\sigma_{y,AR}$ = 278 MPa and $\sigma_{y,RX}$ = 122 MPa.

5.2.1.3 Residual Strain Hardening Model

A strain hardening model based on the microstructural features of AA5083-H116 was developed in Chapter 3. This model was developed with the residual yield strength model to provide a complete description of residual elasto-plastic behavior after fire exposure.

Aluminum alloy strain hardening is due to the competitive evolution of the dislocation structure in terms of dislocation storage and dynamic recovery (dislocation annihilation or rearrangement) [68–70]. The Kocks-Mecking-Estrin (KME) model [68–70] links the evolution in dislocation density, ρ, to the local plastic shear strain, γ. Verdier, *et al.* [27] modified the classical KME relation to account for the effects of subgrains on Al alloy strain hardening. Additional terms related to subgrain dislocation storage and dynamic recovery are added to the classical KME relation, resulting in [27]

$$\frac{d\rho}{d\gamma} = k_1\sqrt{\rho} + k - \left(k_2 + \frac{K_{sg}}{\delta}\right)\rho \tag{101}$$

where $k_1 = 1/b$ accounts for dislocation storage due to obstacle (i.e., solute) pinning, $k = 1/b\delta$ accounts for the additional dislocation storage of subgrain boundaries, $k_2 = L_0/b$ accounts for dynamic recovery of dislocations by mutual annihilation [71] (L_0 is the mean annihilation distance for a dislocation pair of opposite sign), and K_{sg}/δ adds the dynamic recovery from subgrains to the relation. K_{sg} is approximately proportional to the subgrain boundary volume fraction [27], thereby describing the dynamic recovery efficiency of the subgrain structure.

The modified KME relation in Eq. (101) was combined with the relation for dislocation hardening ($\sigma = M\alpha Gb\sqrt{\rho}$) and the Taylor factor (i.e., $M = \sigma/\tau = \gamma/\varepsilon$), resulting in

$$\frac{d\sigma}{d\varepsilon} = \theta_0 + \frac{P_1}{\sigma} - P_2\sigma \tag{102}$$

where P_1 represents subgrain dislocation storage and P_2 is total dynamic recovery. P_1 and P_2 were modified to include subgrain annihilation during recrystallization as

$$P_1 = (1 - X_{RX})M^3(\alpha G)^2\frac{b}{2\delta} \quad \text{and} \quad P_2 = \frac{\theta_0}{\sigma_{sat,0}} + (1 - X_{RX})\frac{K_{sg}M}{2\delta} \tag{103}$$

where M is the Taylor factor, α is a material dependent constant normally 0.15 – 0.5 [99], δ is the subgrain size predicted by Eq. (95), $\theta_0 = M^2\alpha Gbk_1/2$ is the Stage II hardening rate, and $\sigma_{sat,0} = M\alpha Gbk_1/k_2$ is the saturation stress. Note, the relations for θ_0 and $\sigma_{sat,0}$ are defined for pure FCC metals. θ_0 is assumed constant as the baseline material state, defined as that experimentally

measured in the recrystallized state. After recrystallization completes, the modified KME strain hardening law effectively reduces to the classical KME relation.

5.2.1.4 Model Parameters

The model parameters for the AA5083-H116 models, i.e., microstructural evolution, residual yield strength, and strain hardening, for residual constitutive behavior after fire are provided in

Table 15. Details of parameter identification are provided in Chapter 3.

Table 15. AA5083-H116 residual constitutive model parameters.

Parameter	**Significance**	**Value**	**Source**
K_0	Pre-exponential term to recovery model	2 x 10^6 1/s	σ_y from tests at 20°C/min (Fig. 30a)
Q_0	Activation energy for recovery (self-diffusion)	124 kJ/mol	[9,84]
κP_0	Apparent activation energy constant	50 kJ/mol	σ_y from tests at 20°C/min (Fig. 30a)
δ_{AR}	As-received subgrain size	376 nm	Lineal intercept of Fig. 23
Q_g	Activation energy for grain boundary growth	182 kJ/mol	DSC
v_0	Pre-exponential term for grain growth rate	5 x 10^{15} 1/s	Normalized σ_y over RX (Fig. 32a)
L	Total array length per unit volume	280 mm^{-2}	Section 3.5.2
N_0	Total recrystallization nuclei per unit array length	15 mm^{-1}	Section 3.5.2
d_{RX}	Recrystallization grain size	48.2 μm	Lineal intercept of Fig. 25
σ_0	Friction stress including Fe, Si solutes	19.3 MPa	AA1050 [98]
H	Constant for effect of Mg solutes on σ_{ss}	13.8 MPa/(Mg wt%)^n	[98]
n	Hardening exponent for Mg solutes	1.14	[98]
k_g	Hall-Petch constant for grain strengthening	0.22 MPa-$m^{0.5}$	[35]
d_{AR}	As-received grain size	89 μm	Lineal intercept of Fig. 24
G	Shear modulus	26400 MPa	
b	Magnitude of Burger's vector	0.286 nm	
θ_m	Mean misorientation angle of subgrains	2.7°	[34]

(Table 15 continued on next page)

Parameter	Significance	Value	Source
δ_{AR}	As-received subgrain size	376 nm	Lineal intercept of Fig. 23
M	Taylor factor	3.07	[98]
α	Constant linking dislocation density to shear stress	0.3	[27]
L_0	Distance between two moving dislocations of opposite sign	16.6 nm	Mean value from Eq. (52) for 20°C/min tests
K_{sg}	Efficiency of dislocation walls for dislocation annihilation	1030 nm	Least squares fit to data in Fig. 37 and Eq. (52)
θ_0	Stage II hardening rate	5000 MPa	θ of 20°C/min tests in RX state

5.2.2 AA6061-T651 Constitutive Model

5.2.2.1 Precipitate Nucleation, Growth, and Dissolution Model

AA6061-T651 primarily drives its strength from a fine dispersion of Mg-Si precipitates (β″ phase) in the material. Some strength is also provided by the un-precipitated Mg and Si solutes in solid solution. During a fire exposure, the precipitates state evolves thereby altering the precipitate-dislocation interactions governing material constitutive behavior.

As-received AA6061-T651 contains a precipitate size distribution (PSD) defined by needle-like β″ precipitates with a distribution of radii (mean = 2.0 ± 0.3 nm [3]) and lengths (mean = 23.5 ± 3.9 nm). The resulting precipitate volume fraction is f_v = 1.6% [3]. The as-received precipitate state is shown in Fig. 59a. The as-received PSD (Fig. 59b) was adapted from Simar, *et al.* [38]. The PSD evolves during a fire exposure primarily by coarsening and dissolution. Heating to 400°C at 30°C/min results in a mean precipitate radius of 21 ± 3 nm and f_v = 1.1 ± 0.1% [115]. Refer to Chapter 4 for further details.

Classical nucleation and growth theories (CNGTs), such as the Kampmann-Wagner numerical (KWN) model, have been widely used to model PSD evolution at elevated temperatures. The KWN model implementation of Simar, *et al.* [38] was adapted for AA6061-T651. The principal model assumptions are that precipitates are single phase, i.e., assumed Mg_2Si, and spherical, thus simplifying the diffusion-based kinetics. The PSD (Fig. 59b) was modeled using an Eulerian class

size approach implemented in a finite difference framework [114]. The solid state diffusion-based KWN model includes relations for nucleation and growth/dissolution.

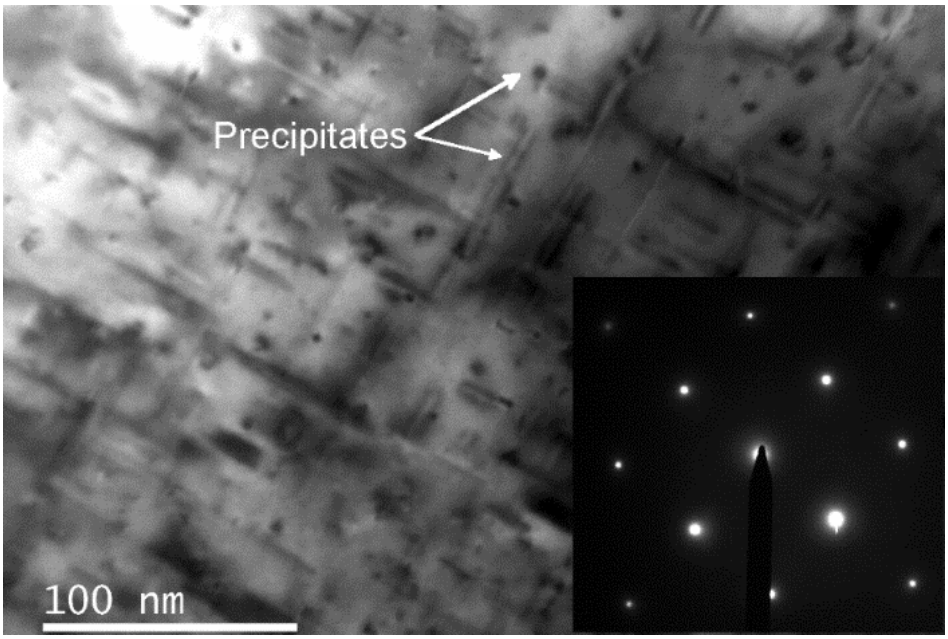

(a)

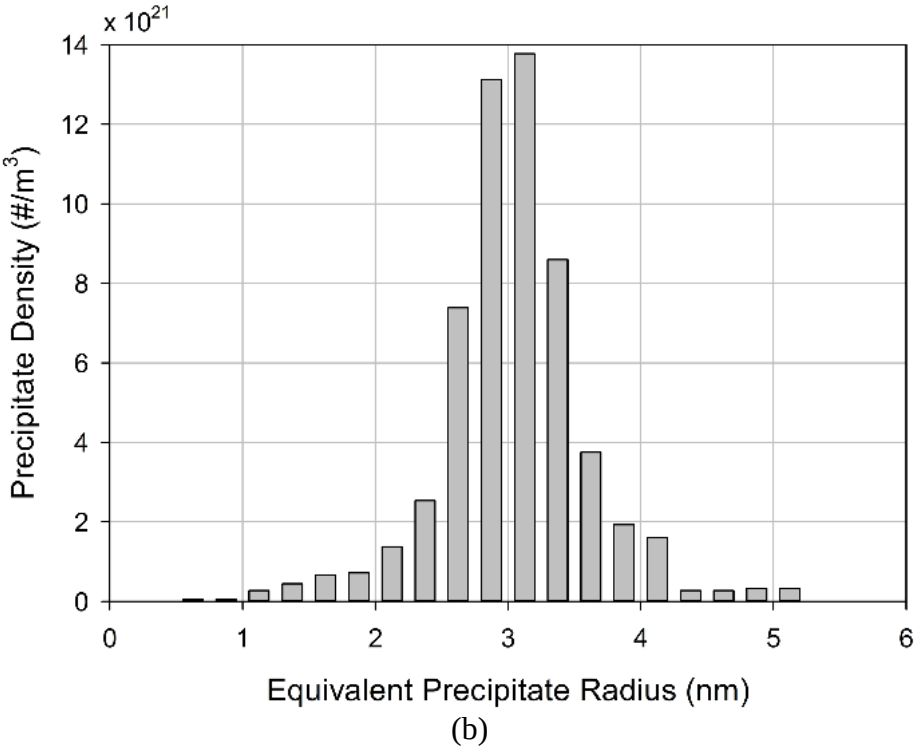

(b)

Fig. 59. AA6061-T651 as-received (a) precipitate state imaged using TEM and (b) the adapted precipitate size distribution, considering all precipitate lengths are equal to the mean length [38].

The steady state precipitate nucleation rate neglecting incubation time is expressed as

$$j = \frac{dN}{dt} = j_0 \exp\left[-\frac{A_0^3}{(RT)^3\left[\ln\left(C_{Mg}/C_{Mg}^{eq}\right)\right]^2}\right]\exp\left(-\frac{Q_d}{RT}\right) \tag{104}$$

where j_0 is the pre-exponential nucleation constant, A_0 is a parameter related to the energy barrier for nucleation, C_{Mg} is the mean Mg solute content in the matrix, C_{Mg}^{eq} is the equilibrium Mg concentration at the precipitate/matrix interface, and Q_d is the activation energy for Mg diffusion. The dependence of C_{Mg}^{eq} on temperature is given by an Arrhenius relationship

$$C_{Mg}^{eq} = C_{Mg,0}^{eq}\exp\left(-\frac{Q_{eq}}{RT}\right) \tag{105}$$

where $C_{Mg,0}^{eq}$ is a pre-exponential equilibrium constant and Q_{eq} is the apparent solvus boundary enthalpy.

The diffusion based precipitate growth/dissolution rate is given by the Whelan formalism as

$$v = \frac{dr}{dt} = \frac{1}{r}\frac{\left(C_{Mg} - C_{Mg}^{i}\right)}{\left(C_{Mg}^{p} - C_{Mg}^{i}\right)}D_0\exp\left(-\frac{Q_d}{RT}\right) \tag{106}$$

where r is the precipitate radius, C_{Mg}^{p} is the precipitate Mg concentration, C_{Mg}^{i} is Mg concentration at the precipitate/matrix interface, and D_0 is the pre-exponential diffusion constant. Precipitate dissolution occurs if $C_{Mg} < C_{Mg}^{i}$ (r decreases) and grows if $C_{Mg} > C_{Mg}^{i}$ (r increases). The interface concentration is given by the Gibbs-Thomson equation, which in the case of binary precipitates is given by

$$C_{Mg}^{i} = C_{Mg}^{eq}\exp\left(\frac{2\gamma V_m}{rRT}\right) \tag{107}$$

where γ is the precipitate/matrix interface energy and V_m is the molar volume of the precipitate. The radius of nucleated precipitates may be deduced from the above set of equations. Assuming precipitation occurs at $C_{Mg} = C_{Mg}^{i}$ (i.e., $dr/dt = 0$) and solving for r in Eq. (107) results in

$$r_c = \frac{2\gamma V_m}{\ln\left(C_{Mg}/C_{Mg}^{eq}\right) RT} \tag{108}$$

where r_c is the critical radius of precipitate nucleation.

The continuity equation for the precipitate number density in a single class size, i.e., a single bin in Fig. 59b, is given as

$$\frac{\partial N_i}{\partial t} = -\frac{\partial (N_i v_i)}{\partial t} + j \tag{109}$$

where the *i* subscript represents the given parameter for a single class. This is linearized with time assuming a timestep of Δt. The continuity equation allows for interactive growth in the number of PSD class sizes with precipitate coarsening. Also, an adaptive timestep is defined based on the maximum dissolution/growth rate. Further details, including implementation of the Eulerian class size approach, are given in Chapter 4.

The volume fraction of precipitates, f_v, is defined as

$$f_v = \sum_i \frac{4}{3}\pi r_i^3 N_i \tag{110}$$

The Mg concentration in the matrix, C_{Mg}, is calculated in terms of f_v as

$$C_{Mg} = \frac{C_{Mg}^0 - C_{Mg}^p f_v}{1 - f_v} \tag{111}$$

where C_{Mg}^0 is the total Mg concentration in the alloy, assuming all Mg will precipitate as Mg_2Si precipitates. The mean precipitate radius, $\bar{r}$, is calculated as

$$\bar{r} = \frac{\sum_i r_i N_i}{\sum_i N_i} \tag{112}$$

5.2.2.2 Residual Yield Strength Model

AA6061-T651 derives its strength primarily from precipitate-dislocation interactions. The Mg and Si solutes remaining in solid solution also contribute somewhat via solid solution strengthening.

During fire exposure, the evolving PSD, predicted by the KWN model, effectively alters the precipitate-dislocation interaction.

The yield strength includes the strengthening contributions of (i) the friction stress (σ_0), (ii) the solid solution content ($\Delta\sigma_{ss}$), and (iii) precipitates ($\Delta\sigma_p$). Grain contributions and dislocation forest contributions are considered negligible. These are linearly superposed to calculate the total yield strength (σ_y) as:

$$\sigma_y = \sigma_0 + \Delta\sigma_{ss} + \Delta\sigma_p \tag{113}$$

Linear superposition is assumed valid as the individual microstructural features strengthen at different length scales, thus there is negligible interaction. The friction stress of AA6061-T651 is taken as the commonly accepted 10 MPa. Solid solution, $\Delta\sigma_{ss}$, and precipitate, $\Delta\sigma_p$, strengthening evolve due to precipitate nucleation, growth, and dissolution; the KWN model was implemented to account for these processes.

The solid solution strengthening contribution, $\Delta\sigma_{ss}$, is expressed as [136]

$$\Delta\sigma_{ss} = H_{Mg_2Si} C_{Mg}^{2/3} + H_{Cu} C_{Cu}^{2/3} \tag{114}$$

where H_{Mg_2Si} is a constant associated with equivalent Mg and Si solid solution strengthening, H_{Cu} is a constant associated with Cu solid solution strengthening, and C_{Cu} is the Cu concentration in the matrix. H_{Mg_2Si} is determined by a precipitate (Mg_2Si) concentration balance of H_{Mg} and H_{Si}

$$H_{Mg_2Si} = H_{Mg} + H_{Si}\left(\frac{100 - C_{Mg}^{p}}{C_{Mg}^{p}}\right) \tag{115}$$

where H_{Mg} and H_{Si} are associated with Mg and Si solid solution strengthening, respectively.

The precipitate strengthening contribution, $\Delta\sigma_p$, is defined assuming a dislocation has to overcome all obstacles during glide on a slip plane to induce a macroscopic strain. Implementing the Friedel statistical model [137] for precipitate spacing in the glide plane, $\Delta\sigma_p$ is expressed as [121]

$$\Delta\sigma_p = \frac{M}{b}\sqrt{\frac{3f_v}{2\pi}}\frac{\bar{F}}{\bar{r}} \tag{116}$$

where $\bar{F}$ is the mean obstacle strength calculated using a mean summation rule on a PSD class size basis, i.e., F_i is calculated for each N_i predicted by the KWN model.

The PSD may contain a distribution of weak, shearable and strong, non-shearable precipitates. For weak precipitates, F_i is proportional to r_i as long as it is smaller than a defined transition radius (r_{trans}) [121]

$$F_i = 2k_\Gamma Gb^2\left(\frac{r_i}{r_{trans}}\right) \tag{117}$$

where k_Γ is a line tension constant ~0.5 [138] and r_{trans} is a radius where the precipitate-dislocation interaction transitions from shearing to Orowan looping. r_{trans} generally corresponds to the precipitate radius at maximum strength (i.e., as-received in the T6 state) [38]. The above relation is extended to precipitates where $r_i > r_{trans}$ as

$$F_i = 2k_\Gamma Gb^2 \tag{118}$$

This relation represents a constant strengthening interaction independent of precipitate radius, such as that due to Orowan looping. The precipitate-dislocation strengthening interaction relations in Eqs. (117) and (118) are implemented in Eq. (116) such that the strengthening proportionalities with precipitate radius, i.e., $r^{1/2}$ for $r < r_{trans}$ and with $1/r$ for $r > r_{trans}$ [118–121], are maintained.

The complete non-isothermal yield strength model is given by

$$\sigma_y = \sigma_0 + H_{Mg_2Si}C_{Mg}^{2/3} + H_{Cu}C_{Cu}^{2/3} + \frac{M}{b}(2k_\Gamma Gb^2)^{-1/2}\sqrt{\frac{3f_v}{2\pi}}\frac{\bar{F}^{3/2}}{\bar{r}} \tag{119}$$

The governing parameters describing PSD evolution are the Mg concentration in the matrix, C_{Mg}, mean precipitate radius, $\bar{r}$, precipitate volume fraction, f_v, and mean precipitate strength, $\bar{F}$. These parameters are a function of the PSD predicted by the KWN model.

5.2.2.3 Residual Strain Hardening Model

A generalized strain hardening model for precipitation hardened Al alloys was adapted from Simar, *et al.* [38] for AA6061-T651 in Chapter 4. This model was developed with the residual yield strength model to provide a complete description of residual elasto-plastic behavior after fire exposure.

The KME relation is used as a basis for this model similar to that for AA5083-H116. Estrin [103] generalized the KME relation, introducing a new term to account for Orowan loop storage around non-shearable precipitates. Simar, *et al.* [38] further adapted this model to include precipitate size dependent effects which affect dislocation storage and dynamic recovery.

The generalized KME relation [103] is given in the Palm-Voce formalism [73,74] as

$$\frac{d\sigma}{d\varepsilon} = \theta - \beta\left(\sigma - \sigma_y\right) \tag{120}$$

where θ is the dislocation storage rate and β is the dynamic recovery rate. These parameters are generalized to account for the follow precipitate induced effects [38]:

- Orowan loop storage efficiency: a precipitate does not become instantly non-shearable during strain hardening when $r > r_{trans}$. A linear transition function, φ, is defined from r_{trans} to the loss of precipitate coherency (r_{cl}). The effects of precipitate radius on θ are included in the $(1/r)$ term in Eq. (121) by multiplication with φ.
- Dynamic precipitation: θ is modified by dynamic precipitation during strain hardening. An additional storage parameter, θ_{dp}, dependent on C_{Mg} is linearly added to θ_0 in Eq. (121), which is assumed as that for the alloy in a maximum precipitated state, i.e., T6 state.
- Orowan loop storage: β is calculated using a function based on the probability of encountering another precipitate with an Orowan loop, which would cause self-annihilation (dynamic recovery). Inclusion of φ accounts for the effects of Orowan loop storage efficiency on β.
- Yield strength effect on β: a dislocation pair annihilates when the interaction stress (Gb/y_a where y_a is the dislocation spacing) exceeds the yield strength. Thus, as σ_y increases, β decreases. For simplicity, a new term, β_0, is assumed inversely proportional to σ_y using the T6 state as a reference. This is included in the probabilistic function for β in Eq. (122).

Schematics are shown in Fig. 60 to elucidate the influence of the described precipitate induced effects on the dislocation storage rate, θ, and dynamic recovery rate, β.

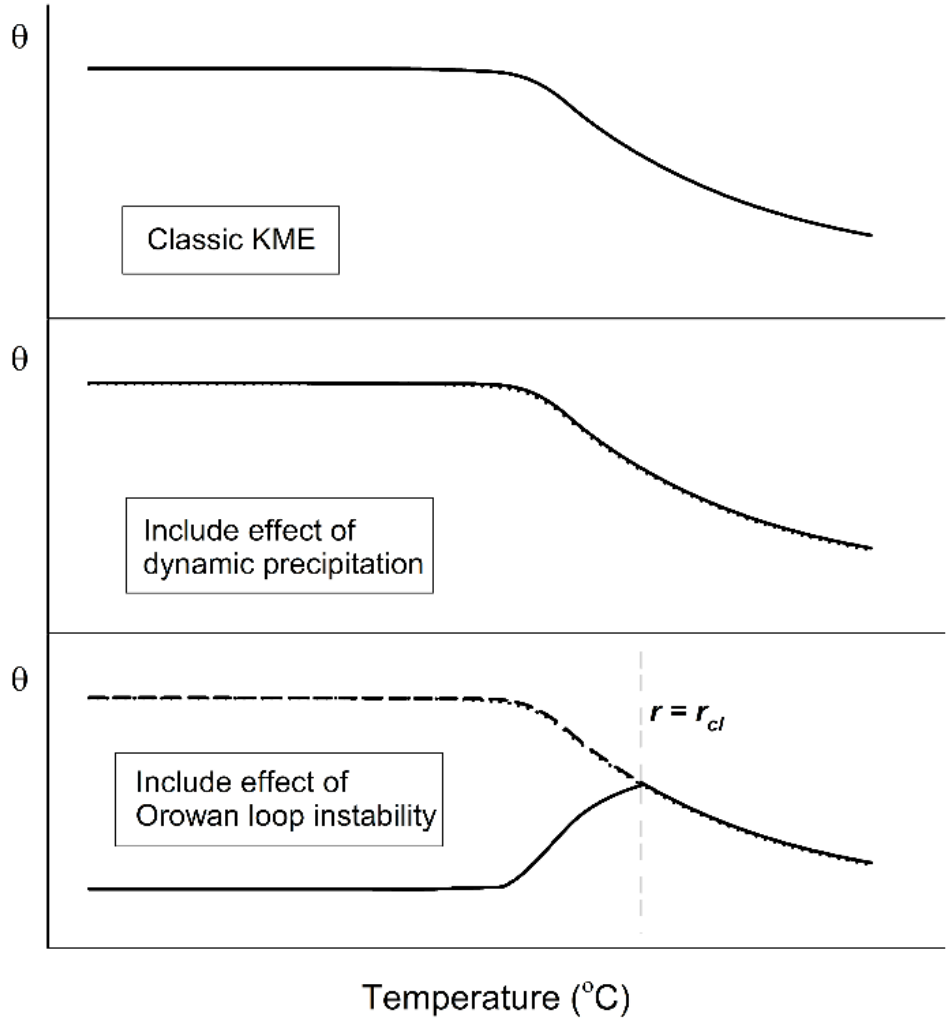

(a)

(Fig. 60 continued on next page)

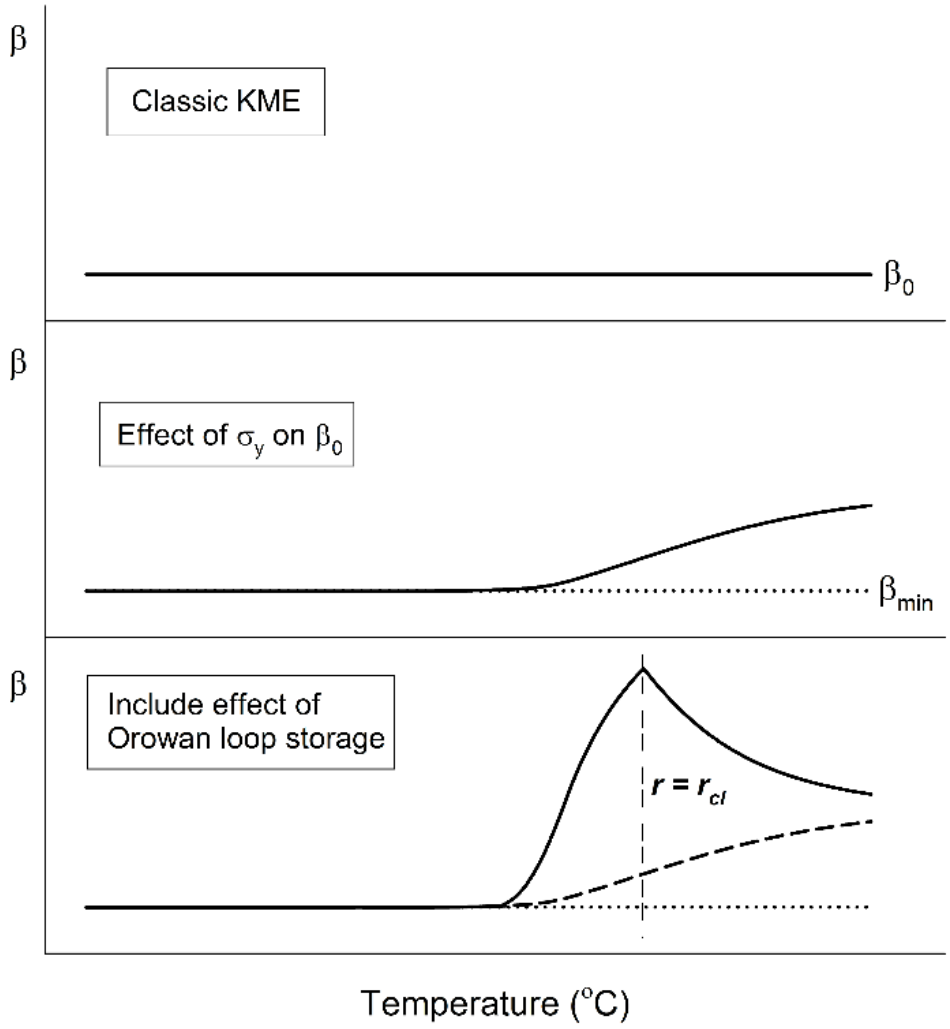

(b)

Fig. 60. Schematic of the effect of including precipitate-induced effects on the generalized KME parameters. A linear, constant thermal exposure at 20°C/min was used to develop the schematic.

Generalized θ and β relations for use in Eq. (120) are defined as

$$\theta = \frac{\theta_0 + \theta_{dp}}{2} + \sqrt{\left(\frac{\theta_0}{2}\right)^2 + \alpha^2 M^3 G^2 \beta \varphi \left(\frac{b}{\bar{r}}\right) \sqrt{\frac{3 f_v}{2\pi}}} \tag{121}$$

$$\beta = \beta_0 \exp\left(-\sqrt{\frac{3}{2\pi}} \frac{\sqrt{f_v} L_0 \varphi}{\bar{r}}\right) + \frac{2 y_p}{b}\left(1 - \exp\left(-\sqrt{\frac{3}{2\pi}} \frac{\sqrt{f_v} L_0 \varphi}{\bar{r}}\right)\right) \tag{122}$$

where L_0 is the mean of y_a, which is estimated using the dislocation hardening relation as $L_0 = 2M\alpha Gb\beta_{min}/\theta_0$ (β_{min} is β in the T6 reference state). y_p is the annihilation distance when at least one precipitate exists between dislocations of opposite sign. The mean precipitate radius, $\bar{r}$, and volume fraction, f_v, are calculated using the PSD predicted by the KWN model.

Details pertaining to model development are described in detail in Refs. [38,134]. Parameter relations in Eqs. (121) and (122) are reproduced from Ref. [38] for clarity. The Orowan loop storage efficiency, φ, is given as

$$\varphi = \frac{\bar{r} - r_{trans}}{r_{cl} - r_{trans}} \tag{123}$$

The dynamic precipitation dislocation storage contribution, θ_{dp}, is given by

$$\theta_{dp} = k_{\theta dp}\left(\frac{C_{Mg} - C_{Mg}^{eq}}{C_{Mg}^{0} - C_{Mg}^{eq}}\right) \tag{124}$$

where $k_{\theta dp}$ is an adjustable parameter based on solution heat treatment of the alloy. The inverse proportionality of β_0 in Eq. (122) with σ_y is given by

$$\frac{1}{\beta_{min}} - \frac{1}{\beta_0} = k_\beta\left(\frac{\sigma_y^{max} - \sigma_y}{G}\right) \tag{125}$$

where k_β is a constant evaluated using a solution heat treated specimen and σ_y^{max} is σ_y in the T6 reference state.

5.2.2.4 Model Parameters

The model parameters for the AA6061-T651 models, i.e., PSD evolution (KWN model), residual yield strength, and strain hardening, for residual constitutive behavior after fire are provided in

Table 16. Details of parameter identification are provided in Chapter 4.

Table 16. AA6061-T651 residual constitutive model parameters.

Parameter	**Significance**	**Value**	**Source**
r_{AR} $(mean)$	As-received equivalent radius	3.044 nm	Fig. 42 [38]
C_{Mg}^{0}	Mg content of AA6061-T651	0.90 wt%	Table 8
C_{Mg}^{p}	Mg content of Mg_2Si	63.4 wt%	[39]
A_0	Energy barrier for nucleation	18.6 kJ/mol	[38]
j_0	Pre-exponential nucleation constant	3 x 10^{37} #/m^3-s	[38]
V_m	Molar volume of Mg_2Si	3.95 x 10^{-5} m^3/mol	[39]
$C_{Mg,0}^{eq}$	Pre-exponential constant to C_{Mg}^{eq}	290 wt%	[40]
Q_{eq}	Apparent boundary solvus enthalpy	41 kJ/mol	[40]
D_0	Pre-exponential constant for Mg diffusion	1.24 x 10^{-4} m^2/s	[108]
Q_d	Activation energy for Mg diffusion	130.6 kJ/mol	[108]
γ	Precipitate/matrix interface energy	0.108 J/m^2	[115]
M	Taylor factor	2	Textured alloy [38]
G	Shear modulus	27 GPa	[37,39,40]
b	Magnitude of Burger's vector	0.286 nm	
σ_0	Friction stress of pure Al	10	[37,39,40]
H_{Cu}	Cu solid solution strengthening constant	46.4 MPa $wt\%^{2/3}$	[37,39,40]
H_{Mg}	Mg solid solution strengthening constant	29.0 MPa $wt\%^{2/3}$	[37,39,40]
H_{Si}	Si solid solution strengthening constant	66.3 MPa $wt\%^{2/3}$	[37,39,40]
r_{trans}	Precipitate strength transition radius	3.044 nm	Mean radius of PSD in Fig. 42
k_Γ	Line tension constant	0.40	σ_y in T6 state
θ_0	θ if no dynamic precipitation or Orowan loops	655 MPa	θ minimum in Fig. 51a
β_{min}	β at maximum σ_y	5.9	β minimum in Fig. 51a
$k_{\theta dp}$	Constant for θ_{dp} in Eq. (84) for dynamic precipitation effects	1210 MPa	θ for a solution heat treated sample and the AR material
σ_y^{max}	maximum yield strength (T6 state)	324 MPa	σ_y of as-received material
k_β	Constant linking σ_y to β	10.6	β for a solution heat treated sample and the AR material

(

Table *16* continued on next page)

Parameter	Significance	Value	Source
r_{cl}	Equivalent radius of loss of coherency	8 nm	$\bar{r}$ of θ and β transition in Fig. 54
L_0	Mean value of distance between two dislocations of opposite sign	42 nm	Eq. (92)
α	Constant linking shear stress to dislocation density	0.15	Optimized from θ of 20°C/min samples
y_p	Annihilation distance when at least one precipitate exists between dislocations of opposite sign	13 nm	Optimized from β of 20°C/min samples

5.3 Experimental

Experimental characterization of the residual constitutive behavior was reported in Chapter 2. The validation tests performed as part of this work used similar heating and mechanical testing methods as Chapter 2. The tensile specimen geometry (50.8 long, 12.7 wide gage section) is identical to that described in Chapter 2. The heating regimens were specifically selected to evaluate model performance for conditions sufficiently different from those used in development. Thus, specimens were heated at 50°C/min to prescribed temperatures, then isothermally held for varying lengths of time. The specimens were then quenched to arrest microstructural evolution. Five specimens were tested for each alloy. A specimen heating summary is provided in Table 17.

Table 17. Tensile mechanical testing specimen heating details.

Alloy	*T* (°C)	Hold (h)	Microstructural Effect
AA5083-H116	150	0.5	Recovery (minimal at *T* in previous tests)
	200	0.5	Recovery
	250	2	Recovery → ~25% recrystallized
	275	0.5	Recovery → ~60% recrystallized
	300	0.5	Just prior to recrystallization → fully recrystallized
AA6061-T651	250	0.5	Low *T* – negligible PSD evolution
	250	2	Low *T* – notable overaging
	275	0.5	Mid *T* – notable overaging
	300	0.25	Mid *T* – significant overaging at short times
	350	0.25	High *T* – massive overaging

Uniaxial, quasi-static tension tests were performed at ambient conditions on previously heated samples using an Instron 5984 150 kN electro-mechanical testing machine. The tensile tests were

performed at a constant displacement rate of 3.048 mm/min, corresponding to an initial strain rate of 10^{-3}/s. Deformation was measured using a 25.4 mm gage length extensometer (+50%/-10% strain range) centered on the highest temperature measured during heating (refer to Chapter 2 for details).

5.4 Model Validation

The tensile mechanical tests of previously heated specimens (refer to Table 17) were conducted to validate the constitutive models for residual mechanical behavior after fire exposure. Model validation was performed by comparing predicted and experimental residual yield strengths and strain hardening behavior.

5.4.1 AA5083-H116 Model Validation

AA5083-H116 constitutive model residual yield strength predictions are compared with validation experiments in Table 18. The model predicts the residual yield strength within a mean error of 6%. Higher errors (10 and 14%) resulted for specimens with heating intended to partially recrystallize the material. As noted in Chapter 2 and 3, recrystallization occurs over a very narrow range in temperatures (~50°C independent of heating rate). Thus, slight deviations in model kinetics from that in the material may result in significant errors in residual yield strength prediction. For example, heating at 20°C/min may result in a 100 MPa difference (~80% error) for kinetics predictions that deviate by only 10°C (see Chapter 3). By this metric, the model predicts the residual yield strength exceptionally.

Table 18. AA5083-H116 constitutive model validation summary for specimens heated at 50°C/min to prescribed temperatures then isothermally soaked.

T (°C)	**Hold (h)**	**Exp. σ_y (MPa)**	**Pred. σ_y (MPa)**	**Error (%)**	X_{RV}	X_{RX}
150	0.5	257	255	1	0.87	0
200	0.5	243	238	2	0.76	0
250	2	222	191	14	0.56	0.23
275	0.5	176	158	10	0.58	0.64
300	0.5	119	126	5	0.51	1

The time-resolved evolution of the predicted residual yield strengths are shown in Fig. 61. The shown specimens were heated to 250 and 300°C and isothermally soaked for 2 h and 0.5 h,

respectively. Upon reaching 250°C, the rapid decrease in residual yield strength due to increasing temperature (at 50°C/min) significantly slows due to the transition to an isothermal exposure. The yield strength reduction is purely due to subgrain recovery until about 2600 s at which point recrystallization initiates. This is evident as a slight downward inflection. The specimen heated to 300°C evolves by a much simpler process. Recrystallization initiates almost immediately after the isothermal soak at 300°C has begun. Recrystallization completes after about 1000 s.

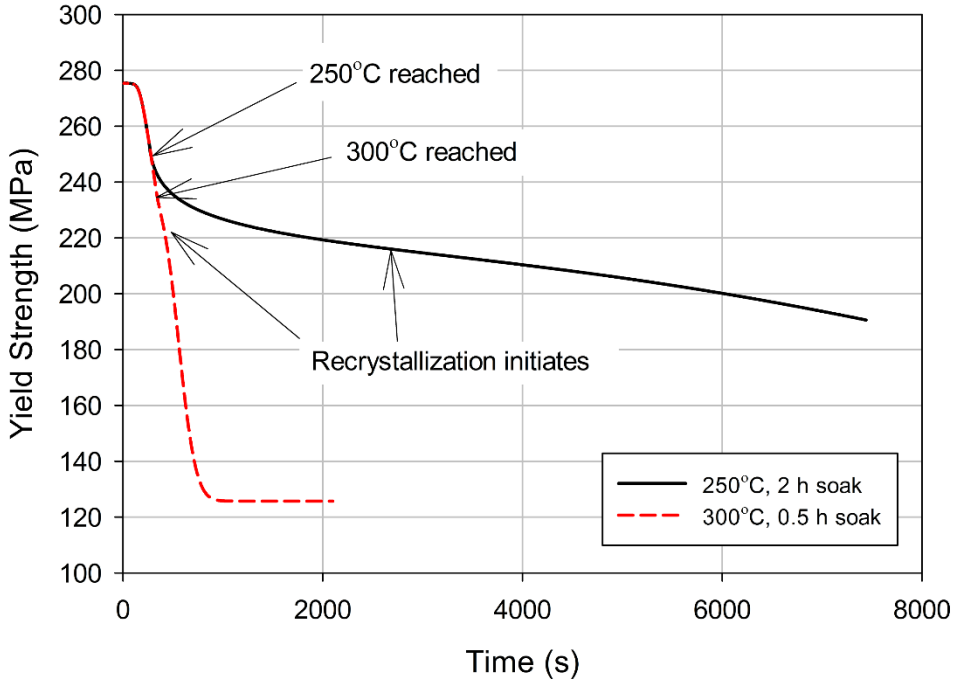

Fig. 61. Predicted time-resolved residual yield strength evolution for AA5083-H116 specimens heated at 50°C/min to 250°C (2 h isothermal soak) and 300°C (0.5 h isothermal soak).

AA5083-H116 strain hardening model predictions are compared against validation experiments in Fig. 62. As discussed in Table 17, several microstructural features were explored in testing, including pure recovery (Fig. 62b,c), extended recovery with partial recrystallization (Fig. 62d,e), and rapid recrystallization during an isothermal soak (Fig. 62f). The model predicts the measured behavior well. The decrease in initial plastic slope (θ) as recovery and recrystallization progresses is well represented. The model also predicts the increased plastic capacity, i.e., nearly constant σ_{sat}, with increasing recovery and recrystallization. This is noted in Chapters 2 and 3 where the ultimate strength is relatively unchanged with AA5083-H116 microstructural evolution. This demonstrates the capabilities of the model in predicting AA5083-H116 strain hardening behavior

after fire exposure regardless of thermal exposures details, including isothermal, non-isothermal, and any combination thereof.

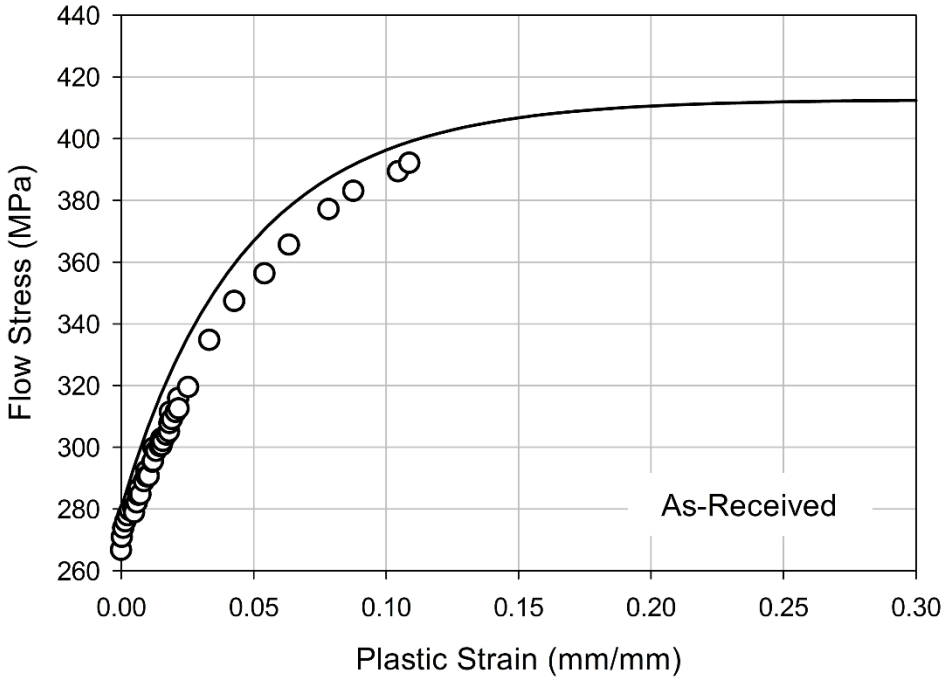

(a)

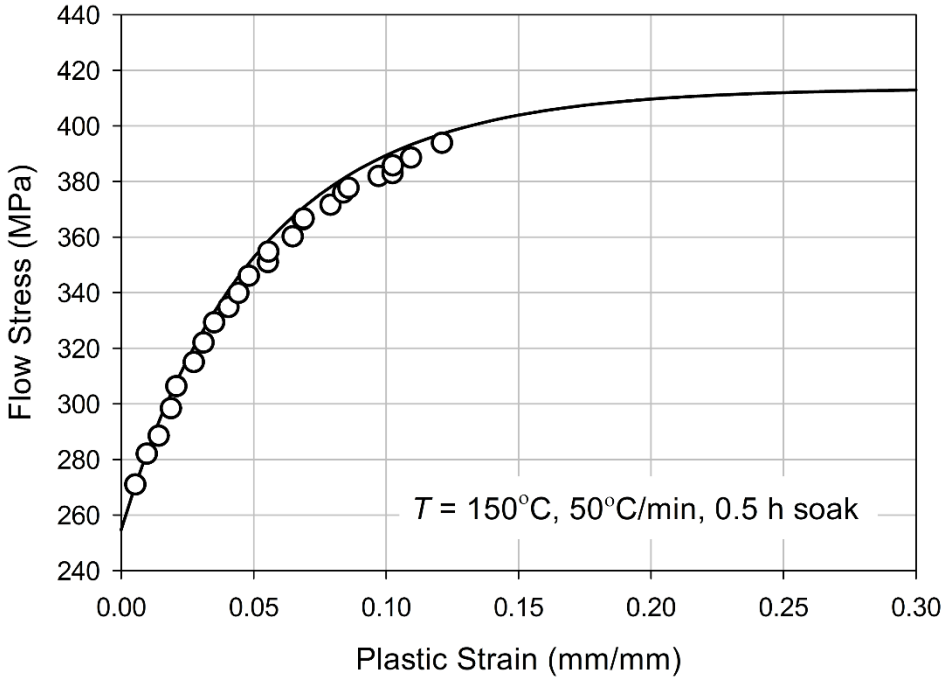

(b)

(Fig. 62 continued on next page)

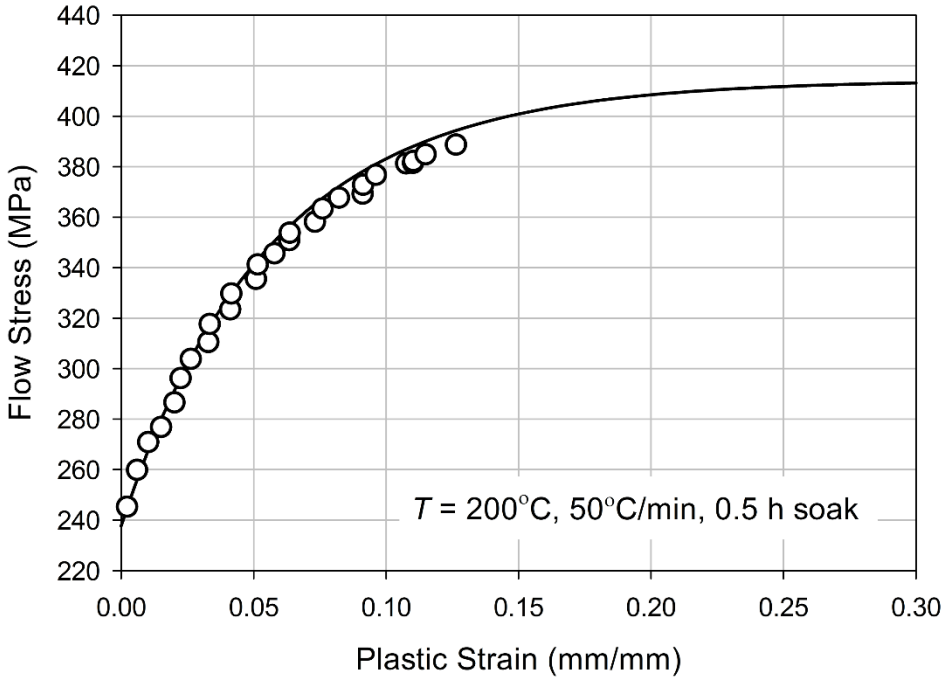

(c)

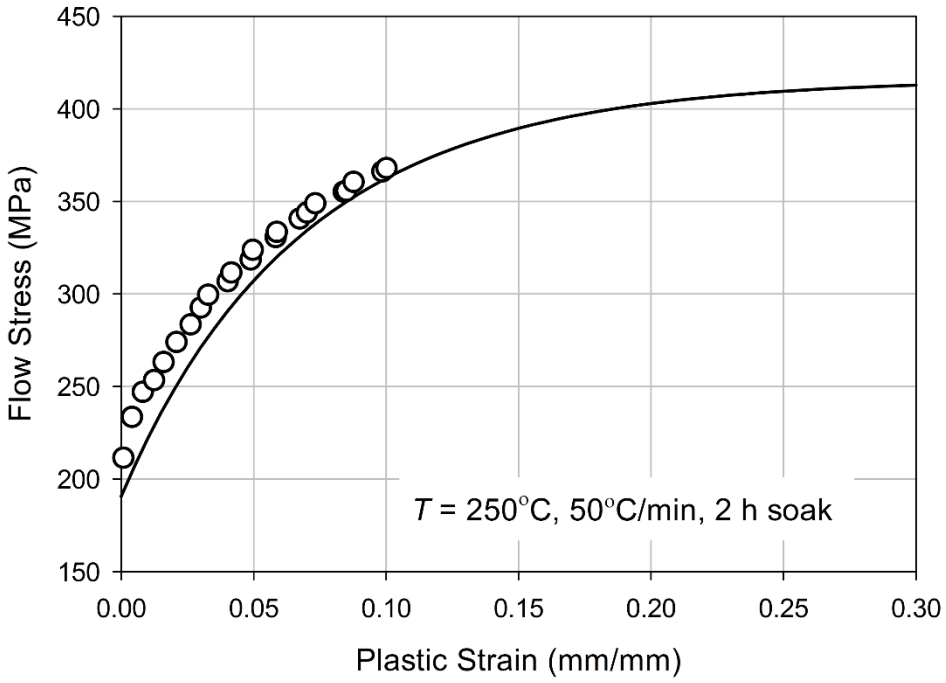

(d)

(Fig. 62 continued on next page)

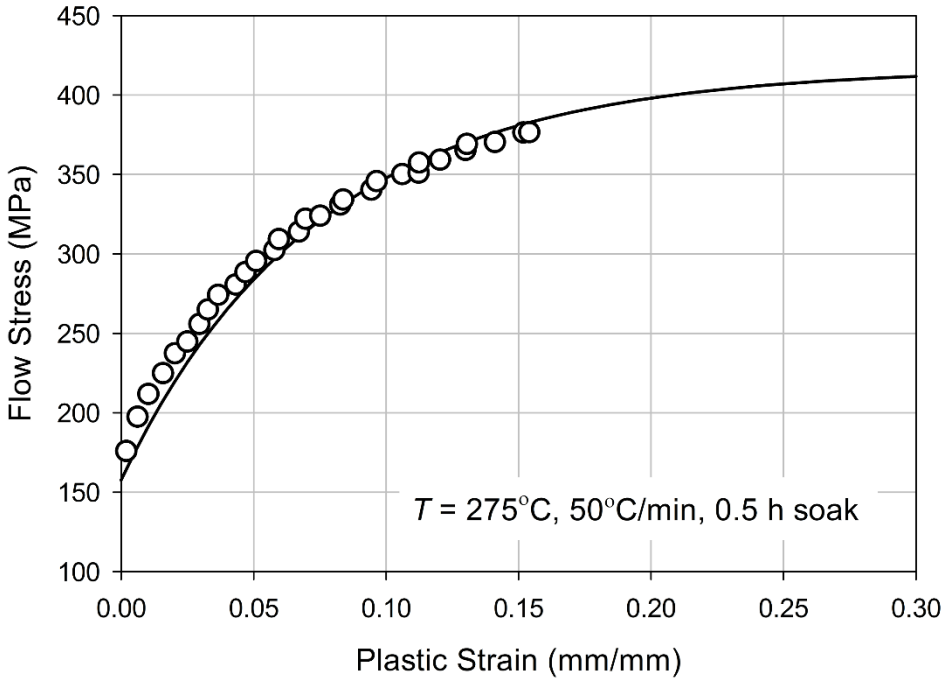

(e)

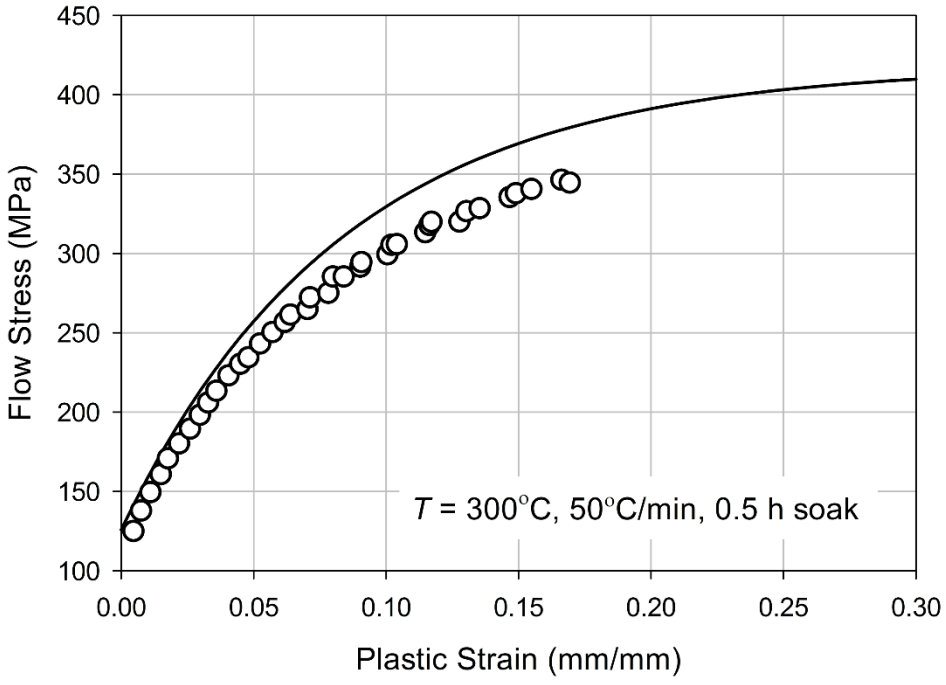

(f)

Fig. 62. AA5083-H116 strain hardening model predictions compared against validation experiments.

5.4.2 AA6061-T651 Model Validation

AA6061-T651 constitutive model residual yield strength predictions are compared with validation experiments in Table 19. The model predicts residual yield strength within a mean error of 11%. Higher errors occur for lower temperature exposures, notably for the specimen soaked at 250°C for 0.5 h (21% error). Similar behavior was observed during model verification for specimens heated at 5, 25, and 250°C/min with no isothermal soak (refer to Chapter 4). Residual yield strengths were predicted to be slightly higher than experiment, with higher error at lower temperatures. Despite this, the lower temperature (T < 350°C) predictions agree reasonably with experiment. Error in model predictions quickly diminishes with increasing temperature. This is reflected in model validation predictions, representing the remaining validation experiments well (mean error of 9% excluding 200°C, 0.5 h soak test). Thus, the residual yield strength model is validated with experiments not used in model development.

The time-resolved evolution of the predicted mean residual yield strengths is shown in Fig. 63. The shown specimens were heated to 250, 275, and 350°C and isothermally soaked for 2, 0.5, and 0.25 h, respectively. Heating to 250°C at 50°C/min causes negligible yield strength reduction (refer to Chapter 2 and 4) which is reflected by model predictions. The yield strength reduction rate (as a function of time) is significantly larger for isothermal heating at 350°C compared to 250°C. 275°C reduces at a rate about half way between these temperatures. This is directly related to the kinetics of precipitate growth and dissolution as described by the KWN model. Also, the increasing trend in predicted $\bar{r}$ after heating is comparable to that which logically corresponds to residual yield strength. This is expected due to the residual yield strength calculation being highly dependent on precipitate radius.

Table 19. AA6061-T651 constitutive model validation summary for specimens heated at 50°C/min to prescribed temperatures then isothermally soaked.

T (°C)	**Hold (h)**	**Exp. σ_y (MPa)**	**Pred. σ_y (MPa)**	**Error (%)**	**$\bar{r}$ (nm)**	**f_v (%)**
250	0.5	241	292	21	3.5	1.35
250	2	208	234	13	4.7	1.36
275	0.5	191	217	14	5.2	1.34
300	0.25	155	178	15	6.5	1.31
350	0.25	103	96	7	14.1	1.23

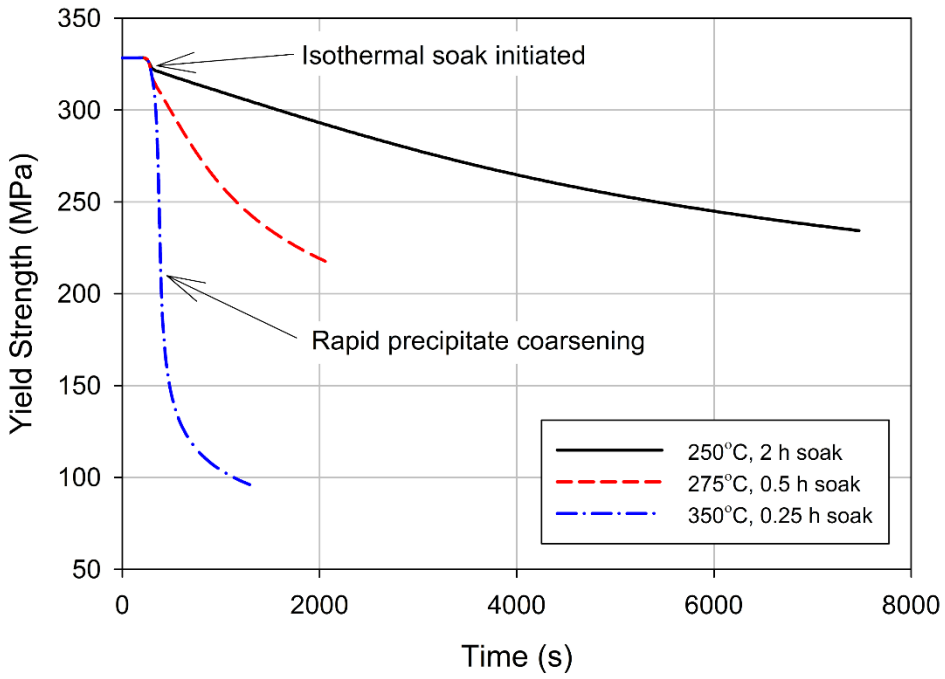

Fig. 63. Predicted time-resolved residual yield strength evolution for AA6061-T651 specimens heated at 50°C/min to 250°C (2 h isothermal soak), 275°C (0.5 h isothermal soak), and 350°C (0.25 h isothermal soak).

AA6061-T651 strain hardening model predictions are compared against validation experiments in Fig. 64. As discussed in Table 17, several microstructural states were explored in testing, including slightly overaged (Fig. 64b,c), significantly overaged (Fig. 64d,e), and massively overaged (Fig. 64f). These states were achieved using a variety of exposure temperatures and isothermal soak times. The measured behavior is well predicted by the strain hardening model. Note, the previously discussed error (~11% mean) in predicted versus measured residual yield strength causes the shift in initial flow stress, i.e., yield strength. Considering this apparent initial offset, the residual strain hardening behavior at different thermal exposures is well represented by the model. The increasing plastic slope (θ) with total thermal exposure (i.e., increasing from Fig. 64a to Fig. 64e) is captured effectively. Likewise, the dynamic recovery term is well captured as evidenced by the rate at which strain hardening saturates. This is depicted in Fig. 64 as the flow stress exponentially saturating, i.e., approaching σ_{sat}, at lower plastic strains. In the massively overaged state (Fig. 64f), θ is reduced while the saturation stress has increased. This is caused by the effects of significantly increased precipitate size on dislocation storage and dynamic recovery, as previously discussed. This observation is reflected by the schematic in Fig. 60. Thus, the

AA6061-T651 strain hardening model is validated for use in predicting residual strain hardening behavior after an arbitrary thermal exposure.

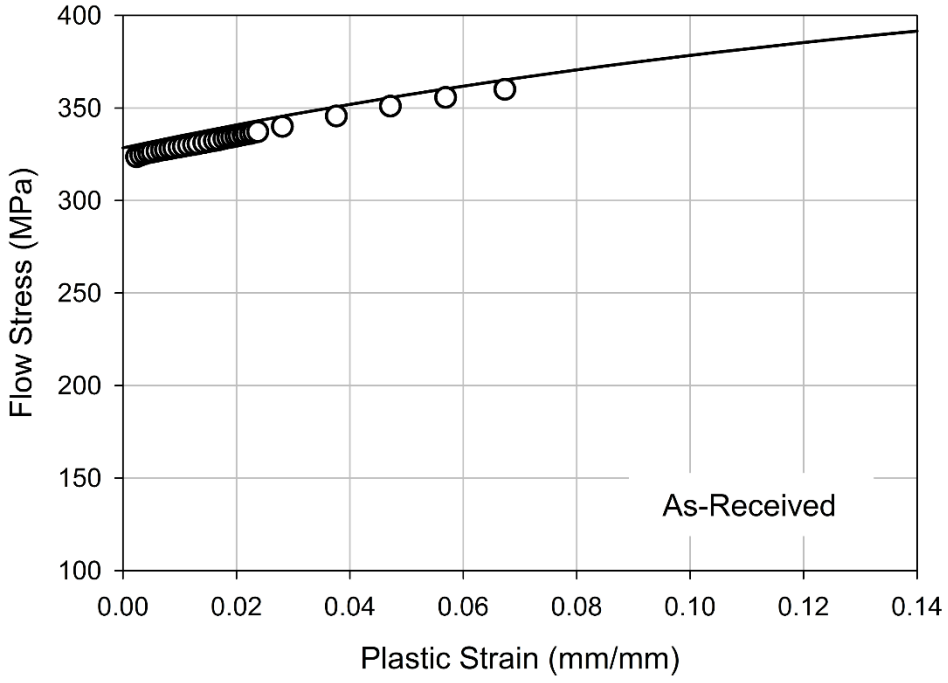

(a)

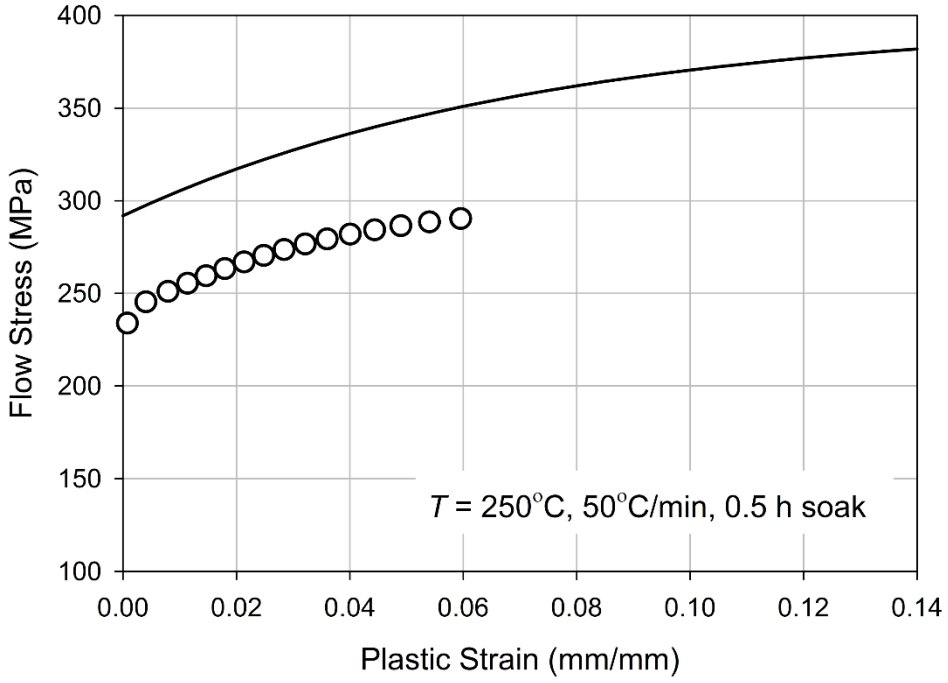

(b)

(Fig. 64 continued on next page)

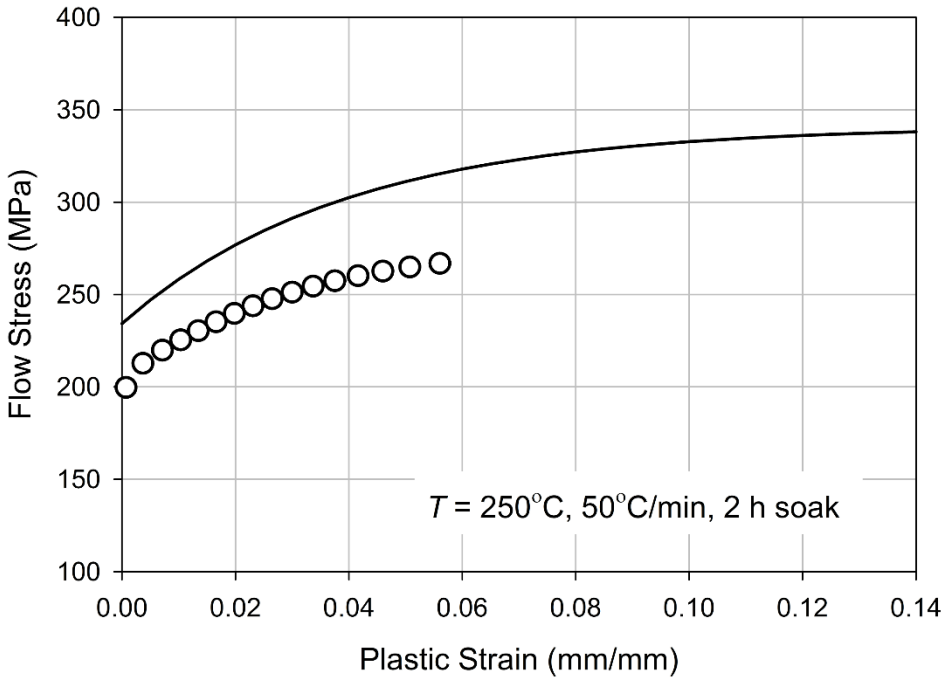

(c)

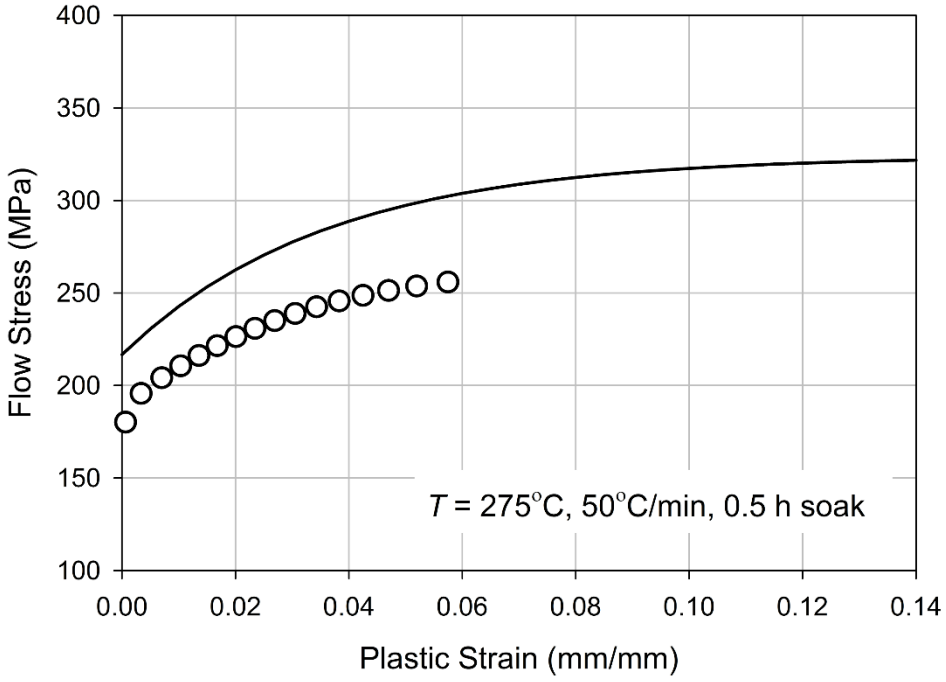

(d)

(Fig. 64 continued on next page)

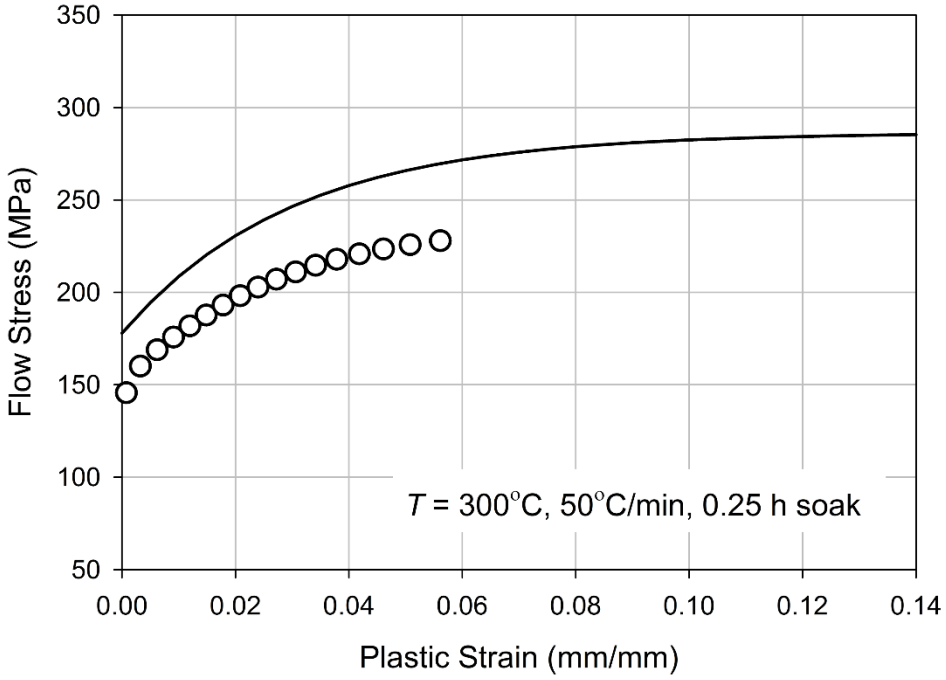

(e)

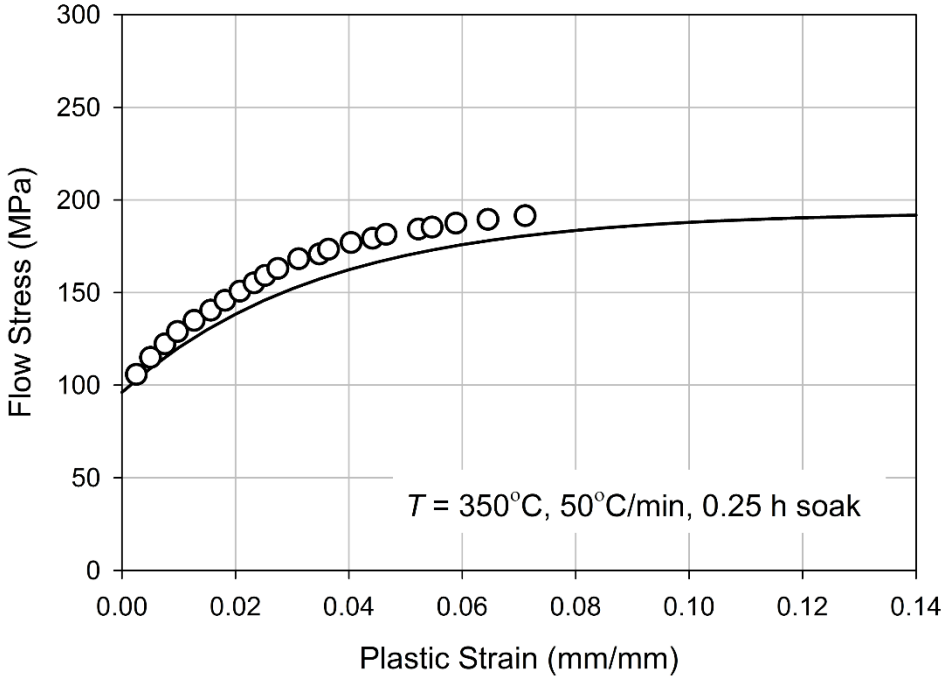

(f)

Fig. 64. AA6061-T651 strain hardening model predictions compared against validation experiments. Refer to Table 17 for details and microstructural evolution.

5.5 Conclusions

Constitutive models for the residual mechanical behavior of AA5083-H116 and AA6061-T651 after fire exposure have been presented in detail. The models present a sequentially coupled approach including distinct sub-models to predict residual mechanical behavior based on microstructural evolution. The constitutive models comprise mechanistic and phenomenological sub-models for (i) microstructural evolution, (ii) residual yield strength, and (iii) strain hardening after prior thermal exposure. The materials are strengthened by different mechanisms (AA5038-H116 – grain refinement from cold work and solid solution strengthening, AA6061-T651 – a distribution of fine precipitates from artificial aging). Thus, appropriate models are implemented to predict microstructural evolution using thermal exposures as the only required input. AA5083-H116 microstructural evolution was predicted using separate recovery and recrystallization kinetics models while AA6061-T651 required implementation of the KWN model to predict the PSD evolution. These models were used to predict evolution of the microstructural strengthening mechanisms, including their independent contributions to the residual yield strength. The strain hardening behavior is predicted using appropriate modifications of the KME constitutive law, which models the competitive evolution of dislocation storage and dynamic recovery during plastic straining. AA5083-H116 required implementation of additional terms for subgrain contributions; AA6061-T651 required modification to both dislocation storage and dynamic recovery, focusing on the efficiency of dislocation (Orowan) looping about a precipitate.

This paper presents the validation of the described constitutive models, thus supporting use of the models for arbitrary exposures such as those experienced in a real fire scenario. Heating regimens were selected such that the bounds of the model were tested while ensuring sufficient deviation from thermal exposures used in model development. AA5083-H116 model predictions well represented the validation experiments. Residual yield strength predictions had a mean error of about 6%. Residual strain hardening predictions also showed excellent agreement with experimental measurements. AA6061-T651 model predictions also well represented the validation experiments. Residual yield strength predictions had decreasing error with increasing thermal exposure time and temperature (mean error of ~11%). The residual strain hardening prediction also well represented experiments, with the evolving plastic slope and plastic capacity captured. Thus, the AA5083-H116 and AA6061-T651 constitutive models are shown capable of

predicting complete residual elasto-pastic mechanical behavior after fire exposure. Using these models, the residual mechanical behavior can be predicted with a given thermal exposure.

References

[1] Accessed 14 March 2014. <http://www.offshore-technology.com/contractor_images/bayards/5-bayards.jpg>., (n.d.).

[2] R.D. Matulich, Post-Fire Mechanical Properties of Aluminum Alloys and Aluminum Welds, Virginia Polytechnic Institute & State University, 2011.

[3] D. Maisonnette, M. Suery, D. Nelias, P. Chaudet, T. Epicier, Mater. Sci. Eng. A 528 (2011) 2718.

[4] C. Gallais, a. Simar, D. Fabregue, a. Denquin, G. Lapasset, B. Meester, Y. Brechet, T. Pardoen, Metall. Mater. Trans. A 38 (2007) 964.

[5] A. Simar, Y. Brechet, B. Demeester, A. Denquin, T. Pardoen, Mater. Sci. Eng. A 486 (2008) 85.

[6] Accessed 15 March 2014. <http://www.nopsema.gov.au/assets/images/imagegallery/Image%20A149248.jpg>., (n.d.).

[7] E.L. Huskins, B. Cao, K.T. Ramesh, Mater. Sci. Eng. A 527 (2010) 1292.

[8] G. Dieter, Mechanical Metallurgy, Second, McGraw-Hill, New York, 1976.

[9] R.A. Vandermeer, N. Hansen, Acta Mater. 56 (2008) 5719.

[10] M. Popovic, E. Romhanji, Mater. Sci. Eng. A 492 (2008) 460.

[11] R.D. Doherty, D. a. Hughes, F.J. Humphreys, J.J. Jonas, D.J. Jensen, M.E. Kassner, W.E. King, T.R. McNelley, H.J. McQueen, a. D. Rollett, Mater. Sci. Eng. A 238 (1997) 219.

[12] G. Edwards, K. Stiller, G. Dunlop, M. Couper, Acta Mater. 46 (1998) 3893.

[13] A.K. Gupta, D.J. Lloyd, S.A. Court, Mater. Sci. Eng. A 301 (2001) 140.

[14] A. Gaber, M.A. Gaffar, M.S. Mostafa, A.F. Abo Zeid, Mater. Sci. Technol. 22 (2006) 1483.

[15] Y. Aouabdia, A. Boubertakh, S. Hamamda, Mater. Lett. 64 (2010) 353.

[16] L.C. Doan, Y. Ohmori, K. Nakai, JIM, Mater. Trans. 41 (2000) 300.

[17] P.T. Summers, R.D. Matulich, S.W. Case, B. Lattimer, in:, ASME IMECE 2012, 2012.

[18] Underwriter Laboratories, UL 1709 - Rapid Rise Fire Tests of Protection Materials for Structural Steel, Northbrook, IL, 1990.

[19] N. Cholewa, (2013).

[20] W. Peters, W. Ranson, Opt. Eng. 21 (1982) 427.

[21] M. Sutton, W. Wolters, W. Peters, Image Vis. Comput. 1 (1983) 133.

[22] M. Sutton, J. Orteu, H. Schreier, Image Correlation for Shape, Motion and Deformation Measurements: Basic Concepts, Theory and Applications, Springer, 2009.

[23] M. Sutton, S. McNeill, J. Helm, Y. Chao, in:, Photomechanics, 2000, pp. 323–72.

[24] M. a. Sutton, J. Yan, X. Deng, C.-S. Cheng, P. Zavattieri, Opt. Eng. 46 (2007) 051003.

[25] A.S. Khan, S. Huang, Continuum Theory of Plasticity, Wiley, 1995.

[26] W. Wen, J. Morris, Mater. Sci. Eng. A 354 (2003) 279.

[27] M. Verdier, Y. Brechet, P. Guyot, Acta Mater. 47 (1998) 127.

[28] F.M. Mazzolani, Aluminum Alloy Structures, 2nd ed., E & FN Spon imprint of Chapman & Hall, London, UK, 1995.

[29] F. Zhou, X.. Liao, Y.. Zhu, S. Dallek, E.. Lavernia, Acta Mater. 51 (2003) 2777.

[30] T. Furu, R. Ørsund, E. Nes, Acta Metall. Mater. 43 (1995) 2209.

[31] T. Hasegawa, U. Kocks, Acta Metall. 27 (1979) 1705.

[32] H.J. McQueen, E. Evangelista, Czechoslov. J. Phys. 38 (1988) 359.

[33] F. Humphreys, M. Hatherly, Recrystallization and Related Annealing Phenomena, Second, Oxford, UK, 2004.

[34] Q. Xing, X. Huang, N. Hansen, Metall. Mater. Trans. A 37 (2006) 1311.

[35] H.R. Last, R.K. Garrett, Metall. Mater. Trans. A 27 (1996) 737.

[36] R.A. Vandermeer, D. Juul Jensen, Acta Mater. 49 (2001) 2083.

[37] O. Myhr, Ø. Grong, S. Andersen, Acta Mater. 49 (2001) 65.

[38] A. Simar, Y. Bréchet, B. de Meester, A. Denquin, T. Pardoen, Acta Mater. 55 (2007) 6133.

[39] O. Myhr, Ø. Grong, Acta Mater. 48 (2000) 1605.

[40] O. Myhr, O. Grong, H. Fjar, C. Marioara, Acta Mater. 52 (2004) 4997.

[41] M. Verdier, M. Janecek, Y. Brechet, P. Guyot, Mater. Sci. Eng. A 248 (1998) 187.

[42] D. Kuhlmann, G. Masing, J. Raffelsieper, Zeitsch Met. 40 (1949) 241.

[43] G. Borelius, S. Berglund, S. Sjoberg, Ark. Fys. 6 (1953) 143.

[44] M. Bever, R. Maddin, Creep and Recovery, ASM, Cleveland, OH, 1957.

[45] E. Nes, Acta Metall. Mater. 43 (1995).

[46] B. Bay, N. Hansen, Metall. Trans. A 10 (1979) 279.

[47] B. Bay, N. Hansen, Metall. Trans. A 15 (1984) 287.

[48] H. Fujita, T. Tabata, Acta Metall. (1973).

[49] Y. Huang, F.J. Humphreys, Acta Mater. 47 (1999) 2259.

[50] H. McQueen, N. Ryum, Scand. J. Metall. 14 (1985) 183.

[51] R. Vandermeer, B. Rath, Metall. Trans. A 21 (1990).

[52] A. Jones, B. Ralph, N. Hansen, Proc. R. Soc. London … 368 (1979) 345.

[53] Y. Huang, F.J. Humphreys, Mater. Chem. Phys. 132 (2012) 166.

[54] A. Kolmogorov, Izv. Akad. Nauk. SSSR 3 (1937) 355.

[55] W. Johnson, R. Mehl, Trans. Soc. Pet. Eng. 135 (1939) 416.

[56] M. Avrami, J. Chem. Phys. 7 (1939) 1103.

[57] C.W. Price, Acta Metall. Mater. 38 (1990) 727.

[58] R.A. Vandermeer, Scr. Metall. Mater. 27 (1992) 1563.

[59] R.A. Vandermeer, R.A. Masumura, B.B. Rath, Acta Metall. Mater. 39 (1991) 383.

[60] R. Vandermeer, R. Masumura, Acta Metall. Mater. 40 (1992) 877.

[61] R. Vandermeer, B. Rath, Metall. Trans. A 20 (1989).

[62] R.A. Vandermeer, D. Juul Jensen, Acta Metall. Mater. 42 (1994) 2427.

[63] R. Vandermeer, in:, N. Hansen, D. Juul Jensen, Y. Liu, B. Ralph (Eds.), Microstruct. Crystallogr. Asp. Recryst., Risø National Lab, Roskilde, Denmark, 1995, p. 193.

[64] R. a. Vandermeer, D.J. Jensen, Textures Microstruct. 26 (1996) 263.

[65] N. Hansen, Scr. Mater. 51 (2004) 801.

[66] N. Hansen, Mater. Sci. Eng. A 409 (2005) 39.

[67] N. Hansen, X. Huang, G. Winther, Mater. Sci. Eng. A 494 (2008) 61.

[68] H. Mecking, U. Kocks, Acta Metall. 29 (1981) 1865.

[69] Y. Estrin, H. Mecking, Acta Metall. 32 (1984) 57.

[70] U. Kocks, J. Eng. Mater. Technol. (1976).

[71] U.F. Kocks, H. Mecking, Prog. Mater. Sci. 48 (2003) 171.

[72] G.I. Taylor, Proc. R. Soc. A Math. Phys. Eng. Sci. 145 (1934) 362.

[73] J. Palm, Appl. Sci. Res. A1 (1949) 198.

[74] E. Voce, J. Inst. Met. 74 (1948) 537.

[75] A. Deschamps, Y. Brechet, C. Necker, Mater. Sci. … 207 (1996).

[76] D.-Y. Park, M. Niewczas, Mater. Sci. Eng. A 491 (2008) 88.

[77] O.R. Myhr, Ø. Grong, K.O. Pedersen, Metall. Mater. Trans. A 41 (2010) 1.

[78] G. Fribourg, Y. Bréchet, a. Deschamps, a. Simar, Acta Mater. 59 (2011) 3621.

[79] P. Lukac, in:, Mater. Sci. Forum1, 1996, pp. 71–81.

[80] C. Zahra, A.M. Zahra, Thermochim. Acta 276 (1996) 161.

[81] M.. Starink, Thermochim. Acta 404 (2003) 163.

[82] J. Friedel, L. Vassamillet, Dislocations, 3rd ed., Pergamon Press, Oxford, UK, 1964.

[83] J. Michalak, H. Paxton, Trans TMS-AIME 221 (1961) 850.

[84] N. Peterson, J. Nucl. Mater. 69 (1978) 3.

[85] Q. Liu, X. Huang, D.J. Lloyd, N. Hansen, Acta Mater. 50 (2002) 3789.

[86] P. Summers, S. Case, B. Lattimer, Eng. Struct. Under Revi (2014).

[87] J. Austin, R. Rickett, Trans. AIME (1939).

[88] R.A. Vandermeer, D. Juul Jensen, Acta Mater. 51 (2003) 3005.

[89] R. Vandermeer, Acta Mater. 53 (2005) 1449.

[90] R. a. Vandermeer, G.L. Wu, D. Juul Jensen, Mater. Sci. Technol. 25 (2009) 403.

[91] R. a. Vandermeer, D.J. Jensen, Textures Microstruct. 26 (1996) 263.

[92] J. Cahn, W. Hagel, in:, Z. and Anderson (Ed.), Decompos. Austentite by Diffus. Process., Interscience, New York, 1960, p. 131.

[93] J. Cahn, W. Hagel, Acta Metall. 11 (1963) 561.

[94] F. Underwood, in:, R. DeHoff, F. Rhines (Eds.), Quant. Microsc., McGraw-Hill, New York, 1968, pp. 77–127.

[95] G. Wu, D.J. Jensen, Mater. Sci. Technol. (2005).

[96] N. Raghunathan, M. Zaidi, T. Sheppard, Mater. Sci. Technolgy 2 (1986) 938.

[97] D.J. Lloyd, Metall. Trans. A 11 (1980) 1287.

[98] Ø. Ryen, B. Holmedal, O. Nijs, E. Nes, E. Sjölander, H.-E. Ekström, Metall. Mater. Trans. A 37 (2006) 1999.

[99] M. Ashby, A. Kelly, R. Nicholson, Strengthening Methods in Crystals, Elsevier, Amsterdam, 1971.

[100] D. Chu, J. Morris, Acta Mater. 44 (1996) 2599.

[101] S. Esmaeili, L.. Cheng, a Deschamps, D.. Lloyd, W.. Poole, Mater. Sci. Eng. A 319-321 (2001) 461.

[102] L. Cheng, W. Poole, J. Embury, D. Lloyd, Metall. Mater. … 34 (2003) 2473.

[103] Y. Estrin, in:, A. Krausz, K. Krausz (Eds.), Unified Const. Laws Plast. Deform., Academic Press, San Diego, 1996, pp. 9–106.

[104] Ø. Grong, H. Shercliff, Prog. Mater. Sci. 47 (2002) 4.

[105] O. Myhr, Ø. Grong, Acta Metall. 39 (1991) 2693.

[106] O. Myhr, Ø. Grong, Acta Metall. Mater. 39 (1991) 2703.

[107] D. Bratland, Ø. Grong, H. Shercliff, O. Myhr, S. Tjøtta, Acta Mater. 45 (1997) 1.

[108] C. Gallais, A. Denquin, Y. Brechet, G. Lapasset, Mater. Sci. Eng. A 496 (2008) 77.

[109] S. Esmaeili, D.J. Lloyd, Mater. Charact. 55 (2005) 307.

[110] A. Deschamps, M. Niewczas, Philos. Mag. A 79 (1999) 2485.

[111] O. Myhr, Ø. Grong, S. Klokkehaug, H. Fjaer, in:, H. Bhadeshia (Ed.), Math. Model. Weld Phenom., Vol. 6, Manley Publishing, London, UK, 2002.

[112] M. Nicolas, Acta Mater. 51 (2003) 6077.

[113] I.N. Khan, M.J. Starink, J.L. Yan, Mater. Sci. Eng. A 472 (2008) 66.

[114] M. Perez, M. Dumont, D. Acevedo-Reyes, Acta Mater. 56 (2008) 2119.

[115] D. Bardel, M. Perez, D. Nelias, a. Deschamps, C.R. Hutchinson, D. Maisonnette, T. Chaise, J. Garnier, F. Bourlier, Acta Mater. 62 (2014) 129.

[116] A. Bahrami, A. Miroux, J. Sietsma, Metall. Mater. Trans. A 43 (2012) 4445.

[117] R. Kampmann, R. Wagner, in:, Decompositions Alloy. Early Stages, Pergamon Press, Oxford, UK, 1984, pp. 91–103.

[118] H.R. Shercliff, M.F. Ashby, Acta Metall. Mater. 38 (1990) 1789.

[119] H. Shercliff, M. Ashby, Acta Metall. Mater. 38 (1990) 1803.

[120] A. Deschamps, F. Livet, Y. Brechet, Acta Mater. 47 (1998) 281.

[121] A. Deschamps, Y. Brechet, Acta Mater. 47 (1998) 293.

[122] M. Song, Mater. Sci. Eng. A 443 (2007) 172.

[123] K. Marthinsen, E. Nes, Mater. Sci. Eng. A 234-236 (1997) 1095.

[124] E. Nes, Prog. Mater. Sci. 41 (1998) 129.

[125] E. Nes, T. Pettersen, K. Marthinsen, Scr. Mater. 43 (2000) 55.

[126] K. Marthinsen, E. Nes, Mater. Sci. Technol. (2001).

[127] E. Nes, K. Marthinsen, B. Rønning, J. Mater. Process. … 117 (2001).

[128] E. Nes, K. Marthinsen, Mater. Sci. Eng. A 322 (2002) 176.

[129] F. Barlat, M. Glazov, J. Brem, D. Lege, Int. J. Plast. 18 (2002) 919.

[130] F. Fazeli, W.J. Poole, C.W. Sinclair, Acta Mater. 56 (2008) 1909.

[131] W. Poole, D. Lloyd, in:, J. Nie, A. Morton, B. Muddle (Eds.), Proceeding 9th Int. Conf. Alum. Alloy., Institute of Materials Engineering Australasia Ltd, 2004.

[132] P. Donnadieu, M. Roux-Michollet, V. Chastagnier, Philos. Mag. A 79 (1999) 1347.

[133] C. Ravi, C. Wolverton, Acta Mater. 52 (2004) 4213.

[134] A. Simar, Y. Bréchet, B. de Meester, A. Denquin, C. Gallais, T. Pardoen, Prog. Mater. Sci. 57 (2012) 95.

[135] E. Nes, B. Holmedal, E. Evangelista, K. Marthinsen, Mater. Sci. Eng. A 410-411 (2005) 178.

[136] P. Haasen, in:, F. Nabarro (Ed.), Dislocations in Solids, Vol. 4, North-Holland, Amsterdam, 1979, p. 155.

[137] V. Gerold, in:, F. Nabarro (Ed.), Dislocations in Solids, Vol. 4, North-Holland, Amsterdam, 1979, p. 234.

[138] A. Ardell, Metall. Trans. A 16 (1985) 2131.

[139] Y. Brechet, F. Louchet, Acta Metall. 37 (1989) 2469.

[140] Y. Estrin, K. Lücke, Scr. Metall. 19 (1985) 221.

[141] R. Vissers, M. Vanhuis, J. Jansen, H. Zandbergen, C. Marioara, S. Andersen, Acta Mater. 55 (2007) 3815.

[142] C. Cayron, P.A. Buffat, Acta Mater. 48 (2000) 2639.

[143] X. Qiang, F.S.K. Bijlaard, H. Kolstein, Eng. Struct. 35 (2012) 1.

[144] Y. Huang, F. Humphreys, Acta Mater. 48 (2000) 2017.

Appendix A - AA5083-H116 Constitutive Model Monte Carlo Analysis

Monte Carlo analysis was performed using 10^4 simulation runs for each non-constant parameter (refer to Table A-1) in the AA5083-H116 constitutive model (heating at 20°C/min). Pseudorandom numbers from the listed distributions were generated with Matlab algorithms using a single command to ensure all pseudorandom numbers were generated using the same seed. Model results (X_{RV}, X_{RX}, and σ_y) were probed at 260°C and 320°C to elucidate the effects of each parameter during recovery and recrystallization. An analysis summary is provided in Fig. A-1. Individual parameter effects are shown in the subsequent figures including (a) model predictions as a function of parameter value, (b),(c) model prediction histograms at 260°C and 320°C, and (d) yield strength as a function of temperature for 100 randomly selected parameter instances.

Table A-1. Parameter distributions for AA5083-H116 constitutive model Monte Carlo analysis.

Parameter	**Distribution**	**Distribution Parameters**	**Assumed From**
K_0	Normal	μ = 2 x 10^6 1/s; σ = 3.8 x 10^5 1/s	[9]
Q_0	Constant		Physical constant
κP_0	Normal	μ = 50 kJ/mol; σ = 1.37 kJ/mol	[9]
δ_{AR}	Lognormal	λ = 5.93; ζ = 0.04	10% of lognormal deviation in [144]
Q_g	Normal	μ = 182 kJ/mol; σ = 1.5 kJ/mol	DSC (Chapter 3)
v_0	Uniform	a = 10^{15} 1/s; b = 10^{16} 1/s	
L	Lognormal	λ = 5.63; ζ = 0.21	25% of lognormal deviation from grain size analysis
N_0	Lognormal	λ = 2.71; ζ = 0.10	Same as for L
d_{RX}	Lognormal	λ = 3.75; ζ = 0.05	10% from lineal intercept grain analysis
σ_0	Constant	19.3 MPa	[98]
H	Constant	13.8 MPa/(Mg wt%)^n	[98]
n	Constant	1.14	[98]
k_g	Constant	0.22 MPa-m$^{0.5}$	[35]
d_{AR}	Lognormal	λ = 4.48; ζ = 0.06	Same as for d_{RX}
G	Constant	26400 MPa	
b	Constant	0.286 nm	
θ_m	Lognormal	λ = 1.00; ζ = 0.10	[34]
M	Constant	3.07	
α	Constant	0.3	
L_0	Triangular	a = 11.6; c = 16.6; b = 21.6 nm	Possible range of values
K_{sg}	Triangular	a = 830; c = 1030; b = 1230 nm	Possible range of values
θ_0	Triangular	a = 4500; c = 5000; b = 5500 MPa	Possible range of values

Normal distribution probability density function definition:

$$f(x) = \frac{1}{\sigma\sqrt{2\pi}} \exp\left(-\frac{(x-\mu)^2}{2\sigma^2}\right) \tag{126}$$

Lognormal distribution probability density function definition:

$$f(x) = \frac{1}{x\zeta\sqrt{2\pi}} \exp\left(-\frac{[\ln(x-\lambda)]^2}{2\zeta^2}\right) \tag{127}$$

Uniform distribution probability density function definition:

$$f(x) = \begin{cases} \dfrac{1}{b-a} & \text{for } a \le x \le b \\ 0 & \text{for } x < a \text{ or } x > b \end{cases} \tag{128}$$

Triangular distribution probability density function definition:

$$f(x) = \begin{cases} 0 & \text{for } x < a \\ \dfrac{2(x-a)}{(b-a)(c-a)} & \text{for } a \le x \le c \\ \dfrac{2(b-x)}{(b-a)(b-c)} & \text{for } c \le x \le b \\ 0 & \text{for } b < x \end{cases} \tag{129}$$

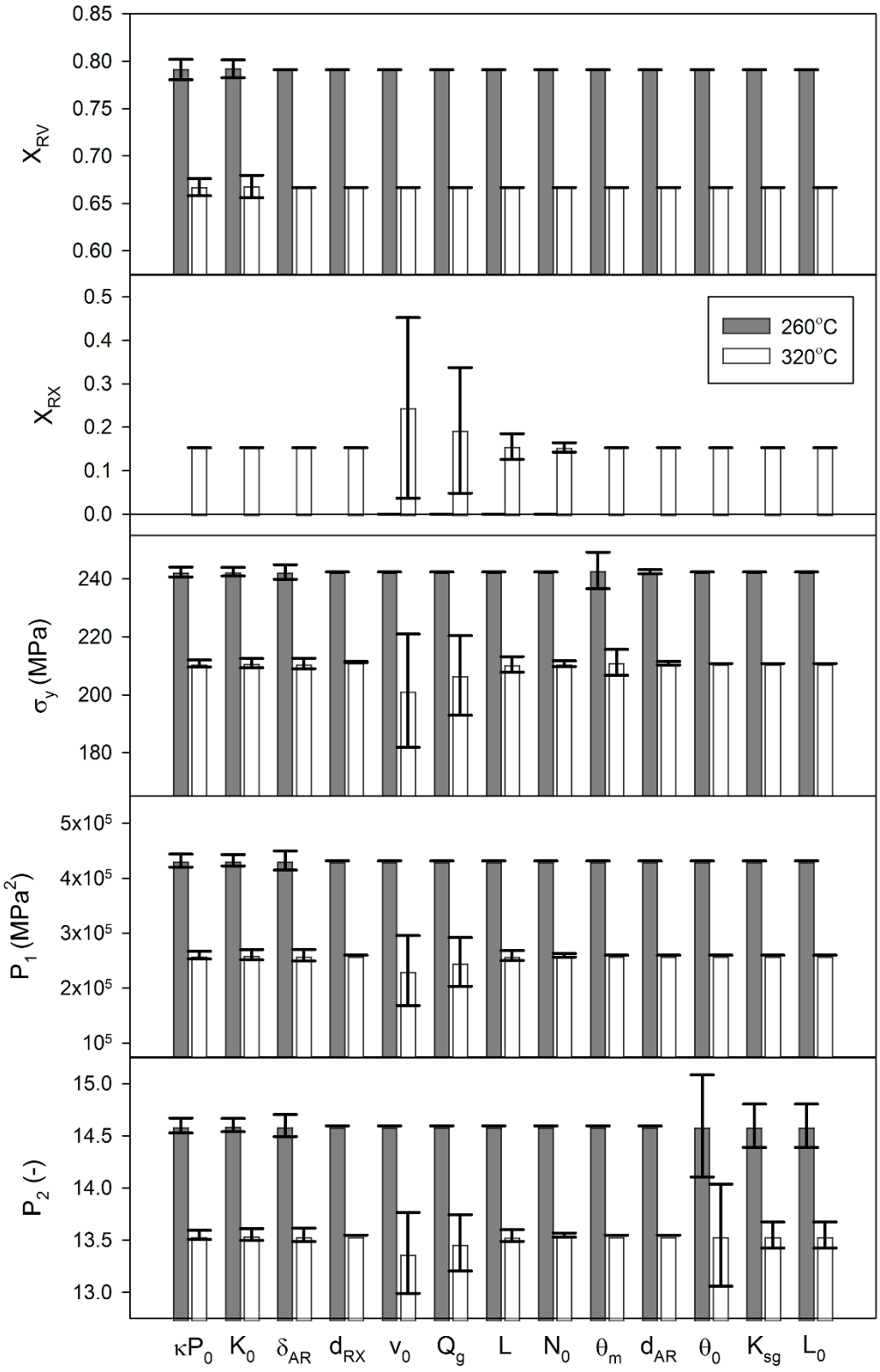

Fig. A-1. AA5083-H116 constitutive model Monte Carlo analysis for mean effects for exposure at 20°C/min to 260°C and 320°C, including effects on microstructural evolution (X_{RV} and X_{RX}), yield strength (σ_y), and strain hardening (P_1 and P_2).

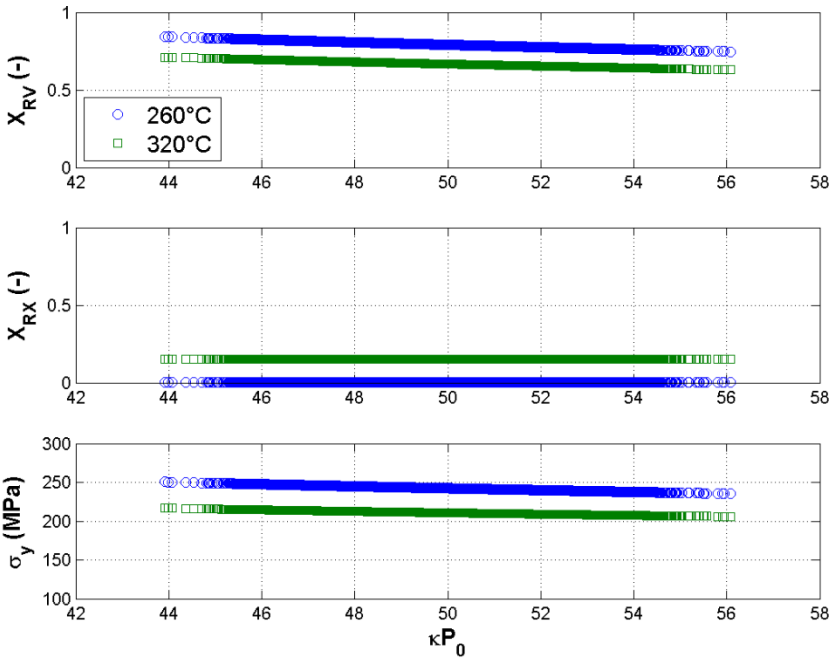

(a)

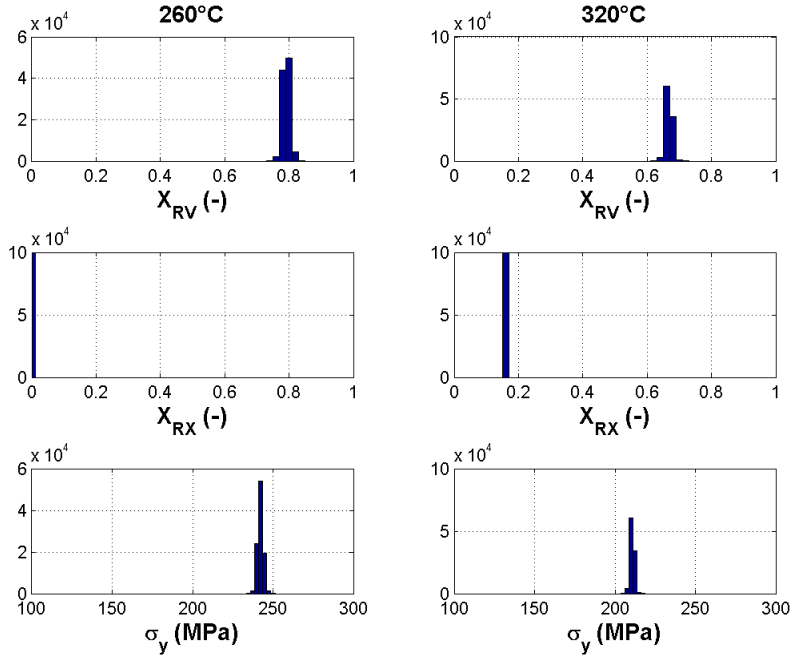

(b)

(Figure continued on next page)

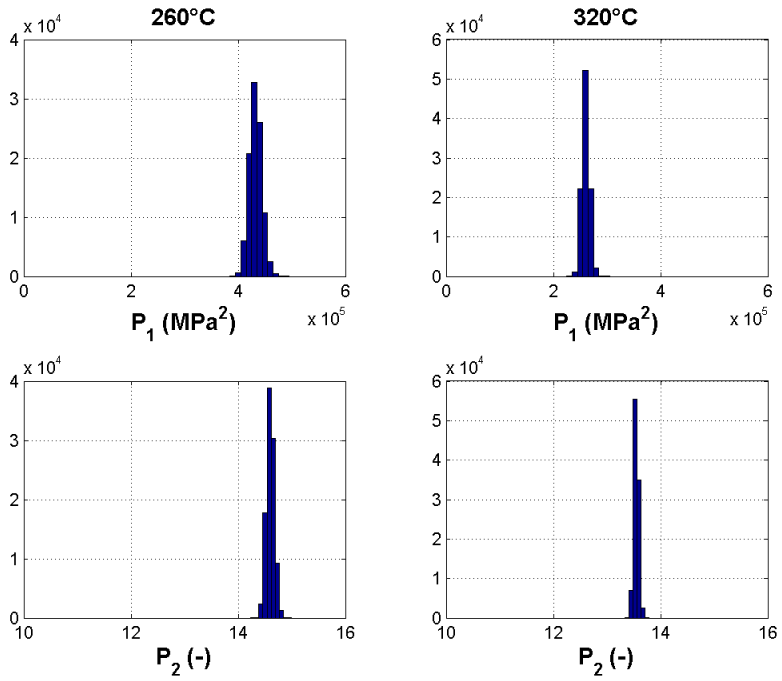

(c)

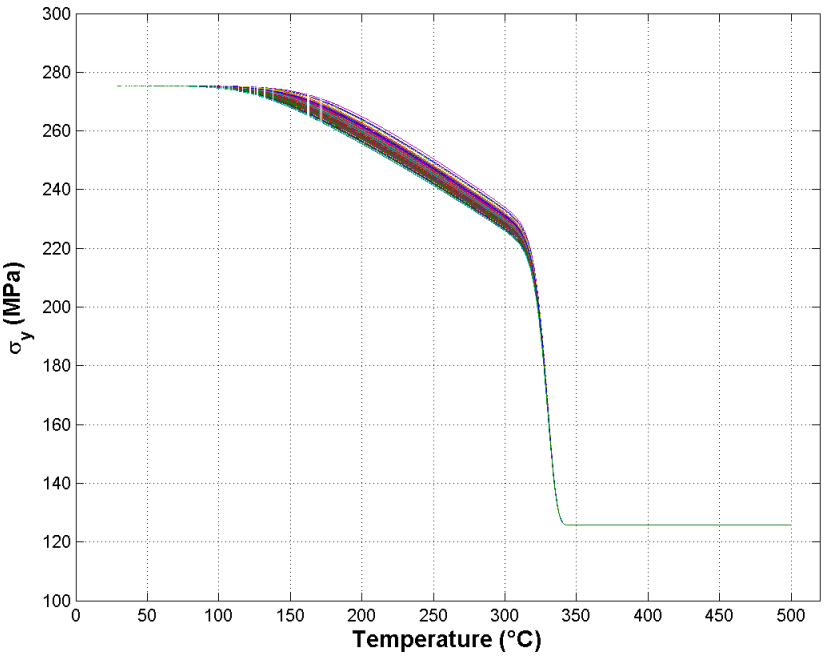

(d)

Fig. A-2. Monte Carlo analysis of κP_0 on AA5083-H116 constitutive model predictions.

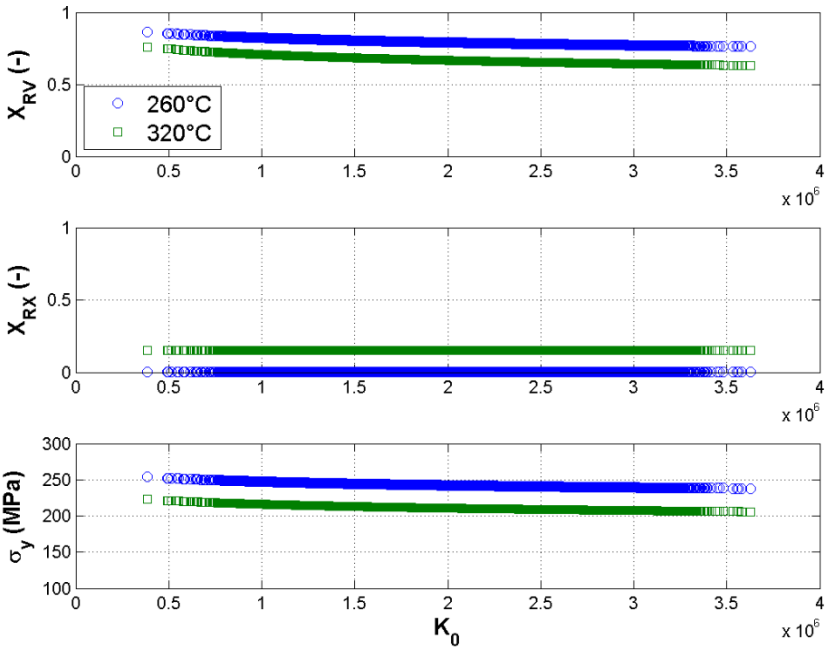

(a)

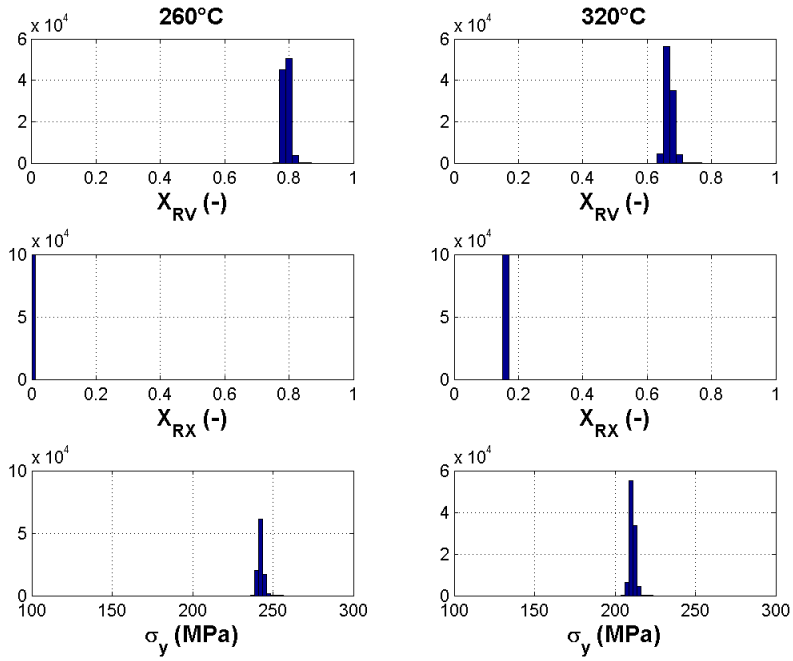

(b)

(Figure continued on next page)

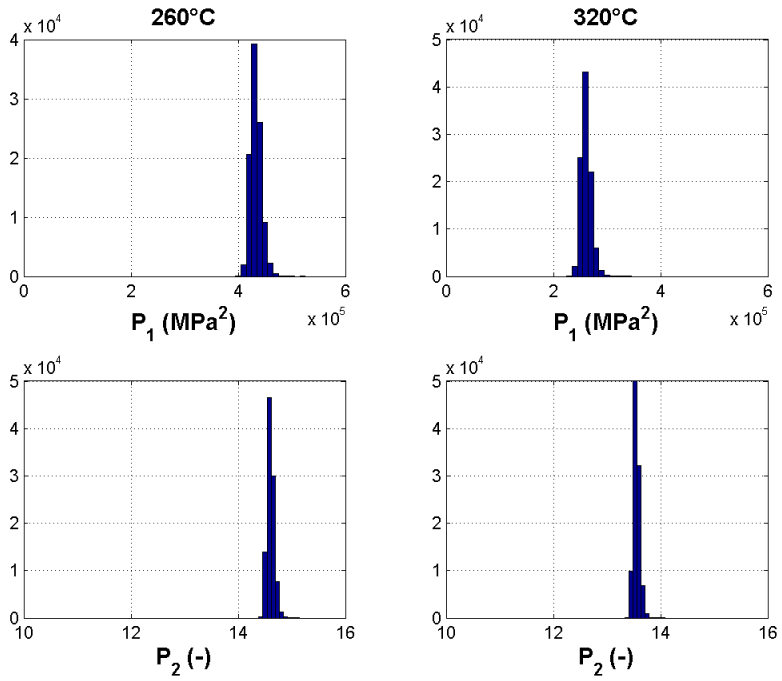

(c)

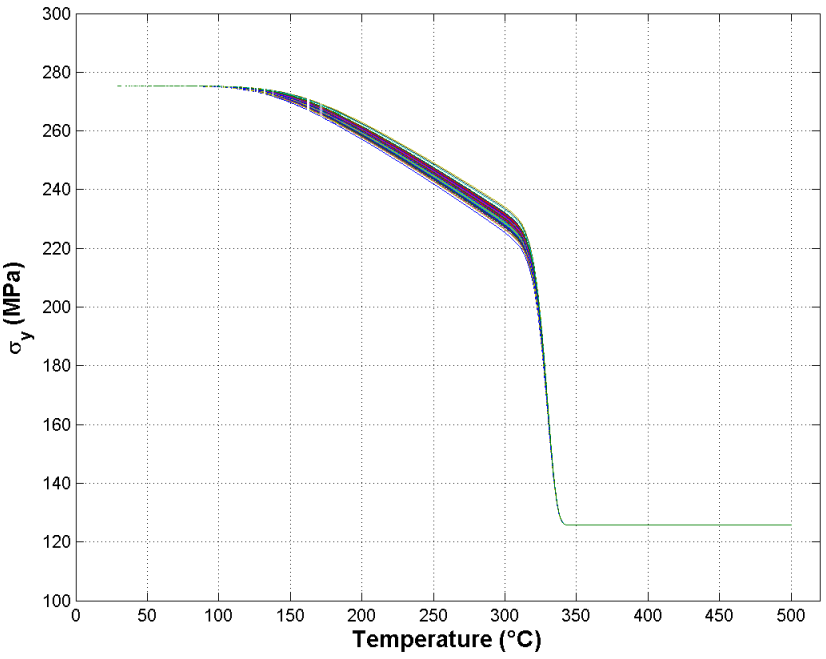

(d)

Fig. A-3. Monte Carlo analysis of K_0 on AA5083-H116 constitutive model predictions.

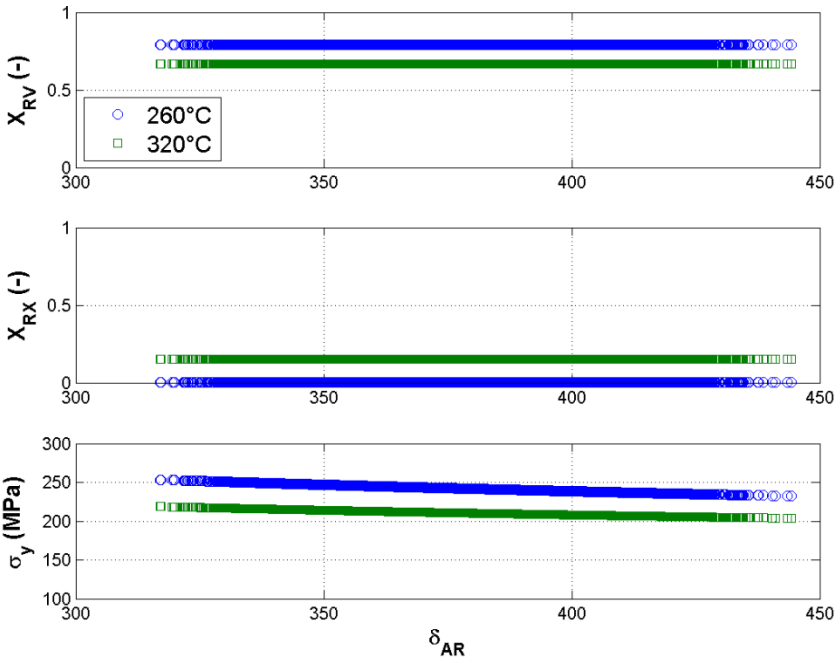

(a)

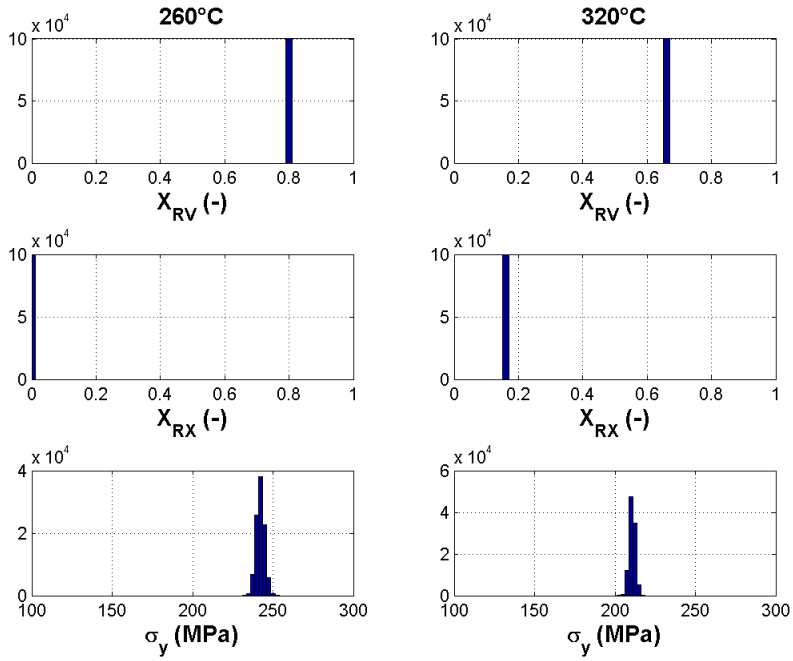

(b)

(Figure continued on next page)

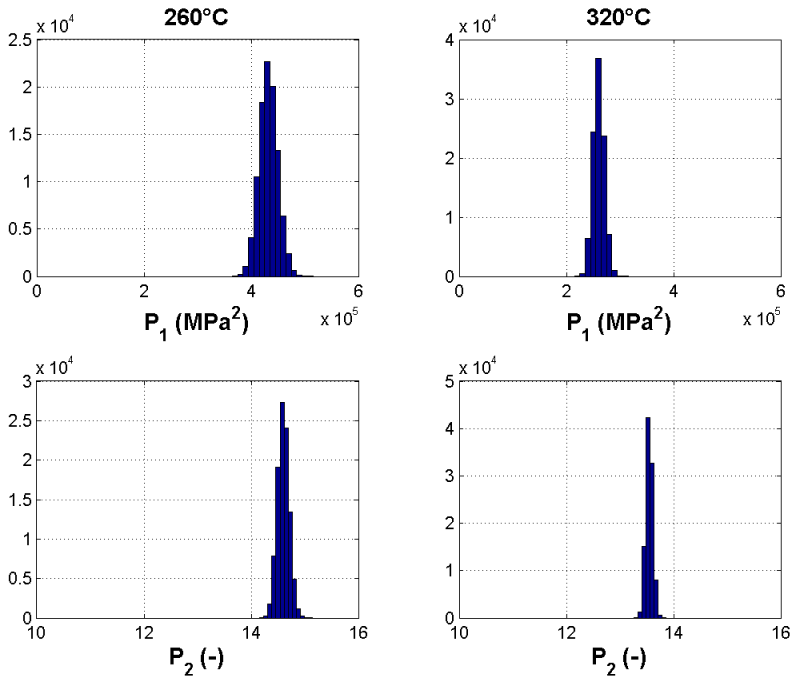

(c)

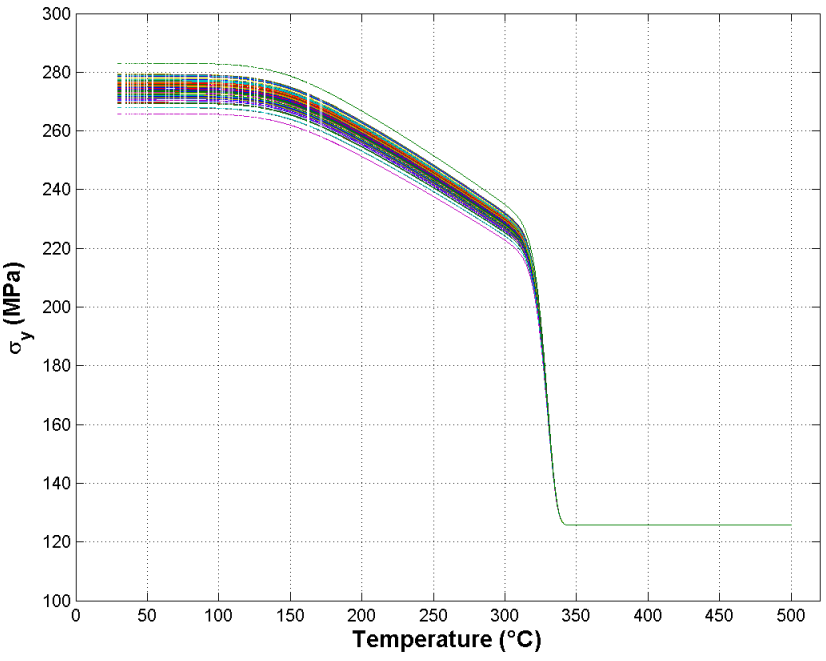

(d)

Fig. A-4. Monte Carlo analysis of δ_{AR} on AA5083-H116 constitutive model predictions.

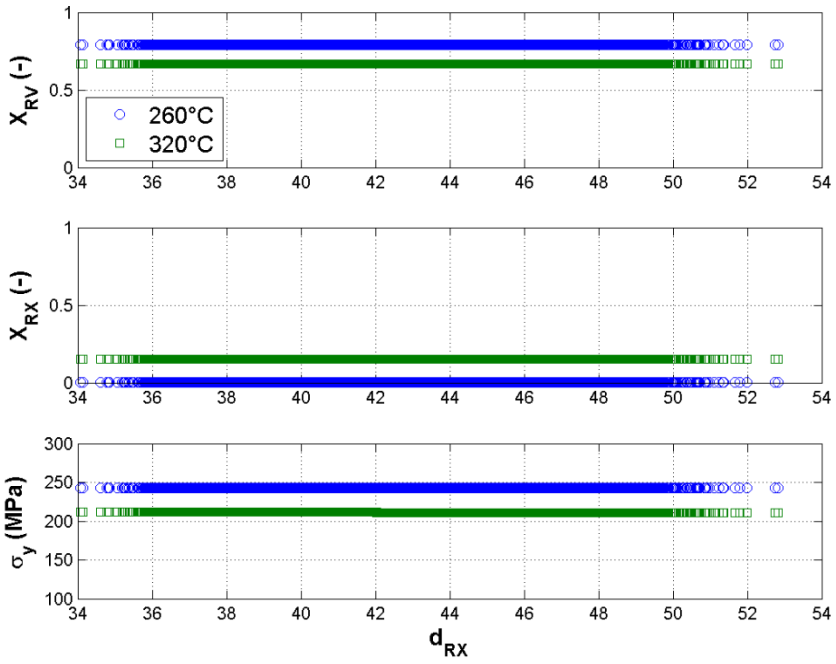

(a)

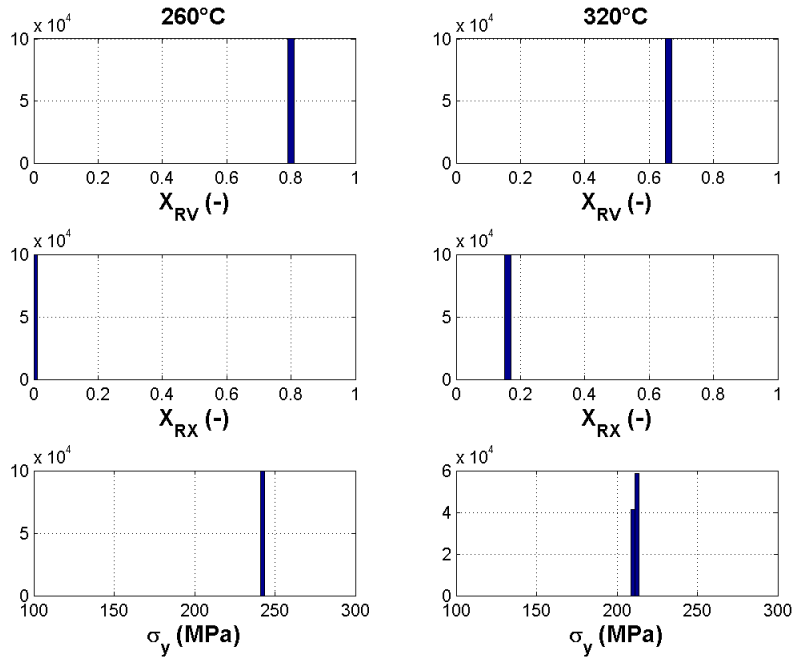

(b)

(Figure continued on next page)

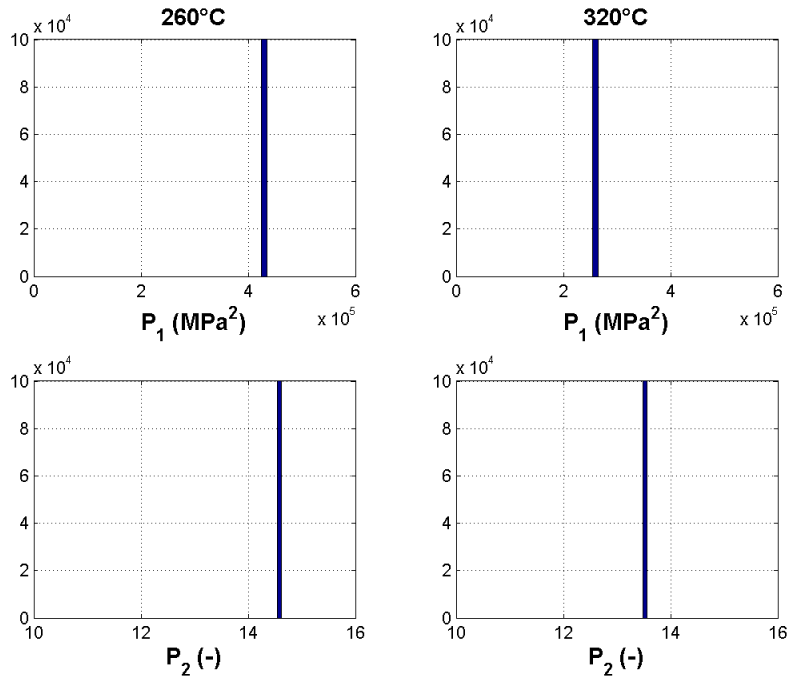

(c)

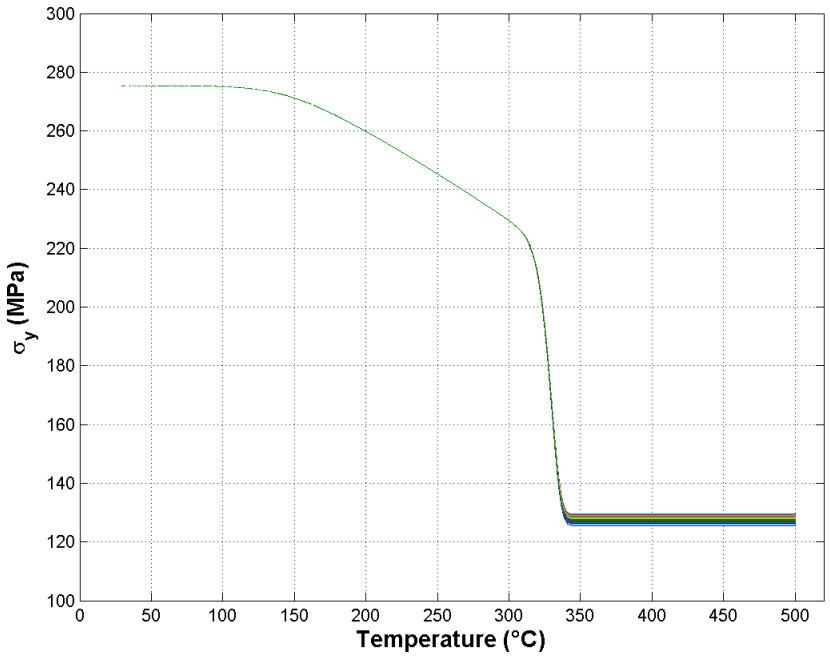

(d)

Fig. A-5. Monte Carlo analysis of d_{RX} on AA5083-H116 constitutive model predictions.

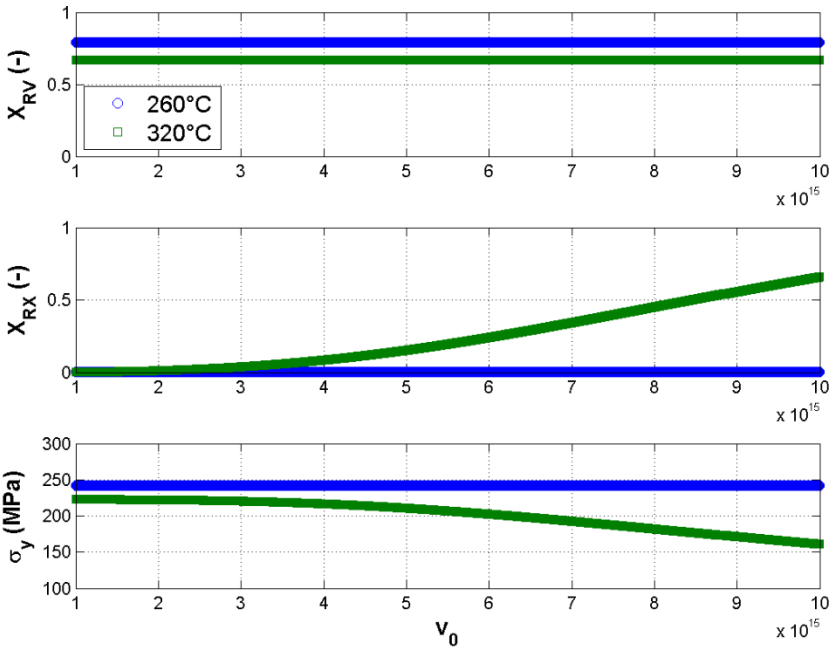

(a)

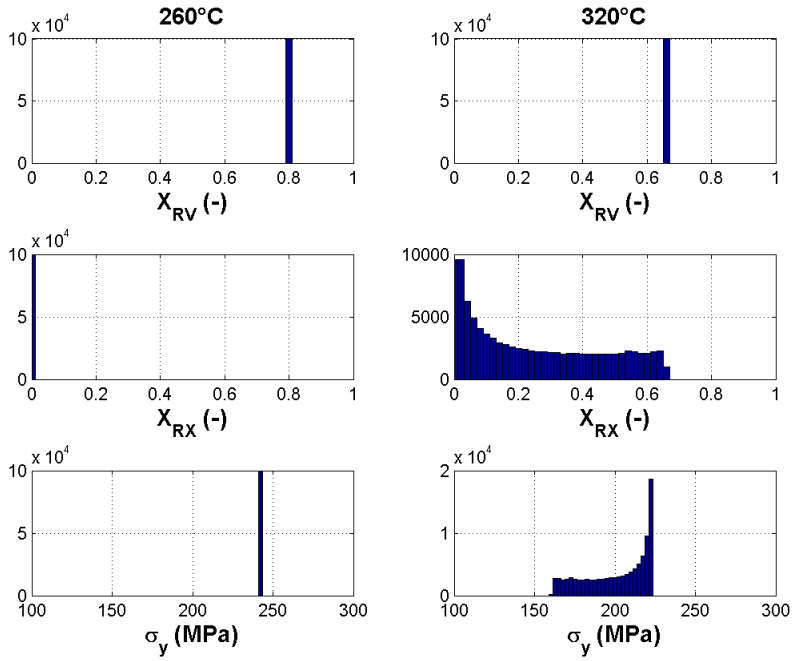

(b)

(Figure continued on next page)

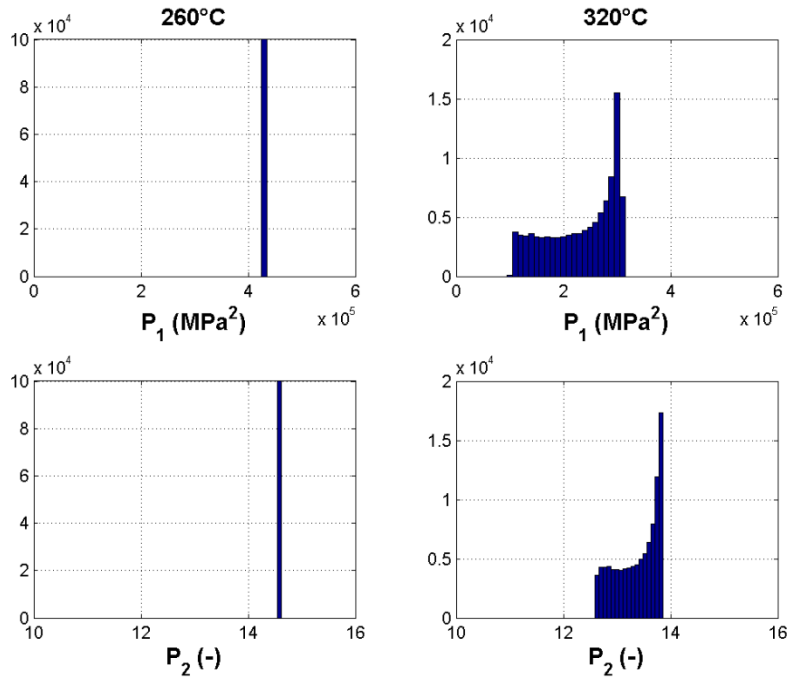

(c)

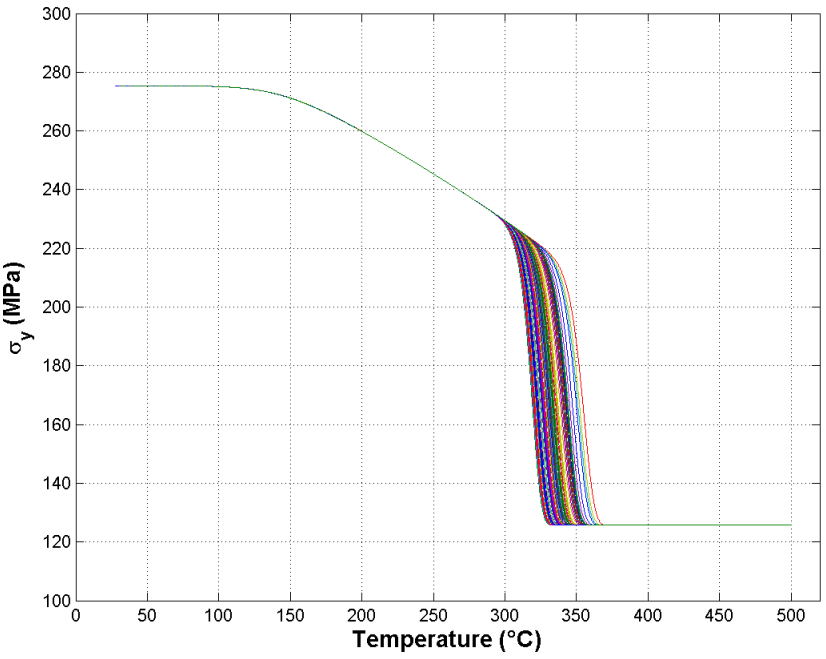

(d)

Fig. A-6. Monte Carlo analysis of v_0 on AA5083-H116 constitutive model predictions.

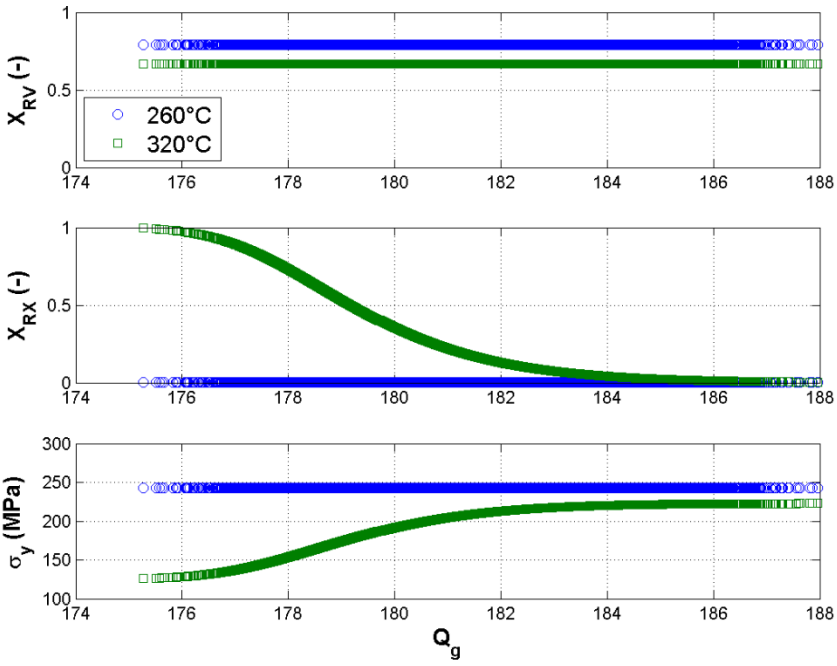

(a)

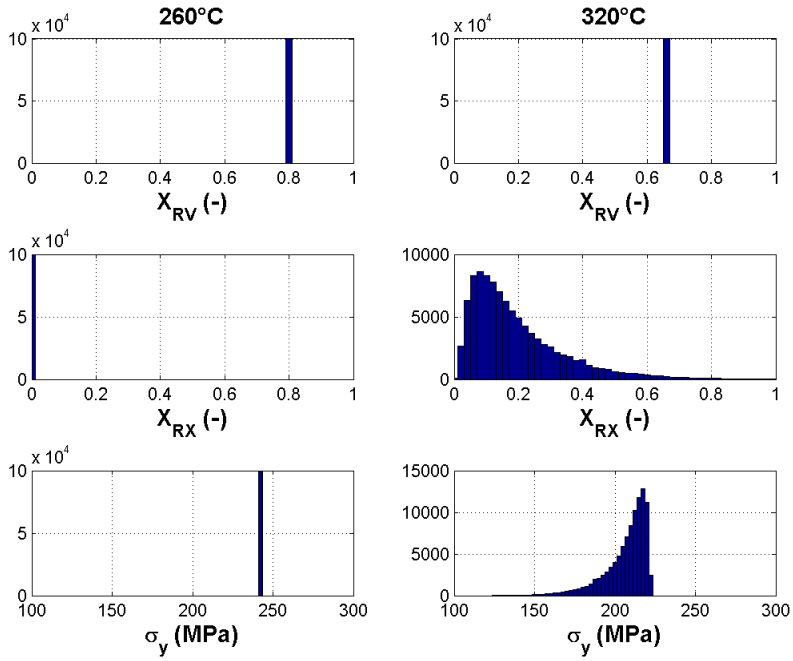

(b)

(Figure continued on next page)

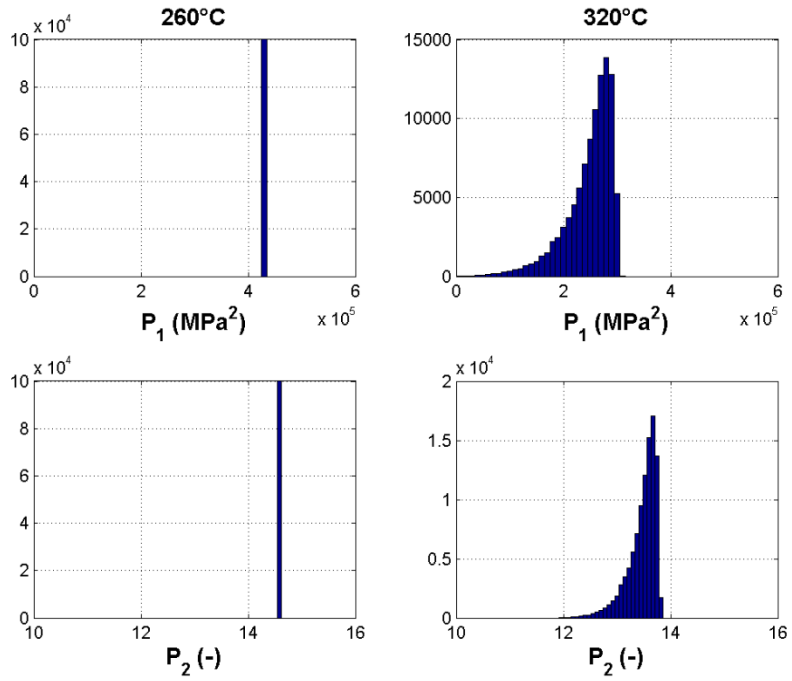

(c)

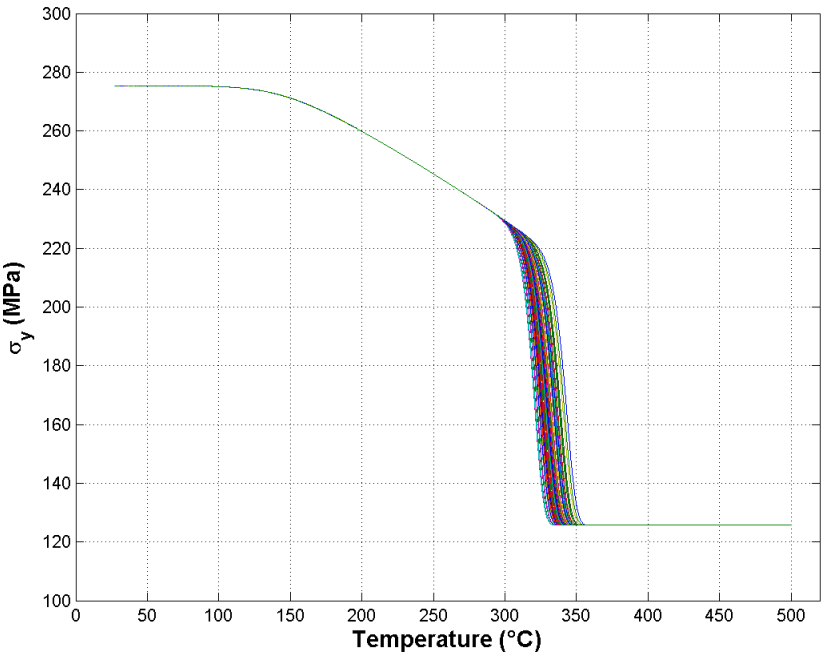

(d)

Fig. A-7. Monte Carlo analysis of Q_g on AA5083-H116 constitutive model predictions.

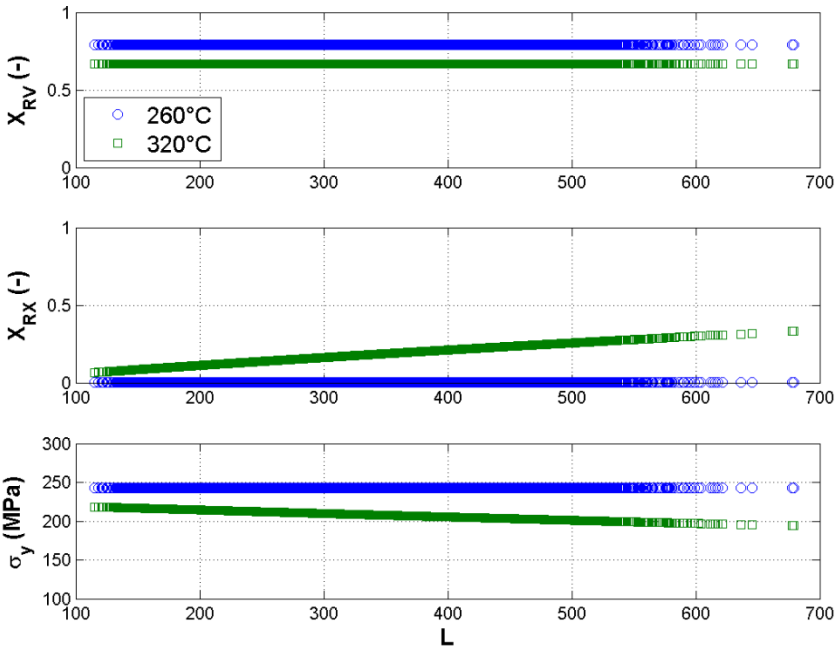

(a)

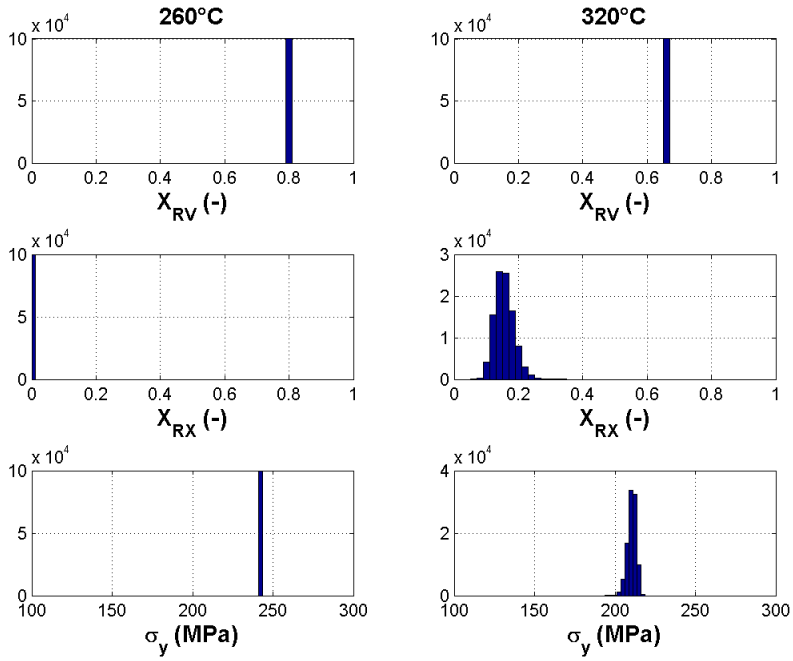

(b)

(Figure continued on next page)

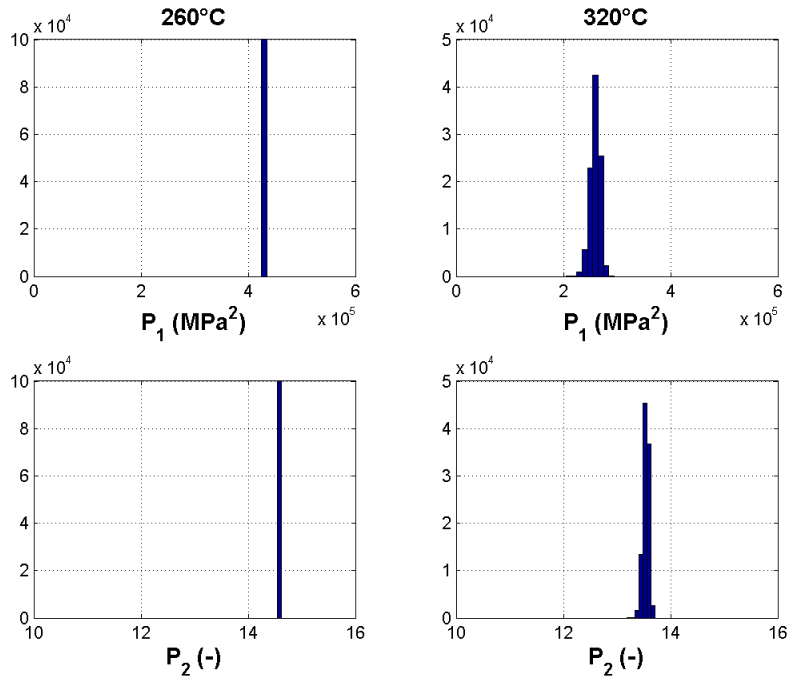

(c)

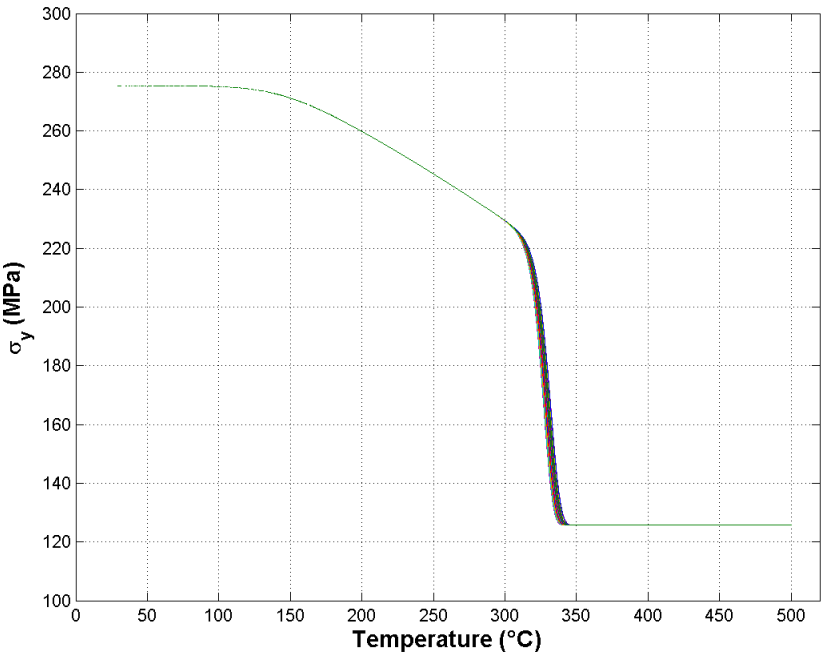

(d)

Fig. A-8. Monte Carlo analysis of *L* on AA5083-H116 constitutive model predictions.

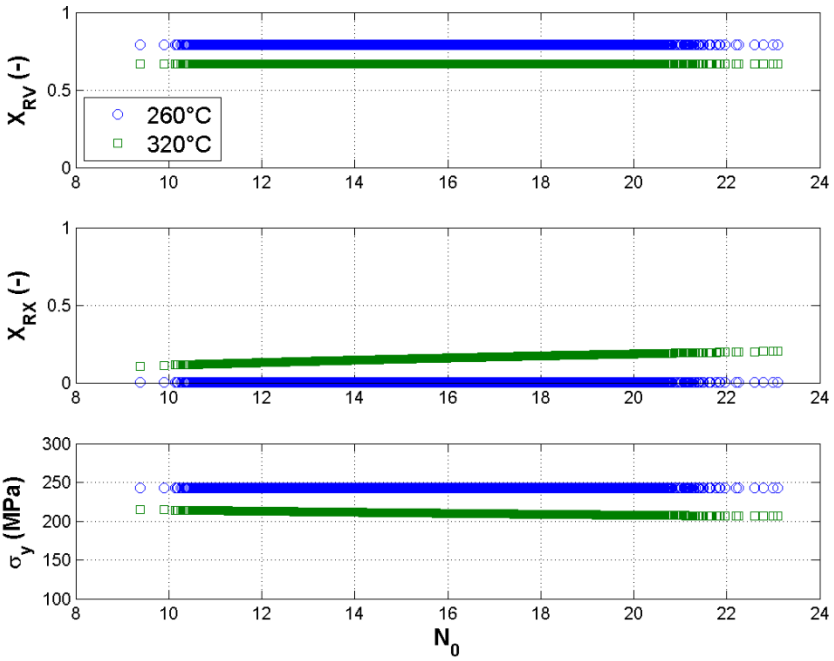

(a)

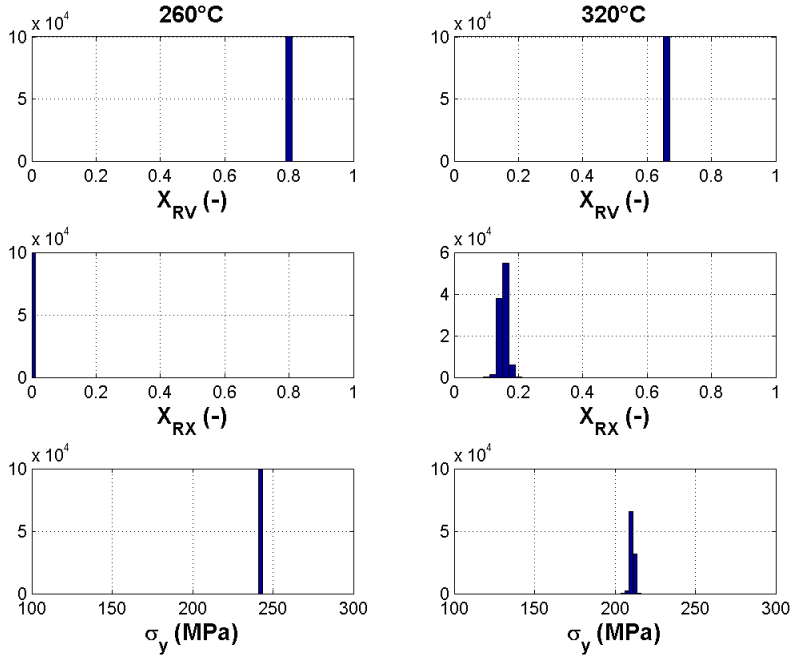

(b)

(Figure continued on next page)

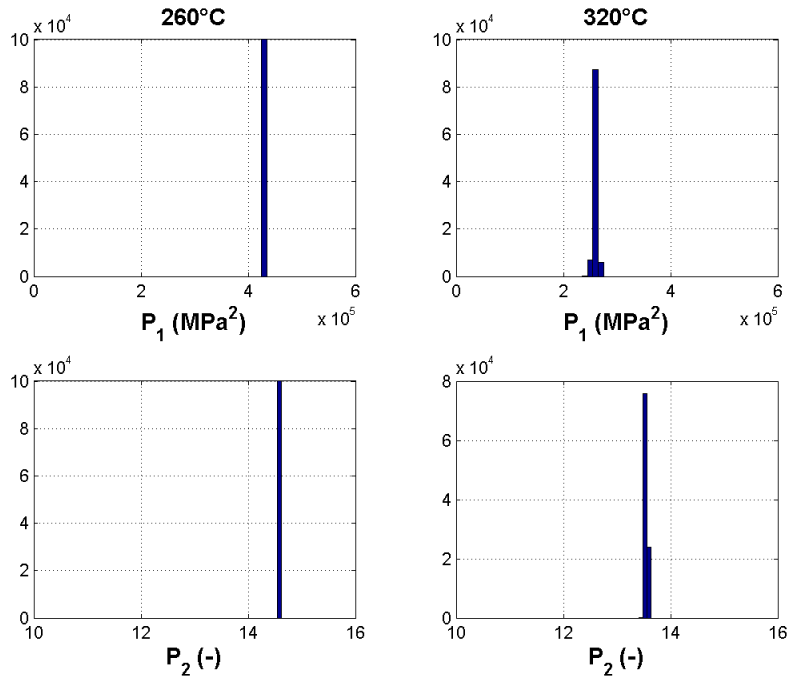

(c)

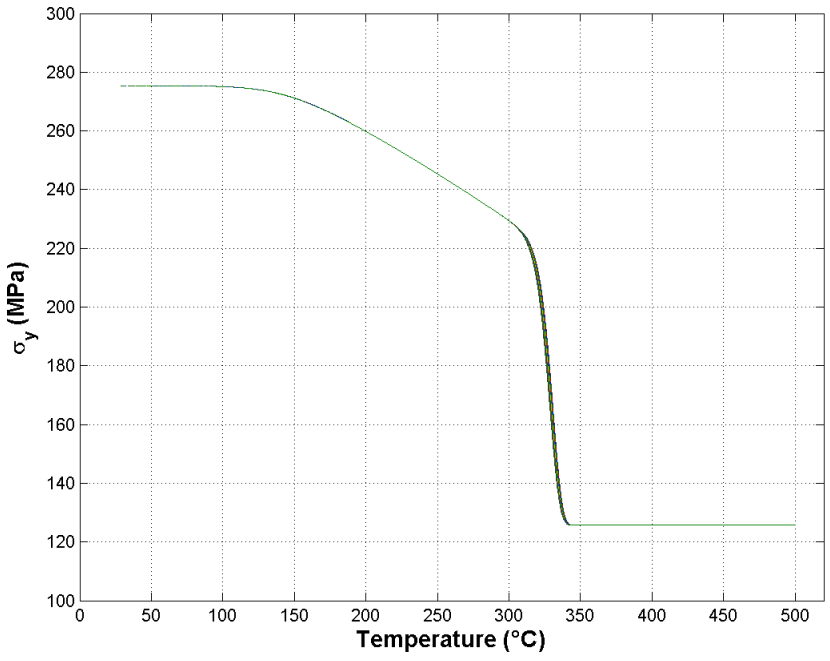

(d)

Fig. A-9. Monte Carlo analysis of N_0 on AA5083-H116 constitutive model predictions.

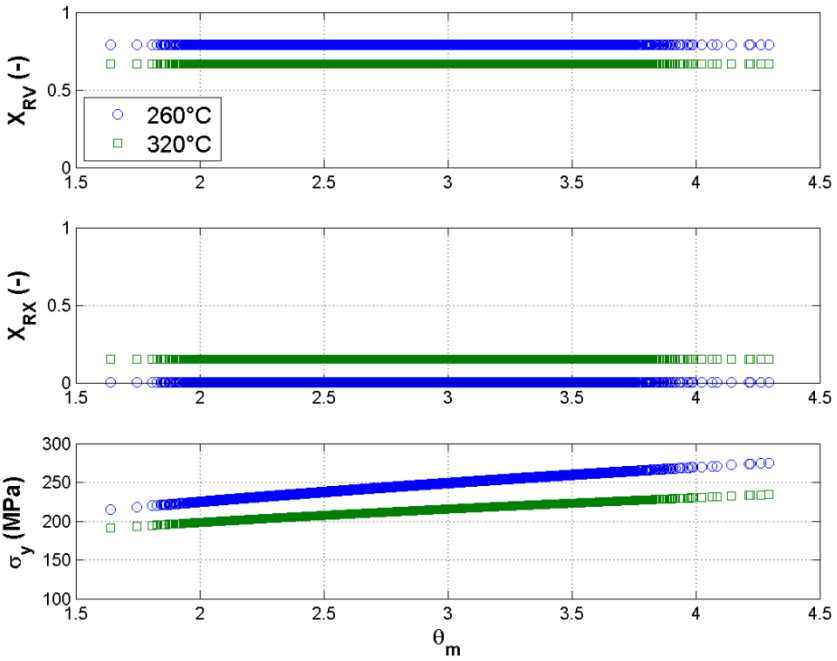

(a)

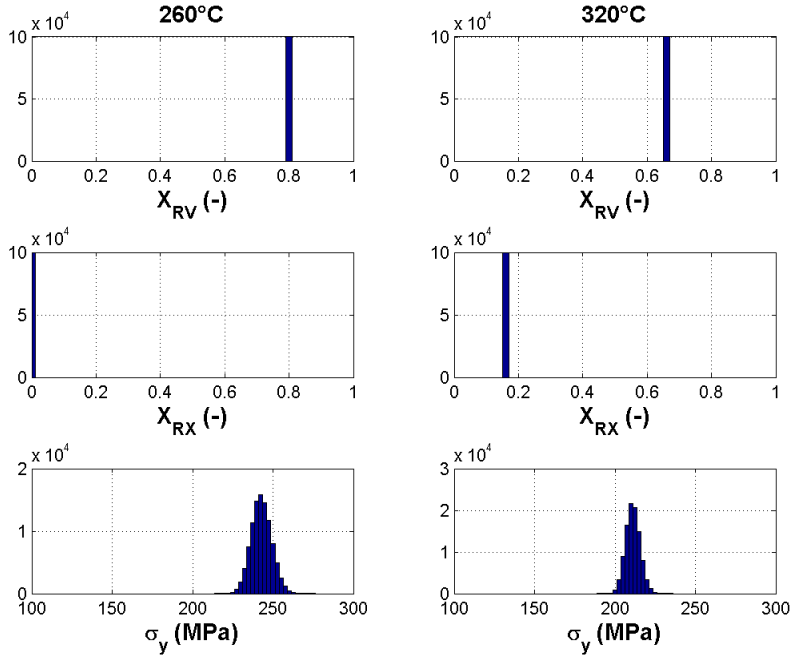

(b)

(Figure continued on next page)

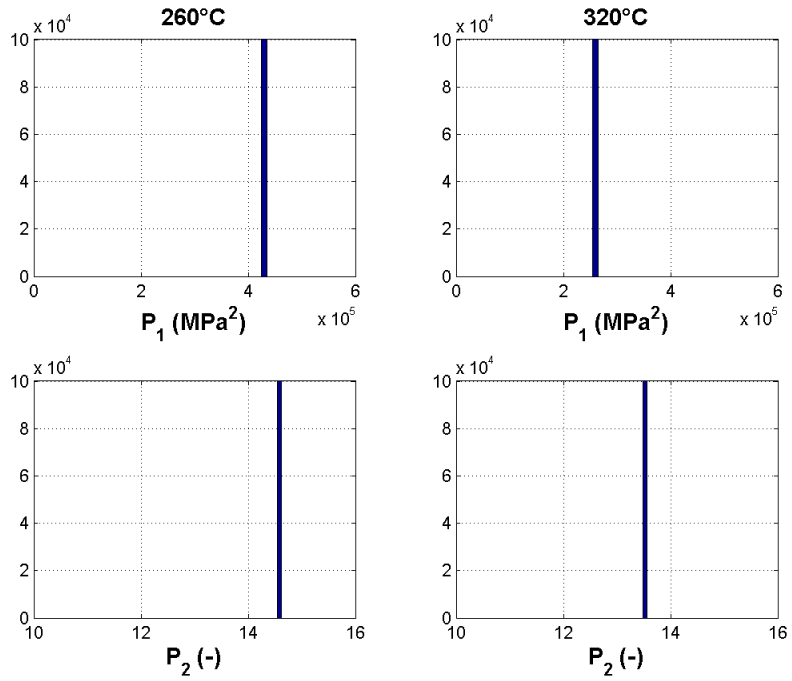

(c)

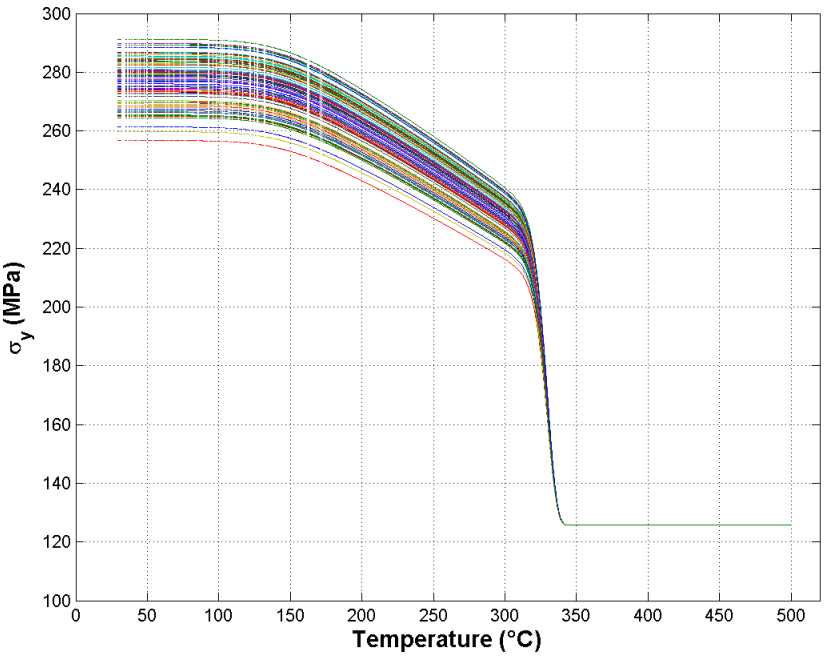

(d)

Fig. A-10. Monte Carlo analysis of θ_m on AA5083-H116 constitutive model predictions.

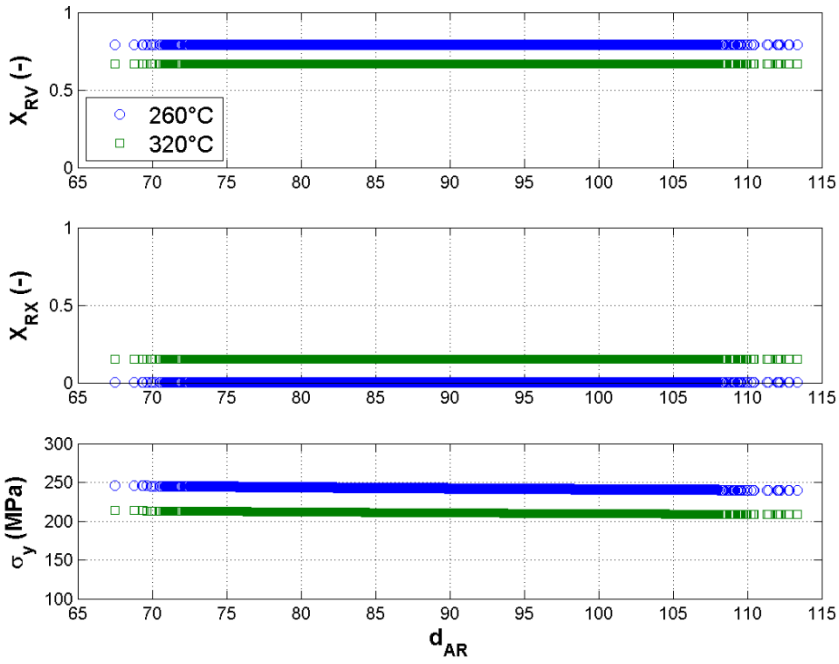

(a)

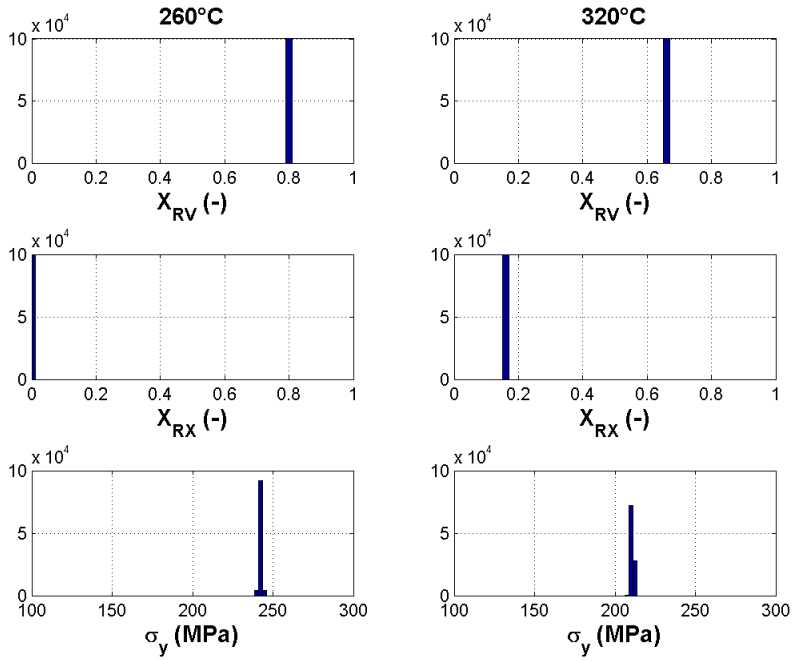

(b)

(Figure continued on next page)

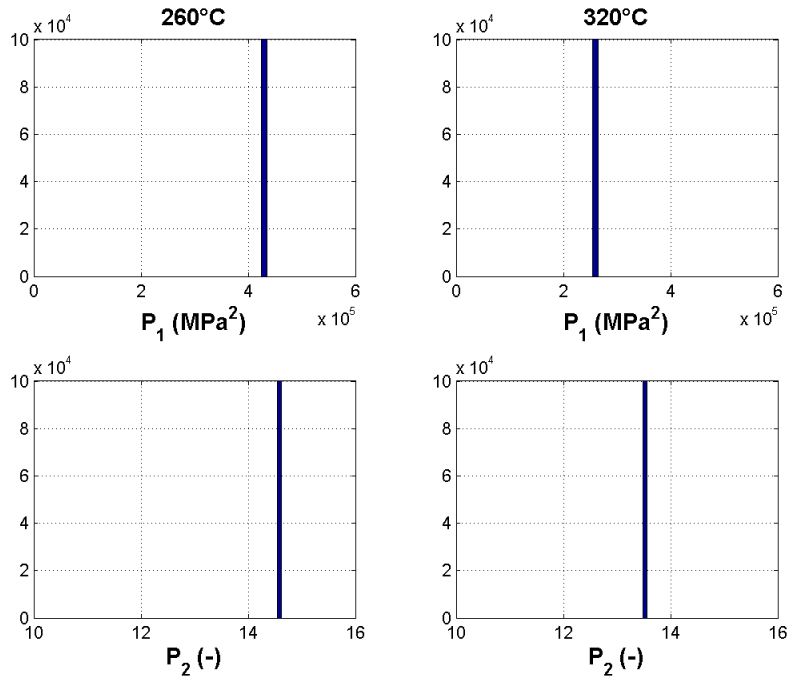

(c)

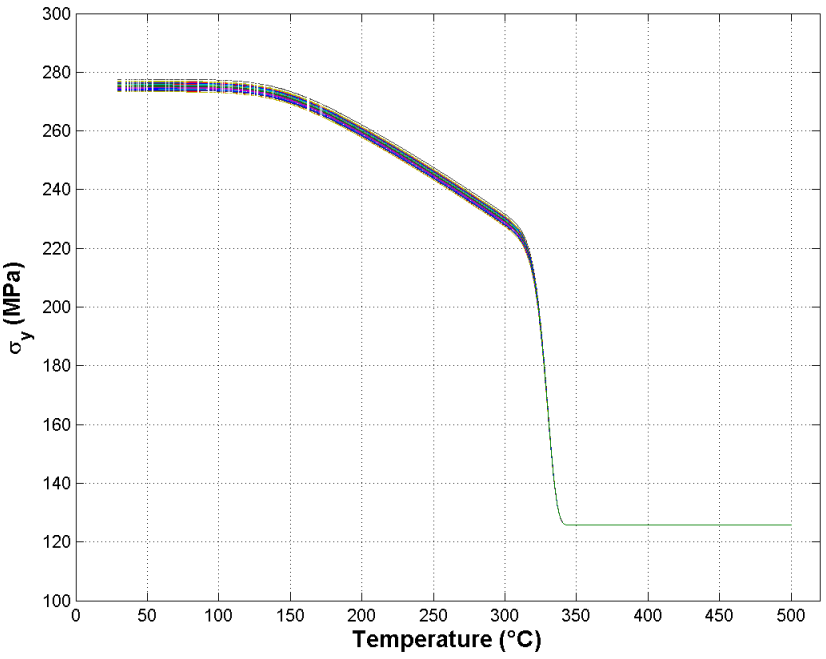

(d)

Fig. A-11. Monte Carlo analysis of d_{AR} on AA5083-H116 constitutive model predictions.

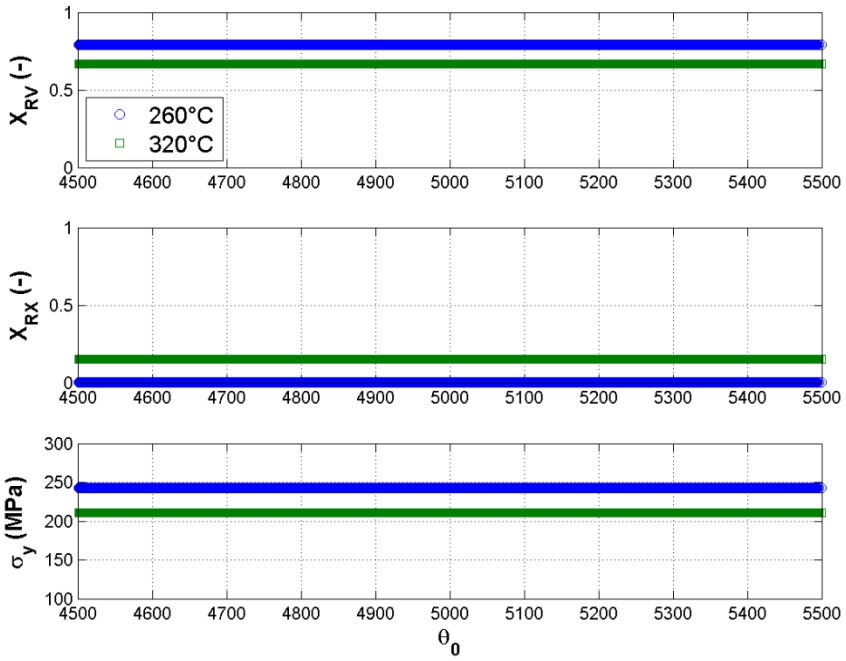

(a)

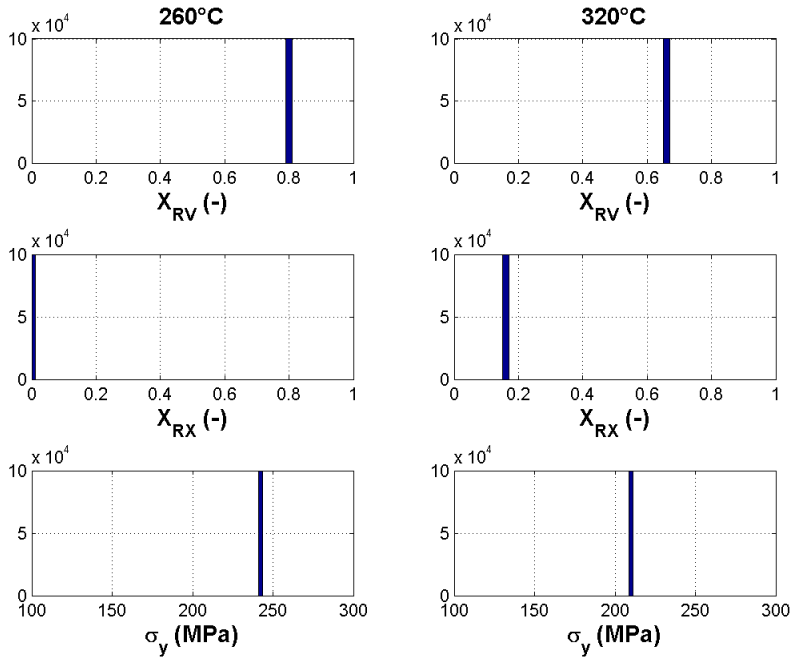

(b)

(Figure continued on next page)

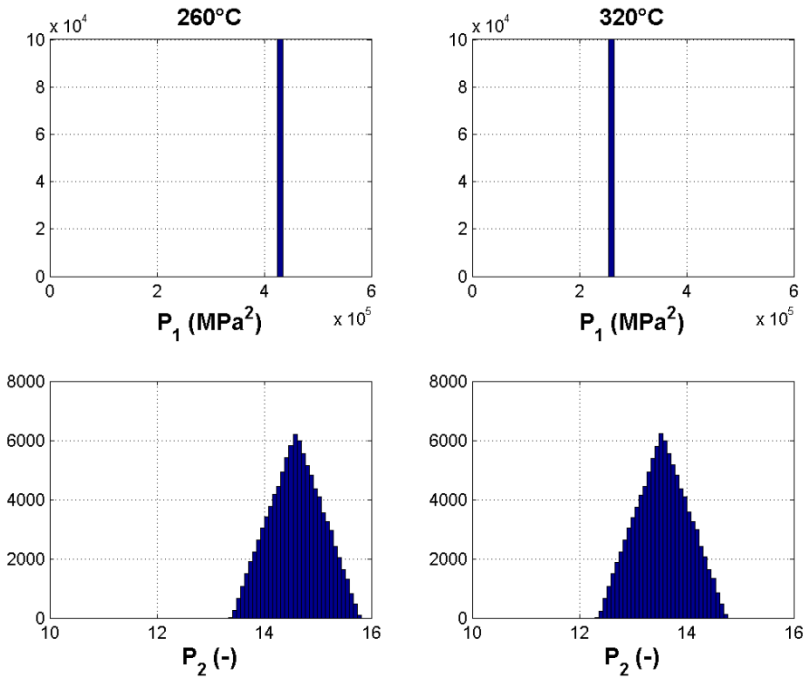

(c)

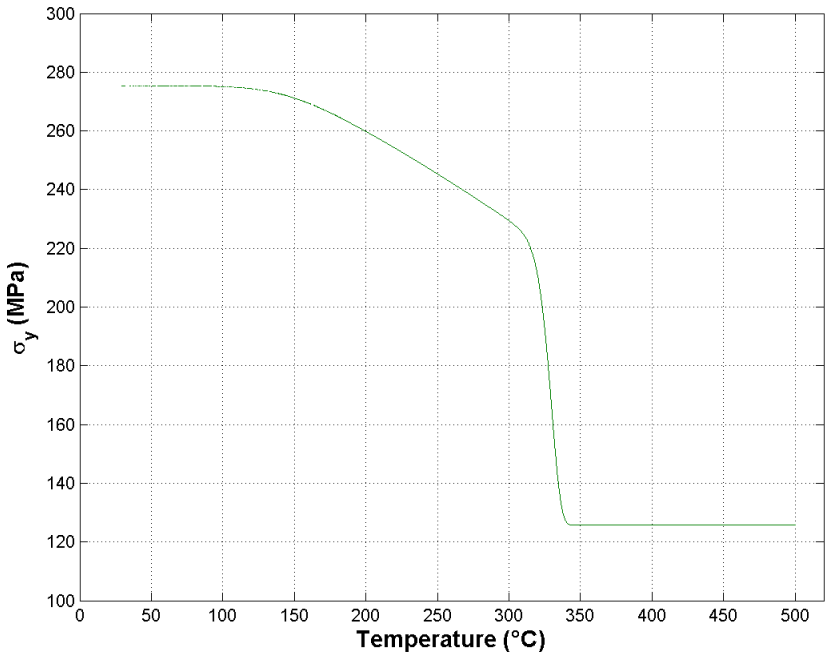

(d)

Fig. A-12. Monte Carlo analysis of θ_0 on AA5083-H116 constitutive model predictions.

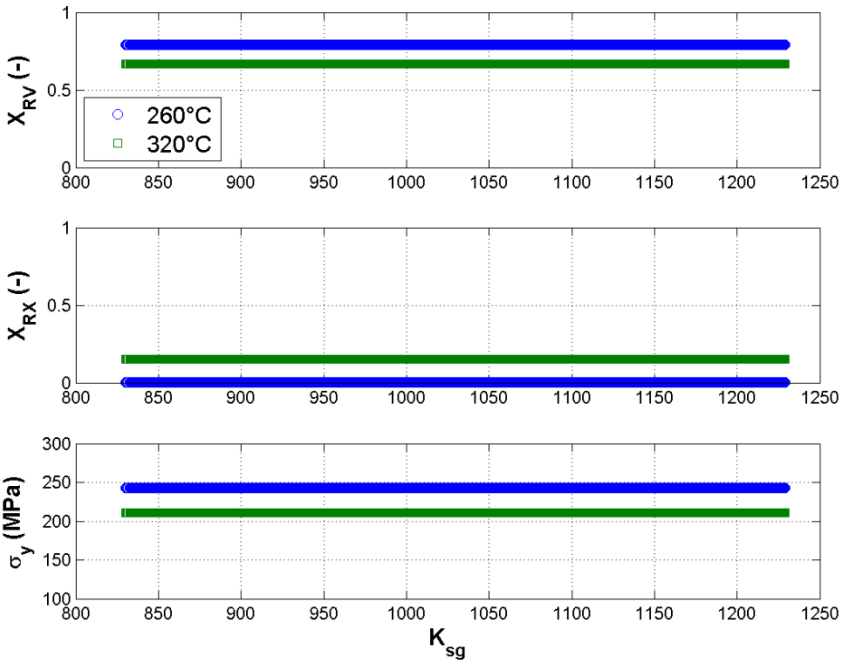

(a)

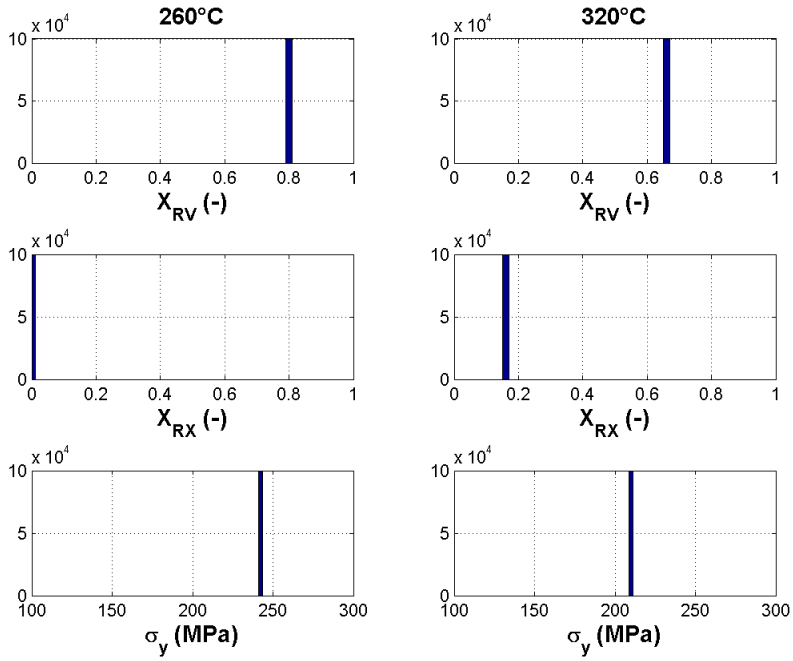

(b)

(Figure continued on next page)

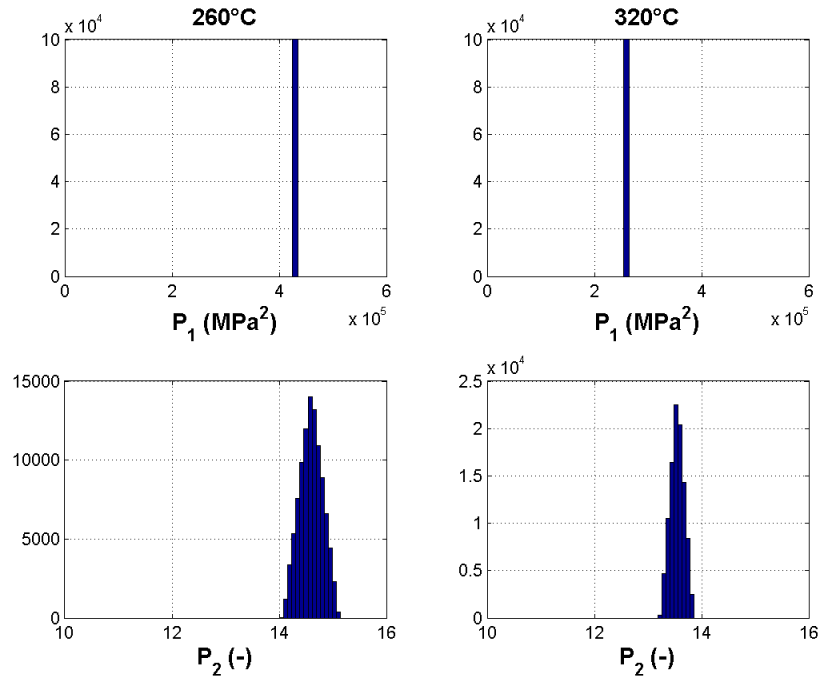

(c)

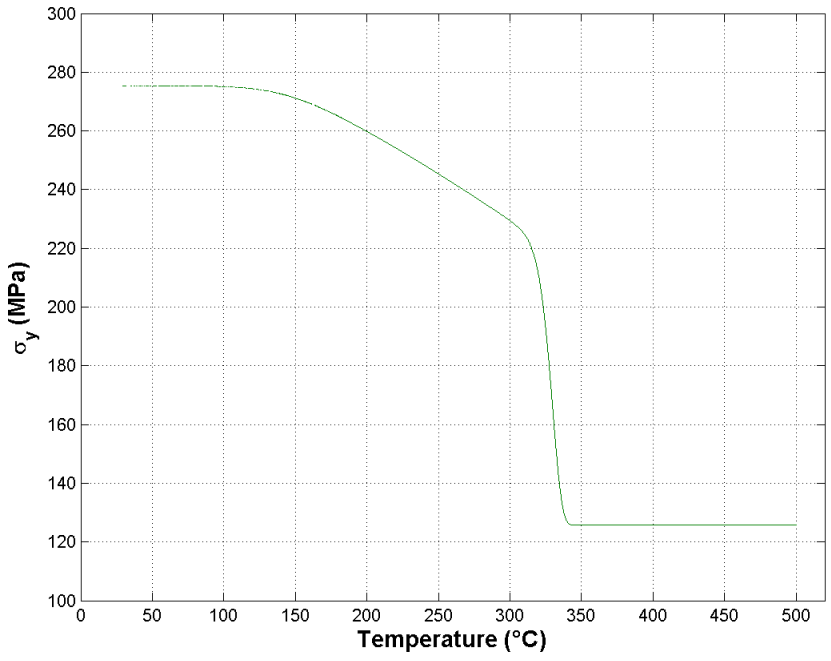

(d)

Fig. A-13. Monte Carlo analysis of K_{sg} on AA5083-H116 constitutive model predictions.

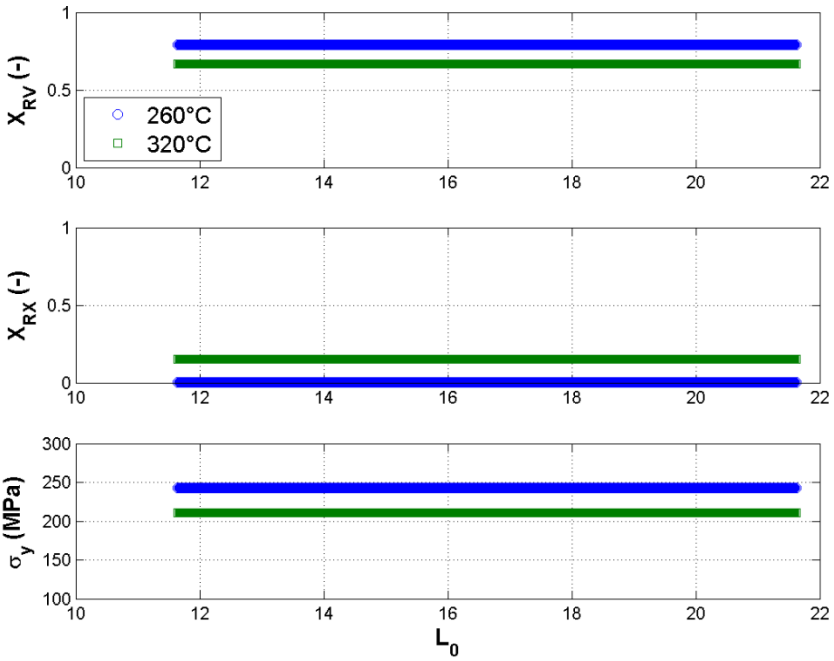

(a)

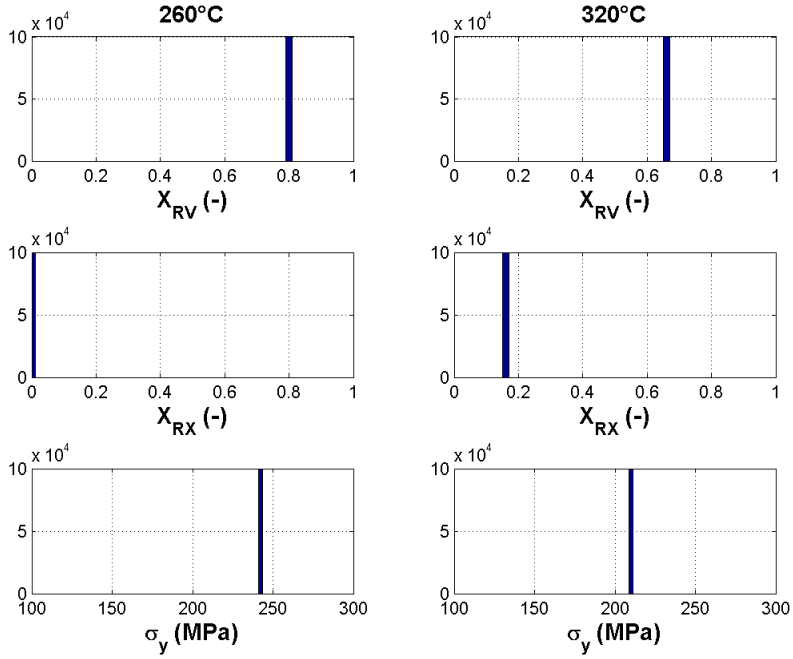

(b)

(Figure continued on next page)

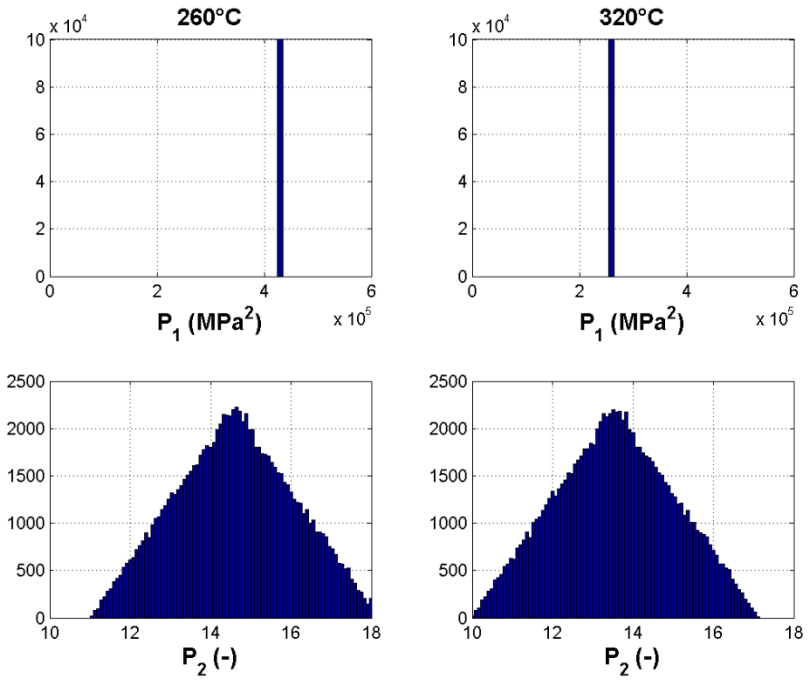

(c)

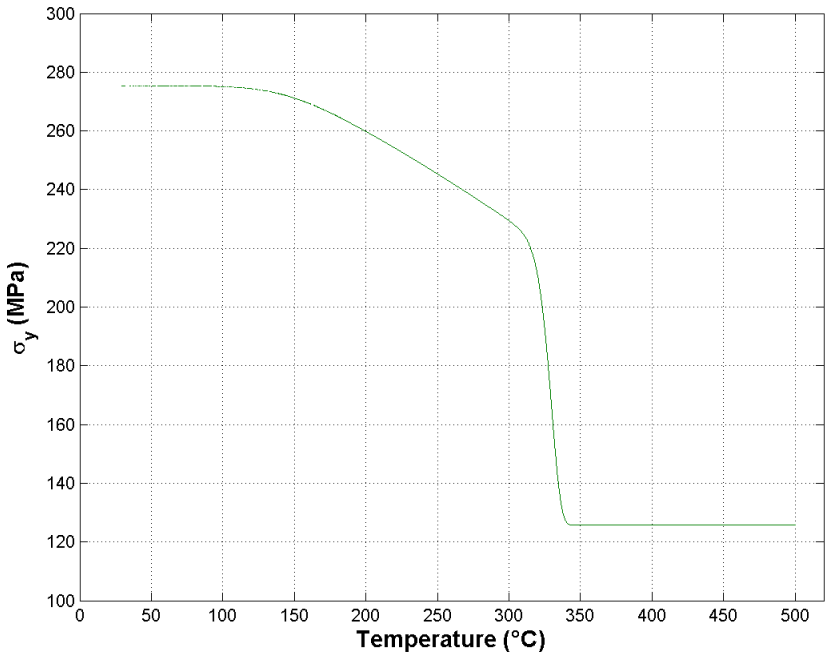

(d)

Fig. A-14. Monte Carlo analysis of L_0 on AA5083-H116 constitutive model predictions.

Appendix B - AA6061-T651 Constitutive Model Monte Carlo Analysis

Monte Carlo analysis was performed using 10^4 simulation runs for each non-constant parameter (refer to Table B-1) in the AA6061-T651 constitutive model (heating at 20°C/min). Pseudorandom numbers from the listed distributions were generated with Matlab algorithms using a single command to ensure all pseudorandom numbers were generated using the same seed. Model results (X_{RV}, X_{RX}, and σ_y) were probed at 300°C and 350°C to elucidate the effects of each parameter during precipitate nucleation, growths, and dissolution. An analysis summary is provided in Fig. B-1. Individual parameter effects are shown in the subsequent figures including (a) model predictions as a function of parameter value, (b),(c) model prediction histograms at 300°C and 350°C, and (d) yield strength as a function of temperature for 100 randomly selected parameter instances.

Table B-1. Parameter distributions for AA6061-T651 constitutive model Monte Carlo analysis.

Parameter	**Distribution**	**Distribution Parameters**	**Assumed From**
$r_{AR}\,(mean)$	Constant		Fig. 42 [38]
C_{Mg}^{0}	Constant		Table 8
C_{Mg}^{p}	Constant		[39]
A_0	Normal	μ = 18.6 kJ/mol; σ = 0.93 kJ/mol	DSC error (5% of mean)
j_0	Normal	$\mu = 3\text{x}10^{37}$; $\sigma = 1.5\text{x}10^{36}$ #/m^3-s	Same as for A_0
V_m	Constant		[39]
$C_{Mg,0}^{eq}$	Normal	μ = 290 wt%; σ = 14.5 wt%	5% mean error
Q_{eq}	Normal	μ = 41 kJ/mol; σ = 2.05 kJ/mol	5% mean error
D_0	Uniform	$a = 10^{-4}$ m^2/s; $b = 2.2\text{x}10^{-4}$ m^2/s	D_0 from Ref. [38] and from Ref. [40]
Q_d	Constant		[108]
γ	Normal	μ = 0.108 J/m^2; σ = 0.011 J/m^2	10% mean error
M	Constant		Textured alloy [38]
G	Constant		[37,39,40]
b	Constant		
σ_0	Constant		[37,39,40]
H_{Cu}	Constant		[37,39,40]
H_{Mg}	Constant		[37,39,40]
H_{Si}	Constant		[37,39,40]
r_{trans}	Normal	μ = 3.044 nm; σ = 0.032 nm	10% of as-received PSD standard deviation
k_Γ	Normal	μ = 0.40; σ = 0.02	95% of possible values lie within 5% of mean

(Table continued on next page)

θ_0	Normal	μ = 655 MPa; σ = 32.8 MPa	5% measurement error
β_{min}	Normal	μ = 5.9; σ = 0.3	5% measurement error
$k_{\theta dp}$	Normal	μ = 1210 MPa; σ = 60.5 MPa	5% measurement error
σ_y^{max}	Normal	μ = 324 MPa; σ = 6.5 MPa	2% measurement error
k_β	Normal	μ = 10.6; σ = 0.53	5% measurement error
r_{cl}	Triangular	a = 8; c = 8; b = 25 nm	Range of possible values
L_0	Normal	μ = L_0 calculated; σ = 5% of L_0	5% measurement error
α	Uniform	a = 0.15; b = 0.30	Range of possible values
y_p	Normal	μ = 13 nm; σ = 0.65 nm	5% measurement error

Normal distribution probability density function definition:

$$f(x) = \frac{1}{\sigma\sqrt{2\pi}} \exp\left(-\frac{(x-\mu)^2}{2\sigma^2}\right) \tag{130}$$

Uniform distribution probability density function definition:

$$f(x) = \begin{cases} \dfrac{1}{b-a} & \text{for } a \le x \le b \\ 0 & \text{for } x < a \text{ or } x > b \end{cases} \tag{131}$$

Triangular distribution probability density function definition:

$$f(x) = \begin{cases} 0 & \text{for } x < a \\ \dfrac{2(x-a)}{(b-a)(c-a)} & \text{for } a \le x \le c \\ \dfrac{2(b-x)}{(b-a)(b-c)} & \text{for } c \le x \le b \\ 0 & \text{for } b < x \end{cases} \tag{132}$$

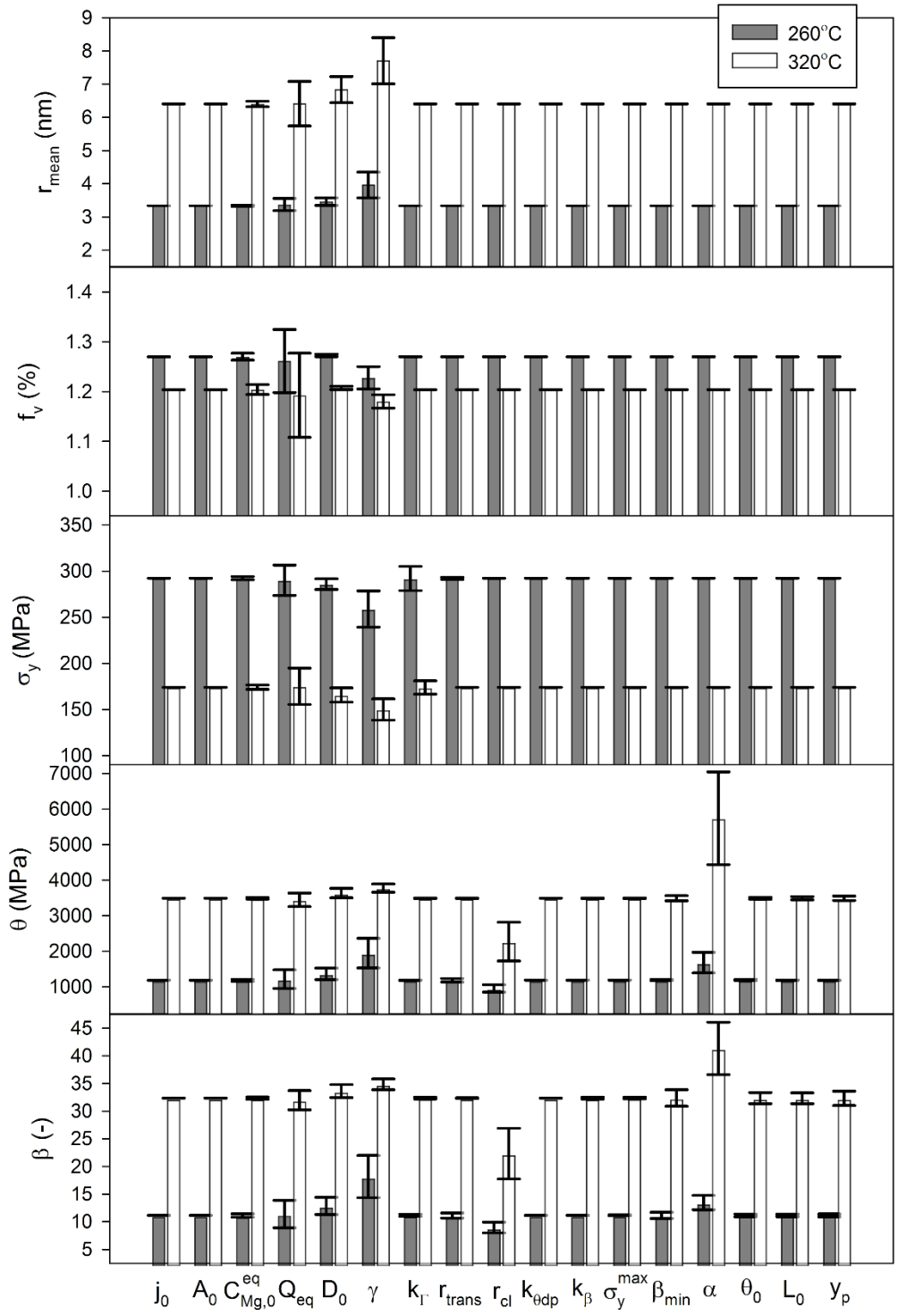

Fig. B-1. AA6061-T651 constitutive model Monte Carlo analysis for mean effects for exposure at 20°C/min to 300°C and 350°C, including effects on microstructural evolution ($\bar{r}$ and f_v), yield strength (σ_y), and strain hardening (θ and β).

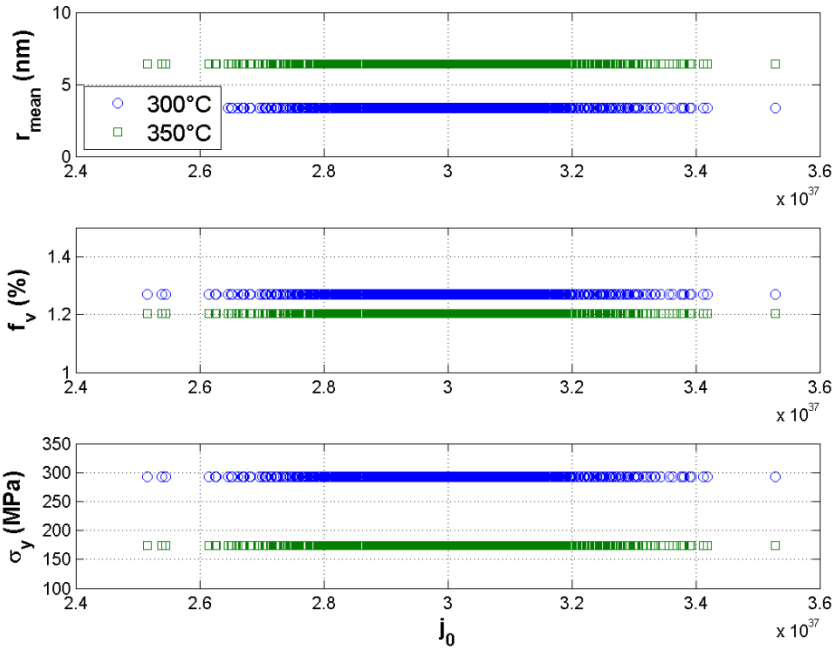

(a)

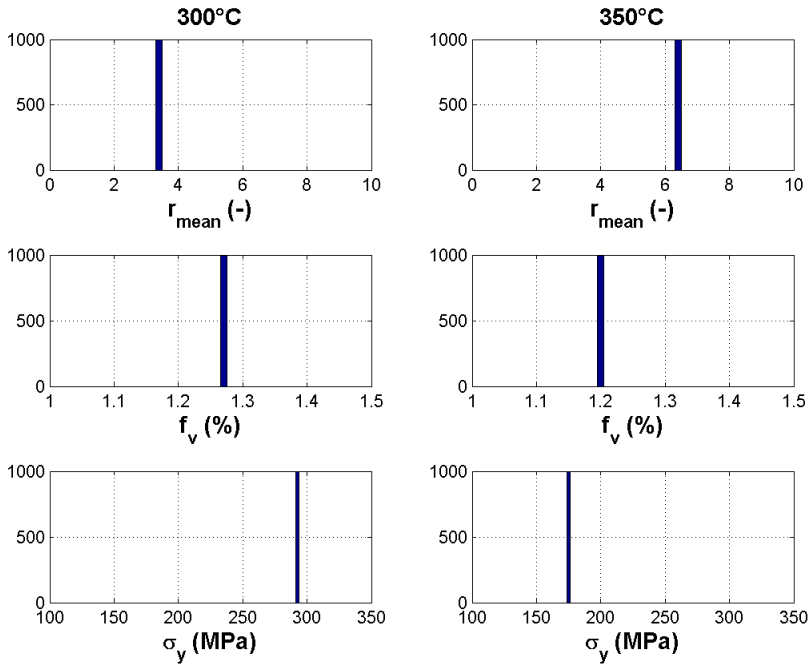

(b)

(Figure continued on next page)

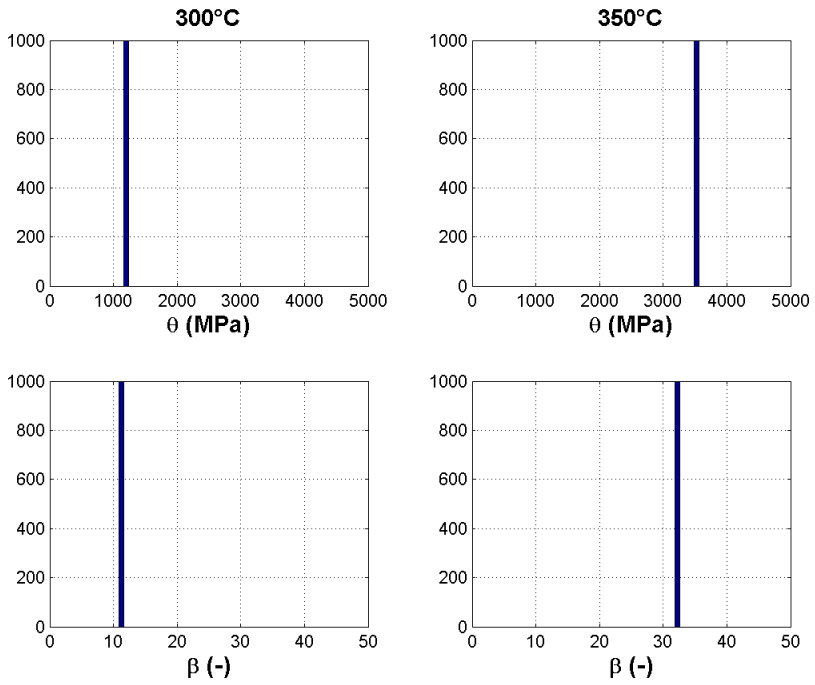

(c)

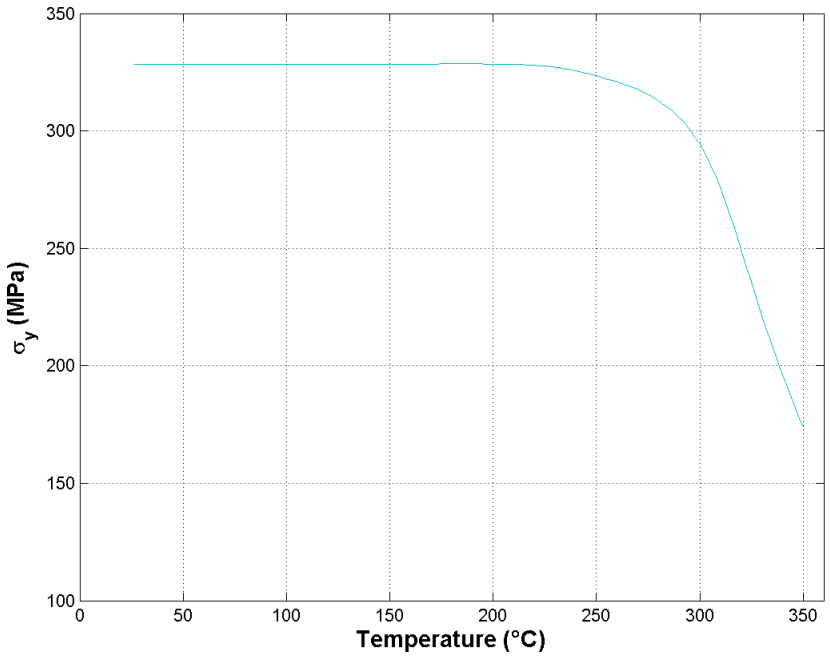

(d)

Fig. B-2. Monte Carlo analysis of j_0 on AA6061-T651 constitutive model predictions.

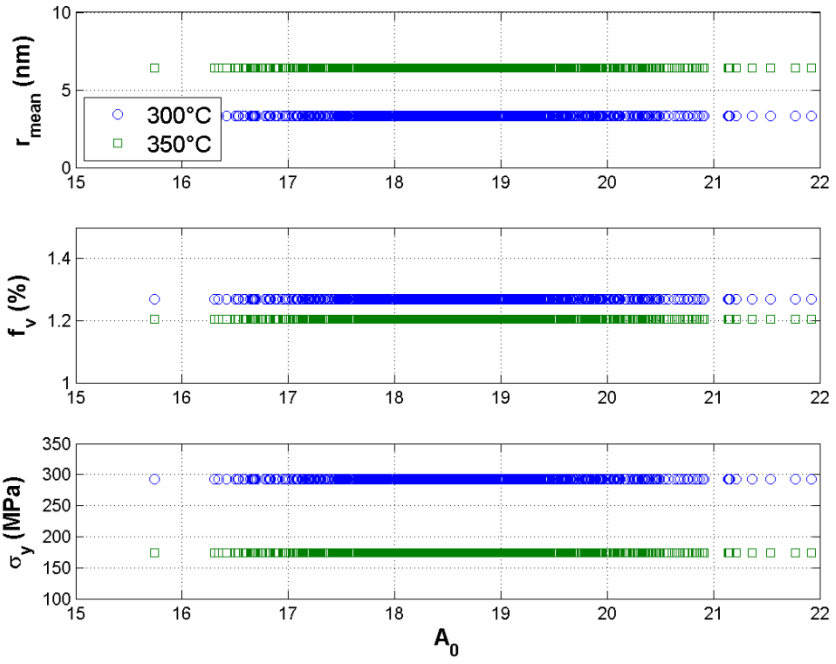

(a)

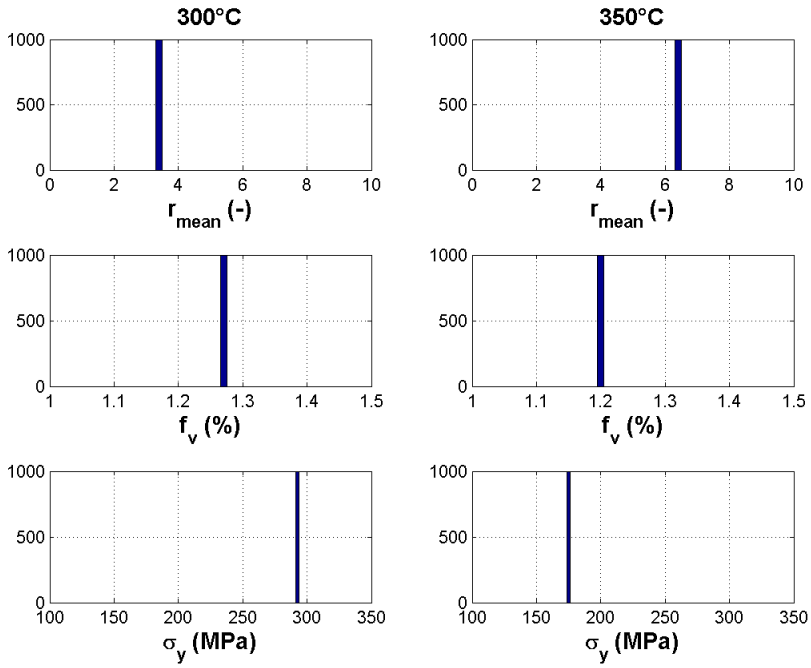

(b)

(Figure continued on next page)

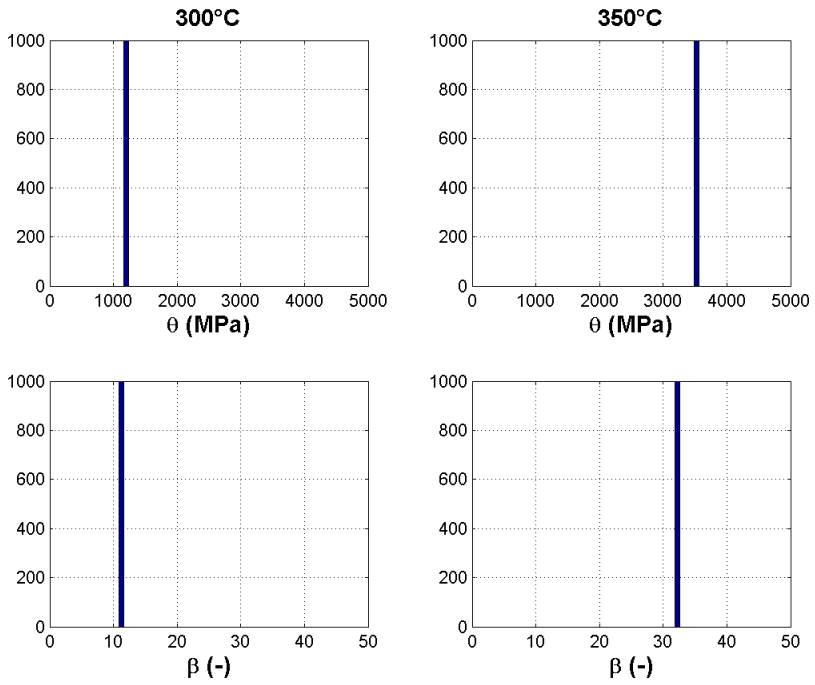

(c)

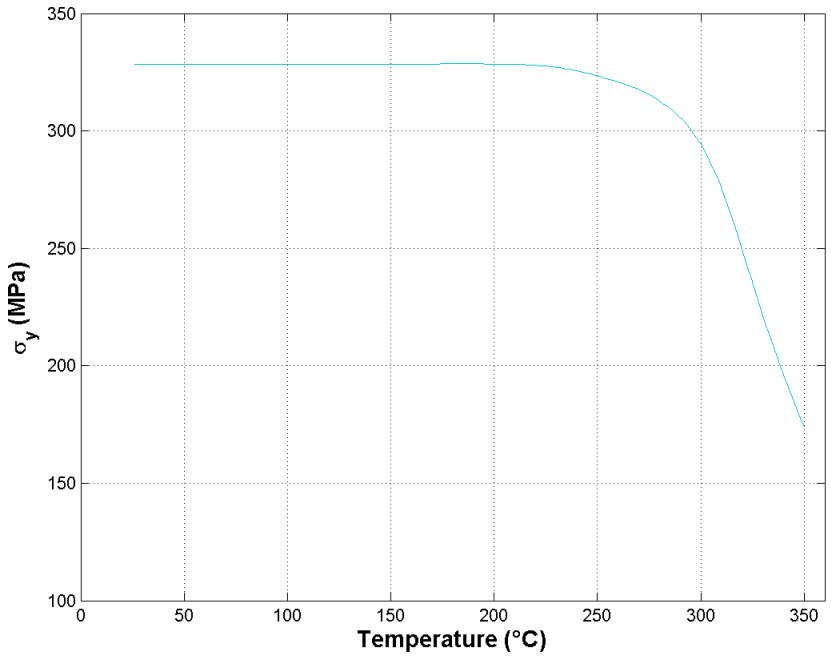

(d)

Fig. B-3. Monte Carlo analysis of A_0 on AA6061-T651 constitutive model predictions.

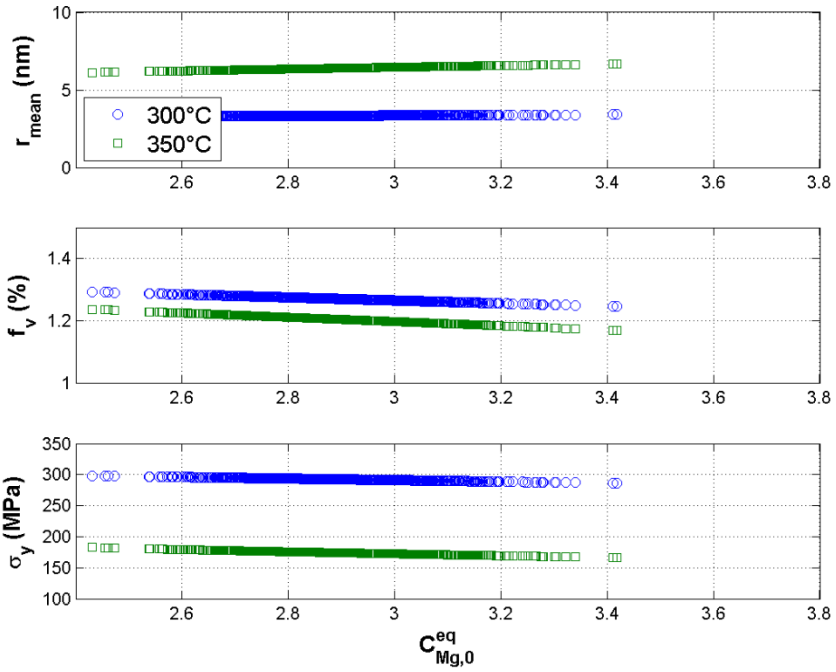

(a)

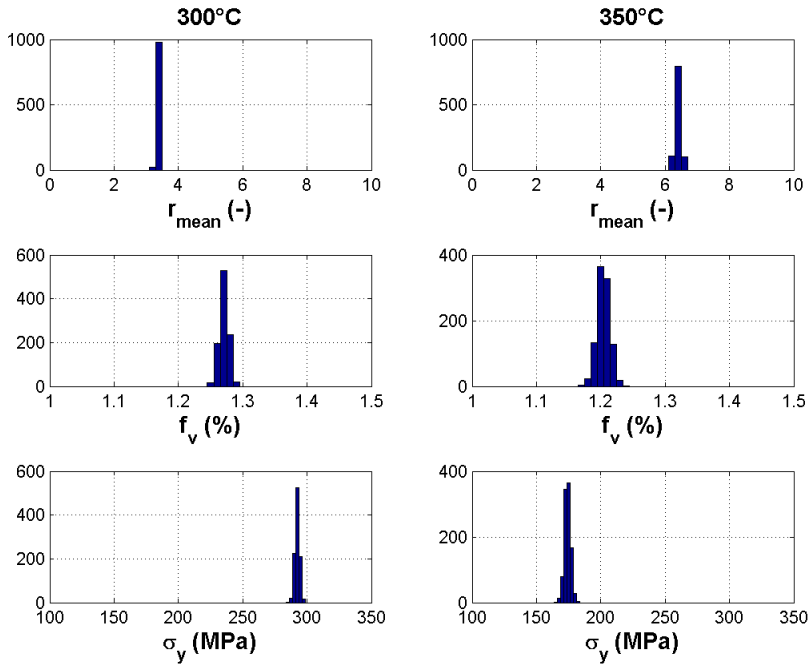

(b)

(Figure continued on next page)

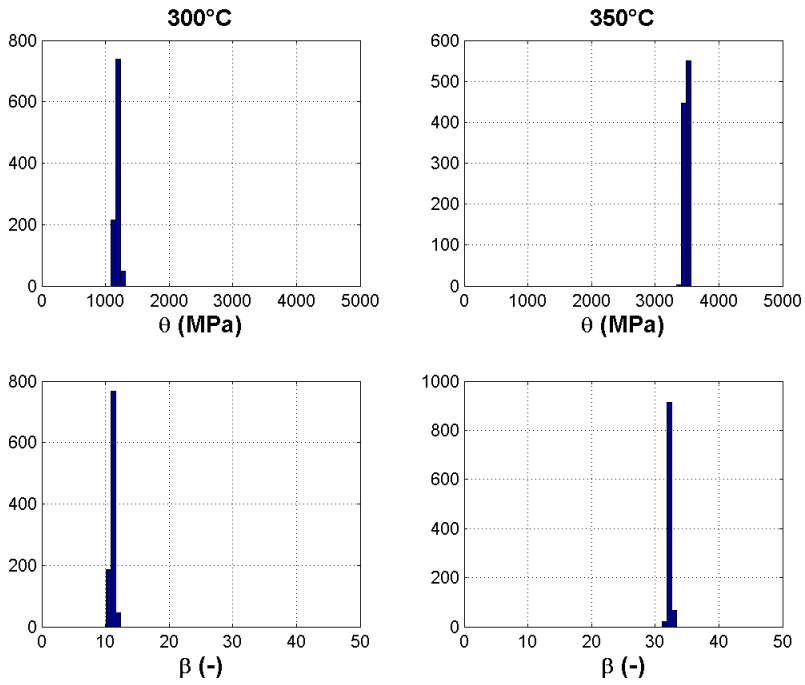

(c)

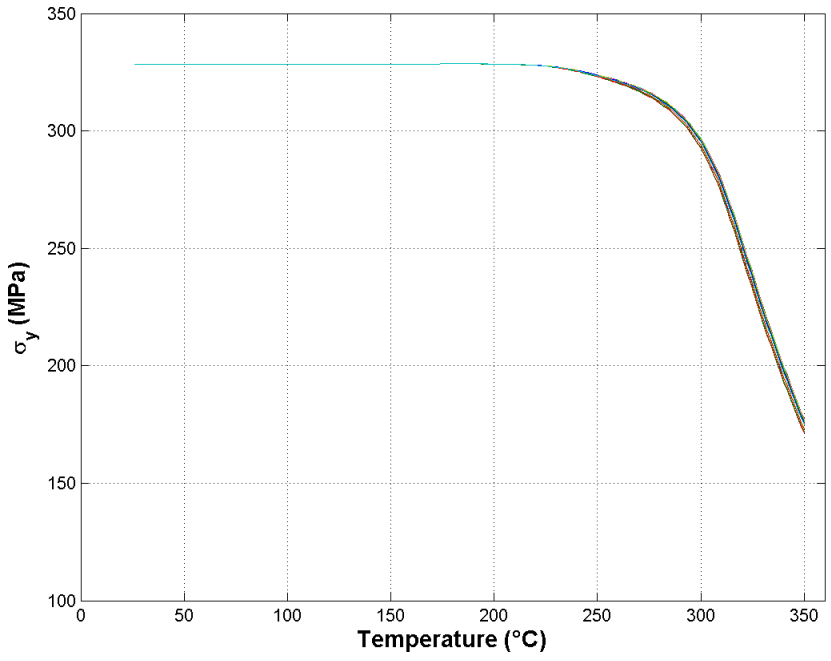

(d)

Fig. B-4. Monte Carlo analysis of $C_{Mg,0}^{eq}$ on AA6061-T651 constitutive model predictions.

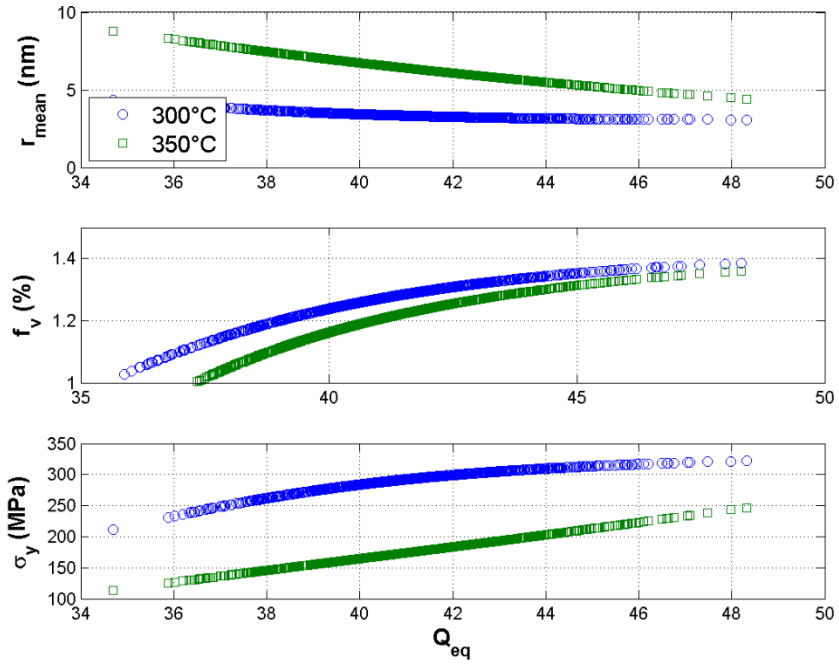

(a)

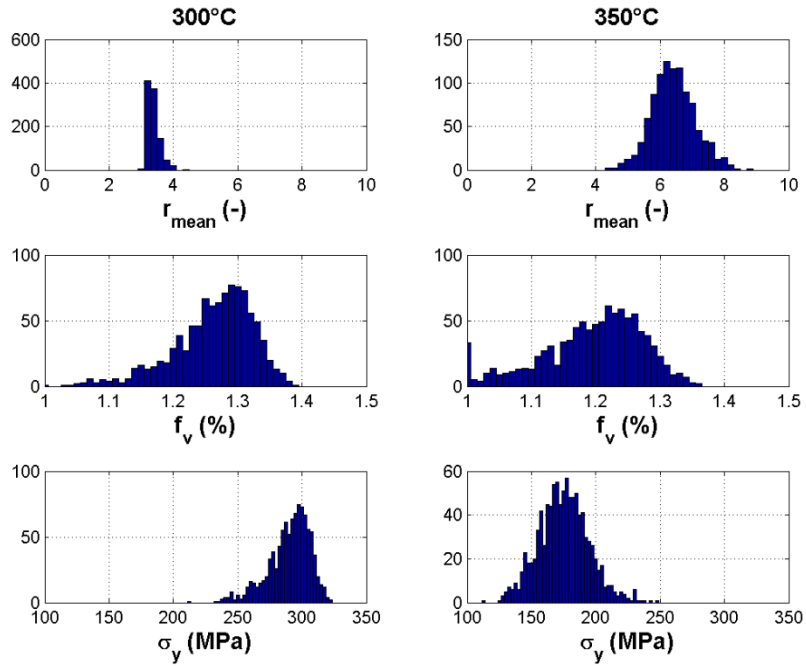

(b)

(Figure continued on next page)

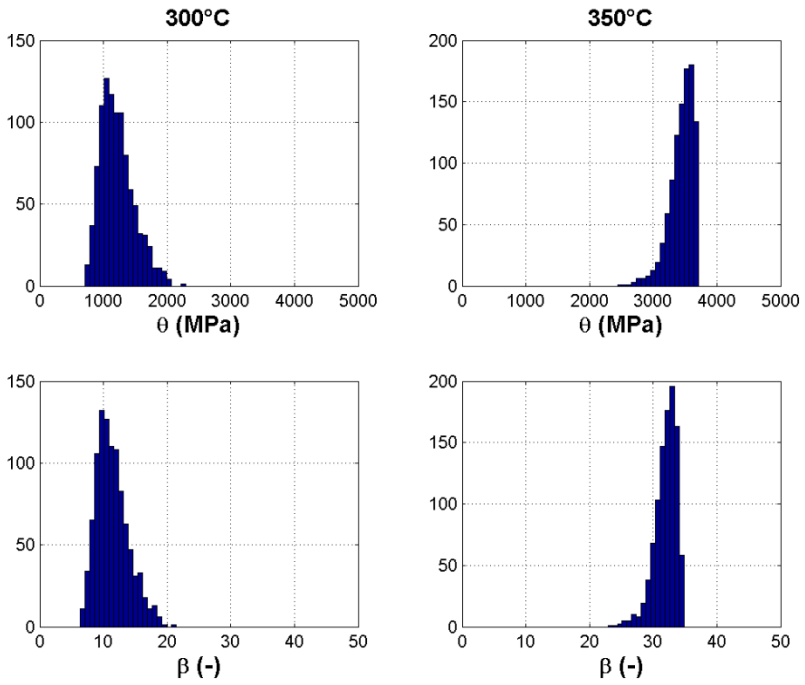

(c)

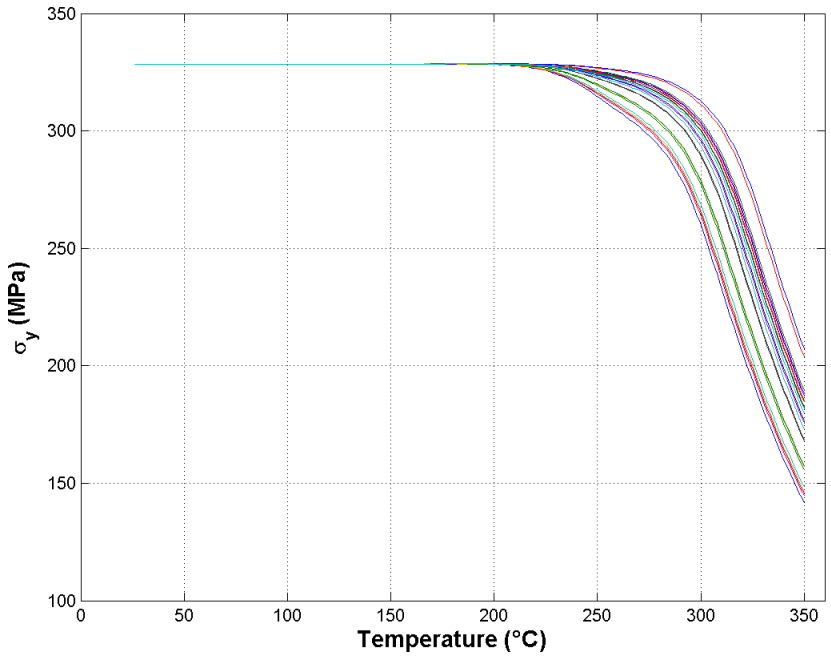

(d)

Fig. B-5. Monte Carlo analysis of Q_{eq} on AA6061-T651 constitutive model predictions.

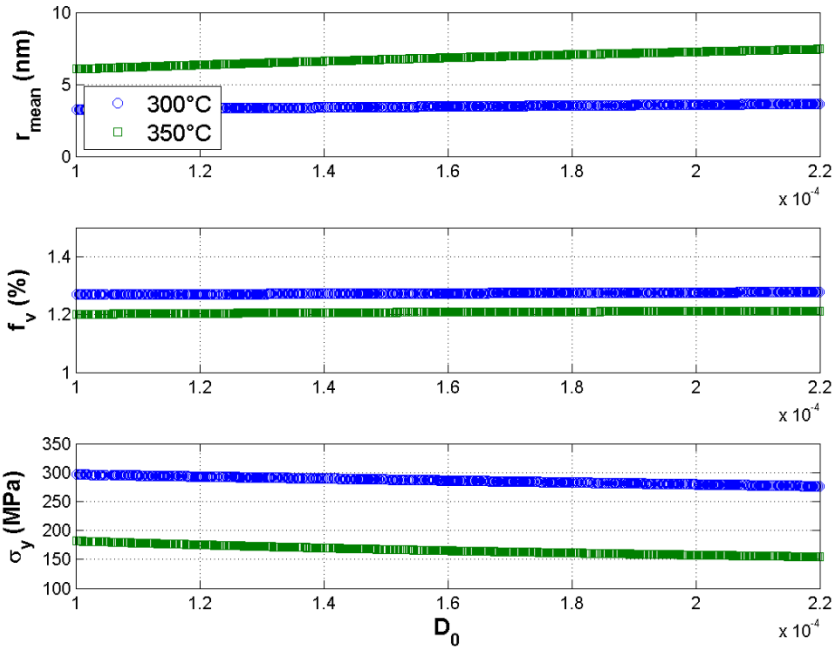

(a)

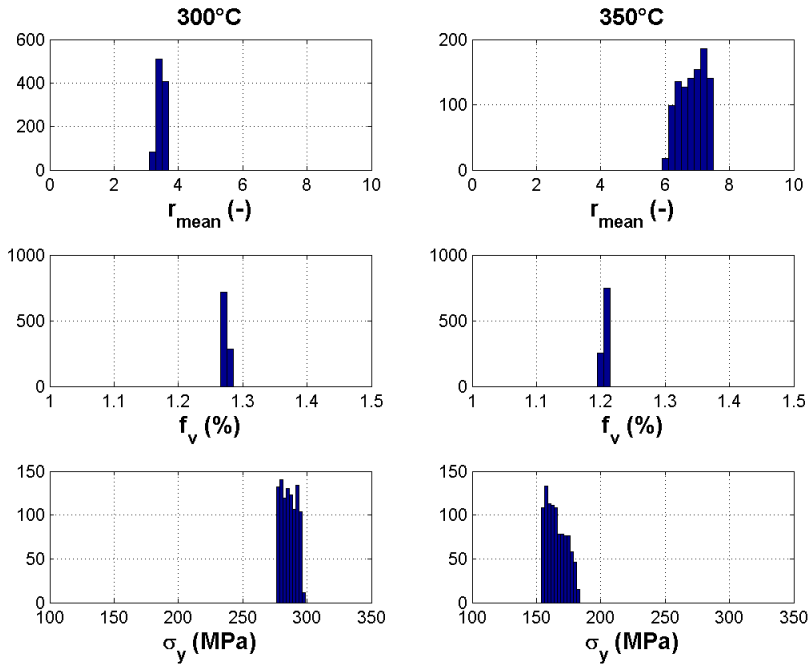

(b)

(Figure continued on next page)

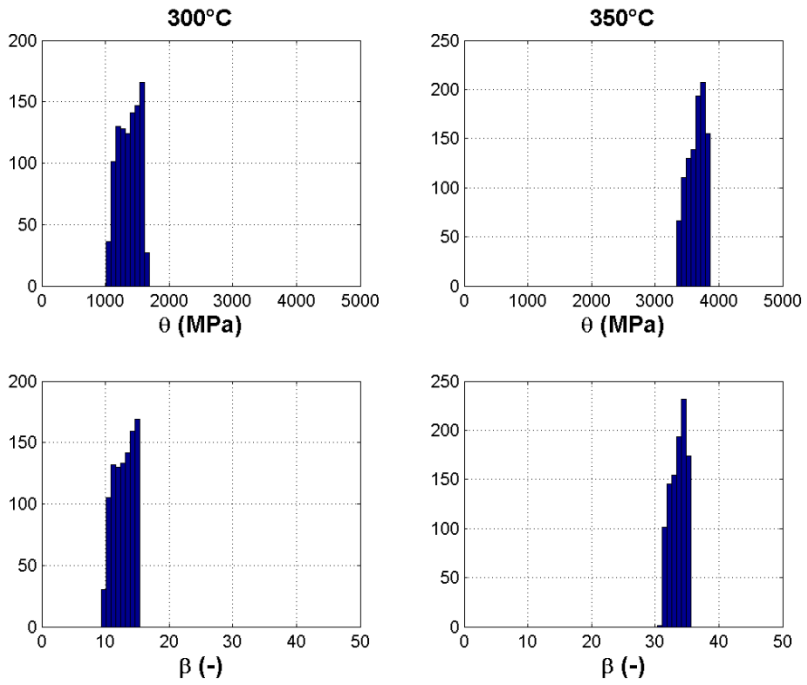

(c)

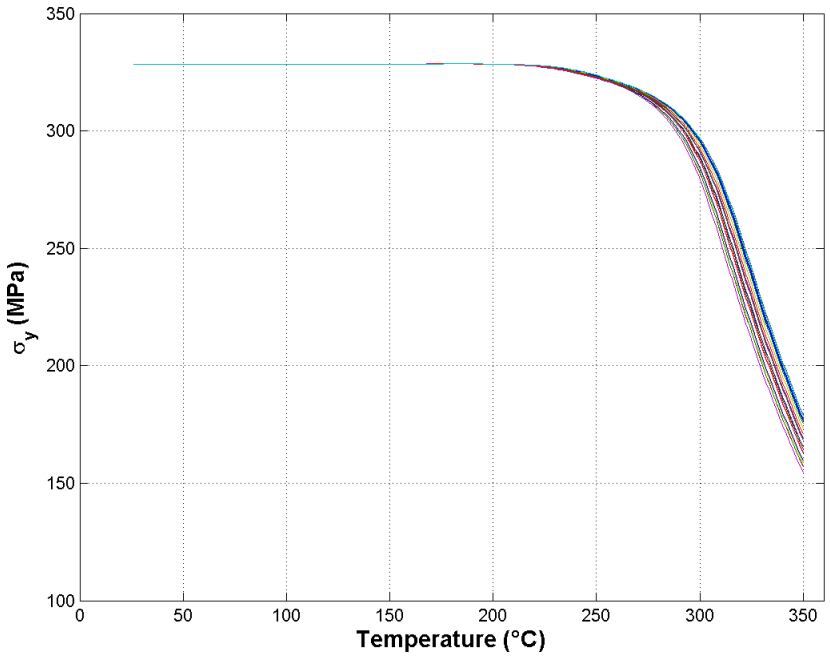

(d)

Fig. B-6. Monte Carlo analysis of D_0 on AA6061-T651 constitutive model predictions.

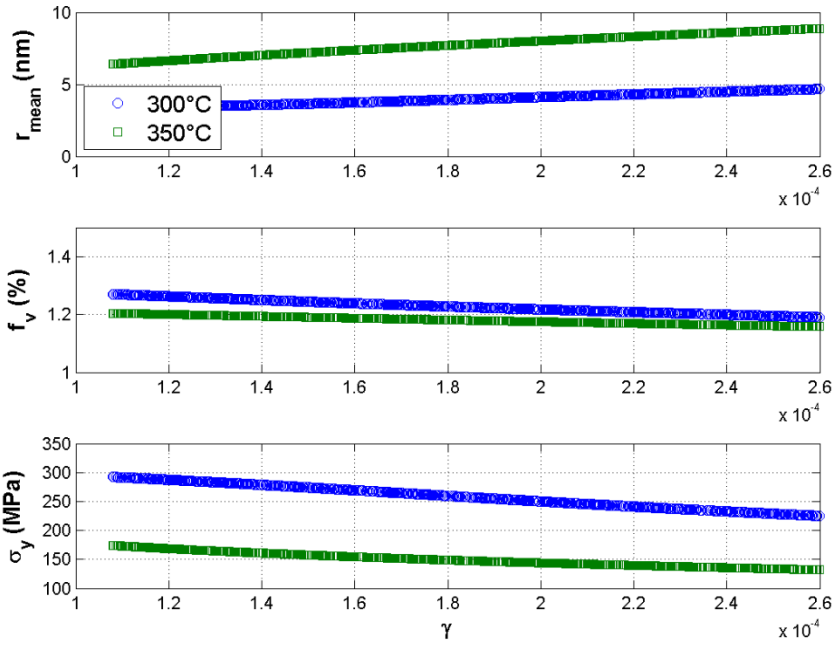

(a)

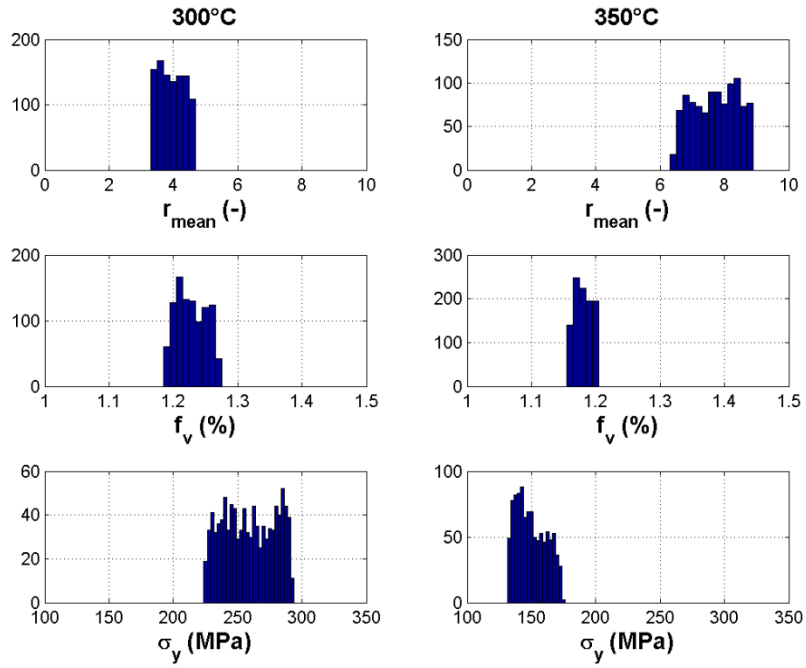

(b)

(Figure continued on next page)

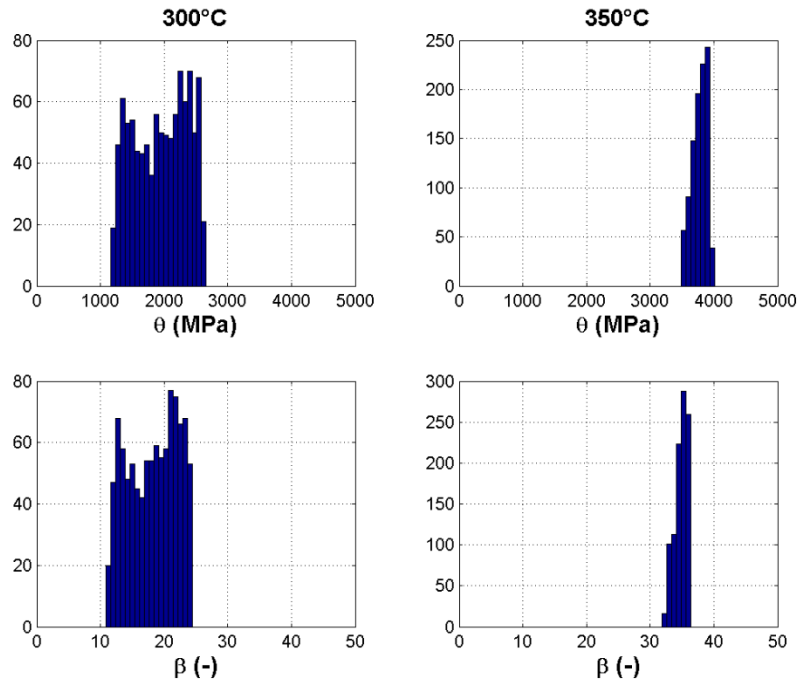

(c)

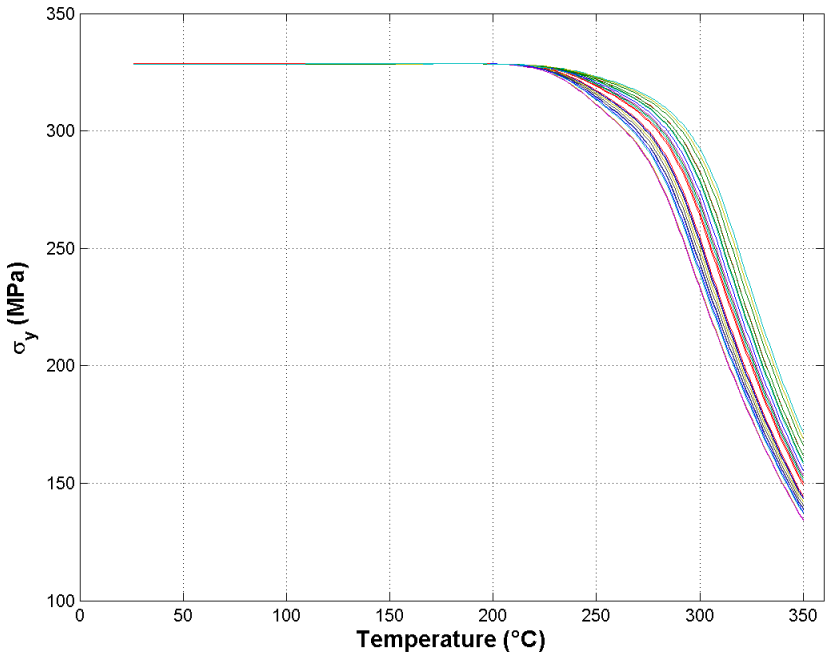

(d)

Fig. B-7. Monte Carlo analysis of γ on AA6061-T651 constitutive model predictions.

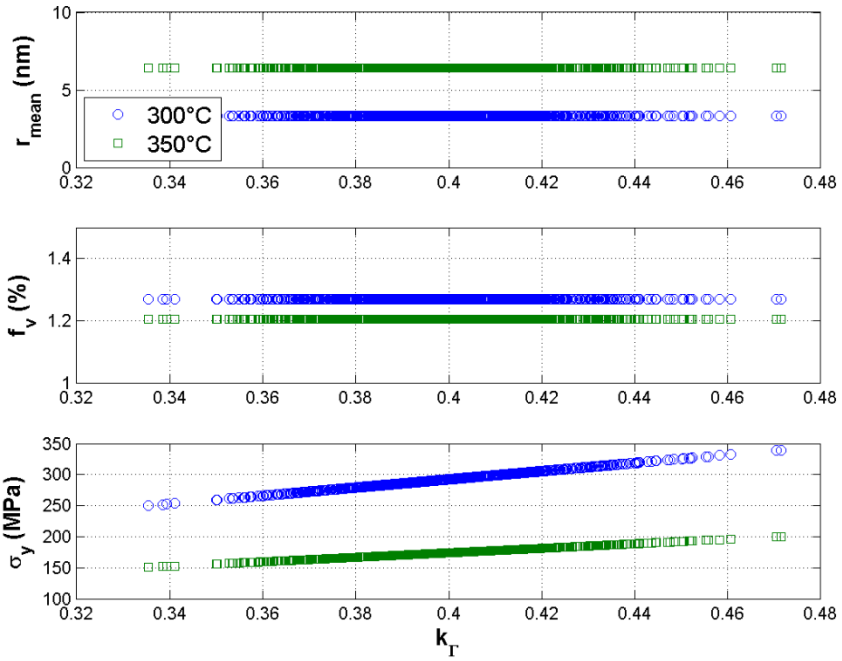

(a)

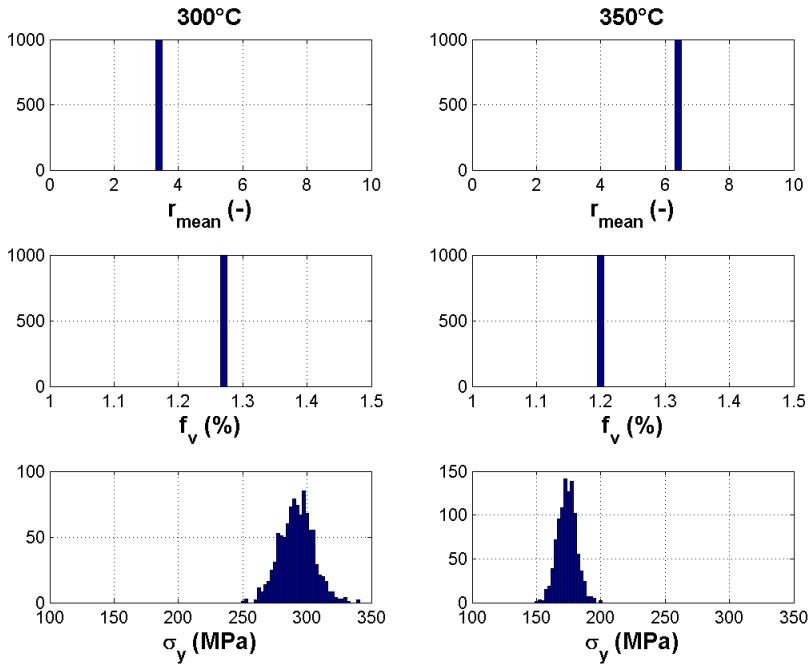

(b)

(Figure continued on next page)

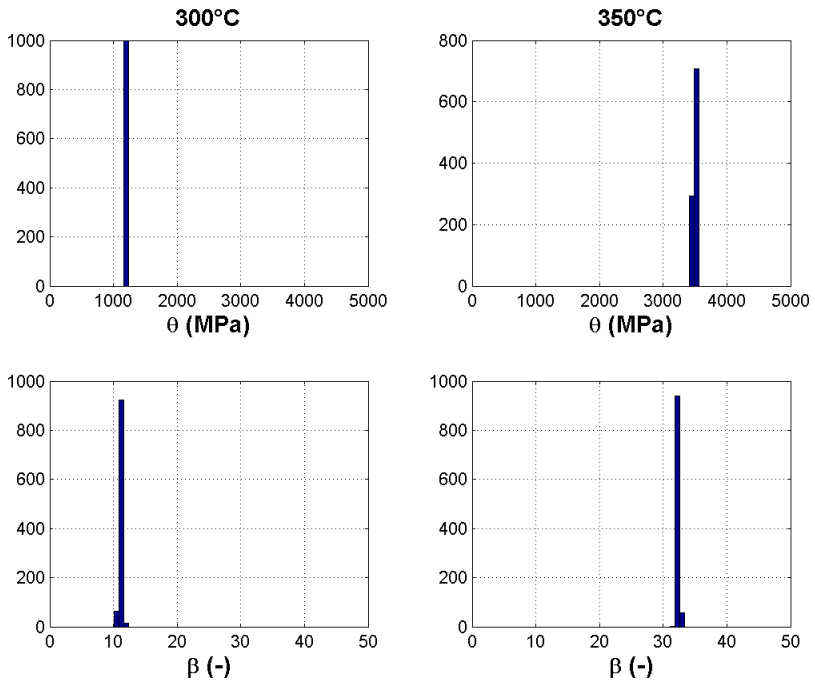

(c)

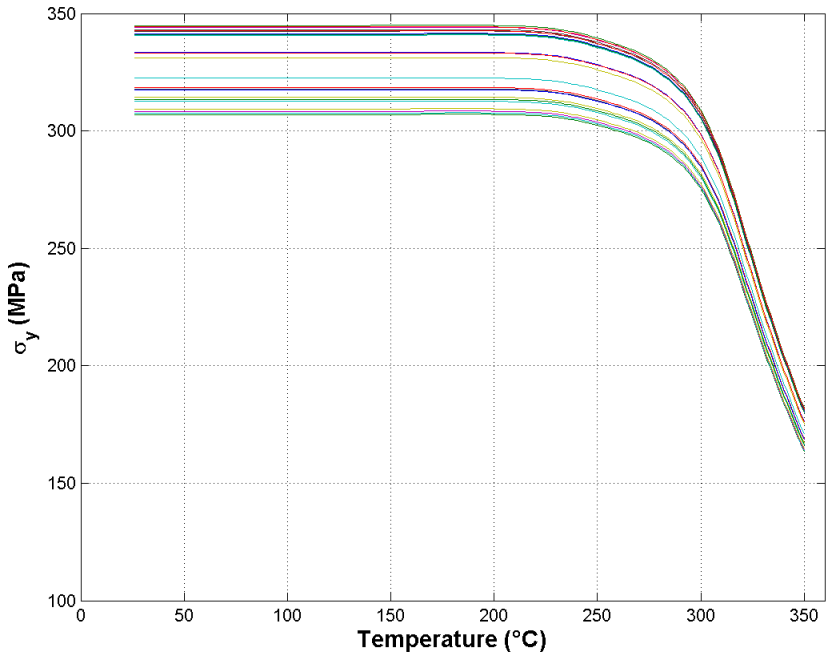

(d)

Fig. B-8. Monte Carlo analysis of k_Γ on AA6061-T651 constitutive model predictions.

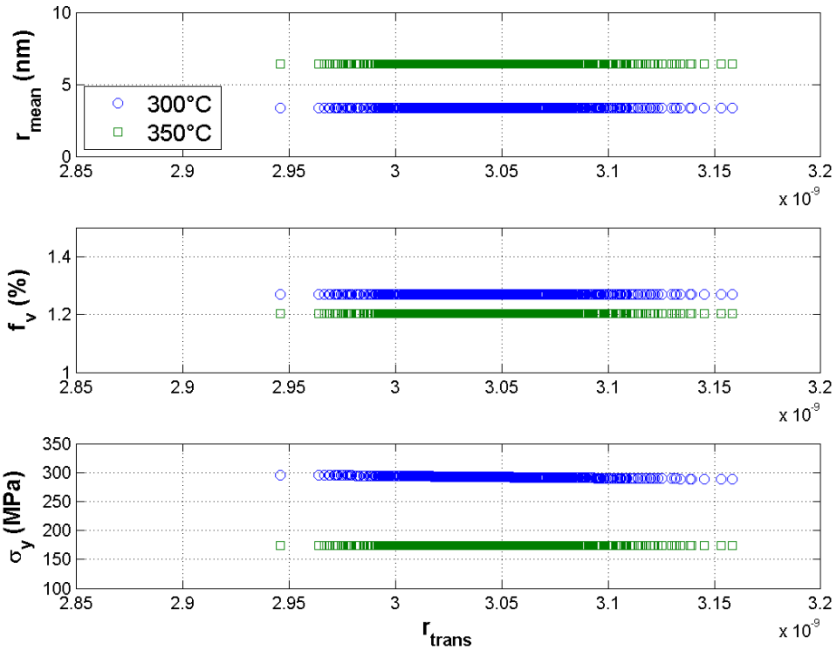

(a)

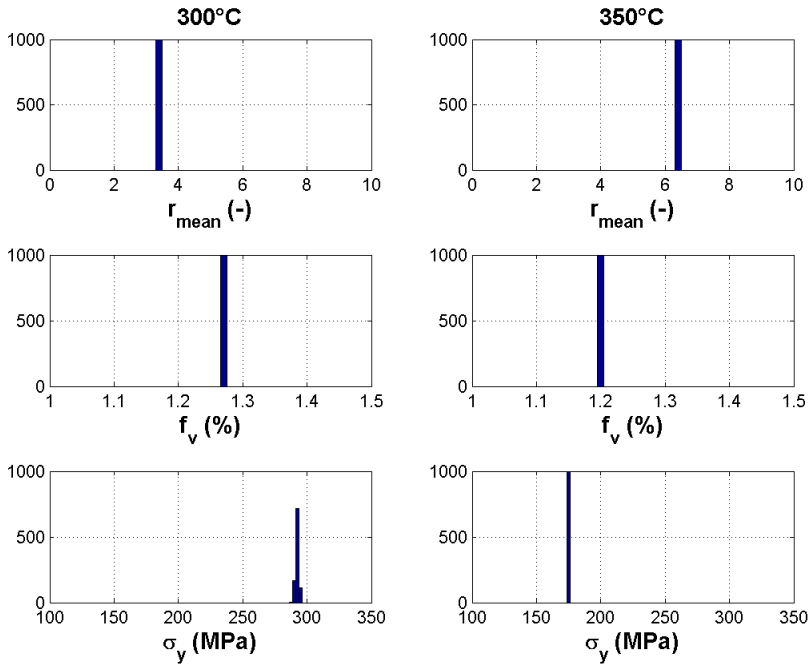

(b)

(Figure continued on next page)

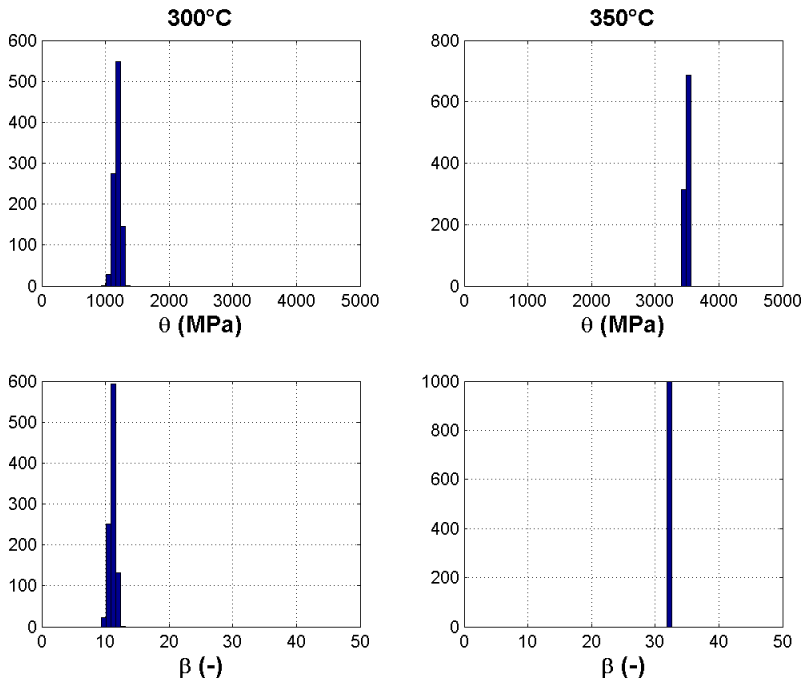

(c)

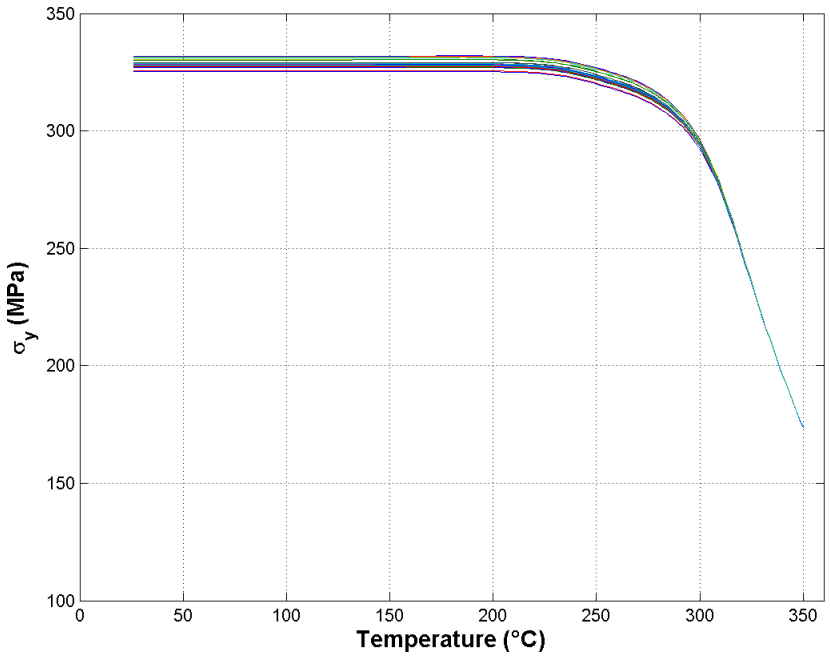

(d)

Fig. B-9. Monte Carlo analysis of r_{trans} on AA6061-T651 constitutive model predictions.

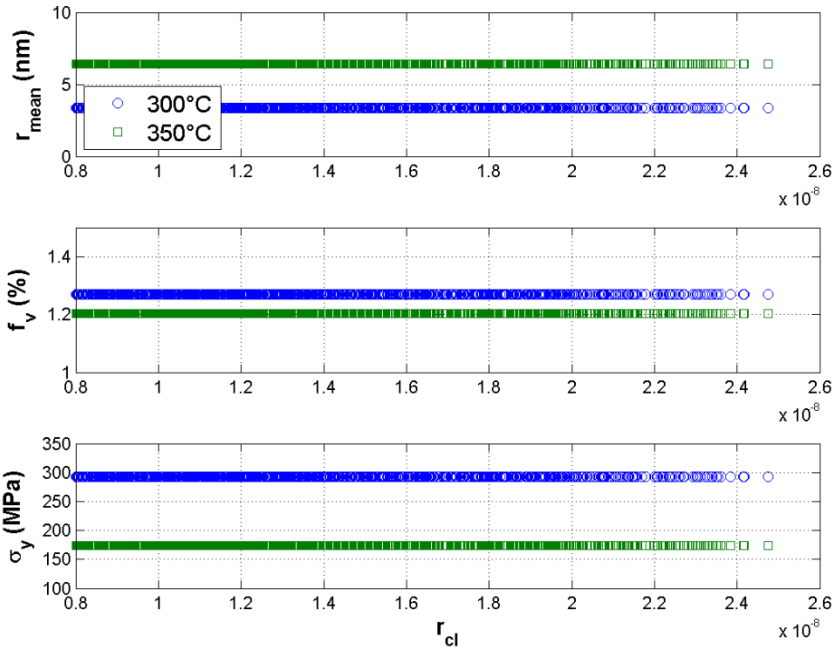

(a)

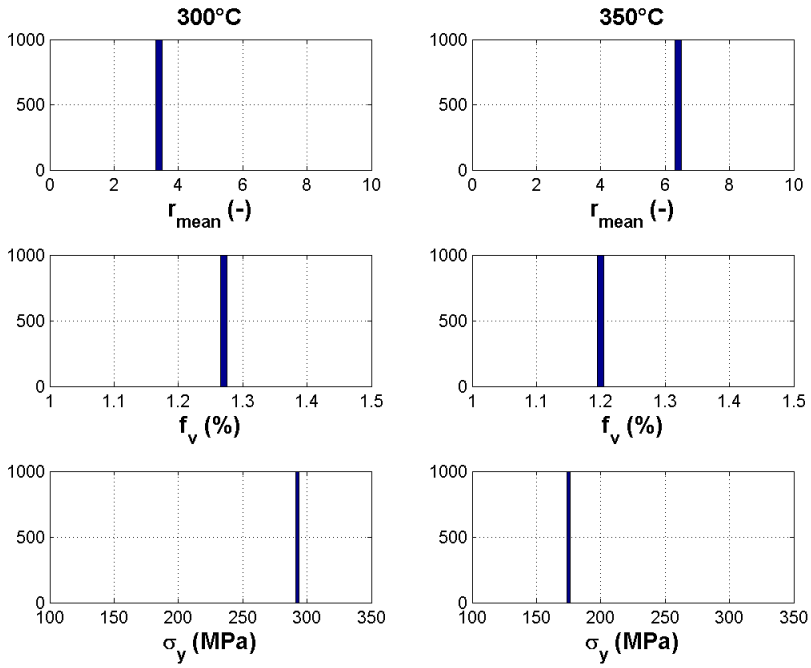

(b)

(Figure continued on next page)

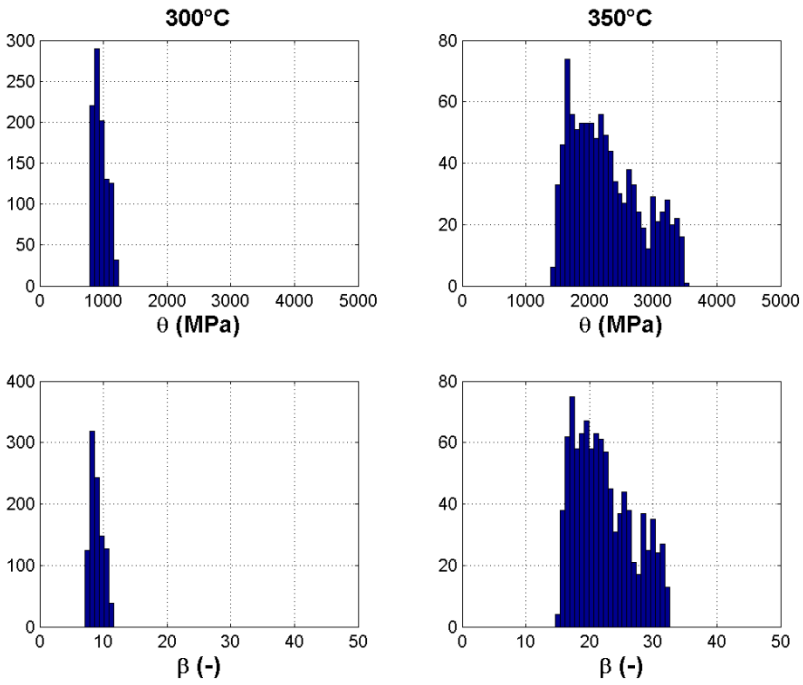

(c)

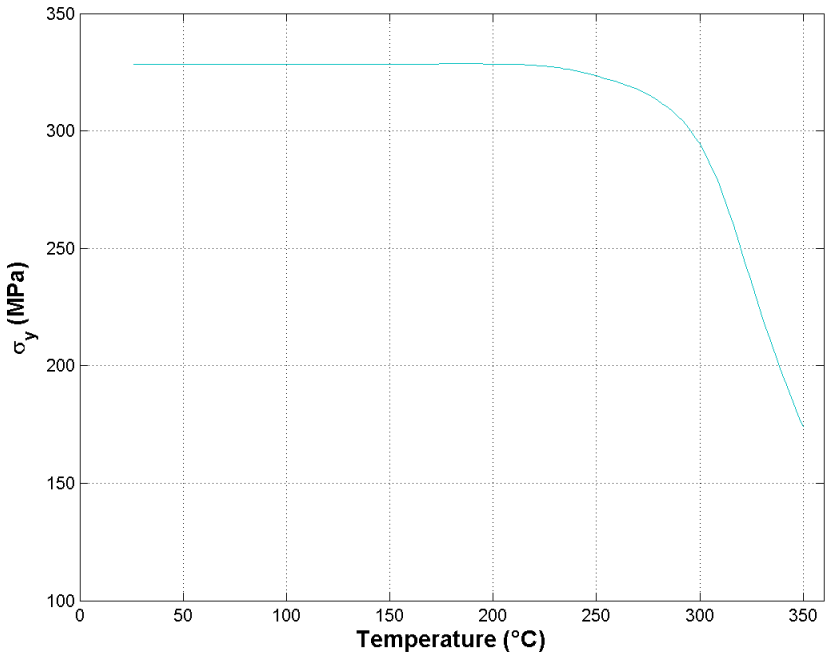

(d)

Fig. B-10. Monte Carlo analysis of r_{cl} on AA6061-T651 constitutive model predictions.

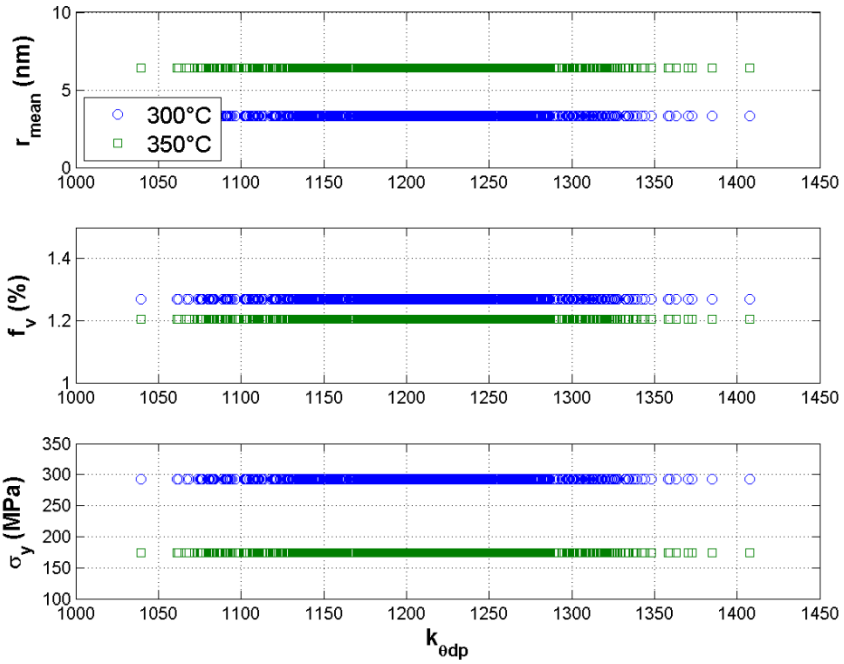

(a)

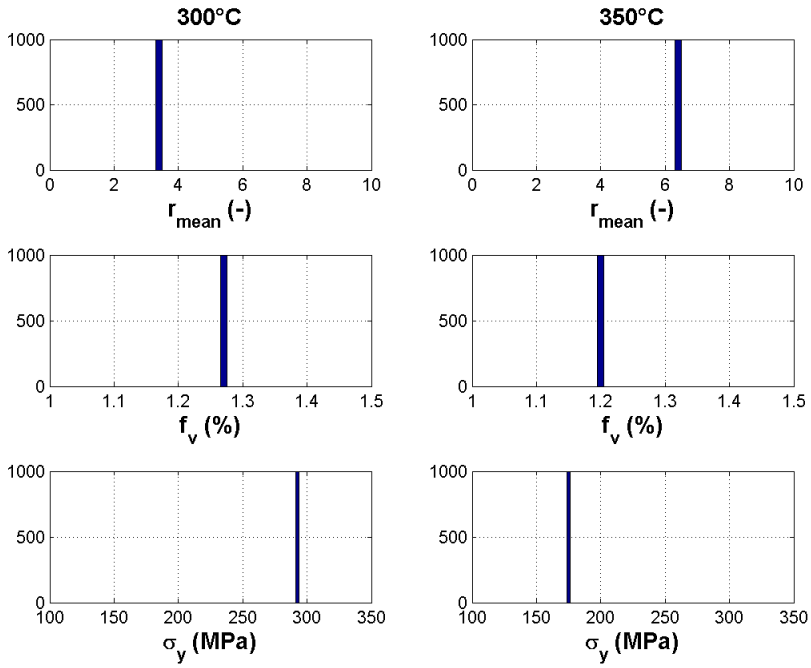

(b)

(Figure continued on next page)

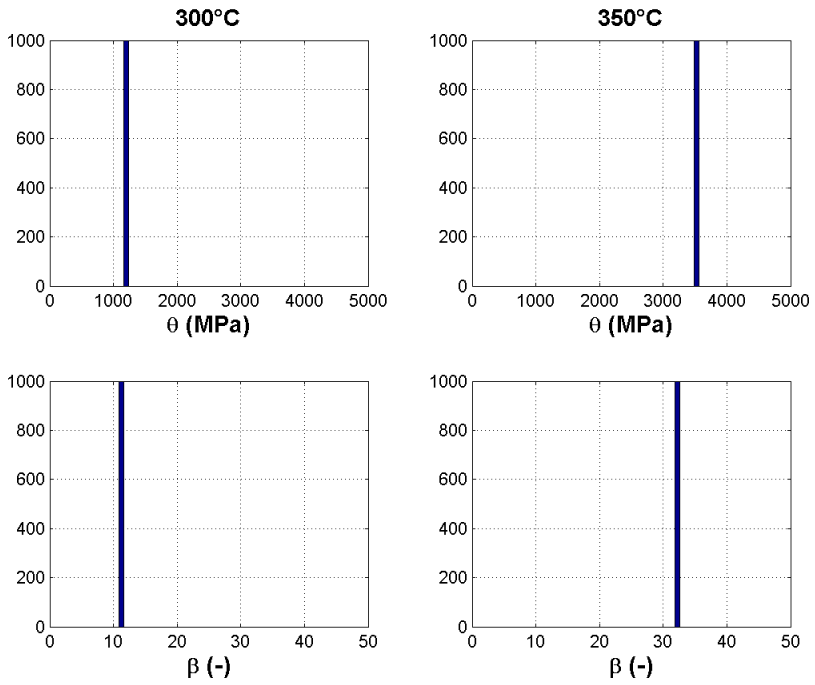

(c)

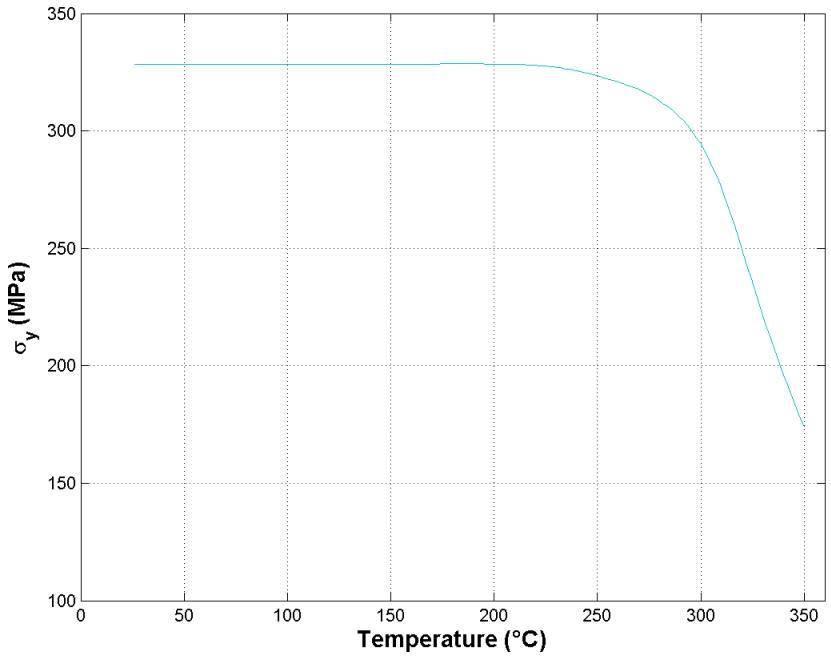

(d)

Fig. B-11. Monte Carlo analysis of $k_{\theta dp}$ on AA6061-T651 constitutive model predictions.

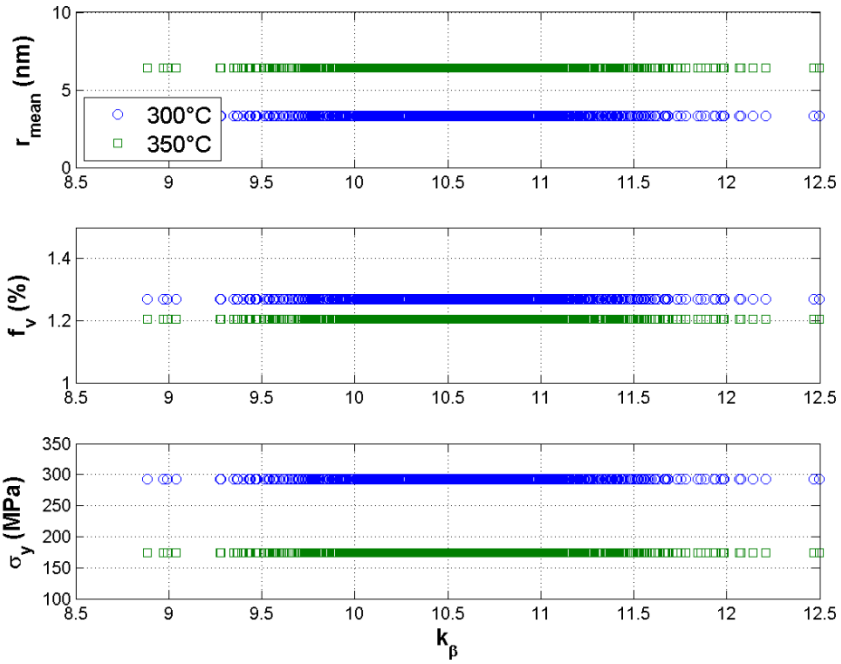

(a)

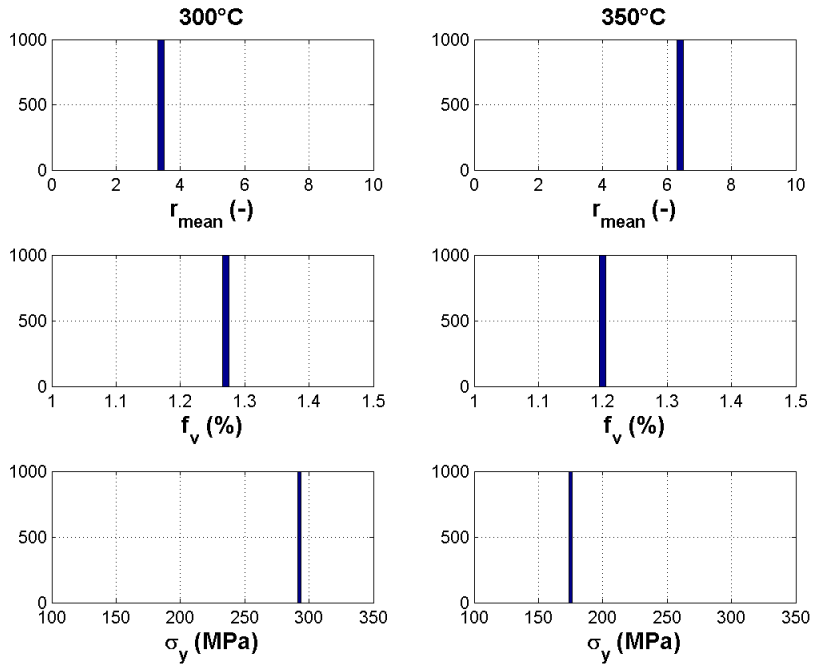

(b)

(Figure continued on next page)

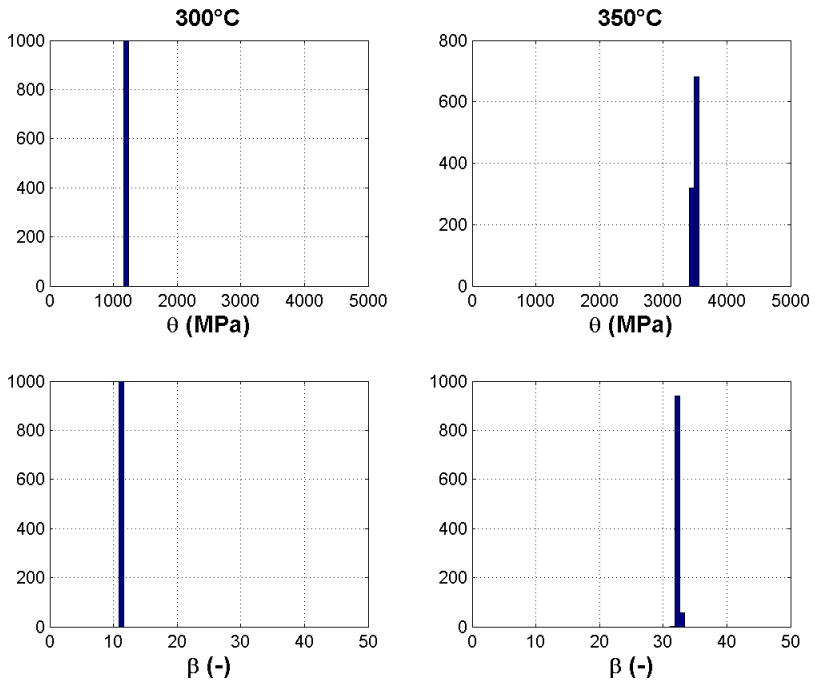

(c)

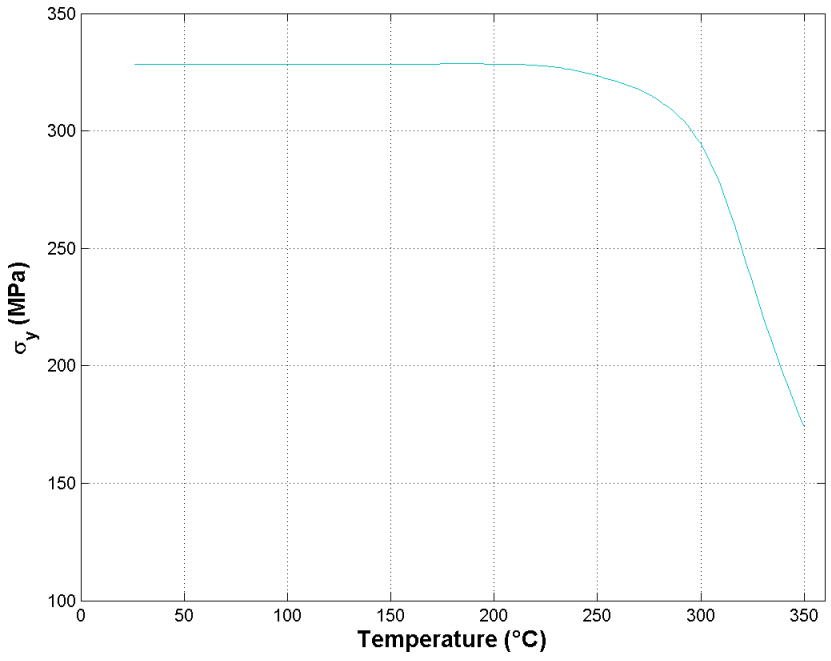

(d)

Fig. B-12. Monte Carlo analysis of k_β on AA6061-T651 constitutive model predictions.

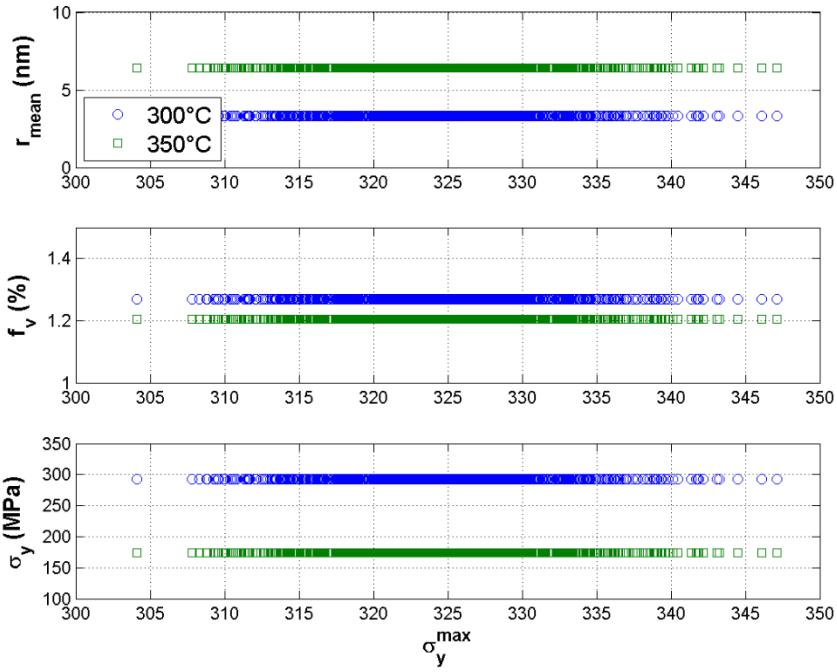

(a)

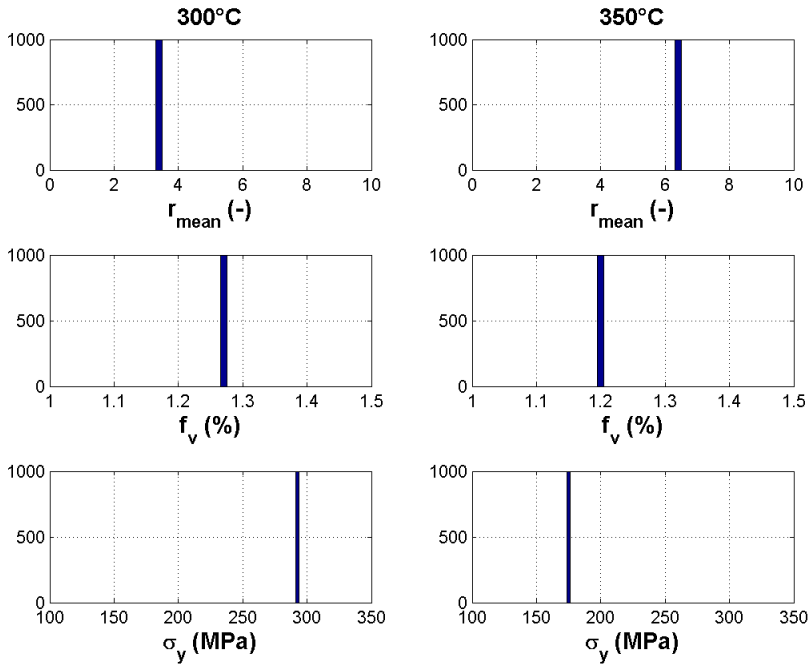

(b)

(Figure continued on next page)

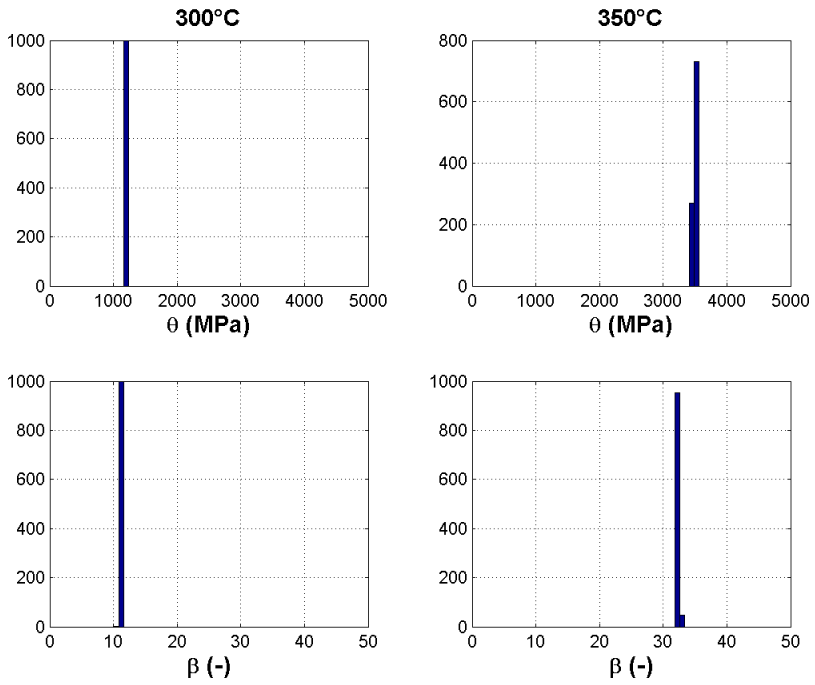

(c)

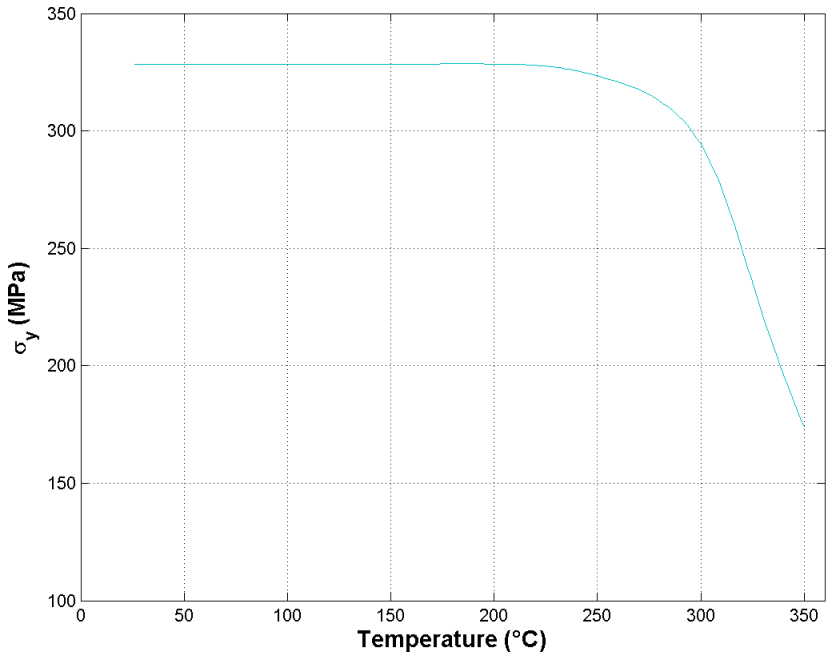

(d)

Fig. B-13. Monte Carlo analysis of $\sigma_y^{\max}$ on AA6061-T651 constitutive model predictions.

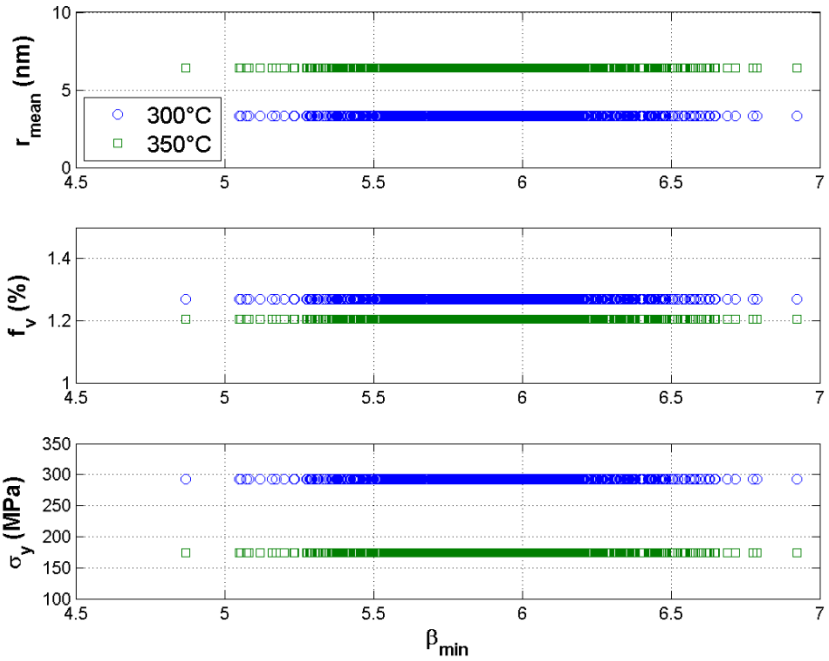

(a)

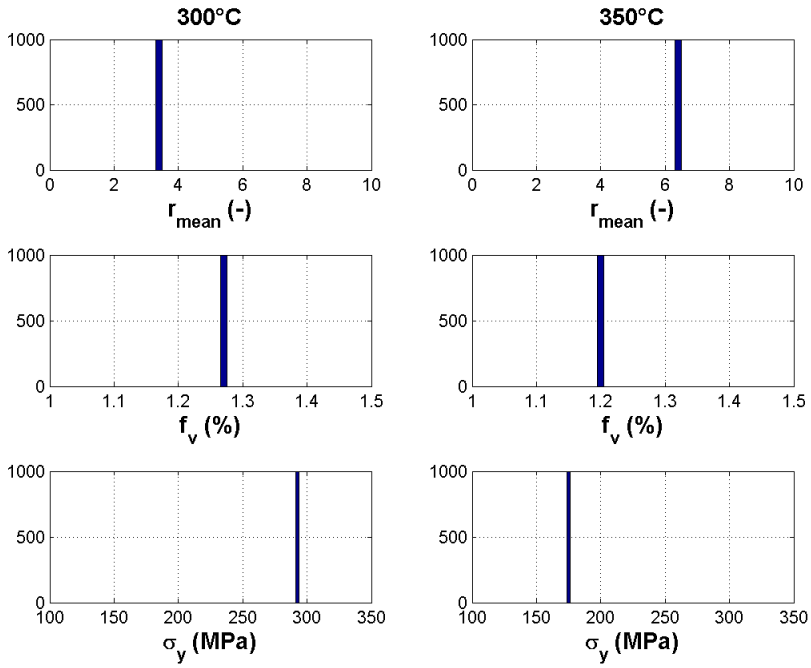

(b)

(Figure continued on next page)

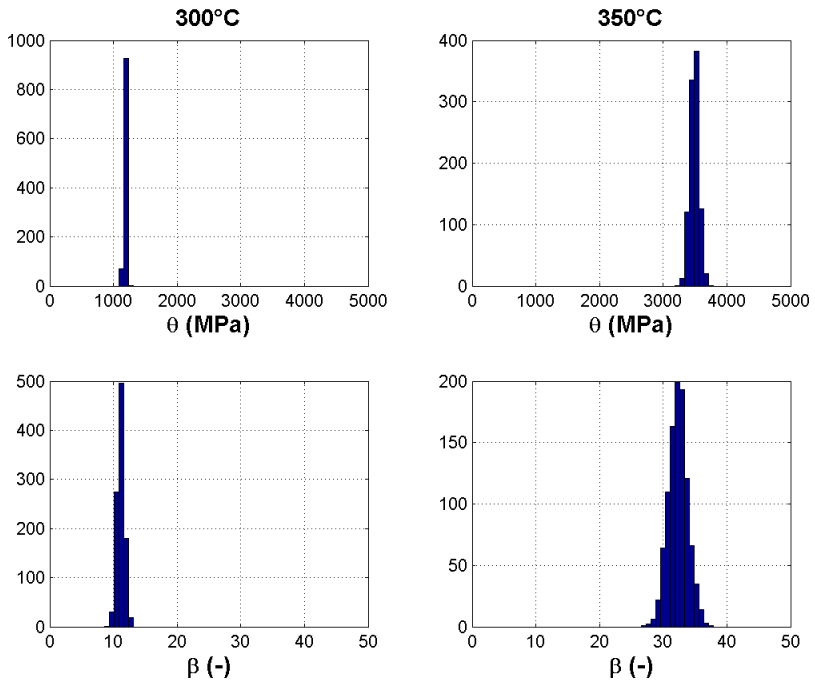

(c)

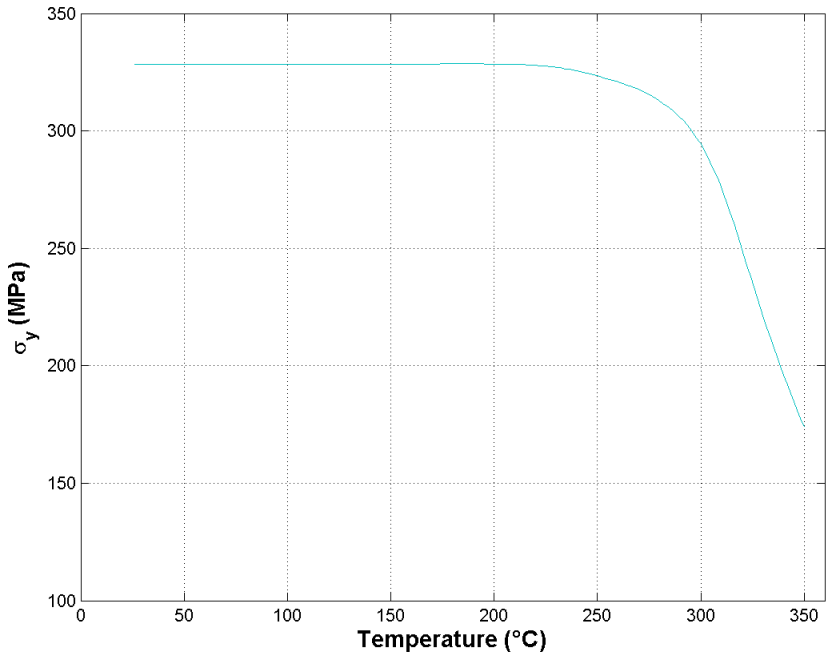

(d)

Fig. B-14. Monte Carlo analysis of β_{min} on AA6061-T651 constitutive model predictions.

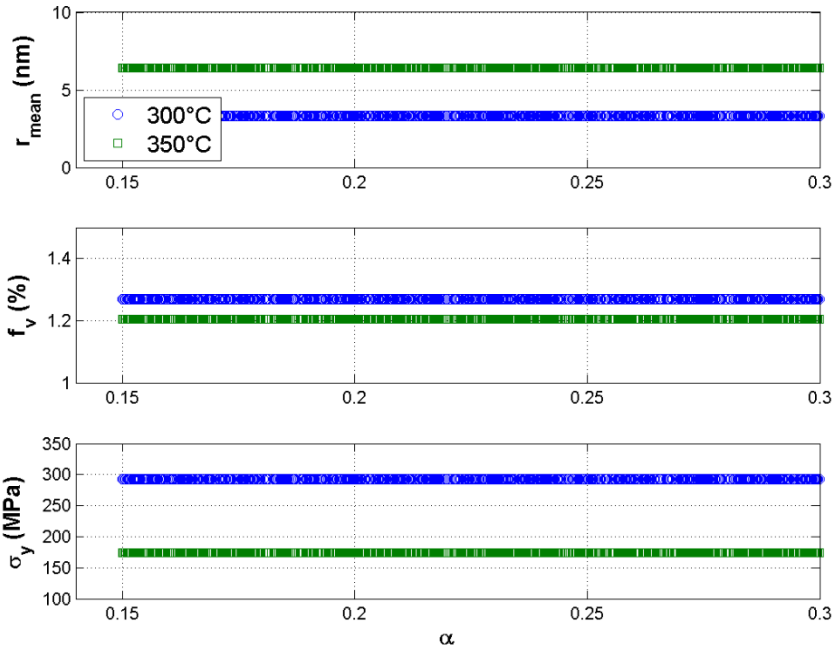

(a)

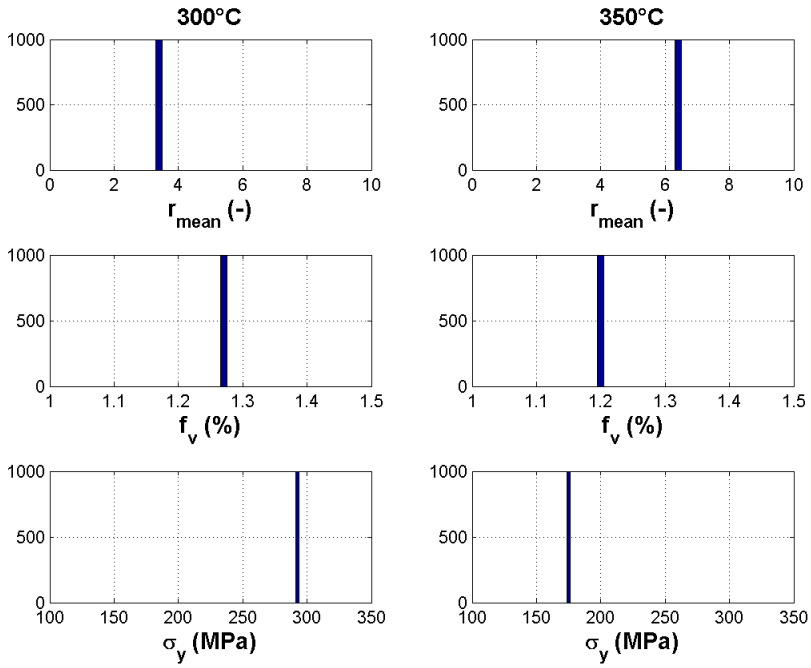

(b)

(Figure continued on next page)

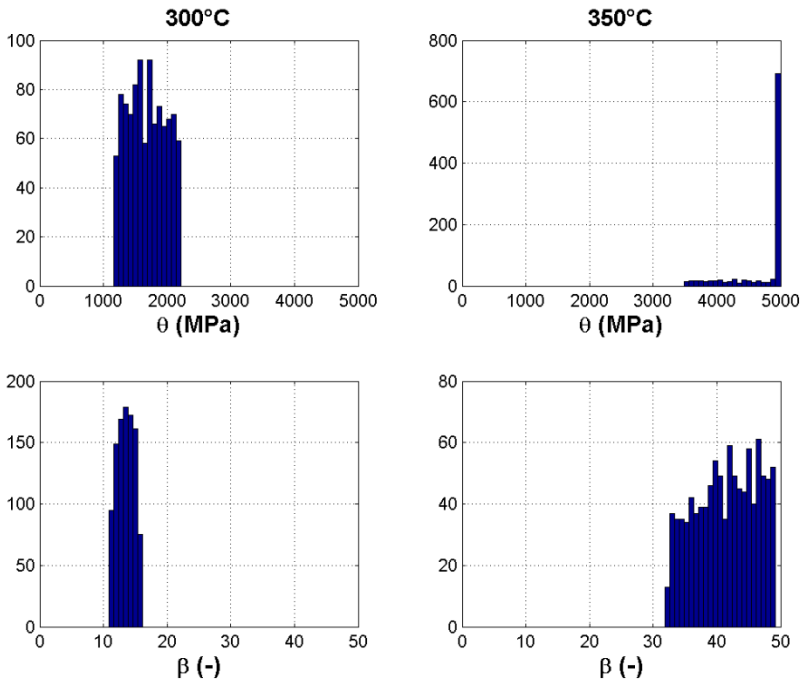

(c)

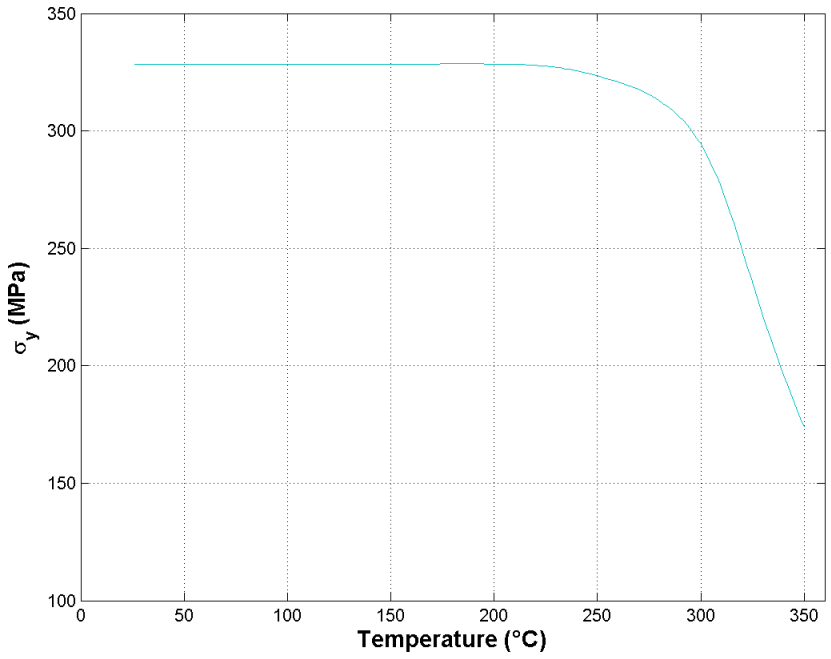

(d)

Fig. B-15. Monte Carlo analysis of α on AA6061-T651 constitutive model predictions.

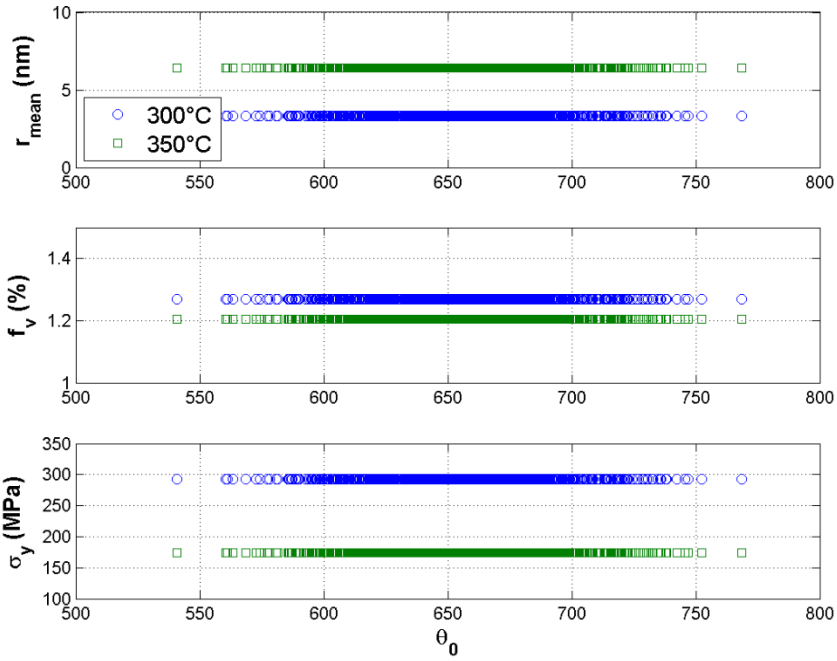

(a)

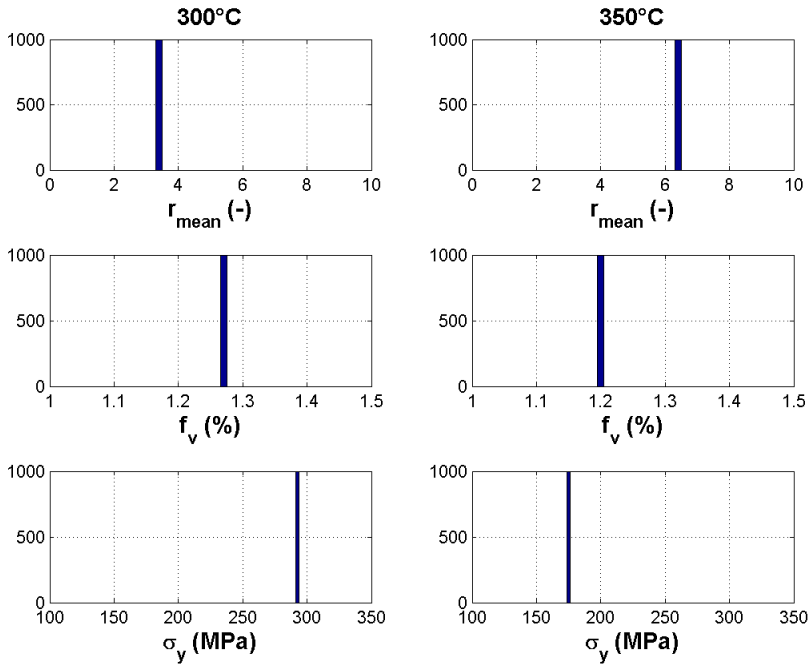

(b)

(Figure continued on next page)

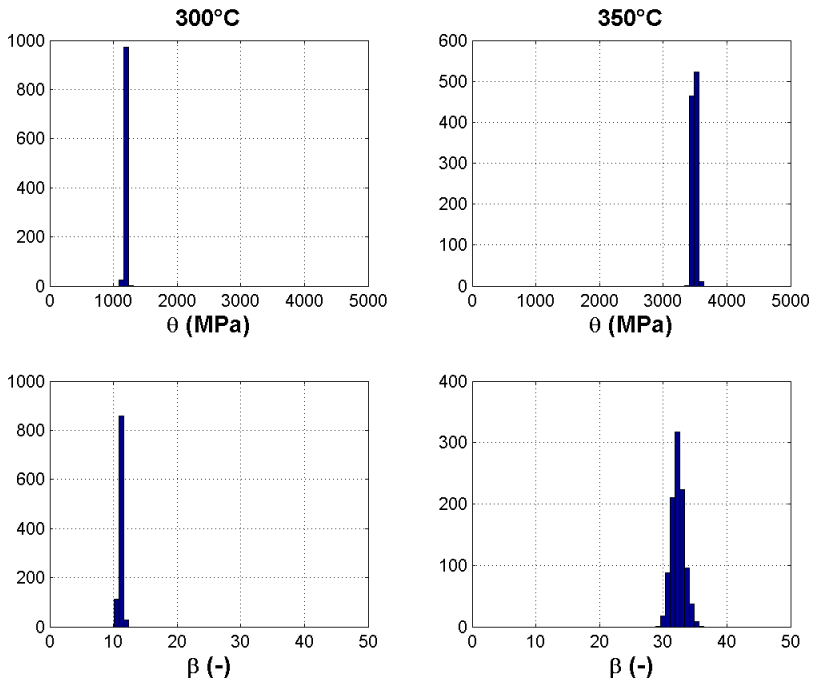

(c)

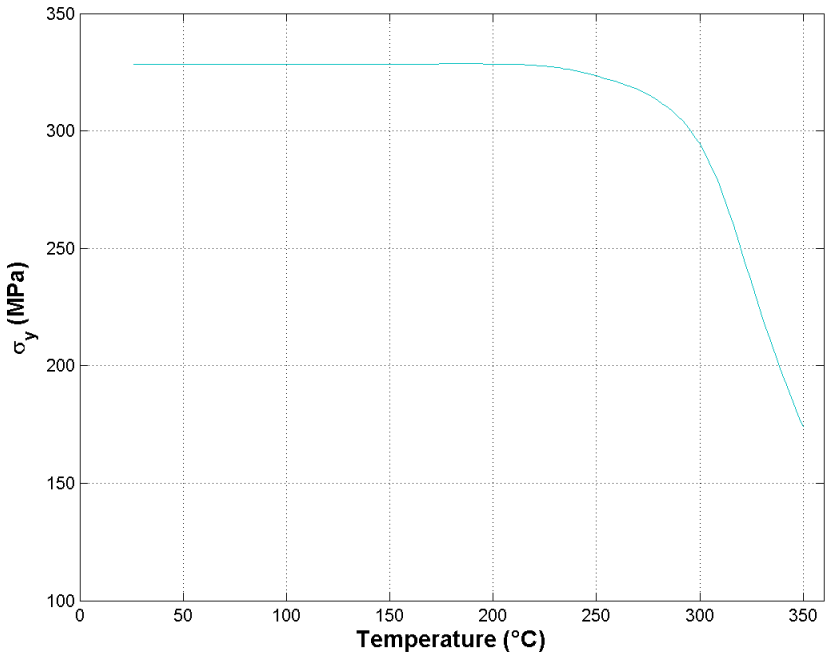

(d)

Fig. B-16. Monte Carlo analysis of θ_0 on AA6061-T651 constitutive model predictions.

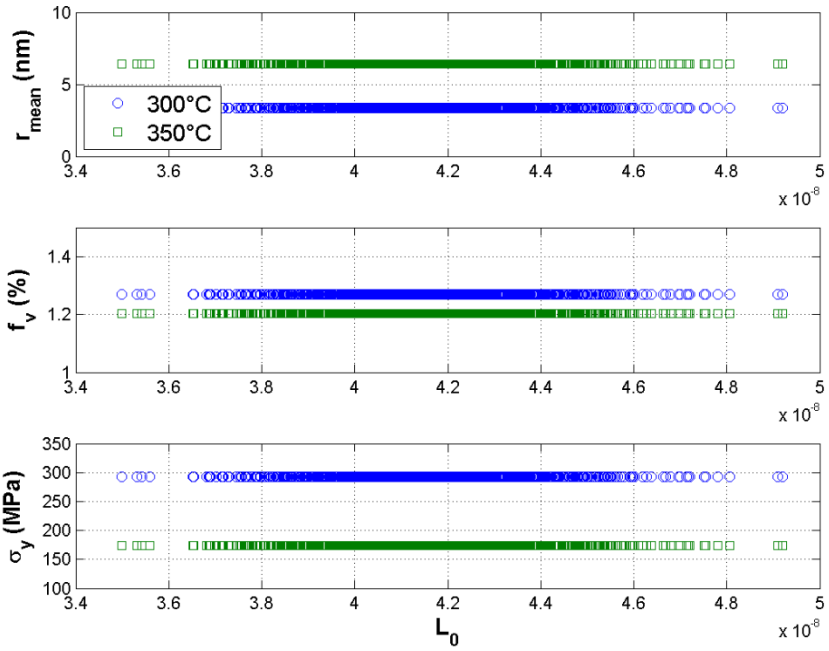

(a)

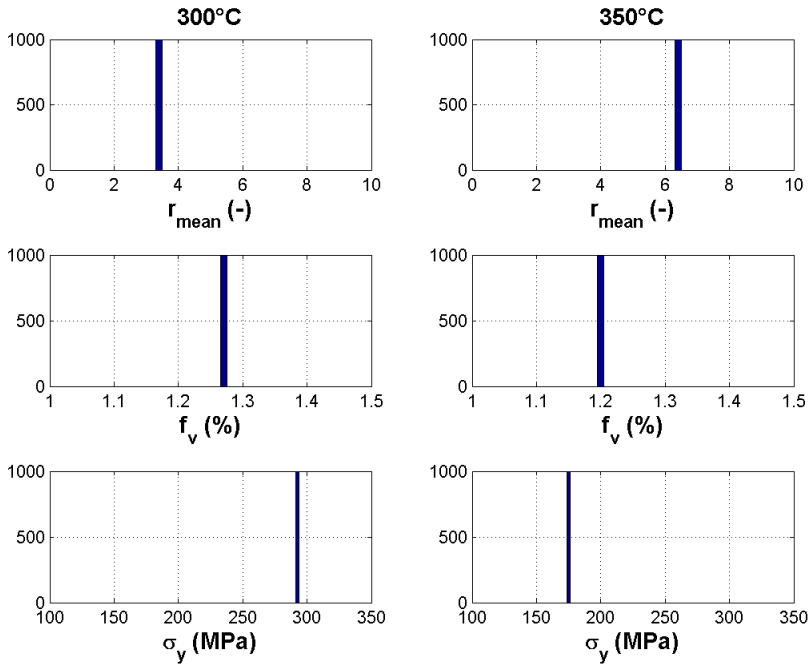

(b)

(Figure continued on next page)

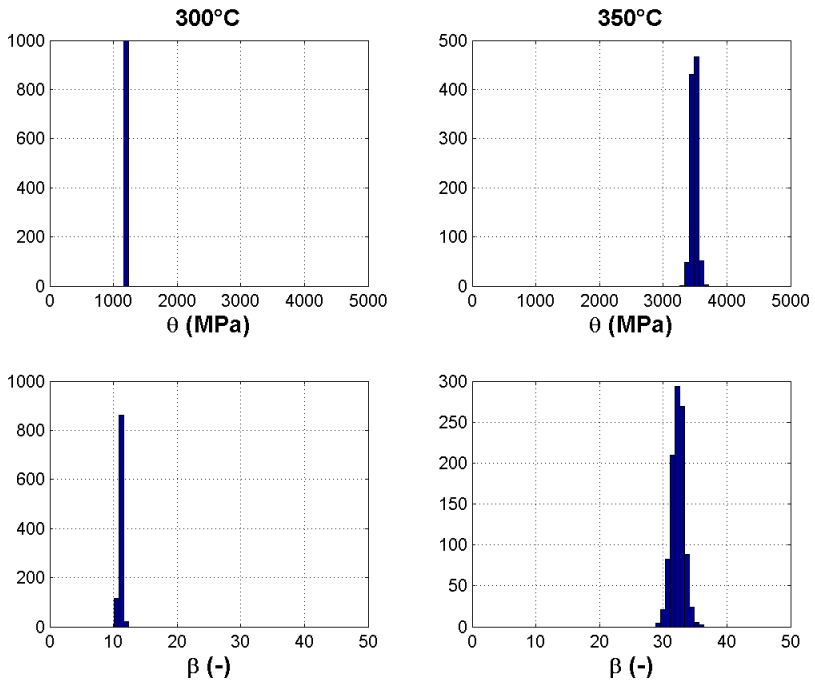

(c)

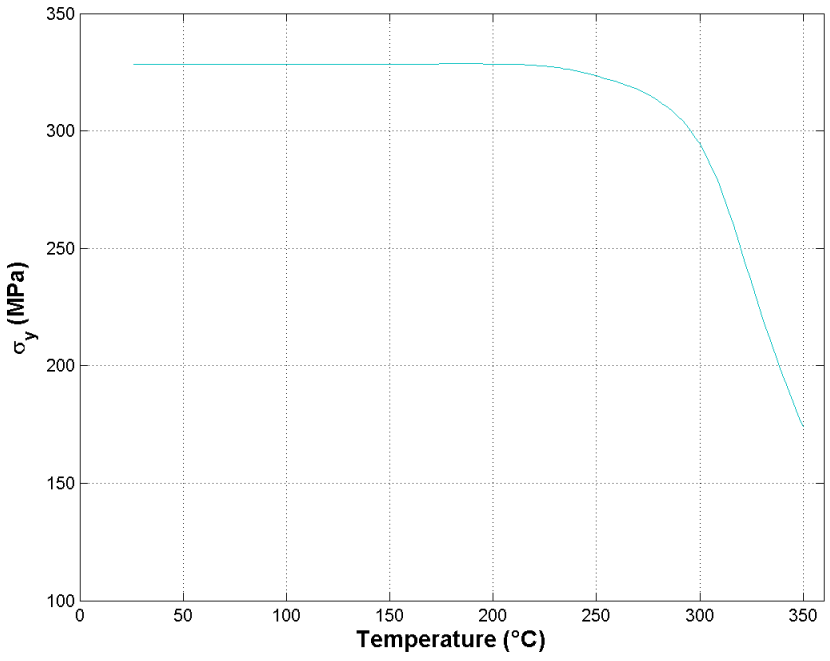

(d)

Fig. B-17. Monte Carlo analysis of L_0 on AA6061-T651 constitutive model predictions.

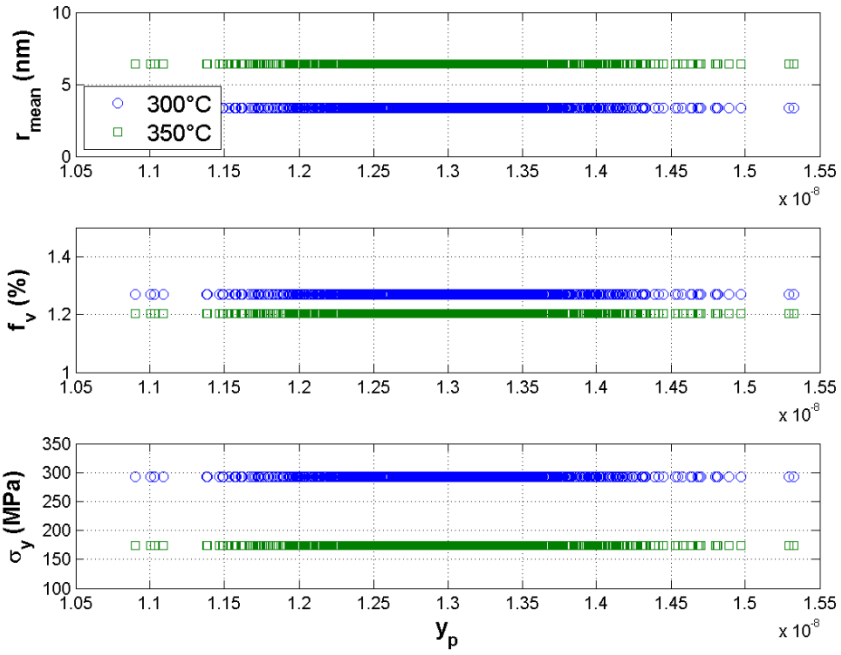

(a)

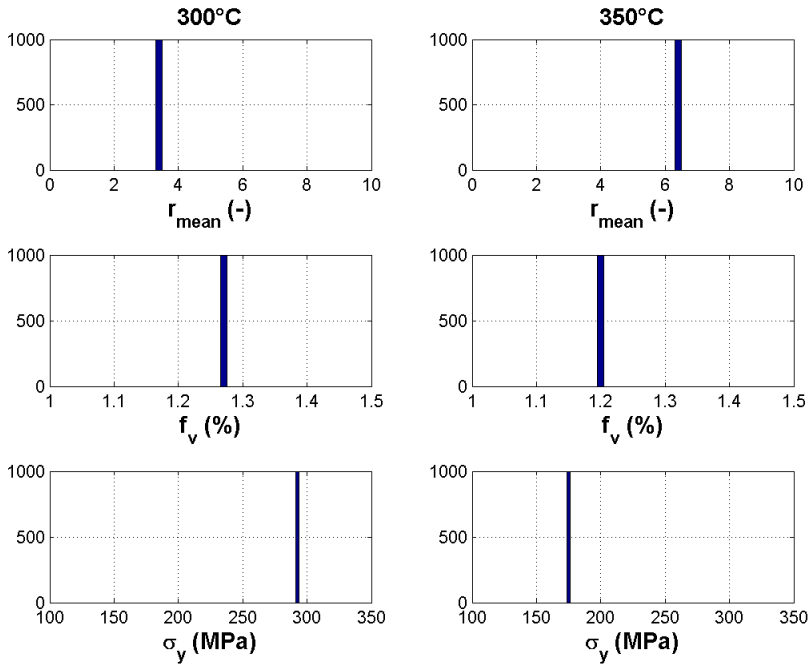

(b)

(Figure continued on next page)

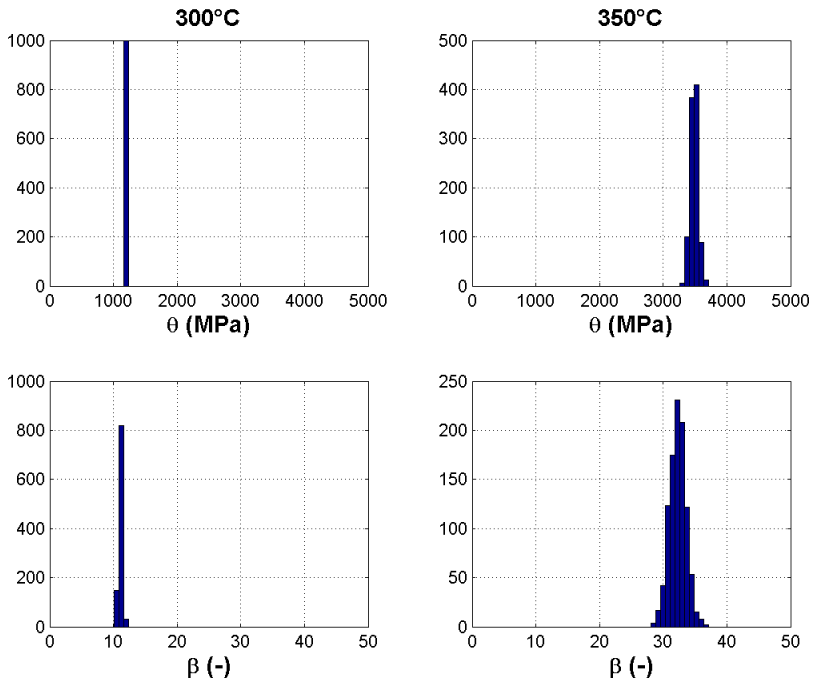

(c)

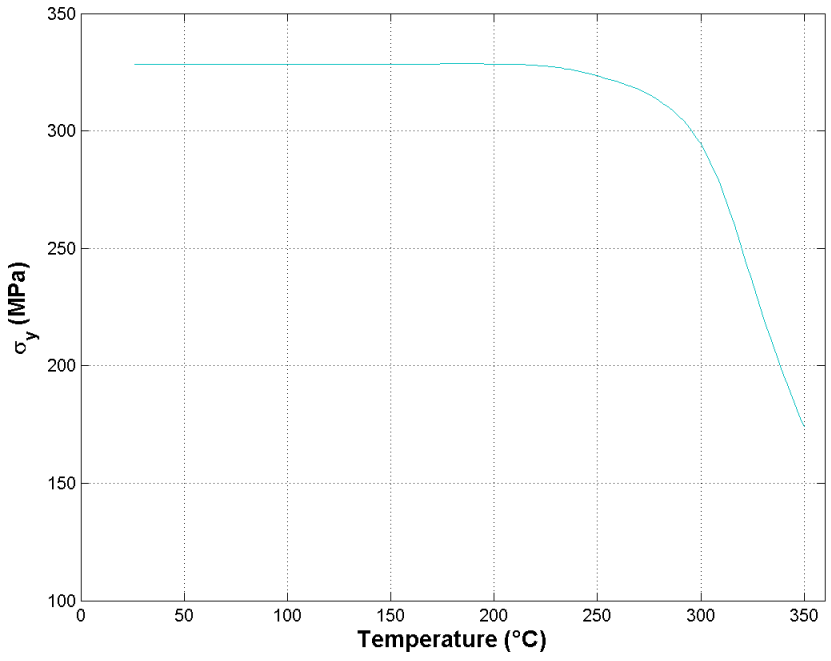

(d)

Fig. B-18. Monte Carlo analysis of y_p on AA6061-T651 constitutive model predictions.

Appendix C - Permissions

Virginia Tech ETD Fair Use Analysis Results

This is not a replacement for professional legal advice but an effort to assist you in making a sound decision.

Name: Patrick Summers

Description of item under review for fair use: 14 March 2014. <http://www.offshore-technology.com/contractor_images/bayards/5-bayards.jpg>.

Report generated on: 04-07-2014 at : 20:03:34

Based on the information you provided:

Factor 1

Your consideration of the purpose and character of your use of the copyright work weighs: ***in favor of fair use***

Factor 2

Your consideration of the nature of the copyrighted work you used weighs: ***in favor of fair use***

Factor 3

Your consideration of the amount and substantiality of your use of the copyrighted work weighs: ***in favor of fair use***

Factor 4

Your consideration of the effect or potential effect on the market after your use of the copyrighted work weighs: ***in favor of fair use***

Based on the information you provided, your use of the copyrighted work weighs: *in favor of fair use*

Fair use determination for Fig. 1.

Virginia Tech ETD Fair Use Analysis Results

This is not a replacement for professional legal advice but an effort to assist you in making a sound decision.

Name: Patrick Summers

Description of item under review for fair use: 15 March 2014.
http://www.nopsema.gov.au/assets/images/imagegallery/Image%20A149248.jpg.

Report generated on: 04-07-2014 at : 20:17:25

Based on the information you provided:

Factor 1

Your consideration of the purpose and character of your use of the copyright work weighs: ***in favor of fair use***

Factor 2

Your consideration of the nature of the copyrighted work you used weighs: ***in favor of fair use***

Factor 3

Your consideration of the amount and substantiality of your use of the copyrighted work weighs: ***in favor of fair use***

Factor 4

Your consideration of the effect or potential effect on the market after your use of the copyrighted work weighs: ***in favor of fair use***

Based on the information you provided, your use of the copyrighted work weighs: *in favor of fair use*

Fair use determination for Fig. 2.

Thank you very much for your order.

This is a License Agreement between Patrick Summers ("You") and Elsevier ("Elsevier"). The license consists of your order details, the terms and conditions provided by Elsevier, and the payment terms and conditions.

Get the printable license.

License Number	3337710943330
License date	Feb 28, 2014
Licensed content publisher	Elsevier
Licensed content publication	Materials Science and Engineering: A
Licensed content title	Effects of heat treatments on the microstructure and mechanical properties of a 6061 aluminium alloy
Licensed content author	D. Maisonnette,M. Suery,D. Nelias,P. Chaudet,T. Epicier
Licensed content date	15 March 2011
Licensed content volume number	528
Licensed content issue number	6
Number of pages	7
Type of Use	reuse in a thesis/dissertation
Portion	figures/tables/illustrations
Number of figures/tables/illustrations	1
Format	electronic
Are you the author of this Elsevier article?	No
Will you be translating?	No
Title of your thesis/dissertation	Microstructure-based Constitutive Models for Residual Mechanical Behavior of Aluminum Alloys after Fire Exposure
Expected completion date	May 2014
Estimated size (number of pages)	250
Elsevier VAT number	GB 494 6272 12
Permissions price	0.00 USD
VAT/Local Sales Tax	0.00 USD / 0.00 GBP
Total	0.00 USD

Elsevier figure use permission for Fig. 41.

Order Completed

Thank you very much for your order.

This is a License Agreement between Patrick Summers ("You") and Elsevier ("Elsevier"). The license consists of your order details, the terms and conditions provided by Elsevier, and the payment terms and conditions.

Get the printable license.

License Number	3337711036627
License date	Feb 28, 2014
Licensed content publisher	Elsevier
Licensed content publication	Acta Materialia
Licensed content title	Modelling of the microstructure and strength evolution in Al–Mg–Si alloys during multistage thermal processing
Licensed content author	O.R. Myhr,Ø. Grong,H.G. Fjær,C.D. Marioara
Licensed content date	4 October 2004
Licensed content volume number	52
Licensed content issue number	17
Number of pages	12
Type of Use	reuse in a thesis/dissertation
Portion	figures/tables/illustrations
Number of figures/tables/illustrations	1
Format	electronic
Are you the author of this Elsevier article?	No
Will you be translating?	No
Title of your thesis/dissertation	Microstructure-based Constitutive Models for Residual Mechanical Behavior of Aluminum Alloys after Fire Exposure
Expected completion date	May 2014
Estimated size (number of pages)	250
Elsevier VAT number	GB 494 6272 12
Permissions price	0.00 USD
VAT/Local Sales Tax	0.00 USD / 0.00 GBP
Total	0.00 USD

Elsevier figure use permission for Fig. 44.

Order Completed

Thank you very much for your order.

This is a License Agreement between Patrick Summers ("You") and Elsevier ("Elsevier"). The license consists of your order details, the terms and conditions provided by Elsevier, and the payment terms and conditions.

Get the printable license.

License Number	3337721052724
License date	Feb 28, 2014
Licensed content publisher	Elsevier
Licensed content publication	Acta Materialia
Licensed content title	Implementation of classical nucleation and growth theories for precipitation
Licensed content author	M. Perez,M. Dumont,D. Acevedo-Reyes
Licensed content date	May 2008
Licensed content volume number	56
Licensed content issue number	9
Number of pages	14
Type of Use	reuse in a thesis/dissertation
Portion	figures/tables/illustrations
Number of figures/tables/illustrations	1
Format	electronic
Are you the author of this Elsevier article?	No
Will you be translating?	No
Title of your thesis/dissertation	Microstructure-based Constitutive Models for Residual Mechanical Behavior of Aluminum Alloys after Fire Exposure
Expected completion date	May 2014
Estimated size (number of pages)	250
Elsevier VAT number	GB 494 6272 12
Permissions price	0.00 USD
VAT/Local Sales Tax	0.00 USD / 0.00 GBP
Total	0.00 USD

Elsevier figure use permission for Fig. 45.